Variably saturated flow through discrete open fractures: Experimental contributions using Geotechnical Centrifuge Modelling

by

Brendon Ronald Jones

10436121

UNIVERSITEIT VAN PRETORIA
UNIVERSITY OF PRETORIA
YUNIBESITHI YA PRETORIA

Engineering Geology and Hydrogeology
Department of Geology
Faculty of Natural and Agricultural Sciences
University of Pretoria

Submitted in accordance with the requirements for the degree of Doctor of Philosophy
(Ph.D. Engineering Geology)

February 2019

Study Supervisor: Prof J. Louis Van Rooy
Study Co-Supervisor: Dr Matthys A. Dippenaar

The financial assistance of the National Research Foundation (NRF) towards this research is hereby acknowledged. Opinions expressed and conclusions arrived at, are those of the author, and are not necessarily to be attributed to the NRF.

This study was undertaken in the Engineering Geology and Hydrogeology Section of the Department of Geology, Faculty of Natural and Agricultural Sciences, University of Pretoria, under the supervision of Prof J. Louis Van Rooy and Dr Matthys A. Dippenaar.

The thesis represents original work by the author and has not otherwise been submitted in any form for any degree or diploma to any tertiary institution. Where use has been made of the work of others, it is duly acknowledged in the text.

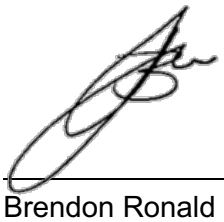

Brendon Ronald Jones
10436121

Date: 15 February 2019

As the candidate's supervisor and co-supervisor, we have respectively approved this thesis for examination.

Prof. J. Louis Van Rooy

Date: 15 February 2019

Dr. Matthys A. Dippenaar

Date: 15 February 2019

ABSTRACT

Implications of improved understanding of partially saturated flow in jointed rock masses are numerous, especially given the complexity, heterogeneity and anisotropy of the intermediate fractured vadose zone. One such implication is the quantification of water movement for engineering purposes. This thesis aims to contribute to the understanding of variably saturated flow through discrete open fractures as it applies to rock engineering and geotechnical engineering applications. The initial phase comprises the analyses of results from Lugeon tests conducted at De Hoop Dam that guide a subsequent experimental phase by identifying field parameters and relationships that influence variably saturated flow processes. The series of flow visualisation experiments are developed using transparent smooth parallel fracture replicas with differing flow rates and inclinations, modelled in a geotechnical centrifuge. The findings show that the geotechnical centrifuge is a viable experimental tool for the replication of variably saturated fracture flow mechanisms. Additionally, it was found that preferential flow occupies the minority of the cross-sectional area despite the flux, and that flow becomes a matter of the continuity principle requiring substantially higher flow rates given the very low degree of saturation. Furthermore, these preferential paths are characterised by non-Darcian flow, which can be successfully evaluated using the Forchheimer relationship. The relevance of how flow occurs through fractures at partial saturation in the engineering context is understated, especially given the quest to achieve better quantification of in-situ tests during site investigations. The results prove that using common Darcian-based empirical correlations to define hydraulic conductivities from in-situ tests is cautioned. Furthermore, these volume-effective approaches do not contribute to fundamental research and require a deeper understanding of the small-scale processes in the intermediate fractured vadose zone. The design of infrastructure therefore cannot be optimised without a thorough understanding of the complex flow conditions in natural and engineered rock masses.

TABLE OF CONTENTS

LIST OF FIGURES

LIST OF TABLES

CHAPTER 1 INTRODUCTION

1.1 Rationale

The intermediate fractured vadose zone comprises rock masses at partial saturation. Flow through this unsaturated rock mass cannot be quantified through commonly applied saturated approaches and needs to be addressed for varying saturation and flow path characteristics. In this fractured region above the water table, the water phase within a fracture is usually at a negative potential, and cannot completely fill the void space, with the remainder of the fracture being filled by air (Zimmerman and Yeo, 2000). These mixed air-water flows behave differently from water-saturated systems, whereby the most notable implication of partial saturation of fracture networks is that gravity does not necessarily force water down near-vertical discontinuities (Dippenaar and Van Rooy, 2016). Although within individual fractures, gravity will play a first-order role in creating vertically extensive liquid phase structures, subsequent fracture intersections, for example, act as capillary barriers that restrict matrix communication (Nicholl et al., 1994).

While surface water and groundwater parameters are readily available, variably saturated flow through soil and rock media is either oversimplified or estimated as input for hydrogeological models. The general approach is to view these fractured systems as bulk systems where flow occurs through fracture networks with possible contribution from the matrix hydraulic conductivity. However, a number of critical parameters (e.g. orientation, aperture, roughness, infill, persistence, connectivity or continuity, and spacing) influence flow through rock fracture networks (e.g. Berkowitz, 2002; Méheust and Schmittbuhl, 2001) with fracture characteristics being the most important variables in the system. Partially saturated fracture flow and the influence of fracture or discontinuity geometry have subsequently been identified as key research questions by, for instance, Berkowitz (2002) and Neuman (2005).

The investigation of unsaturated, two-phase, fracture flow made several advancements during the proposed geologic isolation of high-level radioactive waste in unsaturated fractured rock at Yucca Mountain, in Nevada, USA (see for e.g. Bodvarsson et al., 1997; Ebel and Nimmo, 2009; Fabryka-Martin et al., 1996; Nicholl and Glass, 2007; Nicholl and Glass, 2002). Nicholl and Glass (2007) state that commonly used numerical models are based on conceptual models of flow and transport through unsaturated fractured rock. The authors further emphasise that the exploration of flow in individual fractures is a necessary step towards the construction of improved conceptual models that are consistent with real world flow processes.

Glass et al. (2002a) state that in order to correctly incorporate the findings of these processes into conceptual models applicable to the field, it is crucial to first understand how processes at the local scale (i.e. a single fracture or single fracture–matrix system) combine to determine behaviour at larger scale (i.e. fracture–matrix network). Field observations alone are insufficient to test the hypothesised causes and subsequent behaviour of large scale

preferential pathways. Instead, mesoscale experiments (one to several meters) are required where critical system parameters can be controlled and varied so that network scale behaviour may be understood systematically (Glass et al., 2002a).

The results of experiments by Wood et al. (2004) suggest that common modelling approaches cannot reproduce the behaviour of the experimental results, because they cannot duplicate the non-ideal, dynamical behaviour observed in experiments. There has therefore been a growing body of evidence calling for a paradigm shift in conceptualizing unsaturated flow within the fractured vadose zone (Wood, 2005). Conceptualising flow in fractured rock networks in a volume averaged manner (i.e. bulk system), as commonly assumed, may be incorrect due to significant variation in the location and flux of network discharge that may occur without any apparent external causes (Wood, 2005).

Considering the above, and the realisation that bulk flow generalises fluxes on a more regional scale, further research therefore needs to focus almost exclusively on discrete fractures with the purpose of contributing to the questions as to which properties govern flow. The Cubic law is mostly employed for purposes of quantifying flow through individual fractures and relates the estimated hydraulic conductivity to the cube of the fracture aperture, provided that the fracture is clean, smooth, parallel and completely saturated. The highest estimate of hydraulic conductivity is subsequently represented by the Cubic law and the lowest by incorporation of the matrix conductivity and infill conductivity (see Hoek and Bray, 1981). The validity of the Cubic law; however, is often queried given the difficulty in achieving laminar flow as discontinuities are rarely smooth, parallel and open.

The implications of improved understanding of variably saturated flow are numerous, especially given the complexity, heterogeneity and anisotropy of the intermediate fractured vadose zone. One such implication is the quantification of water movement for engineering purposes. Lugeon tests are the most common method used to assess the permeability of rock masses for engineering purposes (e.g. reservoirs and tunnels) and were primarily developed to determine groutability of dam foundations. However, uncertainties will arise through the often-unsaturated state of the rock mass, and the associated complexity of flow regimes and flow mechanisms in such unsaturated fractured geologic media as outlined above. Both Ewert (1997a) and Widmann (1996) emphasised the uncertainties pertaining to Lugeon tests, and called early on for the better quantification and characterisation of flow path geometries, with limited studies that subsequently builds on the authors requests.

The typical experimental approach comprises the physical modelling of fluid flow through artificial or natural fractures, simulated at a smaller laboratory scale (e.g. Brouwers, 2017; Segole, 2018). Physical models allow one to directly measure or observe the influence that different fracture properties will have on the flow of fluid. If the model is proportionately scaled and one is aware of the assumptions made and their implications on the modelling results, then the model may ultimately be regarded as a representative simplification of the real system (Silberhorn-Hemminger et al., 2005b). If the model is considered to be representative, then the results will aid greatly to the understanding of fluid flow through geologic media. Small

scale physical models offer the user maximum control of the boundary conditions and the tests are more repeatable and less costly than large scale tests (Taylor, 1995).

Geotechnical centrifuge modelling has developed into an important physical modelling tool due to its ability to replicate natural stress conditions in a reduced-scale model, allowing for many complex interaction problems to be investigated. Centrifuge modelling is unique in that the most complex numerical models are only mathematical approximations of reality, while physical modelling negates the need for complex constitutive models to be selected (Jacobsz, 2013a). Unlike constitutive models, no assumptions need to be made, or are otherwise well understood, and an actual physical event can be observed at model scale (Jacobsz, 2013a). Notwithstanding, centrifuge modelling of soil behaviour has received much more attention than the modelling of rock masses. Consequently, the available published research that deals with fluid flow through a rock mass is scarce and limited to transport studies and petroleum industry research. The use of a geotechnical centrifuge applied to unsaturated and fractured systems are, therefore, two important research questions in their own rights.

1.2 Aim and Objectives

The aim of this thesis is to contribute to the understanding of variably saturated flow in discrete open discontinuities as it applies to rock engineering and geotechnical engineering applications.

The scope of work for this thesis is outlined by the following set of objectives:

i. Investigate the link between field permeability parameters and relationships, with variably saturated flow processes at laboratory scales;
ii. Asses the validity of using the geotechnical centrifuge in modelling variably saturated fracture flow using a series of appropriately produced fracture replica models at accelerated conditions;
iii. Identify and suggest new permeability relationships for variably saturated flow, from the findings of the experimental models to the field case study, and the subsequent influence they have on appraising rock mass permeability for rock engineering and geotechnical engineering applications.

1.3 Methodology

1.3.1 Literature Review

A review of the literature related to the research was carried out. This review covered the flow of fluid through discrete fractures and the quantification of flow using the Cubic law, Reynolds number, and the Forchheimer relationship. Furthermore, previous experimental studies investigating partially saturated flow mechanisms are outlined. Structural data gathering for assessing rock mass permeability and the assessment of rock mass permeability for engineering applications summarise the current field techniques. Lastly, aspects of previous research on geotechnical centrifuge modelling pertaining to the modelling of flow and fractures within rock masses is illustrated.

1.3.2 Identification of Discontinuity Parameters Influencing Field Permeability Relationships from a Case Study

Data is obtained from detailed foundation mapping and Lugeon-tests conducted during the construction of the dam wall and grouting operations at De Hoop Dam, in South Africa. These Lugeon-test results are used to calculate the Secondary Permeability Index (SPI), and zone the foundation rock mass accordingly. Additionally, results from boreholes drilled along the dam wall axis during the final detailed exploration phase were used to supplement the results. A back-analyses was thereafter conducted to verify the ground treatments as proposed by the SPI. The results of the back-analysis and verification were used to identify pertinent discontinuity characteristics within the foundation rock mass, with regards to its permeability, and were subsequently used to guide the development of the experimental models.

1.3.3 Experimental Studies

The experimental data collection involves the design and construction of a series of fundamental models in order to qualitatively define flow in discrete fractures pertaining specifically to partially saturated conditions. The initial experimental models comprise flow visualisation experiments conducted on transparent replicas of smooth parallel plates with inlet conditions of constant pressure and differing flow rates over both vertical and horizontal inclination. Furthermore, these fundamental fracture replica models were further complicated by modelling flow from such fractures into their subsequent intersections.

The final experimental phase investigated the flow behaviour when conducting Lugeon tests under conditions of variable saturation in an initially dry free-draining, smooth, clean, open, discrete fracture. The geometry of the flow paths within the fractures is qualitatively or quantitively examined, whilst the flow rate is measured under a series of ascending and descending pressure intervals in order to quantify the flow behaviour. All models are constructed using acrylic Plexiglass sheets.

1.3.4 Analyses of Experimental Results

In addition to qualitatively or quantitatively assessing the geometry of flow paths within the fracture models, the series of experiments seek to investigate the validity of the Cubic law under variable saturation in initially dry free-draining discrete fractures. It is understood that the Cubic law is not intrinsically applicable to unsaturated systems. However, part of the aim of this study was to investigate the wetting of initially dry horizontal and vertical fractures and their intersections. Whether fractures in the experimental setup detailed in this thesis will truly saturate completely will determine whether the Cubic law applies at all.

A significant objective of this project intends to assess geotechnical centrifuge modelling relevant to partial saturation in the fractured vadose zone. In order to assess the use of geotechnical centrifuge modelling, the research seeks to highlight the potential implications for using the geotechnical centrifuge in answering practical problems associated with variably saturated flow. This alone highlights the extreme novelty of this research.

The final analyses of the experimental proponent investigates the use of non-linear (non-Darcian) flow models, which are commonly applied to saturated rough-walled fractured, to describe and quantify non-linear flow during Lugeon testing. The Forchheimer relationship is used to predict the flow rate at the imposed hydraulic heads in the model, and are compared to the measured flow rates. Such empirical and experimental contributions highlight the need for an improved interpretation and understanding of the behaviour of flow in discrete fractures during Lugeon tests under conditions of partial saturation.

1.4 Research Outcomes and Publications

The bulk of the content of this thesis has been published. Articles published in international peer-reviewed journals, as well as full-length papers published in international peer-reviewed conference proceedings, forming part of and emanating from this thesis include:

- JONES, B. R., BROUWERS, L. B., DIPPENAAR, M. A., AND VAN ROOY, J.L. (2017a) Experimental studies of variably saturated flow from a horizontal discontinuity to the vertical with and without an intersection. *In:* JOUGHIN, W. (ed.) *AfriRock 2017 ISRM International Symposium 'Rock Mechanics for Africa'*. SAIMM, Cape Town, South Africa, 605-618.
- JONES, B. R., BROUWERS, L. B., VAN TONDER, W. D. AND DIPPENAAR, M. A. (2017b). Assessing geotechnical centrifuge modelling in addressing variably saturated flow in soil and fractured rock. *Environmental Science and Pollution Research,* 24(15), 13203-13223, doi:10.1007/s11356-016-8333-2.
- JONES, B. R., BROUWERS, L. B. AND DIPPENAAR, M. A. (2018a). Partially to fully saturated flow through smooth, clean, open fractures: qualitative experimental studies. *Hydrogeology Journal,* 26(3), 945-961, doi:10.1007/s10040-017-1680-3.
- JONES B.R., VAN ROOY, J.L., AND DIPPENAAR, M.A. (2018b). Lugeon tests at partial saturation: Experimental and empirical contributions, *Rock Mechanics and Rock Engineering*, doi: 10.1007/s00603-018-1592-0
- JONES B.R., VAN ROOY, J.L., AND DIPPENAAR, M.A. (2018c). On the Differing Role of Contact Obstacles on Variably Saturated Flow in Vertical and Horizontal Fractures. *In:* CATO, K AND SHAKOOR, A. (eds.). *IAEG/AEG Annual Meeting Proceedings*, San *Francisco, California, September 2018*, doi: 10.1007/978-3-319-93133-3_11
- JONES B.R., VAN ROOY, J.L., AND MOUTON, D.J. (2018d) Verifying the Ground Treatment as Proposed by The Secondary Permeability Index during Dam Foundation Grouting. *Bulletin of Engineering Geology and the Environment,* 1-21, doi: 10.1007/s10064-017-1219-9

Additionally, the following research reports as well as international conference abstracts and presentations formed part of the research:

- JONES B.R., VAN ROOY, J.L., DIPPENAAR M.A., BROUWERS L.B., ROUX J.I., JOUBERT A., AND SEGOLE K.P. (2016) Advances in the Understanding of Variably Saturated Fracture Flow, *WRC Report TT, Pretoria, South Africa*

- JONES B.R., BROUWERS L.B., AND DIPPENAAR M.A. (2016) Experimental Studies on the Smooth Parallel Plate Model Addressing the Validity of the Cubic Law under Conditions of Variable Saturation. *35th International Geological Congress, Cape Town;*
- BROUWERS L.B., DIPPENAAR M.A., AND JONES B.R. (2016) Flow regime comparison of a single clean smooth parallel fracture with and without overlying material in variably saturated conditions. *Proceedings 35th International Geological Congress, Cape Town;*
- JOUBERT A., JONES B.R., AND VAN ROOY, J.L. (2016) Finite Difference Modelling of Seepage in a Region of the Foundation Rock Below a Concrete Gravity Dam Wall, *Proceedings 35th International Geological Congress, Cape Town; and*
- JONES B.R., BROUWERS L.B., DIPPENAAR M.A. AND VAN ROOY, J.L. (2016) Advances to the Modelling of Variably Saturated Fracture Flow using the Geotechnical Centrifuge in South Africa, *Proceedings 35th International Geological Congress, Cape Town.*

1.5 Thesis Structure

This thesis comprises a number of published peer-reviewed papers. The publications have been used verbatim. Supporting information and data are available in the referenced literature, and detailed information is supplied in the publications as cited throughout. The thesis is structured such that the methods, results, and analyses for each experiment is grouped together, which allows a complete experiment to be followed without interruption. This greatly improves readability and allows for the final discussion to combine all findings into a suitable conclusion addressing the significance and novelty of the research.

The final discussion is intended solely to motivate for the use of given methods and elaborate on critical contributions to the science of unsaturated flow in fractured rock masses. Therefore, there are no distinct sections on the results and subsequent discussions (such as would be expected in a traditional thesis format), given the publications validated methodologies and case studies in internationally peer-reviewed papers and research reports.

Chapter 1: Introduction

The background to the research is explained and the aims and objectives are stated. The approach and methodology adopted are also stated.

Chapter 2 to Chapter 4: Literature Review

A literature review serves as a research basis to a thesis. A perusal of literature was conducted in order to gain knowledge on previous studies with regard to unsaturated fracture flow, field permeability techniques, and geotechnical centrifuge modelling in flow and rock masses.

Chapter 5: Materials and Methods

The collective approach of the research methodology is introduced and sets a basis for the experiment-specific set-up, procedure, and analyses that are stated within the subsequent

experimental chapters. The method of data collection for field studies as well as the materials used to model the experiments, together with the apparatuses are outlined.

Chapter 6: Rock Mass Permeability at De Hoop Dam

The data during obtained during detailed foundation mapping and Lugeon-tests at De Hoop Dam are presented and analysed. The data is back-analysed, and the ground treatments as proposed by the Secondary Permeability Index (SPI) verified. The results of the back-analysis and verification were used to identify discontinuity characteristics dictating the permeability of the foundation rock mass. These findings were subsequently used to guide the development of the experimental models.

Chapter 7 to Chapter 10: Experimental Models

The procedure for each experimental model is outlined, including the model conceptualisation phase and preparation. The process followed for the model construction is stated, together with any problems experienced. Data gathered from the experimental tests as well as case studies is presented. Qualitative data from the visuals obtained during the tests are introduced in order to identify flow mechanisms, and quantitative data measured in the model is presented. The data from the tests as well as the observed flow mechanisms is analysed and discussed.

Chapter 11: Discussion

The findings from all the experimental models are compared. The observed flow mechanisms and flow data between the tests are outlined. The discussion motivates for the use of the given methods and elaborate on critical contributions to the science of unsaturated flow in fractured rock masses. Thereafter, the critical findings, their implication and application to practical rock engineering and hydrogeological practices, as well as way forward is discussed.

Chapter 12: Conclusion

The research is concluded by providing a set of closing remarks, which satisfy the original objectives of the study. These final comments intend answering the original rationale of the research.

CHAPTER 2 THE CUBIC LAW, REYNOLDS NUMBER, FORCHHEIMERS LAW AND PARTIALLY SATURATED FRACTURE FLOW MECHANISMS

2.1 Introduction

The intermediate fractured vadose zone comprises rock masses under conditions of partial saturation. Flow through such unsaturated rock masses cannot be quantified through commonly applied saturated approaches and needs to be addressed for varying saturation and flow path characteristics. The evaluation of flow through discontinuities at moisture conditions below saturation therefore pose certain challenges. One such challenge is the change in the stage of weathering and discontinuity development that define the primary and secondary porosity.

Moreover, it is the geometry of individual discrete fractures that dictate such challenges, and is generally related to the continuity, persistence, roughness and aperture; and *in-situ* stress conditions, including overburden stresses or induced changes (Dippenaar and Van Rooy, 2016). The following chapter introduces the common quantitative approaches that describe fracture flow under saturated conditions. Such saturated approaches include Darcy's law, the smooth parallel plate model and associated Cubic law, Reynolds number, and Forchheimers law that describes non-Darcian (non-linear) flow.

Thereafter, the chapter seeks to evaluate the influence of individual joint parameters on flow under conditions of partial saturation, highlighting the constraints on the Cubic law and other saturated approaches. Although several models describing flow in fractured medium exist (i.e. double porosity model, discrete fracture network model etc.), only the fundamental parallel plate model is considered in this literature perusal.

2.2 Saturated Hydraulic Conductivity

Rock masses consist of intact rock divided by discontinuities to form rock structures. Both have differing porosity characteristics. If one considers the rock mass as the fractured media, then seepage occurs both through the matrix (the intact rock blocks), and fractures (the discontinuities that divide these blocks). Fractures are characterised by low mean porosity but great lateral continuity, whilst a matrix has a larger porosity and shorter spatial continuity (Singhal and Gupta, 2010). The hydraulic conductivity of the fracture or discontinuity (K_f) and of the hydraulic conductivity of the intact rock matrix (K_m) should vary considerably, where fractures are perceived as pathways of low resistance through which most of the groundwater flow occurs (Singhal and Gupta, 2010). The intact rock material poses a much greater resistance to flow as the water needs to pass through the small interstitial pore spaces

(Dippenaar and Van Rooy, 2016). The conductivity of a rock mass can therefore be considered the sum of the matrix (primary) and fracture (secondary) conductivities as per Equation 2-1, where K_f is far greater than K_m (Indraratna and Ranjith, 2001):

$$K = K_m + K_f \qquad \textbf{Equation 2-1}$$

The interconnection between rock discontinuities and their spacing are important considerations in governing flow through rock masses. Even in rock masses characterised by heavily fractured media, the connectivity may be poor and result in broad distribution of fracture conductivities (Berkowitz, 2002). Moreover, the hydraulic conductivity of single discrete fractures is controlled exclusively by the aperture, roughness, infill, stress conditions, and the depth below ground surface.

2.3 Navier-Stokes Equation

The flow of an incompressible Newtonian viscous fluid is governed by a form of the Navier-Stokes as shown in Equation 2-2 (Zimmerman and Bodvarsson, 1996; Zimmerman et al., 1991).

$$\frac{\partial u}{\partial t} + (\mathbf{u}.\nabla)\mathbf{u} = \mathbf{F} - \frac{1}{\rho}\nabla p + \frac{\mu}{\rho}\nabla^2\mathbf{u} \qquad \textbf{Equation 2-2}$$

Where: ρ is the fluid density, F is the body force vector (per unit mass), p is the pressure, μ is the fluid velocity, and u is the velocity vector. The Bernoulli effect or theorem shows that in fluid flow, pressure is reduced as flow velocity increases, or that fluid velocity increases as the area available for flow decreases. In 1738, Bernoulli theorized that in uniform steady flow in a conduit or stream channel, the sum of the velocity head, pressure head, and gravity head at any given point is equal to the sum of these heads, or sum of the energy potentials, at any other point, plus (if upstream) or minus (if downstream) the losses in head due to friction between the two points. Under irrotational conditions, this energy total remains constant along equipotential lines, as shown in the Bernoulli equation:

$$\emptyset = \frac{p}{\rho} + \frac{V^2}{2g} + z \qquad \textbf{Equation 2-3}$$

2.4 Smooth Parallel Plate Model and the Cubic Law

At sufficiently low flow rates, fluid flow through porous media is commonly described by the well-known linear Darcy's law:

$$Q = \frac{kA_h}{\mu}\ i \qquad \textbf{Equation 2-4}$$

Where: Q is the volumetric flow rate, i the pressure gradient, k the intrinsic permeability, A_h the cross-sectional area, and μ the fluid viscosity. Fluid flow through a rock fracture, on the other hand, is commonly idealised to flow between a pair of two smooth parallel plates.

Flow capacity of a fracture depends on a number of parameters such as; the joint or fracture orientation, aperture, type of infill material, and continuity or persistence in the direction of flow (Eid, 2007). Moreover, aperture and roughness are cited as the most vital properties governing flow (e.g.: Barton and de Quadros, 1997; Brown, 1987; Brush and Thomson, 2003; Gurocak and Alemdag, 2012; Hakami and Larsson, 1996; Li et al., 2008; Liu, 2005).

The quantification of flow through discrete fractures considers a simple model concept of two smooth parallel plates, assuming the matrix as impermeable and that saturated laminar flow conditions apply (Singhal and Gupta, 2010). The simple model concept of two smooth parallel plates that represent the fracture walls, with a fixed opening representing the aperture are shown in Figure 2-1. Singhal and Gupta (2010) provide an explanation of the equations governing the parallel plate model by first stating that the linear Darcy's law for flow in a single fracture can be described by:

$$V = K_f\, i \qquad \textbf{Equation 2-5}$$

Where; V is the specific discharge (Darcy velocity), i is the hydraulic gradient, and K_f is the hydraulic conductivity is the hydraulic conductivity of the fracture defined by:

$$K_f = \frac{\gamma_w a^2}{12\mu} \qquad \textbf{Equation 2-6}$$

Where a is the fracture aperture, γ_w is the unit weight of water, and μ is the viscosity of water. Due to the relationship between hydraulic conductivity (K) and permeability (k), the permeability of the fracture, k_f, can also be expressed by:

$$k_f = \frac{a^2}{12} \qquad \textbf{Equation 2-7}$$

Singhal and Gupta (2010) further explain that by combining Equation 2-5 and Equation 2-6 and assuming that the fracture walls are impermeable, the average velocity, $\overline{V}$, in the fracture expressed by a single parallel plate model is given by:

$$\bar{V}_a = \frac{\gamma a^2}{12\mu}\frac{dh}{dl} \qquad \textbf{Equation 2-8}$$

The transmissivity of the fracture, T_f, can be expressed by:

$$T_f = \frac{\gamma a^3}{\mu 12} = K_f a \qquad \textbf{Equation 2-9}$$

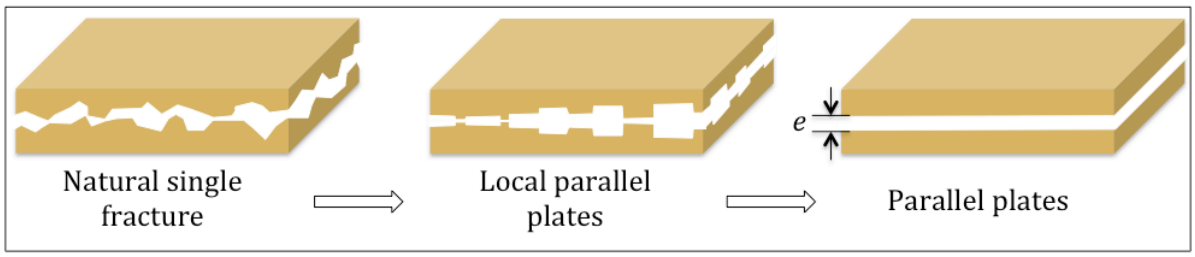

Figure 2-1 Conceptualisation of a rough natural fracture as two parallel plates separated by a constant aperture, *e* (redrawn by Dippenaar and Van Rooy, 2016; after Oron and Berkowitz, 1998).

The smooth parallel plate model is the only fracture model for which an exact calculation of the hydraulic conductivity is possible (Zimmerman and Bodvarsson, 1996). The simplification to smooth parallel plates is needed in order for the set of three coupled Navier-Stokes, non-linear partial differential equations (as presented in Equation 2-2) to be solved analytically. In this case, flow occurs under a uniform pressure gradient in the channel between the two parallel, smooth surfaces, and under such conditions only one component of the velocity vector is nonzero, and the equations simplify greatly (Zimmerman et al., 1991).

From this strong simplification of natural conditions, the Cubic law is valid for laminar flow through parallel wall fractures with smooth surfaces, and relates the estimated hydraulic conductivity to the cube of the fracture aperture and can be expressed as:

$$K_f = \frac{ga^3}{12vs}$$ **Equation 2-10**

Where: a represents the aperture; *v* represents kinematic viscosity; and *s* represents fracture spacing. The flux, *Q,* occurring through a single discrete fracture can subsequently be determined from the Cubic law (Silberhorn-Hemminger et al., 2005b; Singhal and Gupta, 2010; Zimmerman and Bodvarsson, 1996):

$$Q = \frac{we^3}{12\mu}\nabla P = \frac{kA_h}{\mu}\nabla P$$ **Equation 2-11**

where *w* [L] is the fracture width, *e* [L] is the aperture of the idealized parallel smooth fracture, *l* [$ML^{-1}\ T^{-1}$] is the dynamic viscosity of fluid, *k* [L^2] is the intrinsic permeability defined as $e^2/12$, and A_h [L2] is the cross-sectional area equal to e_w. The Cubic law predicts that the discharge (*Q*) is proportional to the cube of the aperture (*e*) of the idealized fractures.

2.5 Non-Linear (Non-Darcian) Flow

The Cubic law as described above, in which flow is described by a linear relation between the flow rate and pressure drop, are only valid when the inertial forces are negligible compared with viscous forces, which can only be anticipated for low flow rates. It has been well

recognized, however, that the linear Darcy's law is not always suitable to describe the flow behaviours in natural fractures (Chen et al., 2015). As the flow rate increases, doubling the pressure drop does not produce double flow rate, which is known as the non-linear flow zone (Zhou et al., 2015). Chen et al. (2015) describe fluid flow in the non-Darcy flow zone as occurring when there is in increase in flow rate, in which the increase in discharge is smaller than the proportional increase of pressure gradient.

2.5.1 Forchheimer Equation

Non-linear (non-Darcy) flow may occur as a result of non-negligible inertial losses arising from variations in flow velocity or direction along the flow paths due to constrictions or obstructions. Inertial losses are also possible as a result of the initiation of turbulence due to localized eddy formation as the flow velocity increases (Chen et al., 2015; Zhang et al., 2013). Forchheimer's law (as introduced by Forchheimer, 1901) has been most widely used to describe the non-linear flow in fractures and porous media:

$$-\nabla P = AQ + BQ^2 \qquad \textbf{Equation 2-12}$$

Where Q is the volumetric flow rate [L^3T^{-1}], ∇P the pressure gradient [$ML^{-1}T^{-2}$], and coefficients A and B are, respectively, the linear and nonlinear coefficients related to the fluid properties and the medium geometries described as:

$$A = \frac{\mu}{kA_h} = -\frac{12\mu}{we_h^3} \qquad \textbf{Equation 2-13}$$

$$B = \frac{\beta\rho}{A_h^2} = -\frac{\beta\rho}{w^2 e_h^2} \qquad \textbf{Equation 2-14}$$

Where w [L] is the fracture width, e_h [L] is the hydraulic aperture of the idealized parallel smooth fracture, μ [$ML^{-1}T^{-1}$] is the dynamic viscosity of fluid, k [L^2] is the intrinsic permeability defined as $e^2/12$, ρ [ML^{-3}] is the fluid density, A_h [L^2] is the cross-sectional area equal to ew, and β is called the non-Darcy flow coefficient or the Forchheimer coefficient with dimension of [L^{-1}]. The Forchheimer's law ultimately reduces to Darcy's law when the nonlinear effect becomes negligible, i.e., $\beta = 0$ (Zhou et al., 2015).

Schrauf and Evans (1986) showed that by using dimensional analysis, the coefficients A and B may be reduced to the dimensionless coefficients a_D and b_D, respectively, and the Forchheimer equation (as presented in Equation 2-12) can therefore be rewritten as follows for one-dimensional flow in fractures (Chen et al., 2015):

$$-\nabla P = a_D \frac{\mu}{e_h^3 w} Q + b_D \frac{\rho}{e_h^3 w^2} Q^2 \qquad \textbf{Equation 2-15}$$

The coefficient a_D depends on the characteristic length of the fracture geometry, or the hydraulic aperture (e_h), and will differ for flow between parallel plates and flow in a pipe (Chen et al., 2015). For parallel plate flow, where e_h refers to the aperture between the opposite plates, a value of 12 is used for the coefficient a_D (Chen et al., 2015). was used for the coefficient a_D. The coefficient b_D is proportional to the friction factor f_D such that $b_D = f_D/2$ (as cited in Chen et al., 2015; Louis, 1969; Schrauf and Evans, 1986).

2.5.2 Reynolds number (Re) and the Forchheimer number (F_o)

For predicting the termination of linear flow and the onset of non-Darcy flow behaviour, two dimensionless numbers, the Reynolds number (*Re*) and the Forchheimer number (F_o) are used to predict the point at which linear flow terminates, and non-Darcy flow behaviour begins. The Reynolds number *Re* is defined as the ratio of inertial forces to viscous forces. For fluid flow in fractures, *Re* is given by (Brush and Thomson, 2003; Chen et al., 2015; Ranjith and Darlington, 2007; Zhou et al., 2015; Zimmerman et al., 2004):

$$Re = \frac{\rho v e_h}{\mu} = -\frac{\rho Q}{\mu w} \qquad \textbf{Equation 2-16}$$

where ρ [ML^{-3}] is the fluid density, v [LT^{-1}] is the bulk velocity in the fractures, e_h (L) is the hydraulic aperture, μ [$ML^{-1}T^{-1}$] is the dynamic viscosity of fluid, and w (L) is the fracture length.

Using Reynolds numbers (*Re*) to describe flow during hydraulic boreholes tests in the field (e.g. Lugeon tests) is complicated because *Re* is not uniquely defined over the flow field in a radial flow test because the hydraulic gradient decreases away from the borehole wall along the fracture with distance (Quinn et al., 2011). In this regard, previous laboratory (Iwai, 1976) and field (Quinn et al., 2011) studies have calculated *Re* for flow at the borehole wall where velocities are highest.

Under certain geometric and kinematic conditions which usually are assumed to hold for rock fractures, the Navier-Stokes equations can be reduced (locally) to the simpler Reynolds equation (Zimmerman et al., 1991). However, in order for the Reynolds equation to be valid, whereby viscous forces dominate inertial forces, the Reynolds number (Re) must be very small, such that:

$$Re = \frac{\rho v e^2}{ul} = \frac{\rho Q}{\mu w} \ll 1 \qquad \textbf{Equation 2-17}$$

where: ρ is the fluid density, v is the average fluid velocity, e is the average aperture, μ is the fluid viscosity, and l the characteristic fracture length in the flow direction. If the abovementioned conditions apply, and if the fracture aperture does not change too abruptly, Equation 2-2 can be simplified to the Reynolds equation (Dippenaar and Van Rooy, 2016; Zimmerman et al., 1991):

$$\nabla.(d^3\nabla P) = 0$$ **Equation 2-18**

The Forchheimer number (F_o) is defined as the ratio of nonlinear to linear pressure losses in the Forchheimer's law (Chen et al., 2015; Cherubini et al., 2012; Javadi et al., 2014):

$$F_o = \frac{BQ^2}{AQ} = -\frac{BQ}{A}$$ **Equation 2-19**

The physical meaning of F_o represents the ratio of the pressure gradient required to overcome inertial forces to that of viscous forces, and it accounts for both velocity (v) and the geometry or structure of the medium (b) (as cited in Chen et al., 2015; Cherubini et al., 2012; Javadi et al., 2014; Ruth and Ma, 1992; Zeng and Grigg, 2006). Combining *Re* and F_o, and eliminating the quantity Q, one obtains a relationship between the Reynolds number and the Forchheimer number (Chen et al., 2015):

$$Re = \frac{A\rho}{B\mu w} F_0$$ **Equation 2-20**

2.5.3 Causes of Non-Linearity

Previous laboratory experiments using single fractures (Konzuk and Kueper, 2004; Nicholl et al., 1999; Zimmerman et al., 2004) found that flow begins to deviate from linearity at a critical Reynolds number (Re_c) of between 1 and 5. These results are consistent with modelling numerical simulations of flow in single fractures (Brush and Thomson, 2003) and field studies (Quinn et al., 2011). Several critical values of F_o, at which flow is considered to enter the non-Darcy flow zone have been suggested. Zeng and Grigg (2006) suggested an α-value of 10% threshold for the non-Darcy effect, which corresponds to a critical F_o of 0.11. Macini et al. (2011) proposed an even higher average critical F_o of 0.40, which corresponds to an α-value of 28% for natural sand.

The different critical values of *Re* and F_o are also ascribed to the different geometrical attributes of the geological media and the different flow channels (Cherubini et al., 2012; Javadi et al., 2014; Zeng and Grigg, 2006). Furthermore, the observation of non-linear flow during borehole hydraulic tests is attributed to a combination of mechanisms that include the effects of dead water zones; aperture variations; contact area; roughness; and multiple fractures of different sizes (Quinn et al., 2011).

Particular to laboratory studies using unidirectional flow, deviation from linearity for flow through natural rough rock fractures has been observed to be very gradual. For unidirectional flow in a single fracture in granite, Sharp (1970) was one of the first to report this extended and gradual transition to a non-linear flow regime. The author described this extended regime as non-linear laminar flow. Maini (1972) observed that the dead water volume decreased with increasing hydraulic gradient and concluded that this would alter the frictional resistance to

the flow and could contribute to non-linear effects. Konzuk and Kueper (2004) observed non-linear flow at low flow rates and attributed the causes to include surface roughness, aperture variations, and obstructions.

Non-linear flow conditions in single fractures with radial flow from a borehole have also been investigated. Non-linearity has been attributed to inertial effects due to fluid bending at the entrance to the fracture (Iwai, 1976), and the increase in the number of asperities and contact area with increasing sample size (Raven and Gale, 1985).

2.6 Validity of the Cubic Law for Discrete Fractures

If the geometry is not constant along the channel (i.e. not the idealised smooth parallel plate model), the set of three coupled Navier-Stokes, nonlinear partial differential equations (as presented in Equation 2-2) cannot-be solved analytically, and one must resort to approximate methods of some sort (Zimmerman et al., 1991). Literature is abundant on the topics of the smooth parallel plate model and the associated Cubic law (Bear, 1972; Berkowitz, 2002; Gudmundsson et al., 2003; Hoek and Bray, 1981; Indraratna and Ranjith, 2001; Liu et al., 2013; Neuman, 2005; Silberhorn-Hemminger et al., 2005b; Singhal and Gupta, 2010; Weiss et al., 2006; Witherspoon et al., 1980; Zimmerman and Bodvarsson, 1996). Importantly, Singhal and Gupta (2010) state that the assumptions of the Cubic law usually do not hold well in natural conditions. Furthermore, the validity of Cubic law is discussed by several researchers (Lee and Farmer, 1993), and some examples where the Cubic law had failed are listed here chronologically:

- Raven and Gale (1985): rough natural discontinuities subjected to high normal stresses with abundant contact points due to surface roughness.
- Pyrak et al. (1985) and Witherspoon (1986): only 30% contact area was achieved at effective stresses of 90 MPa in natural fractures.
- Cook (1992) and Sisavath et al. (2003): flow through a fracture decreases at a rate exceeding the cube of the mean aperture and a nonlinear relationship exists between mean aperture and normal stress.
- Aydin (2001): low flow rates with a wide range of friction affected flow domains.

Some considerations of the validity of the Cubic law concerning aspects of this study are discussed in the following sub-sections.

2.6.1 Considerations with respect to geometry

2.6.1.1 Aperture

According to Hudson (1989), aperture will be (Dippenaar and Van Rooy, 2016):

i. Constant in the instance of parallel planar adjacent surfaces;
ii. Linearly variable for non-parallel planar adjacent surfaces; and
iii. Totally variable for rough adjacent surfaces.

The Cubic law is applicable to both open and closed fractures with aperture being the governing geometrical property. Good agreement with the Cubic law has been reported for apertures of between 4 and 250 μm (Witherspoon et al., 1980) although narrower apertures, higher fluid viscosity and lower fluid density do stabilize flow, which cause flow to become more linear (Zimmerman and Bodvarsson, 1996). The difference in flow mechanisms across differing apertures has recently been investigated by Segole (2018), who found that narrower apertures provide more contact between fluid and joint surface, and thus favour capillary forces. In contrast, wider apertures provide a lesser contact area between water and surface, and therefore favour gravity forces.

The Cubic law has been widely applied to rough-walled rock fractures, but with the aperture, e, being replaced by the so-called hydraulic aperture e_h (Brush and Thomson, 2003; Konzuk and Kueper, 2004; Zimmerman and Bodvarsson, 1996). The relationship between hydraulic aperture and mechanical aperture is shown schematically in Figure 2-2 (Dippenaar and Van Rooy, 2016). The presence of infill material affects the aperture available for the transmission of water, and therefore the term hydraulic aperture refers to the open aperture which can be related to a localised smooth parallel plate model for which the local Cubic law (LCL) holds. Conversely, the infill aperture refers to the aperture with infill material of given hydraulic conductivity, which is different from that of the rock itself.

Aperture measurement is often questioned due to the strong influence of this measurement on the results of the Cubic law (Berkowitz, 2002; Konzuk and Kueper, 2004). The vertical aperture Figure 2-3 has been shown to correlate poorly with the Cubic law, but remains the recommended method by several authors (Konzuk and Kueper, 2004). Average segment apertures are preferred by other researchers, who also caution against measurement on a point-to-point basis (Oron and Berkowitz, 1998). Ball apertures and apertures measurements that are normal to the flow direction, have also been reported to pose problems with changing resolution given their sensitivities to drastic changes in apertures (Berkowitz, 2002). Hydraulic apertures, on the other hand, can possibly be determined through knowledge of the means and standard deviations of fracture apertures (Zimmerman and Bodvarsson, 1996).

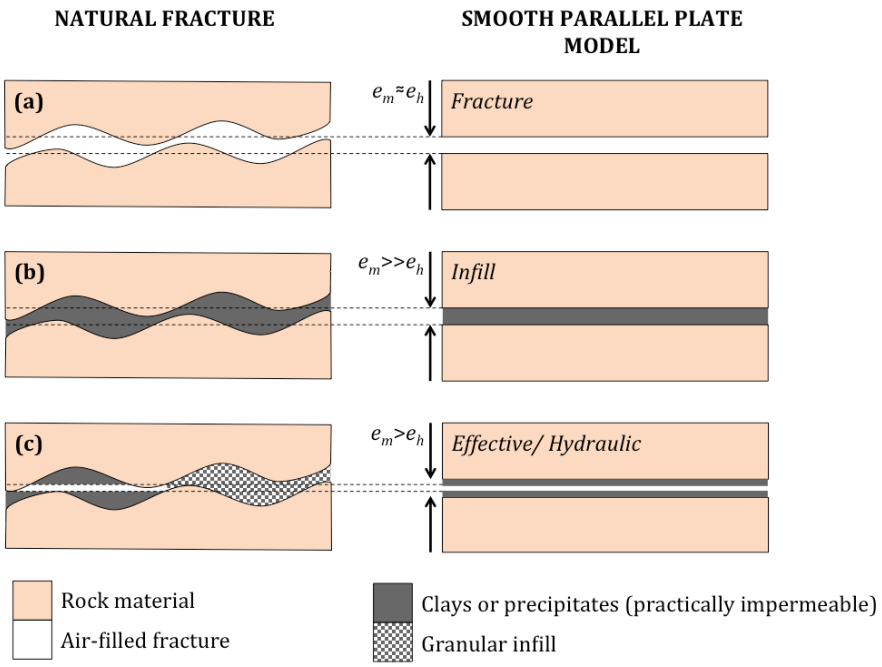

Figure 2-2 Relationships between mechanical (e_m) and hydraulic (e_h) apertures due to roughness and infill (Dippenaar and Van Rooy, 2016).

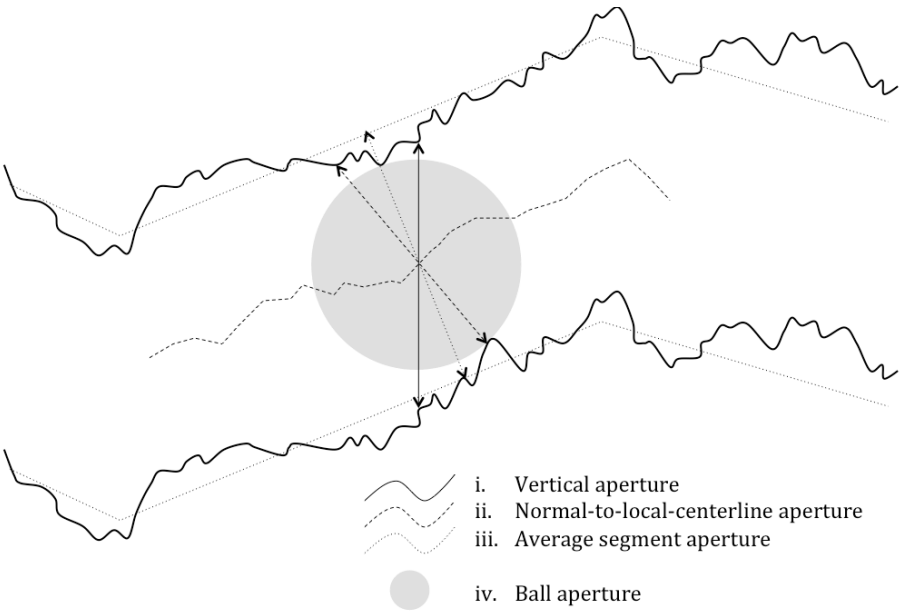

Figure 2-3 Measurement of aperture in a rough fracture: (i) the vertical aperture, perpendicular to the discontinuity, (ii) normal-to-local-centerline aperture, (iii) ball aperture, or (iv) average segment aperture. (in Dippenaar and Van Rooy, 2016; from Oron and Berkowitz, 1998).

2.6.1.2 Roughness and Contact Obstacles

It is well documented by analytical, experimental and numerical studies that the roughness of a fracture has a direct effect on the behaviour of fluid flow in a fracture (Indraratna and Ranjith, 2001). Depending on the orientation of the roughness relative to the hydraulic gradient, roughness may either inhibit or enhance the flow through a fracture, and furthermore the presence of contact points or obstacles resulting in bridging, can obstruct flow (Dippenaar and Van Rooy, 2016). The typical surface of fracture walls contain isolated asperity regions where the two walls are in contact, surrounded by open regions where the two walls are separated by an aperture, h, that may vary from point to point. When fluid flows through such a fracture, it not only must flow around the contact areas, but also has a tendency to flow preferentially through the channels with the largest apertures, as hydraulic conductance is proportional to h^3 (Zimmerman et al., 1992). Furthermore, these contact obstacles together with roughness, keep discontinuities open, even in the absence of infill, and except where joint wall matching is perfect (Dippenaar and Van Rooy, 2016). In order to address the issue that roughness has to the flux occurring through a fracture, the use of the Cubic law locally at each void space in a fracture, termed the local Cubic law (LCL), is often assumed to be applicable (Kishida et al., 2013).

Considering the fundamental influence that the geometry and nature of roughness has on the flow of fluid through a discrete discontinuity, several important research papers present measures to evaluate and quantify the role that roughness has on fluid flow. Oron and Berkowitz (1998) investigated whether the local Cubic law behaviour should be studied on a local basis, and with regards to inertial forces, found that Reynolds number (Re) should be limited to a maximum of <<1. Furthermore, Konzuk and Kueper (2004), in their experimental study, state that inertial forces become significant and the Cubic law no longer adequately models the flow behaviour as the fracture surface roughness and/or the Re increases. The authors summarise in their findings that surface undulations and the abrupt aperture changes created by rock debris trapped within the fracture likely resulted in an increase in the amount of inertial forces. The authors further state that their findings reinforce the need to use realistic models of rock fractures in studies of the Cubic law, in order to assess what criteria dictate the range where the LCL is applicable.

Most fracture samples studied in laboratory flow experiments are usually about 50–400 mm long, and at such size scales the fractal framework should explain most of the flow phenomena observed. However, Berkowitz (2002) states that at larger scales, there can be a change in the correlation of the fracture wall roughness. In these cases, large-scale roughness (waviness) may result in offsets in the wall matching, which may lead to the formation of a stepped fracture surface. In this instance K_f is likely substantially increased due to the large apertures formed by the steps (Dippenaar and Van Rooy, 2016). Offsets as small as 0.5 mm have been shown to significantly affect hydraulic conductivity and deviations of up to five orders of magnitude have been reported (Berkowitz, 2002). If the mean aperture and roughness are in the same order of magnitude, the Cubic law generally fails application (e.g. Cook, 1992; cited in Dippenaar and Van Rooy, 2016) and sinusoidally-varying aperture with

shorter wavelengths and larger amplitudes deviate more from the Cubic law (Liu and Fan, 2012). Zimmerman et al. (1991) explain, for flow through a sinusoidally-varying channel, that *K*-values deviate from those predicted when the spatial wavelength of the dominant roughness component becomes smaller than the order of magnitude of the amplitude of that roughness, i.e. when roughness forms very steep sinusoidal curves (Dippenaar and Van Rooy, 2016). Kumar et al. (1991) derived an expression for the permeability of a fracture that consists of two smooth parallel walls separated by an aperture, and which contains cylindrical asperities with a specific radius. The author's results show that viscous drag along the faces of asperities appreciably reduces the permeability of a fracture. The presence of contact obstacles block off fluid flow, resulting in a tortuosity effect, reducing the overall transmissivity and thus a decrease of flowrate (Yeo, 2001; Zimmerman and Yeo, 2000). The reduction depends on both the percentage contact area, as well as the shape of the contact areas, viewed as projections onto the nominal fracture plane (Zimmerman and Yeo, 2000). Yeo (2001) suggests that too little research has been made to quantify the effect of contact obstacles on fluid flow. The Cubic law and Reynolds equation break down at contact points where the aperture is zero, and therefore research such as that presented by Zimmerman et al. (1992), suggested that contact regions should be treated by a different method from that of conductive void regions.

A natural fracture consists of contact areas in which the aperture is effectively zero, surrounded by areas of varying but non-zero aperture. Zimmerman and Yeo (2000) state that this can be treated by finding an effective hydraulic aperture of the open regions, which is then replaced with a constant-aperture fracture having the appropriate aperture. The effect that contact regions would have on the transmissivity (T) can then be studied for, but becomes a problem of finding the overall conductivity of a two-dimensional medium of initial transmissivity (T_o), with impermeable obstacles imbedded in it Walsh (1981) investigated the effect of circular cylindrical obstacle using the Maxwell's effective medium approach, and arrived at a solution where increasing the fractional area of contact obstacles, the hydraulic aperture decreases, given by Equation 2-21:

$$\frac{T}{T_o} = \frac{1-c}{1+c} \qquad \textbf{Equation 2-21}$$

where c is the fractional contact area. Zimmerman et al. (1992) studied the permeability of fractures with circular, elliptical and irregular asperity shapes, by extending the Walsh-Maxwell approach to randomly oriented inclusion of elliptical shape. They found that the permeability depends not only on the amount of contact area, but also on the shape of the asperities. Zimmerman et al. (1992) simulation showed that Walsh's approximation overestimated the hydraulic aperture for a fracture with irregularly-shaped obstacles, and suggested the following relationship in Equation 2-22:

$$\frac{T}{T_o} = \frac{1-\beta_c}{1+\beta_c}, \text{ where } \beta = (1+\alpha)^2/4\alpha \qquad \textbf{Equation 2-22}$$

where α =1 is the aspect ratio of the elliptical contact areas. Zimmerman and Yeo (2000) cite examples where a large contact area of 30%, arranged as ellipses of aspect ratio 0.5, results in a decrease of transmissivity by about 50%. Kishida et al. (2013) found that flow paths due to contact points in rough fractures, under steady flow conditions, are tortuous and inhomogeneous, and presented results that showed that flow paths are 3–9% longer than the straight-line paths, resulting in a decrease in hydraulic gradient. Kishida et al. (2013) showed the *Re* distribution in a single fracture with a small hydraulic head difference, *Re*-values of less than 1.0 occupies the majority of the fracture, with localized regions of *Re*-values of more than 1.0. On the other hand, in the case of a high hydraulic head difference, the *Re* region of less than 1.0 decreases and the *Re* region of more than 20 can be observed in the concentrated flow area. In this area, the Cubic law cannot be applied to estimate the fracture flow (Kishida et al., 2013). At the same hydraulic gradient, the flow velocity increases as the aperture increases and the roughness remains unchanged, but the flow velocity decreases as roughness increases and the aperture remains unchanged (Qian et al., 2005).

The relative roughness (*F*, often labelled D_h for hydraulic diameter) relates the difference between the maximum and minimum asperity height or absolute wall roughness (*k*) to the fracture aperture (*e*) or mean fissure width (2*a*) as per Equation 2-23 and Figure 2-4 (Aydin, 2001; cited in Dippenaar and Van Rooy, 2016):

$$F = \frac{k}{2e} \qquad \textbf{Equation 2-23}$$

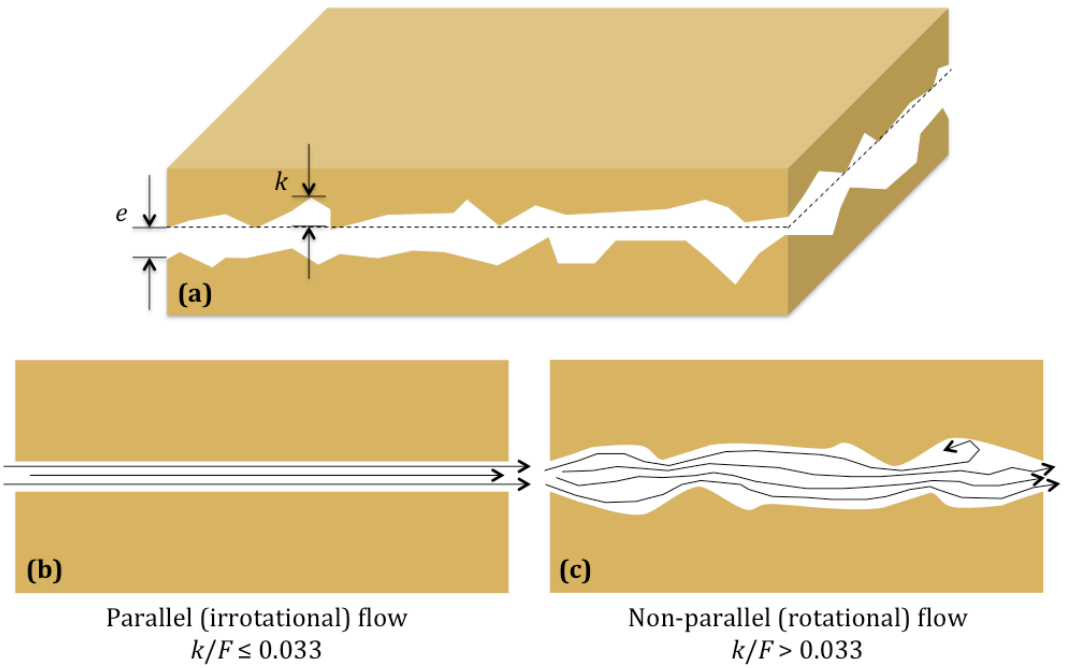

Figure 2-4. Variables related to roughness (a) and types of flow (b,c) (in Dippenaar and Van Rooy, 2016; adapted from Wittke, 1990).

Parallel (irrotational) flow will occur in a fracture where $F < 0.033$ and non-parallel (rotational) flow when $F > 0.033$, as found by Louis (in Indraratna et al., 2002; 1969; and Wittke, 1990). Associated with this, fracture flow may be laminar ($Re < 2000$) or turbulent ($Re > 2000$), depending on the fluid viscosity and the fracture aperture. This was evaluated in great further detail by for e.g. Aydin (2001).

2.6.1.3 Hydraulic aperture

A simplification to estimate hydraulic aperture (e_h) is detailed by (Barton et al., 1985) relating the aperture (e) to the joint roughness coefficient (JRC) as per Equation 2-24:

$$e_h = \frac{e^2}{JRC^{2.5}} \qquad \textbf{Equation 2-24}$$

The JRC of a discontinuity can be calculated as per the method outlined by Barton (1982; as cited in Barton and de Quadros, 1997), which resembles the maximum roughness amplitude (r_a) to place a straight edge along the joint and record the maximum amplitude (a) for a measured profile length (L) as per Equation 2-25:

$$JRC = 400\frac{a}{L} \qquad \textbf{Equation 2-25}$$

Two-dimensional computational fluid dynamics (CFD) simulations conducted by (Hosseinian et al., 2010) were used to calculate the influence of roughness through the joint roughness coefficient (JRC) on pressure and hydraulic aperture. Results showed that with increasing JRC, the normalised pressure drop shows an increase while the normalised hydraulic aperture decreases (Figure 2-5).

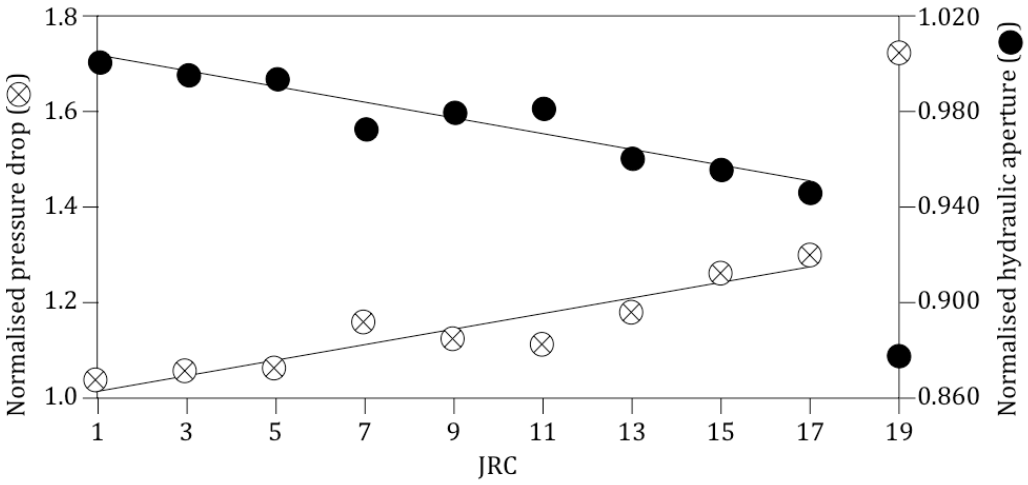

Figure 2-5. Pressure drops and hydraulic aperture for 10 JRC flow channels. (in Dippenaar and Van Rooy, 2016; modified from Hosseinian et al., 2010)

The Reynolds equation, an alternative to the parallel-plate model, has often been adopted to quantify the effect of roughness on flow in fractures. Relative to the parallel-plate model, the Reynolds equation greatly improves the understanding of fluid flow in rough fractures by considering irregularities of aperture distributions. However, the hydraulic aperture based on the Cubic law, in general, is not equal to the mechanical aperture for rough-walled fractures. The mechanical aperture is usually larger in magnitude than the hydraulic aperture due to the roughness of the fracture. Generally, the hydraulic aperture decreases dramatically as the roughness increases and the mechanical aperture decreases (Liu and Fan, 2012). The result presented by Liu and Fan (2012) demonstrates that their new model extends the application range of the Cubic law to more general fractures with complex geometry boundaries.

2.7 Flow Mechanisms in Partially Saturated Fractures

In regions above the water table, the water phase is usually at a negative potential, and cannot completely fill the void space of the fracture, with the remainder of the fracture being filled by air (Zimmerman and Yeo, 2000). Mixed air-water flows behave differently from water-saturated systems (Dippenaar and Van Rooy, 2016). In this unsaturated zone, above the water table, the most notable implication of partial saturation of fracture networks is that gravity does not necessarily force water down near-vertical discontinuities. This is due to the likelihood of adhesion to discontinuity surfaces, which exceed cohesive forces, resulting in significant lateral flow as water moves into near-horizontal discontinuities. In such instances, water molecules will be attracted to near-horizontal discontinuity roofs rather than to each other to induce early-time vertical drainage through fracture or discontinuity intersections (Dippenaar and Van Rooy, 2016).

Research work conducted by both Tokunaga and Wan (1997), and Tokunaga et al. (2000), presented a conceptual model for unsaturated flow through rough-walled fractures. This concept concerns water films on fracture surfaces under near-zero (negative) matric potentials and examines the possibility of fast unsaturated flow under tension. Film flow in this context are a complex network of thick pendular regions that form within topographic depressions and thin films on topographic ridges of the fracture surface, as illustrated in Figure 2-6a, characterised by a zero contact angle. Tokunaga et al. (2000) express that the thickness and connectivity of pendular film regions is important in controlling film flow on individual fracture surfaces. Water will flow down the fracture in the form of a thin film that does not need to bridge the gap between the lower and upper rock surfaces, provided the plane is not perfectly horizontal, filling-in the regions of small-scale roughness on the lower fracture surface, in a manner that leads to a mean film thickness that decreases as the capillary pressure becomes larger. This flow mechanism hypothesized by Tokunaga and Wan (1997) depends on the roughness of the fracture wall, but not on the distance between the two walls, and therefore occurs as thin films of water flowing along the fracture surface without having to fully saturate the fracture. In this flow mechanism the film flows exhibited constant hydraulic conductivity despite varying film thickness, which is dependent on the degree of saturation. In general, films can exist on fractures of any aperture as long as the fracture's surface is wettable, and as long as the film thickness is less than the aperture. Tokunaga and Wan (2001) particularly

present that the boundaries for film flow to occur in unsaturated rocks are a matrix permeability less than 10^{-14} m^2 and aperture width greater than 30 μm, which cover a large range of unsaturated rocks. Small-scale roughness is crucial to film flow under high capillary pressures, as opposed to that of saturated fracture flow. In particular, Zimmerman and Yeo (2000) mention that fracture transmissivity under fully-saturated conditions is primarily controlled by the mean aperture, yet for fracture transmissivity under unsaturated conditions, particularly at very high suctions, is independent of mean aperture, and completely controlled by small-scale roughness. A simple geometrical model of fracture flow developed by Or and Tuller (2000) agreed well with the experimental findings of Tokunaga and Wan (1997) and showed that film contribution in unsaturated conditions is not negligible. A quantitative theory of film flow along rough-walled fractures has yet to be developed, and it is not altogether clear how such a theory will relate to the models for saturated flow that have been discussed above (Zimmerman and Yeo, 2000).

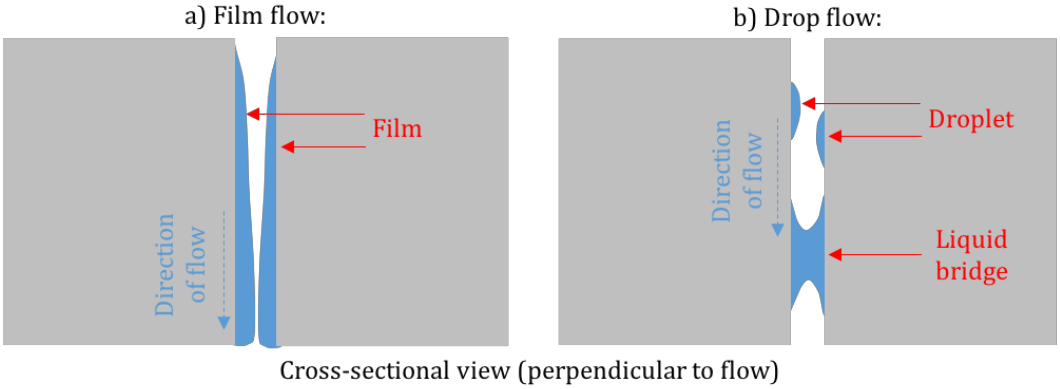

Figure 2-6. Conceptual models of vadose fracture flow processes: a) film-flow model of Tokunaga and Wan (1997); and b) drop-flow model with one-walled and two-walled drops (Doe, 2001).

An alternative flow mechanism recorded in unsaturated fractures is that of drops, which will be subdivided based on whether they occur as single-wall droplets (requires large fracture apertures) or alternatively liquid bridges whereby the drop contacts both-walls within a fracture (Figure 2-6b). It is defined by Doe (2001) in his review paper, that a droplet is an isolated body of liquid that is not continuous with the rest of the liquid phase. Unlike films, which can exist on any aperture fracture, the water in drops are held by capillary forces, which would be weak in large apertures. Furthermore, droplets can exist regardless of surface wettabilty (and can even move down non-wetting fractures). Dragila et al. (2016) showed that droplets and films can coexist in a fracture of small aperture, in their study of epikarst microfractures. Or and Ghezzehei (2007) concluded that the interaction of liquid bridges with fracture walls could supply complex travel velocity-distance relationships due to the formation and detachment of liquid bridges within unsaturated fractures.

Further to the flow mechanism of drops that are characterised by a non-zero contact angle, continuous rivulets of water can form, with non-zero contact angles, where they wet both

fracture walls simultaneously (contact both fracture walls). The existence of rivulets depends on flow rate and aperture. Furthermore, depending on the flow rate into the fracture, three possible rivulet scenarios occur as described by Su et al. (1999):

- At low flow rates, rivulets form but are discontinuous through the length of the fracture, and are characterised by continuously snapping threads;
- At medium flow rates, rivulets form and become discontinuous, by snapping, at the fracture's end; and
- At high flow rates, rivulets form and are maintained continuously throughout the length of the fracture.

Similar results were obtained by Dragila and Weisbrod (2003) who added that the rivulets controlled droplet formation, with longer contact time supplying larger droplets and the possibility for droplets to travel faster than film flow in unsaturated conditions.

The relationship between these described flow mechanisms and their respective adhesive, cohesive, spreading properties as well as contact angles is shown in Figure 2-7 and reviewed in detail by Doe (2001). In contrast to cohesion, which describes interfaces in a single material, adhesion describes the interface between two different materials, such as a liquid and a solid. Adhesion occurs provided the contact angle is less than 180°, where a liquid can produce drops that are capable of "sticking" to a surface when the contact angle is less than 180°. At a contact angle of 180° or higher, there is no adhesion between the liquid and the solid (Doe, 2001).

The process of wetting occurs when liquid is imbibed or drained from a material such as pores or capillary tubes, and is characterised by a critical contact angle of 90°. It is this contact angle that also differentiates capillary rise from capillary depression, and together with the surface-energy processes it represents a fundamental separator of hydrophilic behaviour and hydrophobic behaviour (Doe, 2001). Hydrophilic behaviour occurs if the contact angle is less than 90°, where the liquid spontaneously imbibe into smaller pore spaces, such as pores and fracture asperities that are in contact. At higher contact angles, liquids require work to be brought in contact, and thus are non-imbibing, or hydrophobic.

As to the process of spreading, the critical contact angle is zero, as any positive contact angle produces negative values of the spreading coefficient, and spontaneously forms films on surfaces rather than drops. The zero contact angle thus provides a separator between regimes where film flows will dominate, from those where drops will be more prevalent at lower saturations (Doe, 2001). The definition of the term "wetting" can be confusing as it has many uses depending on the circumstances. In some instances it refers to any system where there is adhesion (i.e. contact angles less than 180°), whilst in others, the term is used nearly synonymously with spreading (i.e. contact angle of zero). Notwithstanding, the most common usage for the term "wetting" is for contact angles less than 90° (Doe, 2001).

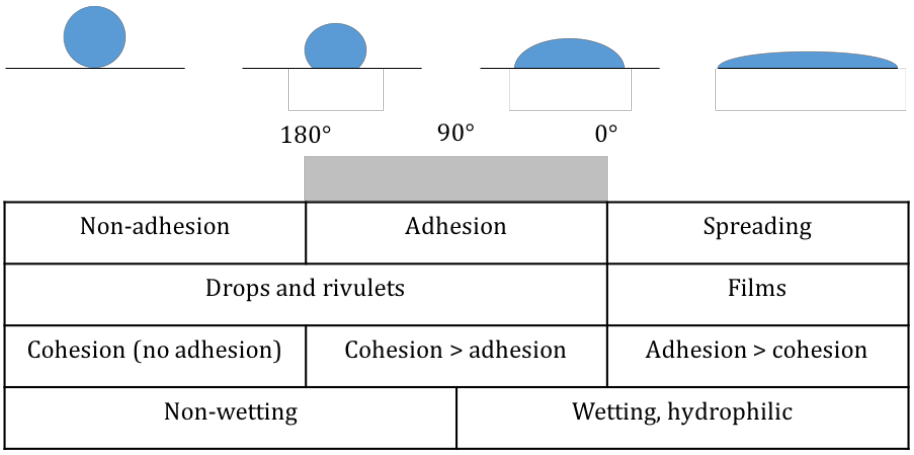

Figure 2-7. Relationship between adhesion, cohesion, wetting, spreading, and contact angle (after Doe, 2001).

Ghezzehei (2004) showed how differing flow mechanisms can also occur over a wide range of contact angles and fluxes (Figure 2-8). Furthermore, the formation of the different flow mechanisms in variably saturated fractures, are dependent on various factors, including the force interactions between gravity, surface tension, capillary pressure, and viscous forces. This results in complex flow phenomena in the unsaturated media such as episodic fluxes, intermittent fluxes and preferential flow paths (Dragila and Weisbrod, 2003; Hakami and Larsson, 1996; Su et al., 1999). Adding to the already complex force interactions system are the influences of varying physical joint parameters such as aperture, continuity, roughness, intersection and fracture orientations, which result in fracture flow tortuosity and flow channelling (Ghezzehei and Or, 2005; Hakami and Larsson, 1996).

In the literature review by Doe (2001), the author specifically emphasizes that literature of contact angle data for geologic materials turns up relatively few references. Of the several reasons for this, most important is that contact angles are commonly assumed to be zero as a matter of convenience due to the complexities that nonzero contact angles introduce to theoretical development. Furthermore, as with any natural material, the issue of heterogeneity is problematic and therefore natural fracture surfaces may display different properties even at small scales. Finally, contact angles are notoriously irreproducible unless care is taken to keep the surface free of contamination, and it is such cleanliness that is not a concern of nature. Despite the concerns regarding contact angles for geological media, its importance to questions of hydrophobicity and preferential flow cannot be denied, even though contact angles are difficult to measure (Doe, 2001).

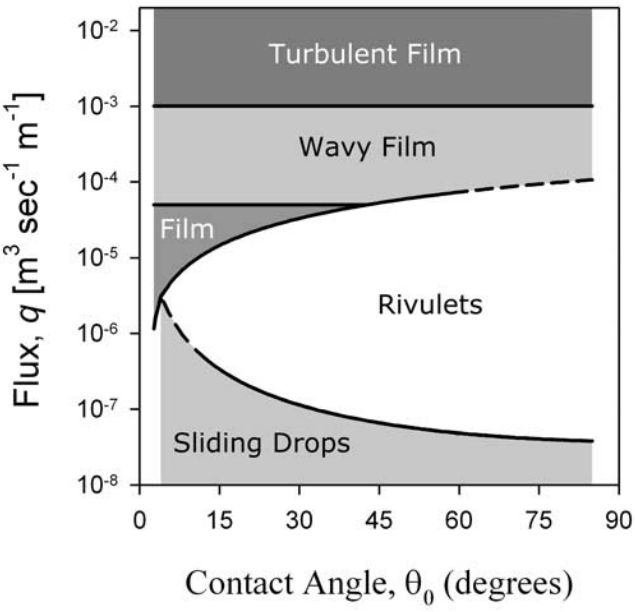

Figure 2-8. Flow regimes for different contact angles at differing fluxes as presented by Ghezzehei (2004).

Speaking specifically of film flow mechanism, Zimmerman and Yeo (2000) state that it is difficult to relate this conceptual model of unsaturated flow to the considerations of fracture flow as presented for single-phase saturated conditions, as those presented in section 2.6.1.2. In understanding the discrepancy between the calculated equivalent hydraulic aperture, which was 17% smaller than the measured mean aperture, Nicholl and Glass (2007), present that the observed discrepancy occurs because the parallel plate model does not fully describe the physics of flow through a variable aperture field as suggested initially by Brown (1987). Under saturated conditions, macroscopic deviation from a linear path was observed to be relatively small. However, small wavelength variations may add significantly to the path length; thereby accounting for a large portion of the observed deviation Nicholl and Glass (2007). Furthermore, the authors expected that flow resistance resulting from the convergence and divergence of flow paths normal to the fracture plane as flow passes through the variable aperture field is also partially responsible for the discrepancy. Although mean aperture does not contain sufficient information to fully characterize flow within a variable aperture field, it can be regarded as a reasonable first order approximation (Nicholl and Glass, 2007).

Pyrak-Nolte et al. (1988) concluded that fracture permeability is controlled by the largest connected channel within the system and that flow through that channel is controlled by its' narrowest aperture, or choke point. Under partial saturation relatively large amounts of fluid are forced to pass through zones of narrow aperture (choke points), which act to restrict flow, causing large localized pressure drops, and therefore in addition to path length, localized variations in channel width act to decrease permeability in a fracture (Nicholl and Glass, 2007). Variations in this cross-sectional flow increases with structural complexity and connection of the entrapped phase. In structurally complicated fractures, flow along those channels are likely to experience the most variation in area and hence local pressure drop. The significance

of choke points will decrease with increasing number of flow channels and interconnection between the channels (Nicholl and Glass, 2007). Upon an increase in saturation when these choke points become less significant, roughness can act to channelize flow into discrete channels, which in turn are expected to act as rapid pathways. Nicholl et al. (1993) state that moisture left by the passage of individual fingers is expected to create preferential pathways for subsequent flow. In inclined fractures, the effects of gravity can destabilize a wetting front, leading to the development of fingers oriented in the direction of gravity (Nicholl and Glass, 2007).

The formation of the different flow mechanisms in variably saturated fractures, shown in Figure 2-9, are dependent on various factors, including the force interactions between gravity, surface tension, capillary pressure, and viscous forces. This results in complex flow phenomena in the unsaturated media such as episodic fluxes, intermittent fluxes and preferential flow paths (Su et al., 1999). Adding to the already complex force interactions system are the influences of varying physical joint parameters such as aperture, continuity, roughness, intersection and fracture orientations, which result in fracture flow tortuosity and flow channelling (Ghezzehei and Or, 2005; Hakami and Larsson, 1996).

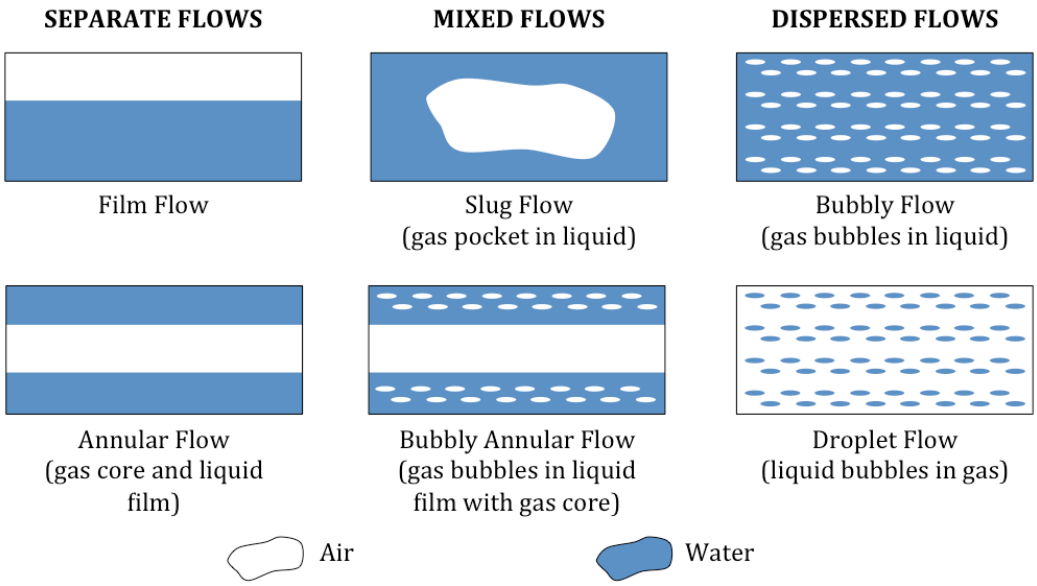

Figure 2-9. Flow mechanisms of water–air systems through single fractures or macropores (in Dippenaar et al., 2014; after Indraratna et al., 2002).

Channelling is a common phenomenon in fractured rocks, whereby preferential flow paths occur in a single fracture, and is related to variations in the fracture aperture (Singhal and Gupta, 2010). Preferential flow paths and channelling is schematically illustrated in Figure 2-10. Studies have questioned the validity of parallel plate model in nature as the channelling effect leads to preferential flow, which make it difficult to predict the flow path in fractured media (Singhal and Gupta, 2010). Considering basic fluid mechanics, water is much denser than air, and will thus form gravity-driven fingers when applied to the top of an air-filled (dry)

fracture (Wood et al., 2005). The deep penetration of water can therefore be expected in arid to semi-arid fractured rock environments.

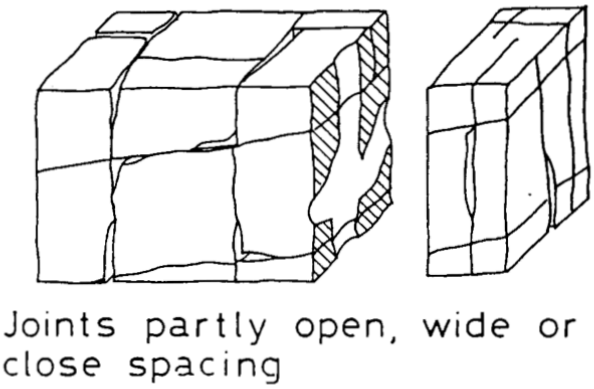

Figure 2-10. Preferential flow paths occurring in partly open discontinuities within a rock mass (Ewert, 1997a).

2.7.1 Water Contact Angles on Laboratory Materials

Sumner et al. (2004) categorised measured contact angles for various laboratory materials into 3 groups, with untreated borosilicate glass, water-rinsed glass and quartz falling into the intermediate category of between 10° and 80°. Aouad et al. (2016) further conducted experiments on glass, polypropylene and Plexiglass substrates to determine the advancing (β_a) and receding (βr) contact angles. Their results are presented in Table 2-1, with their results from glass material agreeing with that of Sumner et al. (2004). The contact angle of glass generally falls between 32° and 36° depending on the treatment of the surface, whilst quartz is lower at approximately 22°. Although, the advancing contact angle of Plexiglas falls into the intermediate category it is closer to the upper threshold, compared to glass which falls towards the lower threshold of the category.

Table 2-1. Contact angles of various materials measured by Sumner et al. (2004)[a] and Aouad et al. (2016)[b].

Material	Water contact angle (β)		
	Advancing contact angle (β_a)	*Receding contact angle* (βr)	Hysteresis (β_a - βr)
Untreated glass [a]	32°±2°		
Water-rinsed glass [a]	35°		
Quartz [a]	22°±4°		
Glass [b]	36°±3°	12°±6°	≈25°
Plexiglass [b]	71°±2°	25°±3°	≈45°
Polypropylene [b]	90°±4°	32°±5°	≈58°

2.8 Flow at Fracture Intersections

The simplest type of fracture intersection investigated are between orthogonal fractures, whereby one is horizontal and the other is vertical, and has been shown to integrate unsaturated flows. LaViolette et al. (2003), in a small two-dimensional porous matrix dissected by a regular fracture network, found that intersections acted to focus flow in some instances, but not in others, thus concluding that fracture intersections may both split and focus flow. Results obtained from field experiments, where a dyed fluid slug was infiltrated from a surface pond, conducted by Glass et al. (2002b); Nicholl and Glass (2002) also suggested such dual behaviour. Subsequent excavation and mapping of dyed fractures showed a structurally complex flow field where widespread flow near the pond fragmented with depth to form multiple pathways, presumably because of the transition from saturated (positive pressure) to unsaturated (tension) conditions (Wood et al., 2005).

Glass et al. (2002a) conducted some of the initial research of the recent advances in unsaturated flow due to intersections, and showed that steady application of fluid to the top of an unsaturated fracture-matrix network can produce dynamic preferential pathways, with flow fluctuating both along individual paths, and between alternate pathways. They further showed that, for flow within the fracture network itself, water was observed to move rapidly along fractures and then wait at intervening intersections, thus suggesting that fracture intersections behaved as capillary barriers. Glass et al. (2003) found that certain intersection geometries and orientations can act to inhibit lateral spreading, and thus maintain slender pathways through fracture networks. In addition to the creation of spatial structure, fracture intersections have also been shown to impose a temporal signal on unsaturated flows, whereby as an alternate mechanism, they suggested that fracture intersections could act as hysteretic gates and switches. Here steady inflow becomes pulsed outflow, where this repeated dynamic tends to create a local pool and finger structure, with filled non-conducting horizontal fractures on either side of the intersection.

While not fully understood, this complex behaviour clearly results from a sudden change in the relative importance of capillary forces that rises from the difference in void geometry between an intersection and the contributing fractures (Ji et al., 2004). In this conceptualisation, the first step of the fracture invasion process involves a downward growing finger reaching the capillary barrier formed by the fracture intersection. Here water begins to pool above the intersection, because pressure in the finger is less than that required to enter the barrier. As a pool grows in height, pressure builds at the intersection. Once the barrier is breached, water enters the adjoining fractures and the pressure at the growing front immediately reduces to the pressure of the wetting finger. If the pressure of the dry capillary barrier is less than the pressure of the wetting finger, the barrier remains open. If not, the barrier will empty after a pulse of water has moved across. Pressure will then build again, followed by breach at wetted barrier, with subsequent pressure lowering and barrier emptying after another small pulse. For a vertical fracture where the pulses can migrate downward and away, this process could carry on indefinitely, whereas for a horizontal fracture, once it fills

entirely to an adjoining intersection, pressure will eventually be pushed above the drying barrier pressure, thus removing the pulsation (Glass et al., 2003).

Wood et al. (2002) confirmed this integrative behaviour in experiments that considered flow across simple orthogonal intersection between two constant aperture fractures. At low flows their intersection accumulated fluid, and then discharged the integrated volume at periodic intervals, taking a high frequency, low volume inflow and transforming it into a low frequency, high volume outflow. Conversely, at higher flow rates, the intersection did not impose a temporal signal. Here, as flow rate increases and viscous forces become important, pulsating flow transitions to a stable configuration where the intersection no longer behaves as a gate. Wood et al. (2002) also observed that in addition to integration, fracture intersections can generate other interesting behaviour, such as multiple tendrils; snap off into the horizontal fracture; migrating tendrils; and spontaneous switching between tendril and dripping behaviour at a constant flow rate.

Glass et al. (2003) reported similar behaviour in a transparent analogue fracture network. Experiments on an inverted Y-shaped fracture intersection performed by Dragila and Weisbrod (2004) revealed complex dynamics in the form of mode switching, where the intersection performed as a capillary barrier forming a liquid bridge (aperture-spanning flow) splitting into film flow at the intersection along each branch. From these experiments, it was concluded that two fluid flows are possible in nature due to the further complexity expected. Research conducted by Ji et al. (2004) support the findings of Glass et al. (2003) and Wood et al. (2002). Furthermore, Ji et al. (2004) noted that the entry of fluid into the horizontal fractures by the wetting phase initiated macroscopic flow convergence as observed by LaViolette et al. (2003), pathway switching as reported by Glass et al. (2002a); and Glass et al. (2003), as well as temporal fluctuations in outflow over a range of scales (Glass et al., 2002a).

Wood et al. (2004) noted the importance of fracture intersections for integrating uniform flow and discharging a “fluid cascade,” where water advances rapidly to the next capillary barrier creating a stop and start advance of water through the network. They showed that flow tended to converge in this simple analogue fractured rock network even under conditions of distributed uniform flux, by observing many instances of pathway switching where discharge from one fracture would increase at the expense of another. The switching of flow from one pathway to another occurred either gradually or abruptly. Periods of pathway switching (either gradual or abrupt) were more common than periods of steady, constant flow. They further observed water accumulating or pooling behind capillary barriers formed by intersections. The discharge of pooled water occurred in a fluid cascade as a critical point was exceeded. The capillary barriers formed by fracture intersections can divert vertically flowing water from one fracture into horizontal fractures, thus, increasing the pool volume relative to storage in a single fracture. Behaviour at fracture intersections will be controlled by competition between capillary, gravitational, viscous, and inertial forces. The balance between these forces will be highly dependent on intersection geometry with geometric variables that will influence unsaturated flow including (Wood et al., 2005):

i. Number of fractures intersecting;
ii. Continuity of individual fractures (i.e., dead ends);
iii. Fracture offsets;
iv. Topology of the individual fractures;
v. Angle of intersection; and
vi. Localized shattering or micro-fractures.

Additionally, Wood et al. (2005) expect behaviour at intersections to be influenced by:

i. Fluid phases involved (air, water, NAPL);
ii. Surface chemistry;
iii. Capillary hysteresis;
iv. Initial fluid structure;
v. Secondary alteration (e.g., coatings, fillings, weathering rinds);
vi. Biologic activity;
vii. Interactions with the adjacent rock matrix;
viii. Nature of flow(s) entering the intersection (i.e., direction, velocity, timing); and
ix. Coupling between behaviour at adjacent intersections.

Both Wood et al. (2002), for a simple orthogonal intersection, and Glass et al. (2003), for vertically offset intersection, observed the formation of a capillary barrier with the ability to act as a hysteretic gate to low flows. Gravity-driven fingers in the fracture above the intersection transport water to the intersection either continuously or in discrete pulses. When the hysteric gate is closed, the intersection integrates inflow into dynamic storage, by pooling water in the vertical fracture above the barrier and possibly in the adjoining horizontal fracture(s). When the hysteric gate opens, discharge from dynamic storage through the intersection is at first rapid, and then as the pool height falls, flow decreases and increased tension is applied by the downward growing fluid body, followed by the hysteric gate closing and the capillary barrier being re-established. When strong enough, viscous and inertial forces may prevent the hysteric gate from closing, and thus limit behaviour as a capillary barrier (Wood et al., 2005). Under these conditions, flow through the restricted capillary connection across the intersection keeps it open against capillary forces, as has been argued by Glass et al. (2003). For orthogonal intersections, water arriving at an air-filled intersection will be blocked and spread laterally (along the axis of the intersecting fractures) to pool across the full width of the fracture. In a highly idealized situation where perfect geometry leads to symmetric behaviour, where both horizontal fractures fill with water (Wood et al., 2005). However, a more likely configuration is by Wood et al. (2002), where discharge involves at least partial filling of a horizontal fracture. In this case, the fluid pressure increases with pool height above the intersection, eventually causing the air-water meniscus to flatten and invade the intersection. The capillary barrier is breached when the meniscus crosses the intersection and contacts the opposite side (Wood et al., 2005). Wood et al. (2005) found that as their supply rate increased, behaviour entered a transition zone where it was erratic, with intermittent fluid tendrils forming both above and below the intersections. In contrast, at higher supply rates, they observed a steady regime where continuous tendrils spanned both vertical fractures. The tendrils were

connected by a capillary constriction across the intersection that caused water to pool above and fill both horizontal fractures (Wood et al., 2005).

The various flow behaviours at various fracture intersections is shown in Figure 2-11: whereby, a) breaching occurs in a symmetric fashion; b) breaching first occurs into one of the horizontal fractures; whilst c) inverted ‘‘T’’ intersection; (d) normal ‘‘T’’ intersection, and e) sideways ‘‘T’’ intersections, will be reflections of one another (Wood et al., 2005).

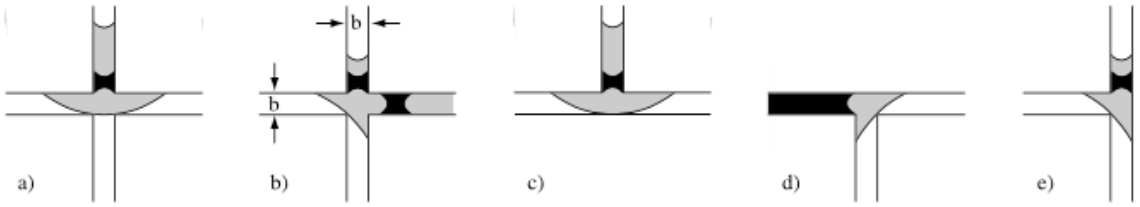

Figure 2-11 – Cross-sectional views of capillary barriers at intersections between horizontal and vertical fractures. Wetting fluid initially pooled at the barrier is shown in black, while grey represents the fluid configuration when the barrier is breached (Wood et al., 2005).

Ji et al. (2006) conducted experiments on orthogonal fracture intersections, and varied the aperture of the horizontal fracture. Comparing estimated maximum and minimum pool heights quantitatively, and comparing these calculated results to their observations, they concluded that the viscous forces remain subordinate to capillary forces and are not enough to overcome the capillary effects at the intersection when water fills only one horizontal fracture. However, if both of the horizontal fractures are filled with water, the authors proposed that the capillary effects are reduced and the viscous forces of water can make for water to cross the intersection without interruption. The strengths of the encountered capillary barriers in their experimental intersections are determined by the combination of capillary and viscous pressures, and the differing aperture between intersecting fractures controls capillary pressure except the first capillary barrier.

Various phase geometries at wetting phase fluid flow vary the capillary effects from superior to coordinate to the viscous effects. Hsieh et al. (2001) mention that inclined surfaces tend to promote film flow, and when progressing to intersections, this inclination will cause flow amalgamation and preferential flow paths. If the fracture is inclined from the horizontal, seepage from the fracture wall will flow down the wall and travel as a free-surface film to the terminus of the fracture (Dragila and Wheatcraft, 2001). As the flow proceeds down an inclined surface, the curtains that begin as uniform fronts may break up into rivulets (Doe, 2001). These flow mechanisms have recently been confirmed by physical models conducted by Brouwers (2017) and Brouwers and Dippenaar (2018) who investigated flow into a single discrete fracture located at the soil-rock interface.

2.9 Summary

The Cubic law is mostly employed for quantifying flow through a discrete fracture, based on the smooth parallel plate model, and is derived from the Navier-Stokes equation. The Cubic law relates the estimated hydraulic conductivity to the cube of the fracture aperture, provided that the fracture is clean, smooth, parallel and completely saturated. However, the validity of Cubic law has been discussed by several researchers, particularly with regards to non-linear flow behaviour, where the Forchheimer equation has better quantified flow through fractures. Notwithstanding, the Cubic law as well as Forchheimer equation are particularly useful to saturated flow, however little research has been done on the quantification of unsaturated fracture flow. Research dealing with unsaturated flow has dealt with flow mechanisms and flow regimes observed from laboratory and experimental model studies.

In light of the inconsistency in the use of terminology to describe the above-mentioned unsaturated fracture flow mechanism in previous literature, the following definitions are provided to ensure consistency about what is observed in the experiments that follow:

- *Droplet*: A drop that is an isolated body of fluid, characterised by a non-zero contact angle, that contacts a single fracture wall, and is discontinuous with the rest of the liquid phase. If these droplets are observed sliding along the fracture they will be referred to as sliding droplets;
- *Liquid bridge:* A drop that is an isolated body of fluid, characterised by a non-zero contact angle, that contacts both fracture walls, and is discontinuous with the rest of the liquid phase (sliding liquid bridges when observed moving along the fracture wall);
- *Film:* A film of fluid that is continuous through the length of the fracture, characterised by a zero contact angle, and contacts only a single fracture wall. During the dynamic saturation from initially dry conditions, the formation of films can be referred to as fingers;
- *Rivulet:* A continuous path of fluid, characterised by a non-zero contact angle, that contacts a single wall or both fracture walls (referred to as an aperture-spanning rivulet). Rivulets may be described as discontinuous if the fluid path terminates to a point where sliding droplets are released, within the fracture length.

CHAPTER 3 ASSESSMENT OF ROCK MASS PERMEABILITY

3.1 Introduction

The assessment of rock mass permeability generally makes use of structural mapping, as well as permeability tests. Typical discontinuity survey data collected in rock mechanical context record parameters for each discontinuity intersecting a line set out along an exposed rock face or surface or core from boreholes. Groundwater measurements are generally limited to visual assessment from joint line surveys, and quantification conducting Lugeon (water pressure) tests in a single borehole over several different hydraulic pressures (Palmstrom and Stille, 2010).

The following chapter presents a review of published literature in order to gain knowledge on previous studies with regard to field permeability measurement techniques, which serves as a basis for the potential findings that unsaturated fracture flow may have on field validation techniques. The chapter introduces the concept of fractures in rock, as well as the assessment of the permeability of a rock mass by *in-situ* tests.

3.2 Structural Data Gathering

Typical discontinuity survey data collected in rock mechanical context are outlined by Brown (1981) and Bieniawski (1989), and shown in Figure 3-1 and Figure 3-2. Parameters recorded include: position; rock type; type of structure; aperture; dip and dip direction (orientation); continuity; roughness; waviness and amplitude; gouge or filling; and water conditions (seepage). These parameters are recorded for each discontinuity intersecting a line set out along an exposed rock face or surface. The same parameters can be recorded on an exposed rock outcrop across an area and is then referred to as joint window mapping. Discontinuity data collection generally depends on accessible, core from boreholes or exposed rock outcrops, such as exposed dam foundations or tunnel faces.

Fracture or discontinuity planes are not always smooth and parallel. As shown in Figure 3-3, *roughness* of fractures comprises large-scale waviness (i_1), as well as small-scale *asperities* (i_2) on the fracture walls that influence strength and stress relationships (Hoek and Bray, 1981; Indraratna and Ranjith, 2001; Look, 2014). Field descriptions simplify roughness and asperities as shown in Figure 3-4.

1. TYPE OF STRUCTURE	
0	Fault zone
1	Fault
2	Joint
3	Cleavage
4	Schistosity
5	Shear
6	Fissure
7	Tension crack
8	Foliation
9	Bedding

3. INFILLING – NATURE	
1	Clean
2	Surface staining
3	Non-cohesive
4	Inactive clay
5	Swelling clay
6	Cemented
7	Chlorite, talc, gypsum
8	Other – specify

2. APERTURE (mm)	
1	Wide (> 200)
2	Moderately wide (6 200)
3	Moderately narrow (20–60)
4	Narrow (6–20)
5	Very narrow (2–6)
6	Extremely narrow (< 2)
7	Tight

4. INFILLING – COMPRESSIVE STRENGTH	
1	Very soft (< 40 kPa)
2	Soft (40–80)
3	Firm (80–150)
4	Stiff (150–300)
5	Very stiff (300–500)
6	Hard/ very weak (600–1250)
7	Weak (1.25–5 Mpa)
8	Mod. weak (5–12.5)
9	Mod. strong (12.5–50)
10	Strong (50–100)
11	Very strong (100–200)
12	Ext. strong (> 200)

6. WAVINESS	
1	Wavelength (m)
2	Amplitude (m)

5. FRACTURE ROUGHNESS	
1	Polished
2	Slickensided
3	Smooth
4	Rough
5	Defined ridges
6	Small steps
7	Very rough

7. WATER	
1	Dry
2	Damp
3	Seepage Flow
4	< 10 ml/s
5	10–100 ml/s
6	0.1–1 l/s
7	10–100 l/s
8	> 100 l/s

Figure 3-1 Descriptors for discontinuity surveys (after Anon., 1977; in Dippenaar and Van Rooy, 2016).

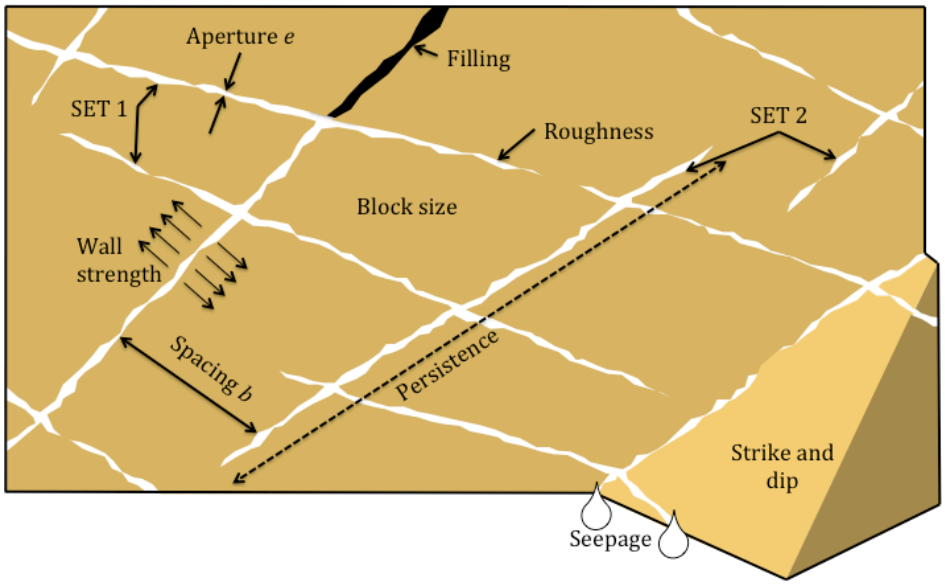

Figure 3-2 Geometric properties of discontinuities to be recorded (adapted by Dippenaar and Van Rooy, 2016; in González de Vallejo and Ferrer, 2011; from Hudson, 1989).

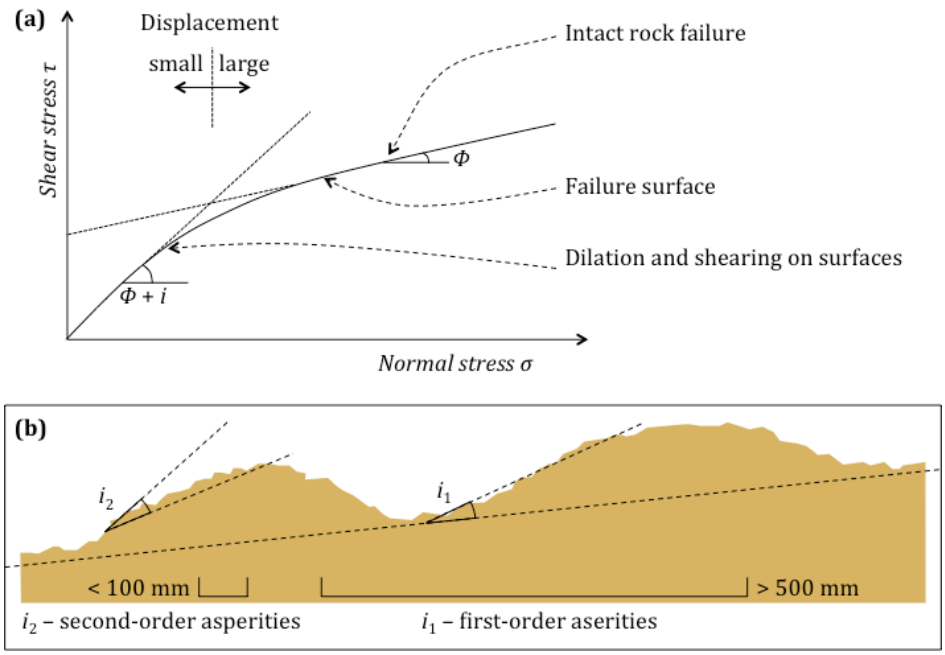

Figure 3-3 (a) Effects of surface roughness *i* on friction *Φ* and (b) different scales of roughness (in Dippenaar and Van Rooy, 2016; e.g. Hoek and Bray, 1981; Indraratna and Ranjith, 2001; Look, 2014).

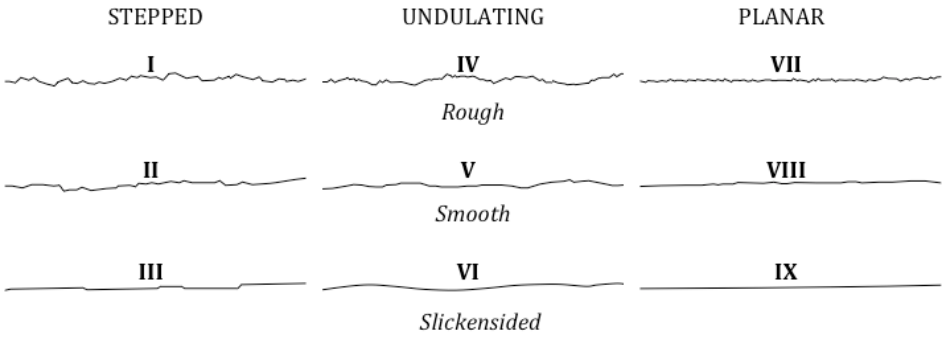

Figure 3-4 Field description of roughness (horizontal scale is 10 cm) (Brown, 1981; in Dippenaar and Van Rooy, 2016).

Barton and de Quadros (1997) summarise that the joint roughness coefficient (JRC) can be estimated by either matching roughness profiles or using gravity tilt tests together with an estimate of the joint wall strength (JCS), measured with a Schmidt hammer, as detailed by Barton and Choubey (1977); and Brown (1981). Barton and de Quadros (1997) further summarise a third technique initially proposed by Barton (1982), which represents a maximum roughness amplitude (r_a), by placing a straight edge along the joint and recording the maximum amplitude (a) for a measured profile length (L). This procedure should be conducted along several profiles in order to gather a representative average. The JRC can then be calculated by the following relationship, at 100 mm scale:

$$JRC = 400\frac{a}{L}$$ **Equation 3-1**

3.3 Lugeon (Water Pressure) Tests

In practice, the common method of assessing water flow through fractured rock masses for engineering purposes is by using the Lugeon test (Lugeon, 1933) or water-pressure test (WPT). The Lugeon test is an *in-situ* test used to determine adequate hydraulic conductivity of a rock mass, and the results of which are expressed in Lugeon (*Lu*) units. The test was mostly developed to determine groutability and efficiency of ground treatment for dam foundations. It is a type of constant-head test that uses inflatable packers to isolate a section of a borehole for water injection through a perforated pipe at a constant pressure over a number of steps or intervals.

3.3.1 Basic Test Description and Procedure

These tests are conducted in a portion of a borehole by pumping water through a perforated pipe at a constant pressure between either a single packer and the base of a borehole as shown in Figure 3-5a, or a section between two packers, and Figure 3-5b. Generally, five tests are conducted at multiple constant pressure intervals per borehole section for a period of 10 min each, with both water pressure and flow rates being recorded for each stage. Common practice for multiple-pressure tests is to increase the pressure for three consecutive steps to a maximum test pressure (P_{max}). Subsequently, the pressure is decreased over two steps at equivalent pressure to the second and first increasing step respectively. Table 3-1 shows the pressure magnitudes customarily used during these five test stages in relation to the maximum test pressure (P_{max}).

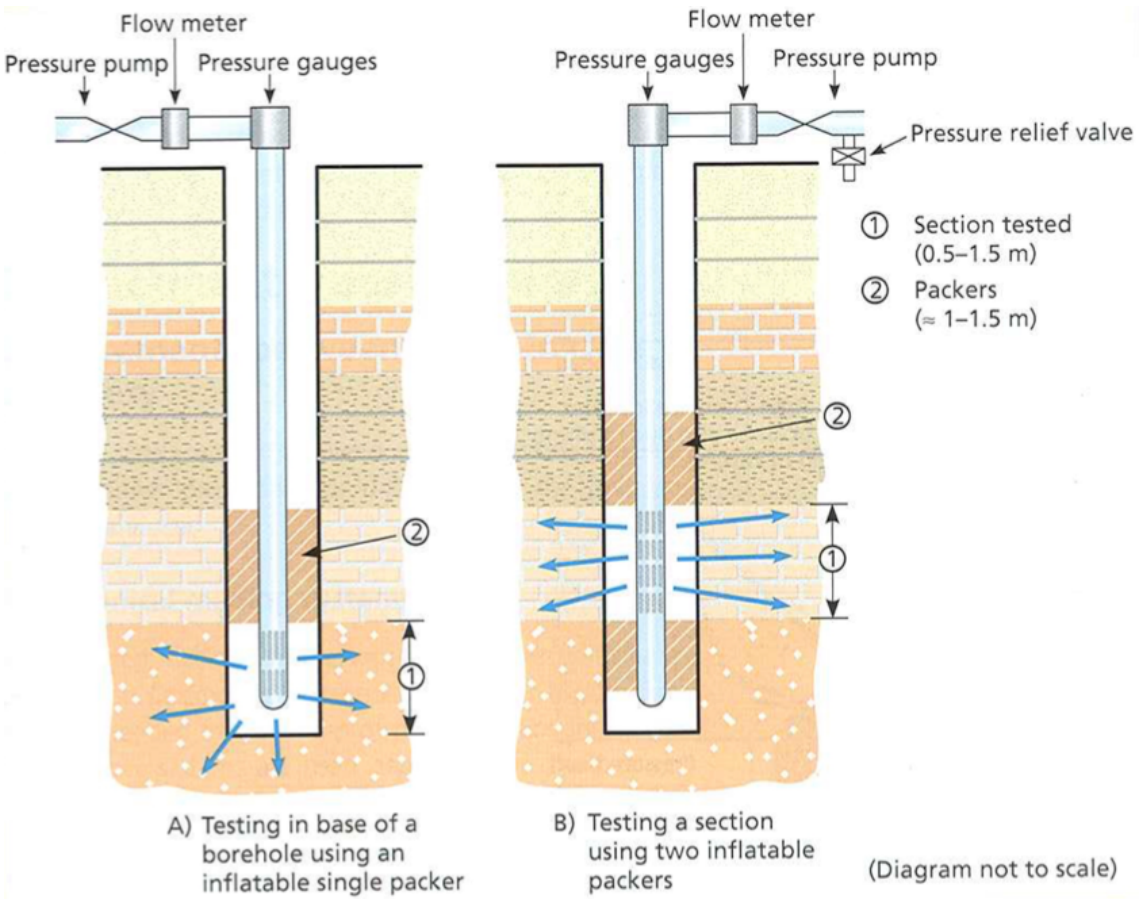

Figure 3-5 Cross-sectional view of a general Lugeon test configuration. a) Single packer; and b) Double packer (González de Vallejo and Ferrer, 2011).

Table 3-1 Pressure magnitudes typically used for each stage (Quiñones-Rozo, 2010).

Test Stage	Description	Pressure	
		Step	Description
1st	Low	Pressure 1	$0.50 \times P_{max}$
2nd	Medium	Pressure 2	$0.75 \times P_{max}$
3rd	Maximum (P_{max})	Pressure 3	P_{max}
4th	Medium	Pressure 2	$0.75 \times P_{max}$
5th	Low	Pressure 1	$0.50 \times P_{max}$

The recorded flow rates are used to calculate the Lugeon-number for each step using the following equation (Nonveiller, 2013; Palmstrom and Stille, 2010):

$$Lu = \frac{Q}{P_e L}$$ **Equation 3-2**

where *Lu* is the Lugeon-number, *Q* is the flow rate (*l*/min); *L* is the length of the studied segment (m); and P_e is the effective pressure in the tested segment (MPa). The average value of the flow rate and the water pressure is then used to calculate the Lugeon value for a specific stage. Moreover, the Lugeon-value can be expressed as (Weaver and Bruce, 2007):

$$1\ Lu = 1l \times m^{-1} \times bar^{-1}, at\ a\ test\ pressure\ of\ 10\ bars$$ **Equation 3-3**

Multiple-pressure tests are typically utilised during exploration investigations, prior to construction. However, these thorough Lugeon tests are not always performed where instead simple single-pressure tests are usually conducted. Such practice is fairly common in curtain boreholes during grout operations, where these single-pressure Lugeon tests generally help decide whether grouting is necessary. Furthermore they provide a basis for the selection of the appropriate starting grout mix formulation, and verify that the desired permeability standard has been achieved (Weaver and Bruce, 2007).

Data Interpretation

Houlsby (1976) proposed that a representative Lugeon-value is chosen by observing the behaviour of the calculated Lugeon-number for each stage, and introduced five flow types from which this Lugeon-value is chosen. The five flow types, their description and the deduction of the representative Lugeon-value is presented in Figure 3-6, and are as follows (Quiñones-Rozo, 2010):

1. Laminar Flow: The Lugeon-number of the rock mass is independent of the water pressure employed. This behaviour is characteristic of rock masses exhibiting low hydraulic conductivities, where seepage velocities are relatively small (i.e., less than four Lugeons).
2. Turbulent Flow: The Lugeon-number of the rock mass decreases as the water pressure increases. This behaviour is characteristic of rock masses exhibiting partly open to moderately wide cracks.
3. Dilation: Similar Lugeon-numbers are observed at low and medium pressures; however, a much greater value is recorded at the maximum pressure. This behaviour, which is sometimes also observed at medium pressures, occurs when the water pressure applied is greater than the minimum principal stress of the rock mass, thus causing a temporary dilatancy (hydro-jacking) of the fissures within the rock mass. Dilatancy causes an increase in the cross-sectional area available for water to flow, and thereby increases the Lugeon-number.
4. Wash-Out: Lugeon-number's increase as the test proceeds, regardless of the changes observed in water pressure. This behaviour indicates that seepage induces permanent and irrecoverable damage on the rock mass, usually due to infillings washing out and/ or permanent rock movements.
5. Void Filling: Lugeon-number's decrease as the test proceeds, regardless of the changes observed in water pressure. This behaviour indicates that either: (i) water progressively fills isolated/non-persistent discontinuities, ii) swelling occurs in the

discontinuities, or iii) fines flow slowly into the discontinuities building up a cake layer that clogs them.

BEHAVIOR	PRESSURE STAGES	LUGEON PATTERN	DESCRIPTION	REPRESENTATIVE LUGEON VALUE
LAMINAR	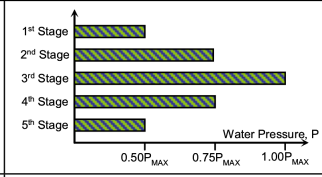	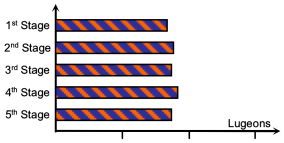	All Lugeon values about equal regardless of the water pressure	Average of Lugeon values for all stages
TURBULENT	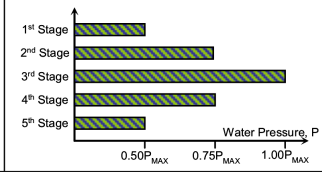	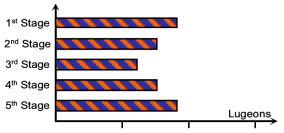	Lugeon values decrease as the water pressures increase. The minimum Lugeon value is observed at the stage with the maximum water pressure	Lugeon value corresponding to the highest water pressure (3rd stage)
DILATION	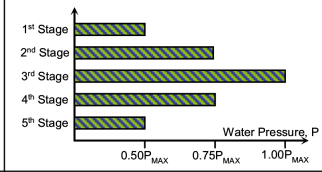	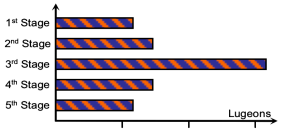	Lugeon values vary proportionally to the water pressures. The maximum Lugeon value is observed at the stage with the maximum water pressure	Lowest Lugeon value recorded, corresponding either to low or medium water pressures (1st, 2nd, 4th, 5th stage)
WASH-OUT	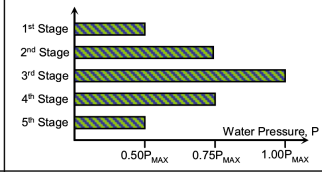	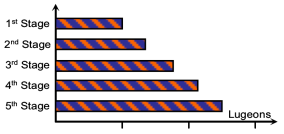	Lugeon values increase as the test proceeds. Discontinuities' infillings are progressively washed-out by the water	Highest Lugeon value recorded (5th stage)
VOID FILLING	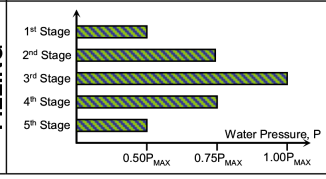	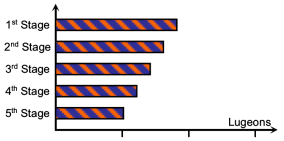	Lugeon values decrease as the test proceeds. Either non-persistent discontinuities are progressively being filled or swelling is taking place	Final Lugeon value (5th stage)

Figure 3-6 Summary of current Lugeon interpretation practice (as proposed by Houlsby, 1976; in Quiñones-Rozo, 2010).

The Lugeon test gives a continuous vertical distribution of hydraulic properties through a rock mass, and is essential to the proper design of the hydrogeological program for the given engineering purpose. Houlsby (1990) suggests that when the decided *Lu* value is below 3, no grouting is necessary; when between 3 and 10, a single row of grouting holes is required, while with a value of over 10, a grout curtain should include three rows of grouting holes. Furthermore, Ewert (2003) suggests that small *Lu* values (<2-5 *Lu*) usually indicate ungroutable rock, moderate values (<5-10 *Lu*) usually indicate poor groutability, and large *Lu* values may indicate a groutable rock. Weaver and Bruce (2007), however caution against these guidelines, with specific emphasis that they had found it possible to grout to a 1 *Lu* standard.

3.3.2 Determination of Hydraulic Properties

The *Lu*-value can also be expressed by the tangent slope of the Pressure-Flux (*PQ*) diagram, and can also provide useful guidance on the properties of the rock mass and the interpretation of the flow behaviour (Ewert, 1997b; Palmstrom and Stille, 2010; Widmann, 1996). Furthermore, Nonveiller (2013) suggests that this tangent slope of the *PQ* diagram is a valid expression of the Lugeon value during Lugeon-water pressure tests, and expresses a representative value at any point on the diagram. Six flow behaviours and their specific relationship on the *PQ* diagram is shown in Figure 3-7 and are identified as follows (Widmann, 1996):

a) Laminar flow;
b) Turbulent flow;
c) Hydraulic fracturing;
d) Erosion of joints;
e) Plugging of joints; and
f) Probable flow around the packer.

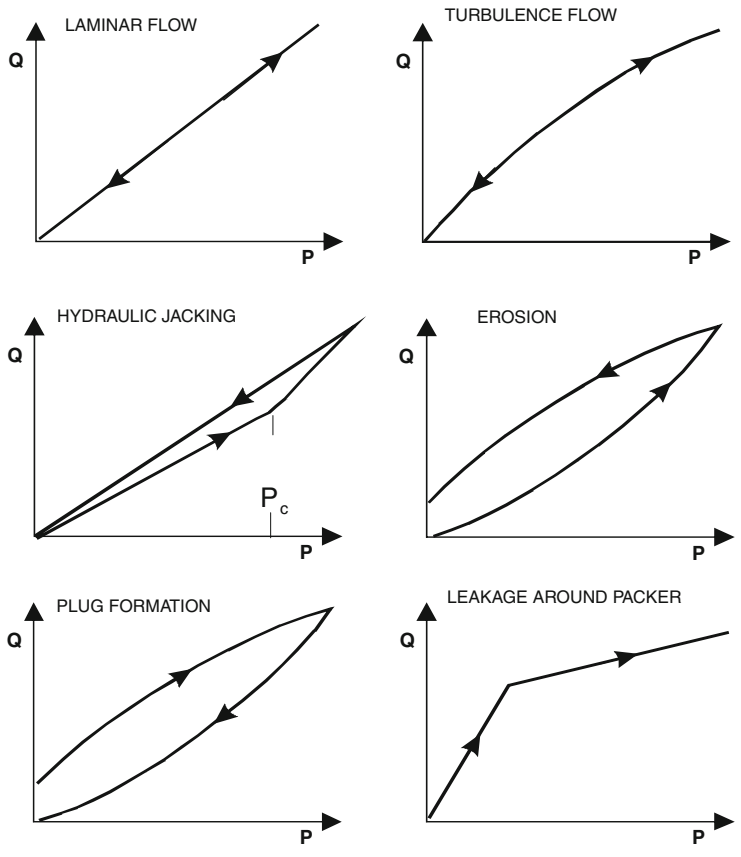

Figure 3-7 Staged Lugeon tests and different interpretations for *PQ* diagrams (Palmstrom and Stille, 2010).

Barton (2004) and Weaver and Bruce (2007) suggest that the Lugeon-value is related to the hydraulic conductivity (*K*) and intrinsic permeability (*k*) by the following relationship:

$$1\ Lu \approx 1.3 \times 10^{-7} m/s \approx 10^{-14} m^2$$ **Equation 3-4**

Furthermore, Palmstrom and Stille (2010) present that the water loss measurements can be used to calculate the hydraulic conductivity of the rock mass using Moye's formula:

$$k = \frac{Q}{L\Delta H}\left(\frac{1 + \ln\frac{L}{D}}{2\pi}\right) \approx \frac{Q}{L\Delta H}$$ **Equation 3-5**

Where, Q is the flow (m^3/s), ΔH is the excess pressure in metres of a water column (m), L is the length of the test section (m), and D is the diameter of the borehole (m). The transmissivity (T) can be evaluated with the following equation (Palmstrom and Stille, 2010):

$$T = \frac{Q}{\Delta H}$$ **Equation 3-6**

The hydraulic conductivity can thereafter be related to the transmissivity by the following equation (Palmstrom and Stille, 2010):

$$T = kL$$ **Equation 3-7**

Notwithstanding, using the approach to that of Quinn et al. (2011), the value of PQ where the graph is linear provides the transmissivity (T) for the Lugeon-test interval by using the Thiem equation (Wenzel, 1936):

$$T = \frac{Q}{2\pi dH}\ln\left(\frac{r_o}{r_w}\right)$$ **Equation 3-8**

where r_o is the radius of influence of the test [L] and r_w is the well radius [L]. The Thiem equation is based on the assumption that flow is radial and that Darcian flow conditions occur through a horizontal, confined, "infinite" homogeneous aquifer (Quinn et al., 2011). Due to the equation originally being developed for pumping tests in confined porous media aquifers whereby two observation boreholes are used, when using the equation for single-packer Lugeon-water tests in fractured rock, an uncertainty arises in the assumption of the radius of influence (r_o). Royle (2002) and Yihdego (2017) both explain that a r_o value of between 5 m and 10 m is reasonable and yields a realistic value for K. Quinn et al. (2011); however, cites ranges from as small as 0.6 m (Zeigler, 1976) to as large as 60 m (Maini, 1972), but followed the example of Haimson and Doe (1983) by using 30 m for their T calculations.

Despite the relationships described above, Ewert (1985, 1992) and Ewert and Hungsberg (2018) argue that Darcy's Law does not apply in these tests, mostly due to the characteristic anisotropy and large-scale inhomogeneity's in the rock mass, coupled with the unknowability of the nature and distribution of flow paths. Therefore, the coefficient of permeability as defined by Darcy's Law cannot be determined quantitatively (Weaver and Bruce, 2007).

Stille et al. (2012) explain that the *Lu* tells little of the properties of the section of the borehole to grout and its ability to take grout and the predicted sealing caused by grouting. The authors explain that a test section with some 10s of fractures, the most transmissive fracture carries more than 75 % of the flow, whilst for a longer test section with 100 to 1000 fractures, the largest fracture still carries about 50 % of the flow. Furthermore, Gustafson and Fransson (2006), found that the transmissivity of a test section followed a Pareto (power law) distribution, which indicates that Lugeon-test data is dominated by a few very high values (i.e. highly transmissive fractures) compared to many small value data (i.e. poorly transmissive fractures).

The fact that the magnitude of the fracture transmissivity decreases rapidly with the rank leads to the conclusion that only a few groutable fractures carry significant water flows. These are critical for the design and performance of grouting and the aperture of these are critical for grout penetrability and penetration length. Stille et al. (2012) conclude that the averages, which the Lugeon-value represents, are therefore not significant for that, which is the reason why transmissivity is the better parameter over hydraulic conductivity.

3.3.3 Considerations and Uncertainties

Particular to grout operations, Widmann (1996) state that prior to the interpretations of any Lugeon test data, the structure and geometry of the flow paths need to be understood and conceptualized, as they may vary considerably at the local intersection of the borehole and fracture. During these tests, flow from the borehole along the fracture is initially turbulent and becomes laminar farther from it, as shown in Figure 3-8 (Widmann, 1996). Important geometric factors of flow paths are both the cross-sectional area of flow and the structure of the flow paths, which determine the change in dimensions of the flow area away from the borehole (Widmann, 1996). In addition to the findings of Iwai (1976), who attributed non-linear flow to inertial effects due to fluid bending at the entrance to the fracture, Widmann (1996) also states that considerable pressure losses are expected at the intersection of the borehole with a fracture at high flow velocities. Despite its limitations, these tests remain the only practical method of investigating the permeability of fractured rock masses for engineering purposes.

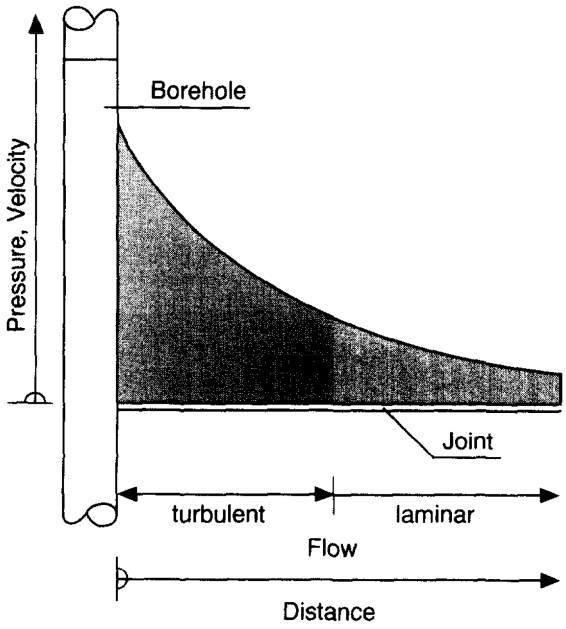

Figure 3-8 State of flow around a borehole (Widmann, 1996).

3.4 Secondary Permeability Index (SPI)

Foyo et al. (2005) combined a modified form of the Lugeon relation with the radial permeability of a rock mass, as well as the borehole geometry (radius) to propose a new equation that yields a value that is closer to the permeability coefficient than that yielded by the Lugeon relation:

$$SPI = C \times \frac{\ln\left(\frac{2L_e}{r} + 1\right)}{2\pi L_e} \times \frac{Q}{H.t} \qquad \textbf{Equation 3-9}$$

Where: SPI is the Secondary Permeability Index, (*l*/s per m^2 of the borehole test surface); *C* is a constant that depends on the fluid viscosity at 10°c (1.49 x 10^{-10} for water); L_e is the length of the tested borehole interval (m); *r* is the borehole radius (m); *Q* is the water flow absorbed by a fissured rock mass (*l*); *t* is the duration of the pressure applied in each step (s); and *H* is the total pressure expressed as a water column (m). The SPI establishes a permeability-based rock mass classification as defined in Table 3-2.

Table 3-2. Rock mass classification based on the SPI and ground treatment considerations (Foyo et al., 2005).

	Secondary Permeability Index (l/s m^2)			
	<2.16 x 10^{-14}	2.16 x 10^{-14} - 1.72 x 10^{-13}	1.72 x 10^{-13} - 1.72 x 10^{-12}	>1.72 x 10^{-12}
Rock mass Classification	Class A	Class B	Class C	Class D
	Excellent	Good-fair	Poor	Very poor
Ground treatment	Needless	Local[(i)]	Required	Extensive

[(i)]Requires separation of 2 possible solutions

The SPI is calculated for each stage per grout borehole and thereafter classified accordingly. In much the same way as analysing Lugeon data via calculating the *Lu*-value per step, the SPI classification also requires the identification of flow types in order to specifically identify any modifications to the joint characteristics induced from the Lugeon-test. This is done by plotting the Total Pressure (Pt) versus SPI graphs in order to identify one of four flow types and selecting the correct SPI value, as shown in Figure 3-9. Additionally, Foyo et al. (2005) places emphasis on identifying hydraulic fracturing, however due to the low pressures used in the WPT hydraulic fracturing was likely to be initiated.

The rock mass classification defined by the SPI, coupled with the degree of jointing with the drill core, permits the rock mass foundation to be zoned into different quality classes and each zone to be treated separately (Foyo et al., 2005). This consideration is shown in Figure 3-10 for the calculated SPI class and the degree of jointing. If the zone is classified as Class A, it implied that ground treatment is needless. However, as Foyo et al. (2005) emphasise, a SPI Class B suggests that it is important to separate two possible situations related to the number of joints present in the test section. If the test section shows a medium or low degree of jointing, it is deduced that at least one joint with an intense activity exists, with regard to permeability. Under this condition, the rock mass requires a local ground treatment and it must be grouted with a medium or thick mixture; 1:1 or 0.5:1 W:C ratio (Foyo et al., 2005). On the contrary, if the test section contains multiple joints, the ground treatment can be considered needless.

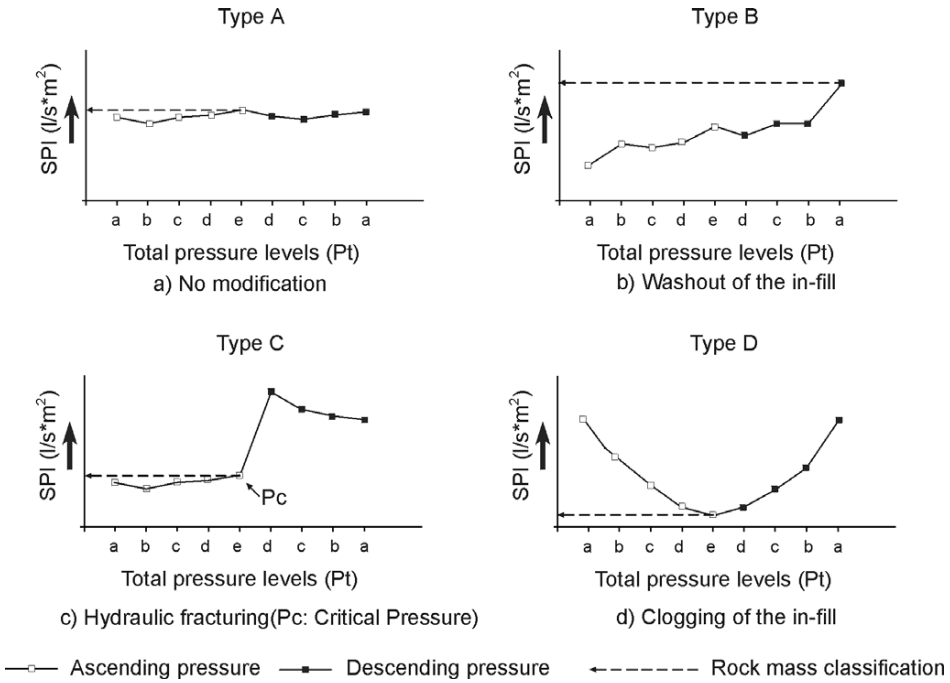

Figure 3-9. Types of Total Pressure (Pt)-SPI graphs for process identification and rock mass classification criteria as presented by Foyo et al. (2005).

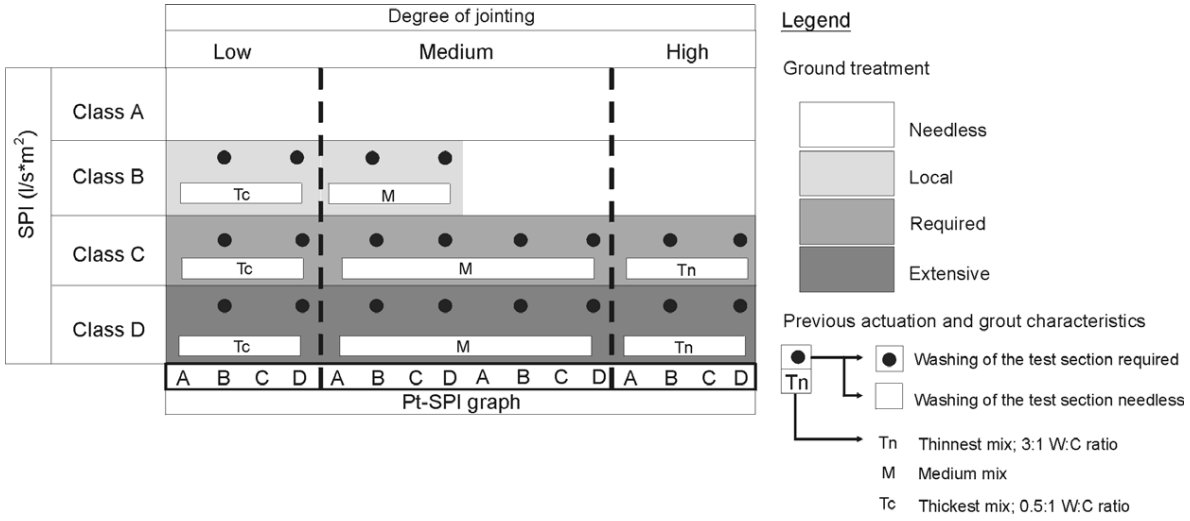

Figure 3-10. Considerations on the ground treatment design based on the calculated SPI (Foyo et al., 2005).

3.5 Relationship between Hydraulic Properties and the Geotechnical Characterisation of Rock Masses

The hydraulic conductivity of fractured rocks is strongly related to the geometric properties and the weathering degree of the flow paths (Foyo et al., 2005; Hamm et al., 2007). Dippenaar and Van Rooy (2016) further propose that partial saturation can be accommodated in the typical discontinuity survey descriptors, despite pore water pressure generally being calculated for saturated conditions.

As discussed in the previous chapter, the hydraulic conductivity of rock masses is closely related to the fracture characteristics that includes the fracture orientation, spacing, persistence, wall strength, roughness, filling and interconnectivity. Hamm et al. (2007) investigated a potential relationship between hydraulic conductivity and fracture properties from several boreholes at their study site. The authors related fracture spacing, orientation and aperture individually to hydraulic conductivity. The hydraulic conductivity is high in areas of high fracture spacing, related to areas with the same fracture spacing having low hydraulic conductivity. Their findings showed that hydraulic conductivity estimations are variable due to fracture persistence; the presence of hydrological boundaries; influence of free water surfaces; and the possibility of water flowing around the packer of the Lugeon test. In contrast, low hydraulic conductivity values in fractures is plausibly due to clay matrix infillings; and the closeness and healed character and poor connectivity in the testing area.

The authors also found a higher correlation between the fracture apertures and hydraulic conductivity, than between fracture spacing and hydraulic conductivity. A lower relationship exists between hydraulic conductivity and fracture aperture of major orientation opposed to the case of not considering the orientation for fracture aperture, which could be due to the flow direction being against the orientation of the fractures. Furthermore, Gurocak and Alemdag (2012) analysed the relationship between permeability and discontinuity surfaces, and

concluded that the discontinuity orientation is very important as the direction of water flow is governed by this parameter. The infilling of the discontinuities as well as the roughness will have a major effect on the permeability value.

This findings were echoed by Öge and Çırak (2017) who found a positive correlation with the Rock Quality Designation value (RQD - a function of the fracture spacing), as well as the surface condition (i.e. weathering) of the fractures, with Lugeon-values. Additionally, they stated that the influence of depth contributed even more so to the Lugeon-value.

Following the rationale of Hamm et al. (2007), Jones et al. (2016) investigated the potential for a correlation to exist between a single or set of discontinuity parameters a section of the De Hoop dam wall, which might be responsible for high or low Lugeon values in a rock mass. The authors concluded that it is highly unlikely that only a single discontinuity parameter would be responsible for high or low Lugeon values. Furthermore, a single discontinuity parameter may play a greater role, but will not be solely responsible for high or low Lugeon values.

Barton et al. (2001); and Barton et al. (2002) attempted to explore the possibilities for using the *Q*-system for evaluation of permeability and grouting of tunnels, with the proposal of the following connection between the Lugeon-value and the *Q*-value (Equation 3-10) for hard, jointed, clay-free rock masses:

$$Lu \approx \frac{1}{Q} \qquad \textbf{Equation 3-10}$$

Barton et al. (2001); and Barton et al. (2002) state that the permeability in a rock mass generally increases with increasing degree of jointing, whereby the *Q*-value decreases. However, Palmstrom and Broch (2006) point out that joint aperture and possible channel formation, which both are very important in ground water movement, are not included in the input parameters to obtain a *Q*-value. Palmstrom and Broch (2006) therefore emphasise the opposite, by stating that for single joints the highest permeability has the highest (*Jr*/*Ja*) value, and therefore the highest *Q*-value, as they indicated for case B in Figure 3-10. They therefore concluded that these two simple contrary conditions are so important, that the *Q*-system can hardly be regarded as suitable for evaluation of permeability, water inflow and grouting.

Singh and Goel (2011) cite a training course by Barton (2008), whereby the permeability (*k*), m/sec, of the rock mass is roughly given by Equation 3-11 at 20°:

$$k \approx \left(\frac{0.002}{Q}\right)\left(\frac{100}{JCS}\right)\left(\frac{1}{H^{5/3}}\right) \qquad \textbf{Equation 3-11}$$

Where: *Q* is the in-situ rock mass quality, as defined by the *Q*-system in Barton et al. (1974); *JCS* is the joint wall compressive strength (MPa); and *H* is the depth of a point under consideration below ground surface (m). Without any further reference to published research Singh and Goel (2011) state that this equation has been confirmed by work on hydroelectric projects in the Himalayas.

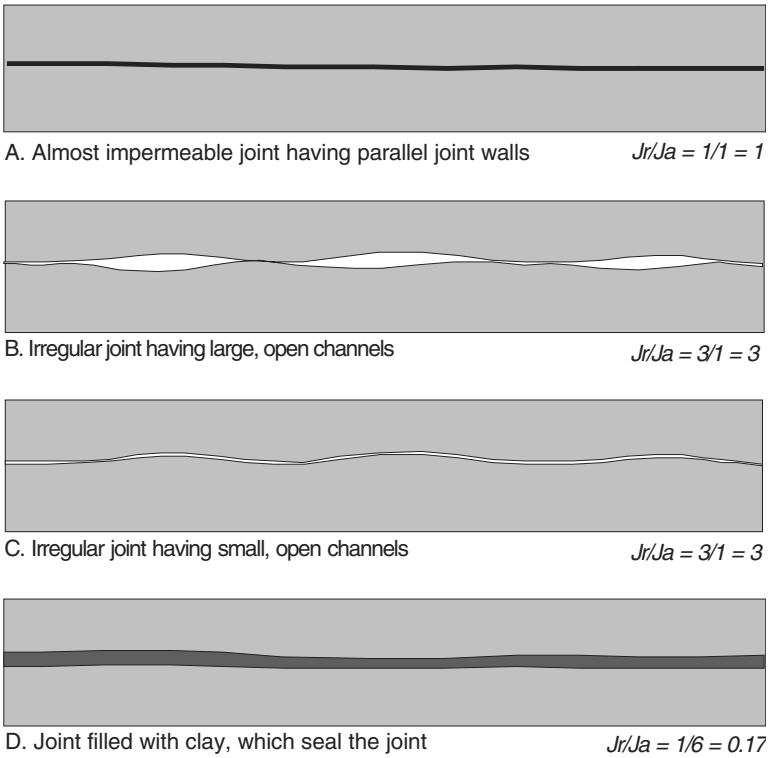

Figure 3-11 Four types of joints with different joint properties. (A) and (D) have very low conductivity, but different impact on the Q value, while (B) and (C) have the same influence on the Q value, but different conductivity (from Palmstrom et al., 2002; in Palmstrom and Broch, 2006).

3.6 Summary

Rock masses in a rock engineering context are mapped by joint line surveys (JLS), with the aim of recording joint properties. The assessment of rock mass permeability is conducted by Lugeon tests that involve the injection of water into a section down a borehole. The intake of water is used to characterise the permeability of the discontinuities that intersect the rock mass within the test section, and is primarily used for the design of grouting operations and ground treatment in civil engineering projects.

CHAPTER 4 GEOTECHNICAL CENTRIFUGE MODELLING

4.1 Introduction

Physical modelling is concerned with replicating an event comparable to what may exist in the prototype. The two events should be similar, and that similarity needs to be related by appropriate scaling laws. The geotechnical centrifuge is an important piece of equipment available to the geotechnical profession as it enables the study and analysis of geomechanical problems by using geotechnical materials, in the centrifuge model. Particularly, processes that are affected by gravitational forces are enhanced in geotechnical centrifuge models, with the fundamental requirement for the model and prototype to be similar is that the dimensionless groups are identical (Butterfield, 2000; Phillips, 1995).

4.2 Principles of Geotechnical Centrifuge Modelling

The fundamental issue with modelling geotechnical problems is the necessity of reproducing the ground behaviour both in terms of strength and stiffness. In this regard, the fundamental principles and scaling laws of geotechnical centrifuge modelling have been based on the successful replication of stress-strain properties of soil (Jones, 2014). The field of geotechnics covers a wide range of soil behaviour relevant to a particular problem. One major reason for this is that *in situ* stresses change with depth and it is well known that soil behaviour is a function of stress level and stress history. It is therefore obvious that in a successful physical model these features will be important to replicate (Taylor, 1995). Centrifuge modelling is unique in that the most complex numerical soil mechanics models are only mathematical approximations of reality, while the use of physical modelling negates the need for complex constitutive models to be selected (Jacobsz, 2011). Unlike constitutive models, no assumptions need to be made and an actual physical event can be observed, at model scale (Jacobsz, 2013b).

Geotechnical centrifuge modelling is a useful tool available in the profession to replicate *in situ* stresses. Models placed at the end of a centrifuge arm can be accelerated so that they are subjected to an inertial radial acceleration field which, as far as the model is concerned, seems like a gravitational acceleration field but many times stronger than acceleration due to gravity (Taylor, 1995). The soil material placed in the container has a free unstressed upper surface and within the material body the magnitude of stress increases with depth at a rate related to the soil density and the strength of the acceleration field (Taylor, 1995). Centrifuge modelling allows the increase of self-weight by the increase of gravitational acceleration, which is equal to the reduction of the model scale, as well as the reduction of time for model tests as the scale is reduced (Schofield, 1988).

Before results from models may be extrapolated to prototype scales, similitude must be achieved, which occurs when three types of similarities are satisfied (Kumar, 2007):

1. Geometric similarity, which is satisfied when there is a constant ratio of lengths in the model and prototype;
2. Kinematic similarity, which is satisfied when the ratios of velocities and acceleration between the model and the prototype are constant; and
3. Dynamic similarity, which is achieved when there is a constant ratio of forces between the model and prototype, where the force may be due to self-weight, viscosity or pressure.

Often the geometric scale factor is selected to fit a prototype situation that causes the least amount of boundary effects in the model (Phillips, 1995). This scaling factor is constrained by the maximum model size, but often this scale factor is made as small as possible and the acceleration level in the centrifuge is normally identical to the geometric scaling factor.

4.2.1 Basic Scaling Laws

If the model is subjected to a similar stress history ensuring that the packing of the soil particles is replicated, then for the centrifuge model subjected to an inertial acceleration field of N times Earth's gravity, the vertical stress at depth h_m will be identical to that in the corresponding prototype at depth h_p, such that (Taylor, 1995):

$$h_p = Nh_m$$ **Equation 4-1**

This is the basic scaling law of centrifuge modelling for linear dimensions. Fundamentally, this law enables a stress similarity to be achieved at homologous points by accelerating a model of scale N to N times Earth's gravitation field, as illustrated in Figure 4-1 (Taylor, 1995). If an acceleration of N times Earth's gravity is applied to a material of density, ρ, then the vertical stress, $\sigma_{v,}$ at depth, h_m, in the model is given by (Taylor, 1995):

$$\sigma_{vm} = \rho N g h_m$$ **Equation 4-2**

And the vertical stress in the prototype, is given by:

$$\sigma_{vp} = \rho g h_p$$ **Equation 4-3**

Therefore:

$$\sigma_{vm} = \sigma_{vp}$$ **Equation 4-4**

Then:

$$h_m = h_p N^{-1}$$ **Equation 4-5**

And the scale factor (model:prototype) for linear dimensions is; 1:N. Therefore, for example, a model with a scale of 1:20 has to be accelerated to 20 times earth's gravity, or 20g, in order to create the correct stress distribution.

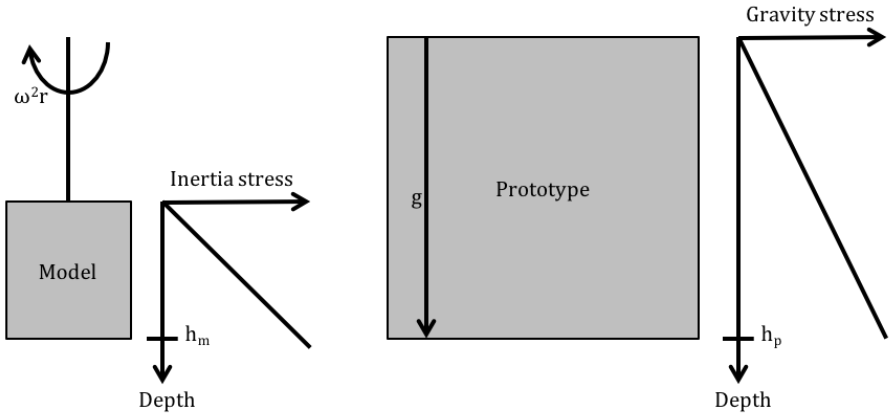

Figure 4-1 Inertial stresses in a centrifuge model induced by rotation about a fixed axis correspond to gravitational stresses in the corresponding prototype (Taylor, 1995).

Due to this linear scaling law for model dimensions, other physical properties can subsequently be derived and scaled. The scaling law for force is derived by considering Newton's second law (Jacobsz, 2013a), $F_p=m_p a_p$, where m_p is the mass, and a_p is the acceleration of the prototype (subscript p). If the material to be scaled is assumed to be a cube with density, ρ, and side length, l_p, and it is stationary on earth's surface, Newton's second law can be expressed as (Jacobsz, 2013a):

$$F_p = \rho\, l_p^3\, g$$ **Equation 4-6**

Where, g is gravitational acceleration. Newton's second law for the model can be written as:

$$F_m = m_m a_m$$ **Equation 4-7**

Where, F_m is the force at model scale, m_m is the mass of the model, and a_m is the acceleration at model scale. In general, the standard practice in geotechnical centrifuge modelling is to use the same material that occurs in the full-scale situation, in the model, such that the material properties remain identical. Therefore, if the prototype material with density, ρ, is used in the model, and the model is N times smaller than the prototype, and therefore accelerated to N times earth's gravitational acceleration, Equation 4-7 can be rewritten as (Jacobsz, 2013a):

$$F_m = \rho l_m^3 Ng$$ **Equation 4-8**

And Equation 4-8 becomes:

$$F_m = \rho \left(\frac{l_p^3}{N}\right)^3 Ng = \frac{\rho l_p^3 g}{N^2} = \frac{F_p}{N^2}.$$ **Equation 4-9**

Therefore, proving the scaling law for force. It is on the same scaling basis that all physical properties can be scaled.

4.2.2 General Scale Effects

Centrifuge modelling is often criticised for having significant scaling errors due to non-uniform acceleration field and difficulty of creating a representative model of the prototype (Taylor, 1995). One effect is the induced gravitational acceleration created by a geotechnical centrifuge, which acts towards the centre of rotation and may lead to the inertial stress variations in model depth. However, this non-linear stress distribution is generally minor when care is taken in selecting an effective centrifuge radius that occurs at one-third model depth (Taylor, 1995). Additionally, there is a change in direction of the relative vertical acceleration, which results in a lateral component of acceleration. This effect is significant near the sidewalls of the container, but may be mitigated by ensuring that the major observations of the model occur in the central region of the model.

Furthermore, since linear dimensions are scaled by a factor of 1:*N*, this implies that the individual particles should be scaled in conjunction with other linear dimensions by the same scaling factor, where in certain circumstances particle size effects could be important (Taylor, 1995). With this reasoning, it is possible to model fine sand with clay in the model. However, this is not a requirement when modelling using the centrifuge as clay is a cohesive material while sand is non-cohesive, and therefore each material has remarkably different stress-strain and seepage behaviours. Therefore, in centrifuge modelling, a microscopic length dimension scaling factor is also defined. To ensure similitude between model and prototype, this linear dimension does not scale and incorporates dimensions in the order of magnitude of individual grain sizes, pore spaces, and fracture apertures.

4.3 Scaling of seepage

For all scaling factors regarding seepage flow in a geotechnical centrifuge, it is assumed that the soil is fully saturated and these scaling factors are derived from using one-dimensional expressions (Culligan-Hensley and Savvidou, 1995). However, the scaling factors are also valid for multi-dimensional problems and unsaturated conditions, but when the model is in fully saturated conditions, the flow of the liquid does not depend on surface tension, but only depends on gravitational force, viscosity and average grain size (Laut, 1975).

4.3.1 Darcy's Law

The rate of seepage flow in a geotechnical centrifuge is determined through Darcy's Law and is increased by a scaling factor of *N*. However, there is currently some controversy behind how the scaling factor is determined with the debate focusing on two main factors (Taylor, 1995). These factors are the interpretation of the hydraulic gradient and permeability used in Darcy's equation.

If the same fluid is used in the model and prototype, then the permeability is apparently a function of gravitational acceleration and scales as $k_m = Nk_p$, while the hydraulic gradient does not scale as it is a dimensionless ratio and therefore $i_m = i_p$. Therefore, from Equation 4-10, which relates the seepage velocity (*v*) between the model and prototype, it can be seen that the seepage velocity in the model occurs *N* times faster than the prototype seepage velocity and supplying a scaling factor of 1:*N*.

$$v_m = i_m k_m = i_p N k_p = N v_p$$ **Equation 4-10**

This implies a worrying situation where soils are impermeable under a zero-gravity field. This implication assumes that seepage is gravity driven and therefore at zero gravity there would be no driving force to induce seepage flow. With this in mind, it is more realistic to think of hydraulic gradient as a pressure gradient. By treating the permeability as a constant material property such that $k_m = k_p$. Then, since the stresses are the same, while distances reduced by a scaling factor of *N* times between the prototype and model, implies a scaling factor of $i_m = Ni_p$ for the hydraulic gradient. Substituting this assumption into seepage velocity, as shown in Equation 4-11, provides the same scaling factor as in Equation 4-10.

$$v_m = i_m k_m = N i_p k_p = N v_p$$ **Equation 4-11**

A study conducted by Thusyanthan and Madabhushi (2003) evaluated this conundrum and proposed that Darcy's law is equivalent to Navier-Stokes equations and that the flow is not gravity driven but rather pressure driven. They proposed that Equation 4-12 should be used to calculate seepage velocity:

$$v = \frac{k}{\mu} \times \frac{\Delta[p + zpg]}{\Delta L}$$ **Equation 4-12**

In this equation, the $\Delta[p + zpg]$ term represents the pressure difference that drives flow in Darcy's law.

4.3.2 Reynold's Number

Darcy's law is only valid at low Reynolds numbers where flow is laminar (Culligan-Hensley and Savvidou, 1995). In order to obtain strict similitude between the prototype and the model, the fluid motion in the model must equal the fluid motion in the prototype and is only satisfied

when $R_{em} = R_{ep}$ (Culligan-Hensley and Savvidou, 1995). Since seepage flow velocities in the geotechnical centrifuge are scaled by a factor of 1:*N*, Reynolds number is scaled by a factor *N* as shown in Equation 4-13 to ensure strict similitude.

$$R_{em} = NR_{ep}$$ **Equation 4-13**

However, even if $R_{em} \neq R_{ep}$, there can still be similarity of fluid motion in the model and prototype provided the same manner of flow occurs in both cases. It is therefore always necessary to confirm that laminar flow conditions are present to ensure that Darcy's law is valid and can be suitably modelled in the test (Culligan-Hensley and Savvidou, 1995).

4.3.3 Time

When performing seepage flow scenarios in a geotechnical centrifuge, another parameter that is scaled is time (Taylor, 1995). Since the scaling factor for seepage velocity is 1:*N* and the scaling factor for the flow paths is 1:*N*, since it may be considered as linear dimension, the time scaling factor for seepage flow can be derived as shown in Equation 4-14, providing a scaling factor of 1:N^2:

$$t_m = \frac{L_m}{vm} = \left(\frac{L_p}{N}\right)\left(\frac{1}{Nv_p}\right) = \frac{1}{N^2}t_p$$ **Equation 4-14**

It is possible that if soils in the model and prototype have different permeabilities that this effect can be taken into account as shown in Equation 4-15 (Taylor, 1995):

$$t_m = \frac{1}{N^2}\frac{K_p}{K_m}t_p$$ **Equation 4-15**

4.4 Modelling of Flow through Rock

Modelling of soil behaviour in the geotechnical centrifuge is well studied with a large amount of studies available. Unfortunately, the same cannot be said for centrifuge modelling of rock masses, with literature limited to geotechnical problems of rock slopes or mining instabilities (e.g. Cecconi et al., 2006; Chen et al., 2006; Chikatamarla et al., 2006; Einstein et al., 1990; Günzel and Davies, 2006; Itoh et al., 2006; Joseph and Einstein, 1988; Li et al., 2014; Stone et al., 2013). This is due to the inability of using the prototype material in the model due to the discontinuous nature of a rock mass and the lack of suitable analogue material alternative (Chen et al., 2006).

Adopting the reasoning of Culligan and Barry (1998) for the problem of fracture flow, the ratio of body gravity to capillary forces must be correct in order to simulate fluid invasion in a fracture, and therefore the fracture aperture does not scale. Once fluid is in the fracture, similitude will depend on the flow mechanisms themselves. Adopting fractures as a microscopic linear dimension from the reasoning of Culligan and Barry (1998), Levy et al.

(2002) investigated dense-NAPL invasion into a fracture. The authors concluded that there is good agreement between scaled centrifuge data and prototype data provided that inertial forces in the fracture remain negligible. From these findings, Levy et al. (2003) formulated an equation to quantify the influence of inertial forces by three regime criterion, in addition to the scaling laws proposed by Culligan and Barry (1998). Beyond the discussed modelling of rock slope stability problems, and dense-NAPL experiments, no literature exists relating to the modelling of unsaturated fracture flow in the geotechnical centrifuge.

4.5 Summary

Centrifuge modelling has become a powerful physical modelling tool in the geotechnical profession. The most fundamental reason for this is that it replicates the *in situ* stresses in a ground profile, which other small-scale physical models cannot do. This is achieved by placing the model at the end of the centrifuge arm, and thereafter subjecting it to an increased gravitational field, which creates the correct stress distribution within the model. This is necessary to ensure realistic ground behaviour. The centrifuge model and associated prototype are related by the scaling laws for various physical quantities as summarised in Table 4-1.

Table 4-1. Geotechnical centrifuge scaling factors (Culligan and Barry, 1998; Garnier et al., 2007; Taylor, 1995).

Parameter	Symbol	Scale factor
Model scale	-	N
Acceleration	g	N
Macroscopic length (i.e. soil height)	l	$1/N$
Microscopic length (i.e. fracture aperture)	l	1
Stress	σ	1
Strain	ε	1
Mass	m	$1/N^3$
Force	F	$1/N^2$
Dynamic viscosity	μ	1
Intrinsic permeability	κ	1
Density	ρ	1
Seepage velocity	v	N
Time	t	$1/N^2$
Reynolds number	R_e	N

CHAPTER 5 MATERIALS AND METHODS

5.1 Introduction

The thesis is structured such that the test preparation for a specific experiment is presented with that chapter, so that a complete experiment can be followed without interruption. This greatly improves readability. The following chapter therefore presents an overview of the methodology adopted for the research as presented in this thesis. The initial section outlines the field methods used to obtain the data from the De Hoop Dam. The results and analyses of this data from the field were used to guide the development of a series of centrifugal experiments in order to investigate several fundamental conceptual models of flow within the fractured vadose zone. The general materials and methods of these experimental models are thereafter outlined in order to introduce the basis for the set-up of each experiment as detailed in the relevant chapter.

5.2 De Hoop Dam

Geotechnical centrifuge models are usually scaled down from a prototype site to benchmark the results obtained from the scaled and accelerated tests. However; due to the complexity involved in both rock mass modelling as well as the uncertainties of unsaturated flow, the De Hoop Dam was rather used to provide a prototype benchmark. The intention was therefore not to replicate the exact rock mass conditions at the De Hoop Dam, but rather investigate the field data in order to, and in conjunction with previous literature, would guide the model set-ups tested in the centrifuge.

5.2.1 Background

The De Hoop Dam, located in the Limpopo Province of South Africa (Figure 5-1), has been constructed as the bulk water supply for infrastructure, mining activities as well as providing domestic water to approximately 800 000 people living in the region. The dam can potentially hold a bulk water reserve volume of 346 $x10^6$ m^3. The construction of the dam is part of the second phase of the Olifants River Water Resources Development Project, conducted by the Department of Water and Sanitation in South Africa. Preliminary feasibility investigations were conducted in the late 1980's, with the design investigation being carried out during mid-2005. Construction of the dam commenced in June 2007, as a Roller Compacted Concrete (RCC) dam with a final length of 1016 m and a height of 81 m at the highest section.

Figure 5-1. Locality plan of the De Hoop Dam, South Africa.

5.2.2 Data

Data from the investigation phase, foundation mapping during construction and Lugeon testing prior to and during grouting were made available from both the Department of Water Affairs and Knight Piésold.

5.2.2.1 Foundation Mapping

Data was obtained during the construction phase and comprised geological mapping of each block on the dam foundation that was conducted once the block was cleaned and ready for concrete placement, as shown in Figure 5-2. Mapping is conducted by joint line surveys (JLS) with the aim to record and measure the discontinuity parameters, including: position; rock type; type of structure; aperture; dip and dip direction (orientation); continuity; roughness; waviness and amplitude; gouge or filling; and water conditions (seepage).

JLS are conducted on each cleaned foundation block, in two directions; firstly, parallel to the dam reference line, with the second survey being conducted perpendicular to the reference line. The parallel surveys are conducted from the river towards the uppermost direction of the respective flank. The perpendicular surveys are conducted from the upstream side of the dam reference line to the downstream side, either down the length of the foundation block or along the length of the block interfaces. The size of the parallel surveys are equivalent to the block width (±10 m), whilst the size of the perpendicular surveys varied according to the length of

the foundation block for the dam wall, ranging between 15 to 65 m. Larger blocks, such as the outlet and the spillway spillway, contain up to three to four line surveys.

Figure 5-2 Foundation excavation at De Hoop Dam: a) dam wall axis at the left flank; b) cleaned foundation block ready for detailed geological mapping before concrete placement; and c) as-built geological plan of the respective block (photographs and drawing courtesy of Knight Piésold).

5.2.2.2 Lugeon Testing and Secondary Permeability Index (SPI)

The WPT data for the De Hoop Dam study are obtained from primary grout curtain boreholes (i.e., before the foundation rock had been affected by grouting). Primary grout holes are drilled at 8 m wide intervals. The diameter of each hole is 89 mm and boreholes were drilled and tested downstage, with single-pressure Lugeon-tests carried out in each stage using surface packers. Unfortunately, the disadvantage of conducting single-pressure WPT's is that they do not provide typical flow types. However, the purpose of identifying the flow types under single-pressures in this paper, is primarily to observe washout and void filling conditions. These assisted in identifying potentially erodible infillings in the fractures, as well as highly fractured zones. It was, therefore, not possible to differentiate between laminar, turbulent, and dilation flow types. The Lugeon data is used to calculate the SPI in order to classify the rock mass according to its permeability and give an approximation as to what should have the necessary ground treatment.

5.2.3 Analyses

The analyses of the data initially comprised the calculated SPI value and classes being compared against the grout take obtained for each respective stage per primary grout borehole. The degree of jointing inferred from the production grout boreholes is then validated by 32 rotary cored boreholes drilled during the final detailed investigation, whose location

coincided with the grout curtain axis as well as depth of foundation excavation (as the overburden had subsequently been removed). The intention of this comparison was to correlate typical rock characterisation methods with depth, and in particular to compare the recorded RQD index. Furthermore, the borehole logs contain descriptions used to validate the presence and orientation of geological features within the rock mass.

Due to the grouting boreholes being percussed, an investigation of the degree of jointing with depth was not directly possible. However, as the grout mix and success of the grouting is already known, a back-analysis was conducted in order to infer the degree of jointing. The process involves assessing the SPI class, followed by a decision as to the success of the grout borehole, which is then compared to the grout mix. Based on the success of the grouting, a degree of jointing is assumed. This is then to be compared to the RQD obtained from the detailed exploratory investigation boreholes, and was used to verify whether the correct grout mix meant that the rock mass indeed showed the correct degree of jointing.

Based on the outcome of validation results for each of the Blocks, the orientations of the joint sets where assessed by examining the stereographic projections of each specific Block. This allowed the primary orientation of the joint sets to be compared between blocks that showed positive or negative. Furthermore, the joint water seepage conditions were also assessed in order to identify if the presence of water influenced the results and analyses. The findings were thereafter used to conceptualise, develop and construct the experimental models.

5.3 Experimental Studies

Prior to attempting any full-scale field and laboratory testing, and modelling for verification of results, fundamental principles pertaining to variably saturated fracture flow and geotechnical centrifuge modelling were evaluated. A set of experiments are developed that seek to to investigate the fundamental concept of the Cubic law under conditions of variable saturation, both at 1g and under increased gravitational acceleration. The findings of these tests are expected to provide insight into the validity of the Cubic law to unsaturated conditions, as well as assessing the use of geotechnical centrifuge modelling in addressing problems associated with unsaturated fracture flow in rock masses.

5.3.1 Geotechnical Centrifuge at the University of Pretoria

The University of Pretoria's laboratory is fitted with a 150 G-ton Actidyn C67-4 centrifuge (Figure 5-3). This centrifuge is a beam centrifuge, with a swinging platform. The platform surface will always be normal to the resultant acceleration, provided the hinges remain frictionless and the platform symmetrically loaded. The centrifuge radius is 3 m from the rotation axis to the model platform. The model platform measures 0.8 m x 1.0 m and the available free space above the model platform is 1.3 m. An aerodynamic shield has been fitted to the front of the platform to minimise the drag during testing. A plan and elevation of the centrifuge are presented in Figure 5-4. The centrifuge is capable of carrying a payload of 1500 kg to 100 G, and thereafter 950 kg, up to 130 G. At its maximum capacity the rotational speed is 208 RPM (Jacobsz et al., 2014).

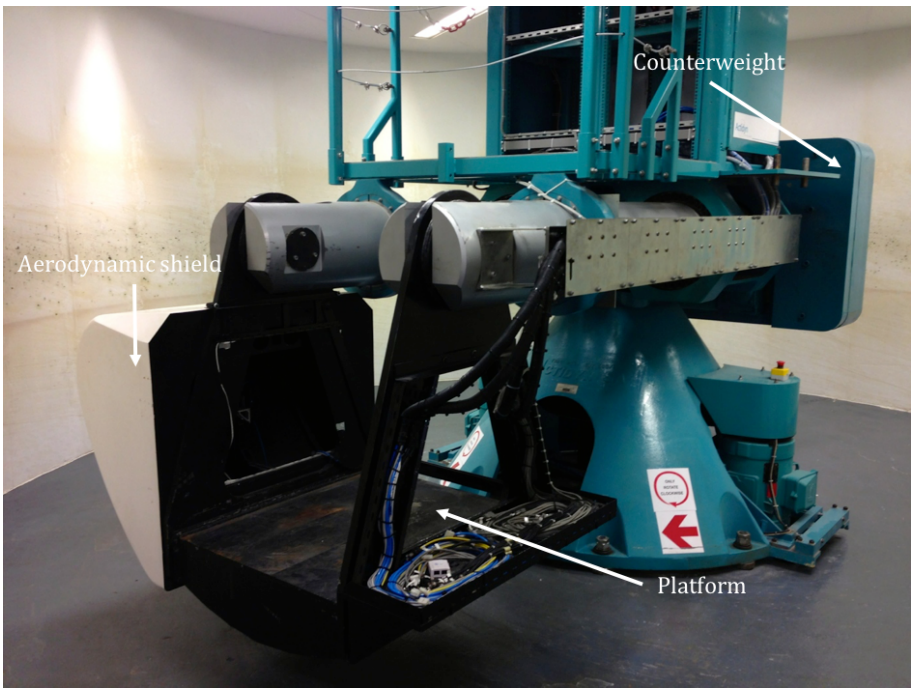

Figure 5-3 The Department of Civil Engineering's geotechnical centrifuge, at the University of Pretoria.

The drive assembly comprises twin AC variable speed induction motors with a maximum combined output of 120kVA operating by means of a belt and pulley transmission system. During testing a constant temperature in the centrifuge enclosure is required and therefore a powerful cooling system has been installed which has sufficient capacity to dissipate the heat released by the drive motors at maximum power. The air is introduced above the machine and withdrawn from vents below the centrifuge base before being cooled and recirculated (Jacobsz et al., 2014). The centrifuge is balanced by an adjustable counterweight, which is automatically adjusted from the centrifuge's control computer. The model weight, desired acceleration and position above the swing platform where the g-level should be balanced are used to estimate the required position of the counterweight before the test commences. The counterweight will then adjust to the calculated position while the centrifuge is still stationary. When the test commences the centrifuge will accelerate to 4.5 G where minor adjustments are made to the counterweight. Once the out-of-balance sensors in the centrifuge pedestal indicate satisfactory balance, acceleration to the desired level will begin. Thereafter, minor fine-tuning of the centrifuge balance during testing occurs via moveable masses inside the hollow centrifuge arms (Jacobsz et al., 2014).

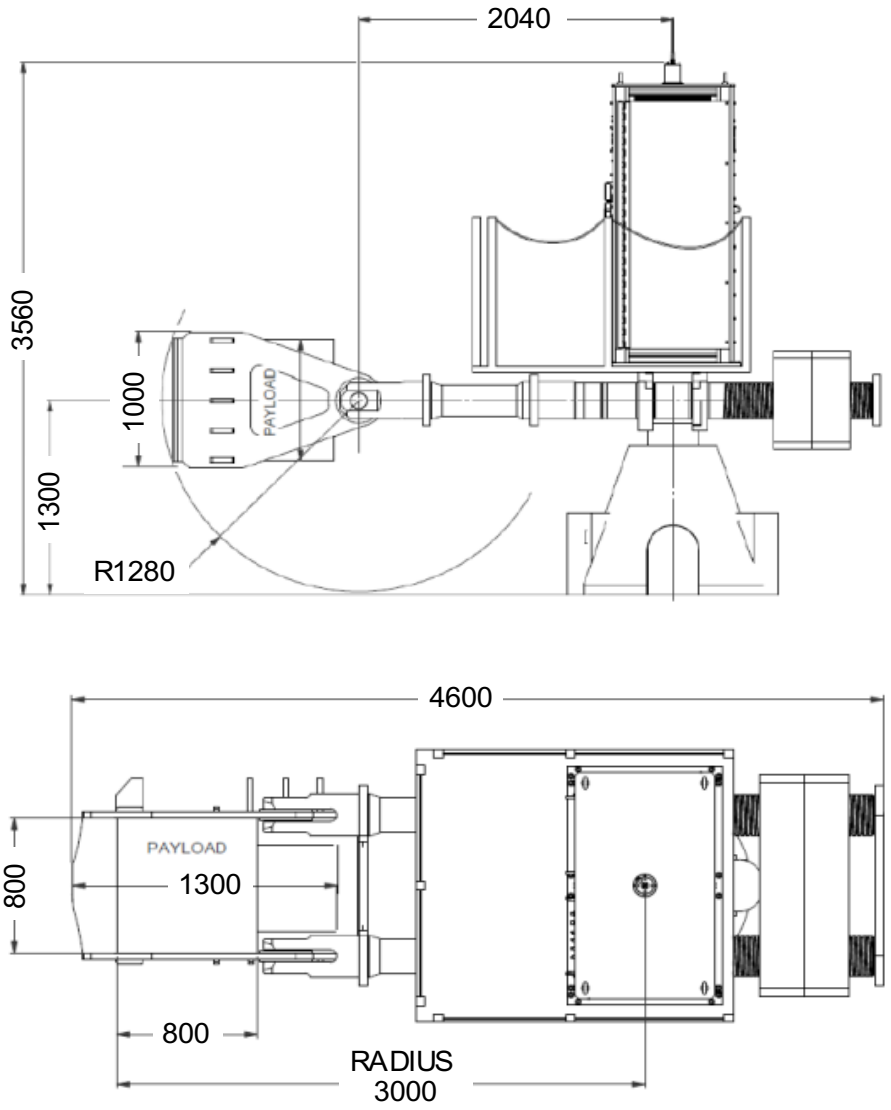

Figure 5-4 Elevation and plan on of the geotechnical centrifuge at the University of Pretoria (Actidyn-Systemes, 2011).

The centrifuge enclosure is fitted with fluorescent lights, installed radially around the rotation axis in the ceiling. LED strip and spot lighting, both above and on the side of the model platform has been installed to enhance viewing of the model during testing. These are controlled from the control computer (Jacobsz et al., 2014). Two cameras have been installed on the centrifuge to observe models during testing. One camera is housed inside the aerodynamic shield and observes the model's cross sectional profile, and can be adjusted according to the elevation relative to the model, as well as further and closer to it. This camera may be detached from its mounting and fixed anywhere on the model itself. The second camera is installed near the axis of rotation and looks down onto the model in plan view, when the model has swung up (Jacobsz et al., 2014). The centrifuge laboratory also has four portable Go-Pro cameras, which can be placed at any position on the model.

Two model container boxes, called strongboxes, are available to be used for the models to be constructed and tested in. Both are aluminium containers, with internal dimensions of 600 mm x 400 mm x 400 mm. One of the containers is fitted with a transparent window so that the model can be viewed from a cross sectional profile (Figure 5-5).

The centrifuge's operation is managed via a personal computer which controls the three-phase power system driving the machine. In addition to defining the input values for the automatic balancing (desired acceleration and model mass), the rate at which the centrifuge accelerates to the required G-level (in G per minute) can also be controlled. The screen displays a number of system checks, warning messages and presents general data like temperature and humidity in the centrifuge enclosure (Jacobsz et al., 2014).

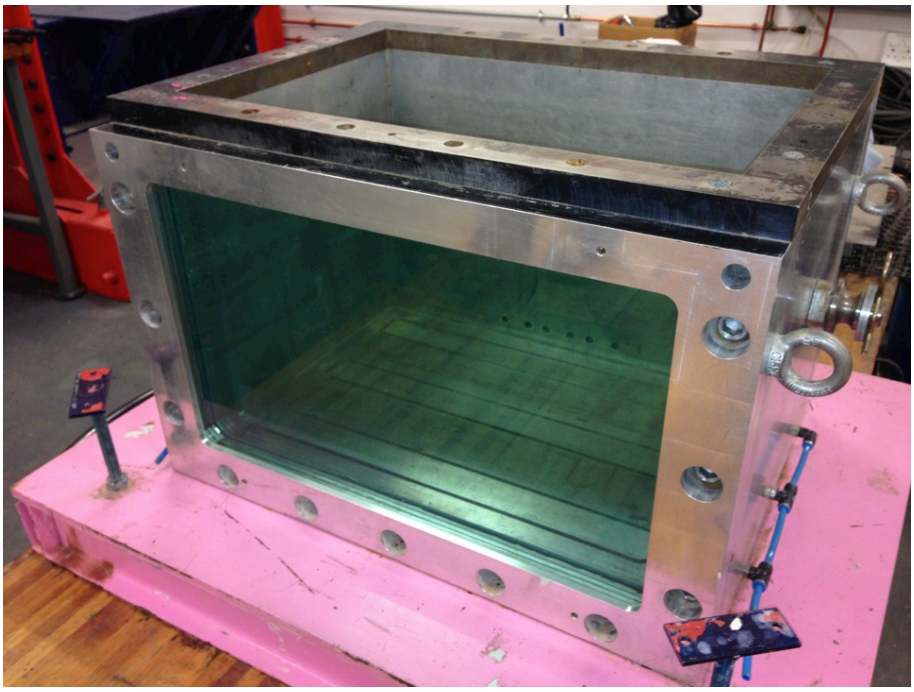

Figure 5-5 Model test container (strongbox) with transparent glass window.

The centrifuge is equipped with electric power slip rings as well as fluid slip rings mounted at the centrifuge base. The fluid slip rings allow water, pneumatic systems, as well as hydraulic systems to be supported. A large instrumentation cabinet, rotating with the centrifuge, is mounted above the centrifuge axis of rotation and provides space for data acquisition and control systems (Jacobsz et al., 2014). Electric power is supplied to the centrifuge instrumentation cabinet via these slip rings, which are rated to provide 50 A at 380 V (Jacobsz et al., 2014). A step-down transformer in the instrumentation cabinet converts the power to 220V. Currently a 12 V 400 VA transformer and a smaller 24 V transformer have been installed to provide power to utilities on the model platform (Jacobsz et al., 2014).

Power to various utilities on the model platform, including the data aquisition system, is controlled via two six-channel digital input/output controllers operating a total of 12 relays. It is controlled via a 1 Gbit local area connection to the centrifuge through a fibre optic rotary link, which provides excellent noise immunity (Jacobsz et al., 2014).

The centrifuge is also fitted with a fluid rotary joint enabling hydraulic and pneaumatic connection to the model to drive actuators of various types. The seamless fibre optic network link to the centrifuge enables electric actuators to be controlled from the control room. The control room is equipped with the pneumatic and hydraulic control panel from which hydraulic and pneumatic pressure, applied to the centrifuge model, are controlled. Flow meters and pressure regulators are installed to monitor and control flow rates (Jacobsz et al., 2014).

All communication between the data acquisition systems and the control room occurs via the centrifuges Ethernet network. The centrifuge is equipped with three modules of the Digidaq data acquisition system developed by the University of Western Australia (Gaudin et al., 2010), providing a total of 24 channels. This system is capable of logging a range of instrumentation at a wide range of frequencies and provides the user with much flexibility. The Digidaq system is complemented by a 24 channel HBM QuantumX System. This adds to the capabilities of the Digidaq system as the HMB system supports LVDTs, bender elements, 4-20 mA sensors and others. An HBM CX22W solid state computer, a modular system capable of being expanded to the user's requirements, was installed on the centrifuge. It currently controls the on-board cameras for image processing

5.3.2 Set-ups

Acrylic Plexiglas sheets are selected to construct the experimental models. This material was primarily selected as it is an impermeable solid, such that matrix imbibition of water is unimportant, permitting isolation of unsaturated flow dynamics. Due to the novelty of unsaturated fracture flow in the centrifuge, it is vital to first validate the fundamental conceptual models presented in literature. Therefore, to emulate a smooth clean parallel plate model in a centrifuge, Plexiglass sheets are selected due to the transparency and machinability of the material. An average contact angle for the acrylic sheets is reported as ca. 70° by Della Volpe et al. (2002).

The dimensions of the acrylic Plexiglas used for Experiment 1 through to Experiment 3 are constructed using various configurations of four acrylic sheets with 10 mm thickness and are bent into a L-section measuring 299.5 mm long and 150 mm wide. Two of these L-section sheets are shown being placed during model construction in Figure 5-6. Spacers are used between the L-section sheets in the models in order to maintain the specifically desired aperture for the fracture. In Experiment 4, two acrylic Plexiglas sheets measuring 400 mm length x 290 mm width x 10 mm thickness are used and are also separated by spacers along both the long boundaries of the fracture in order to maintain the desired constant aperture for the experiment. The series of experiments evaluating the fundamental conceptual models of fracture flow in discrete fractures are introduced in the following sub-sections. Detailed experimental set-ups and procedures are provided in each chapter.

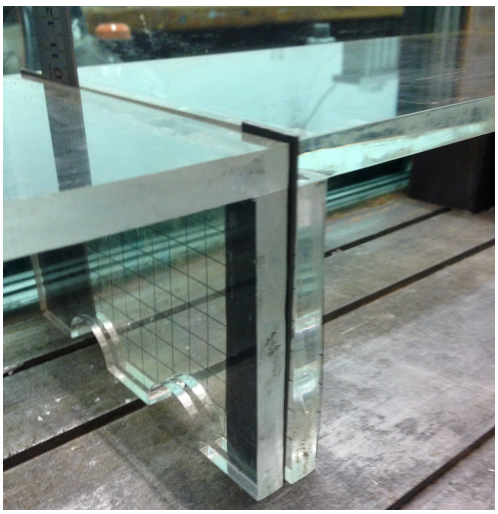

Figure 5-6 Acrylic Plexiglas L-sections (10 mm thick) being placed during construction with 1 mm thick spacers in order to maintain a constant width through the fracture.

5.3.2.1 Experiment 1

The first experiment examines the fundamental conceptual model of a clean smooth parallel plate for a discrete fracture at vertical and horizontal orientations. Due to the novelty of unsaturated fracture flow in the centrifuge, it is vital to first validate the fundamental conceptual models and whether similar flow mechanisms presented in literature occur. Therefore, to emulate a smooth clean parallel plate model in a centrifuge, acrylic Plexiglas sheets are selected due to the transparency and machinability of the material.

5.3.2.2 Experiment 2

The second experiment aims to investigate the flow mechanisms at discrete open fractures and intersections by constructing conceptual orthogonal intersections to produce several flow visualisation experiments conducted with flow from both vertical (and inclined sub-vertical) and horizontal fractures (and inclined sub-vertical). The first test seeks to investigate the flow into a non-inclined inverted “T” intersection with a vertical fracture, rather than an open unconfined wall as presented in Experiment 1, with flow occurring from the horizontal fracture. The second test is conducted on a set of non-inclined orthogonal intersections, whereby flow occurs from the vertical fracture above the intersection.

5.3.2.3 Experiment 3

The third experiment aims to investigate the role that inclination has on variably saturated flow mechanisms from discrete open fractures and intersections. This is achieved by constructing conceptual orthogonal intersections to produce several flow visualisation experiments conducted with flow from both vertical (and inclined sub-vertical) and horizontal fractures (and inclined sub-vertical). The first test replicates the orthogonal intersections; however, the model is inclined at 23° with flow from the inclined sub-horizontal (ISH) fracture up-dip of the intersection. The second tests also replicate the orthogonal intersection, inclined at 23°, with flow introduced from the inclined sub-vertical (ISV) fracture above the intersection.

5.3.2.4 Experiment 4

The last experiment presents research that seeks to investigate the use of the Forchheimer law to predict non-linear flow behaviour under unsaturated conditions in an initially dry free-draining discrete fracture. The experiment presented in this Chapter expands on the previous models by subjecting the smooth parallel plates to commonly used WPT.

5.4 Summary

The chapter presents the overall materials and methods used in this research, for both the initial field and subsequent experimental phase of the research. The field data was obtained from the construction of the De Hoop Dam, from both detailed foundation mapping of the rock mass before concrete placement, and Lugeon testing during grouting operations. This data was analysed in order to provide guidance on the experimental set-ups.

The general materials and methods used for the experimental phase is briefly outlined and introduced, with the experiment-specific methodology being described in detail in each chapter where the specific experiment is presented. The experimental models are constructed and tested in a 3 m balanced beam geotechnical centrifuge housed at the Department of Civil Engineering, University of Pretoria. The experiments are constructed using various configurations of 10 mm thick acrylic Plexiglas sheets.

CHAPTER 6 ROCK MASS PERMEABILITY AT DE HOOP DAM

6.1 Introduction

The Secondary Permeability Index (SPI), as proposed by Foyo et al. (2005), typically classifies rock masses using the degree of jointing from borehole core drilled during the final detailed exploratory investigation stage. However, during the construction phase, grout production boreholes are typically percussed, and as such the degree of jointing is not directly known. Nevertheless, by following the methodology of the SPI, the success of a grouting operation (i.e. grout mix and take) can be used to infer the degree of jointing in the borehole.

In this regard, the aim of this chapter is to investigate the discontinuity structure that influence the characterisation of rock mass permeability at De Hoop dam, in South Africa. This is realised by back-analysing and verifying the ground treatments as proposed by the SPI, at the De Hoop Dam in South Africa. In order to conduct this verification, detailed mapping of the foundation rock mass was used together with single-pressure Lugeon-tests in 204 primary grouting boreholes drilled along the dam axis, for curtain grouting purposes. These Lugeon-test results are used to calculate the SPI, and zone the foundation accordingly. Furthermore, data obtained from the primary production grout boreholes are evaluated, together with results from 32 boreholes drilled along the dam wall axis during the final detailed exploration phase. The findings of this chapter is presented in detail in Jones et al. (2018d), and are used, in conjunction with previous literature, to guide the development of the subsequent experimental models.

6.2 Site Characterisation

6.2.1 Study Area

The dam wall foundation is divided into four zones, namely: i) the upper left flank (ULF); ii) middle left flank (MLF); iii) lower left flank (LLF); iv) the river section (including the outlet block and spillway) and right flank (RSRF). These zones are then further subdivided into foundation blocks to aid with positions within the foundation; each block being allocated a specific number depending on the location, whereby even-numbered blocks were given to blocks located in the left flank (western), whilst odd-numbered blocks to the right flank (eastern). The centre of the river section acts as the starting point (Block 1) from which the numbering is initiated. Each block is approximately 10 m wide, with the specific exception of block 16 and block 13, which were 15 m and 20 m wide, respectively. The four sections with their respective chainages and blocks are presented in Table 6-1.

Table 6-1. Sections of the De Hoop Dam wall and their associated blocks and chainages.

	River section and right flank (RSRF)	Lower left flank (LLF)	Middle left flank (MLF)	Upper left flank (LLF)
Chainage (m)	0-225	225-496	496-756	756-1016
Block numbers	1-35 and 2-10	12-66	68-118	120-170
Total no. of blocks	23	27	26	26

6.2.2 Drainage and Topography

The dam is situated on the Steelpoort River, with contributions from the Klip River located roughly 500 m upstream of the dam wall, as well as the Masekete stream situated 11 km upstream of the dam wall. The Steelpoort valley has a gradual continuous gradient from the western escarpment towards the river bed (left flank). The eastern side (right flank) consists of variable tors and steeply sloped valleys. The left flank dips gradually toward the Steelpoort River at approximately 4°, from approximately 922 meters above mean sea level (mamsl) at Ch 1016, towards 846 mamsl at the centre of the Steelpoort River bed. The right flank has a steep slope at approximately 22°, from 906 mamsl at the the Mampurukop tor at Ch 33, towards the river bed over a short distance of approximately 150 m. The regional slope and flow direction are towards the Steelpoort River bed, which then drains to a northern and north-easterly direction.

6.2.3 Geology

Regionally, the De Hoop dam site is situated on the 2.05 Ga Bushveld Complex (Scoates and Friedman, 2007), which constitutes the most voluminous preserved mafic layered intrusion in the world, covering an aerial extent of approximately 65 000 km^2 (Eales and Cawthorn, 1996). Emplacement of the Complex was preceded by the extrusion of bimodal lavas of the Rooiberg Group, which is the uppermost constituent of the mostly sedimentary Transvaal Supergroup (Clarke et al., 2009). The Bushveld Complex is subdivided into the Rustenburg Layered Suite (RLS), an early mafic phase, and a later granitic phase comprising the Lebowa Granite Suite, and the Rashoop Granophyre Suite (Cawthorn et al., 2006; South African Committee for Stratigraphy, 1980). The RLS hosts the largest known deposits of economically important chromium, vanadium and platinum group metals in the world. This sequence of mafic layered rocks comprising the RLS has a thickness of 7–9 km and occurs in five discrete limbs known as the Western, Eastern, Far Western, Northern and Southern limbs (Eales and Cawthorn, 1996), of which, the De Hoop dam is situated in the Eastern limb.

The Lebowa Granite Suite intruded above the RLS, whilst the metamorphic granophyres of the Rashoop Granophyre Suite owe their origin to metamorphism of rocks of the Pretoria and Rooiberg Groups, due to emplacement of the mafic and granitic rocks (Cawthorn et al., 2006). The originally horizontally placed layers of the Bushveld Complex rocks dips centripetally at between 10° and 20° (Perritt and Roberts, 2007), which is attributed to the effect of crustal

flexure in response to the load of the RLS and associated granites (Cawthorn and Webb, 2001). The present geometry of the Bushveld Complex can, therefore, be considered as a single, gentle, non-cylindrical basin fold (i.e. a synform with hinge line depression), with limb lengths of approximately 180 km (Perritt and Roberts, 2007). Traditional zonal stratigraphy of the RLS comprises a subdivision into a noritic Marginal Zone, an ultramafic Lower Zone, an ultramafic to mafic Critical Zone with prominent layering, a gabbronoritic Main Zone, and a ferrogabbroic Upper Zone (Cawthorn et al., 2006).

Locally, the reservoir basin is underlain by rocks of the Upper Zone, whilst the centreline of the dam wall footprint consists of rocks of the Main Zone, as illustrated in Figure 6-1a. At the dam site, the Main Zone consists of a thick succession of norite and gabbronorite, with minor anorthosite and pyroxenite layers (Cawthorn et al., 2006). The Upper Zone is intermittently well layered and is dominated by rocks ranging from gabbronorite to anorthosite, with the most striking feature being the presence of 24 magnetite layers (Cawthorn et al., 2006). These economically important magnetite bands were a major constraint for the construction of the De Hoop dam. As such, the underlying magnetite ore body was first stripped and utilised before the construction of the dam commenced. A cross-section showing the major geological features within the foundation rock mass is shown in Figure 6-1b.

Faulting in the eastern compartment can be reconciled with a left-lateral simple shear strain ellipsoid, with the major Ysterberg fault and its associated en échelon faults representing Riedel shears (Du Plessis and Walraven, 1990). The small floor domes in the eastern compartment probably originated as en échelon fold structures which developed into diapiric structures subsequent to emplacement of the Rustenburg Layered Suite (Du Plessis and Walraven, 1990). Extensional features in the eastern compartment are oriented NE-SW (Du Plessis and Walraven, 1990), including the Steelpoort Fault, which runs approximately 0.5 km north of the site. In the eastern limb, the Nebo Granite is absent southeast of the Steelpoort Fault, and the RLS is rather overlain by granophyric rocks of the Rashoop Granophyre Suite and volcanic rocks of the Rooiberg Group. This relationship suggests that the Steelpoort Fault was active during emplacement of the Nebo Granite, and may, therefore, have acted as a feeder to the main granite intrusion (Cawthorn et al., 2006).

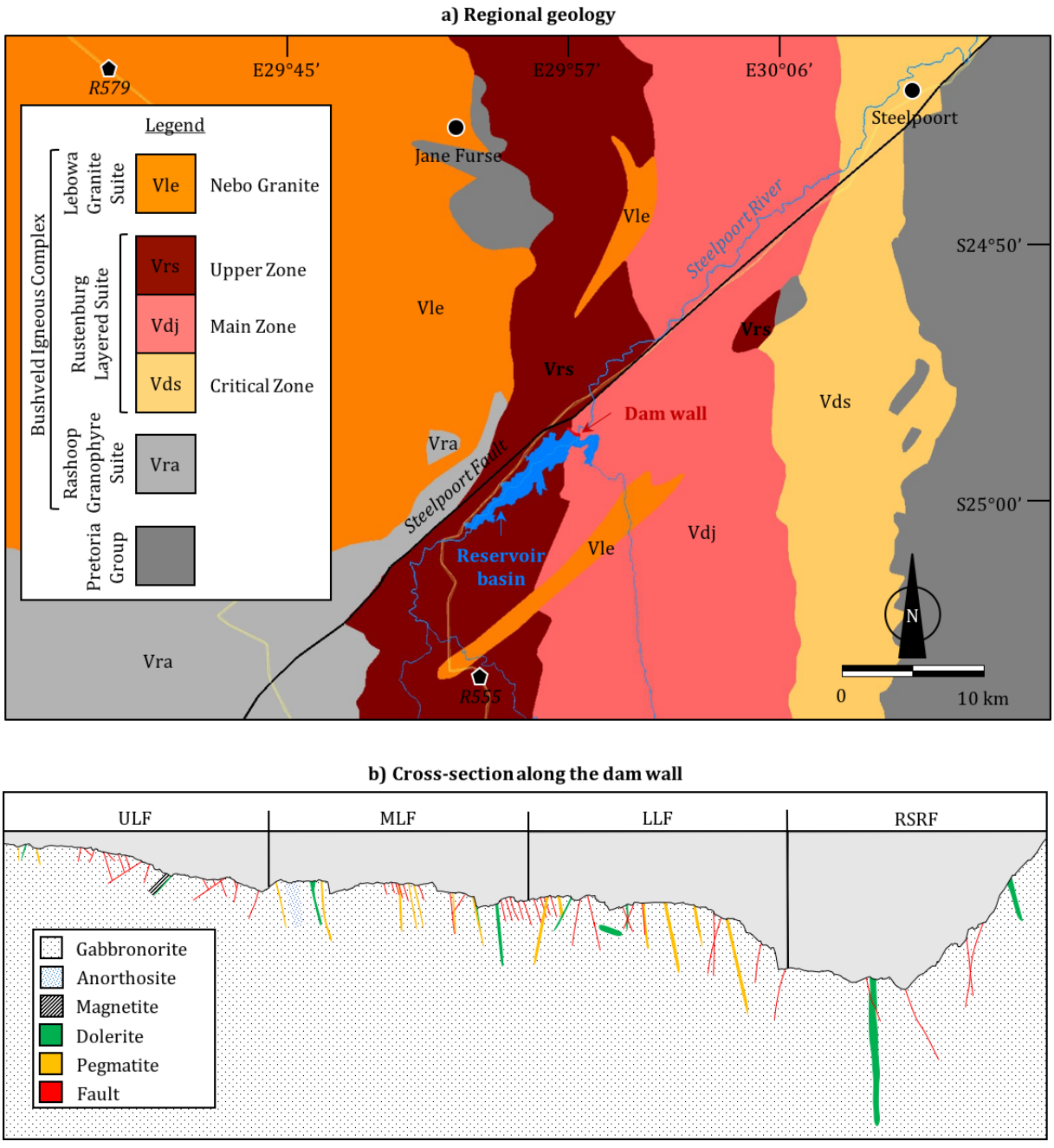

Figure 6-1. a) Regional geology of the De Hoop dam site in the Eastern limb of the Bushveld Complex; and b) Cross-section along the dam wall showing the major geological features.

6.2.4 Hydrogeology

Du-Toit et al. (1998) presented that borehole yields in the RLS typically range between 0.5 and 2.0 *l*/s. This is further emphasised by Barnard (2000) who states that 81% of the boreholes on record produce less than 2 *l*/s, and, therefore, the yield potential of the rocks of the RLS is classified as poor. Moreover, according to Vegter and Seymour (1995) typical depths to the groundwater are 10 to 20 m below surface, with a standard deviation of 8 to 15

m, and a storage coefficient of less than 0.001 orders of magnitude, within the fractures. Groundwater occurrence is largely structurally controlled, and in this regard, is associated with dykes that cut through and across the norite (Barnard, 2000; Holland, 2012). Within the unweathered bedrock, groundwater exploration in the area has successfully targeted structural features and geological contacts at depth; however, Holland (2012) notes that boreholes within 150 m of major surface drainages have above-average transmissivity (two to three times higher) compared to boreholes further away, indicating the strong influence of surface-water bodies on borehole productivity. Although these higher transmissivities are often associated with primary alluvial aquifers, drainage channels tend to follow zones of structural weaknesses (e.g., lineaments) in the near surface, and; therefore, rock masses in the vicinity of rivers might be more intensely fractured, jointed and/or weathered (Holland, 2012).

6.3 Methodology

6.3.1 Foundation Mapping

Detailed geological mapping of each block on the dam foundation is conducted once the block was cleaned and ready for concrete placement. Mapping is conducted by joint line surveys (JLS) with the aim to record and measure the discontinuity parameters, including those outlined by Brown (1981) and Bieniawski (1989), consisting of the: position; rock type; type of structure; aperture; dip and dip direction (orientation); continuity; roughness; waviness and amplitude; gouge or filling; and water conditions (seepage). JLS are conducted on each cleaned foundation block, in two directions; firstly, parallel to the dam reference line, with the second survey being conducted perpendicular to the reference line. The parallel surveys are conducted from the river towards the uppermost direction of the respective flank. The perpendicular surveys are conducted from the upstream side of the dam reference line to the downstream side, either down the length of the foundation block or along the length of the block interfaces. The size of the parallel surveys are equivalent to the block width (±10 m), whilst the size of the perpendicular surveys varied according to the length of the foundation block for the dam wall, ranging between 15 to 65 m. Larger blocks, such as the outlet and the spillway, contain up to three to four line surveys.

6.3.2 Lugeon Testing

The Lugeon number for each step is calculated using Equation 3-2. The Lugeon-test data for the De Hoop Dam study are obtained from primary grout curtain boreholes (i.e. before the foundation rock had been affected by grouting) using single-pressure WPT. Primary grout holes are drilled at 8 m wide intervals. The diameter of each hole is 89 mm and boreholes were drilled and tested downstage, with Lugeon-tests carried out in each stage using surface packers. Weaver and Bruce (2007) state that test intervals longer than 5 m jeopardise the confidence of the assessment between the relationship of permeability and the geological conditions. Unfortunately, the length of tested stages in the grout boreholes was far longer than this, with the average length per stage per section presented in Table 6-2. In the ULF,

the total length drilled is approximately 28 m depth per grout borehole, whilst in the MLF, LLF, and RSRF, the final depths are approximately 31 m, 66 m, and 72 m respectively. Unfortunately, the disadvantage of conducting single-pressure Lugeon-tests is that they do not provide typical flow types as identified by Houlsby (1976). However, the purpose of identifying the flow types under single-pressures is primarily to observe washout and void filling conditions. These assisted in identifying potentially erodible infillings in the fractures, as well as highly fractured zones. It is, therefore, not possible to differentiate between laminar, turbulent, and dilation flow types.

Table 6-2. Average drilling lengths per stage (i.e. test section length) in each section of the foundation of the dam wall (m).

	ULF	MLF	LLF	RSRF
Stage 1	9	11	19	20
Stage 2	11	11	9	9
Stage 3	7	8	15	16
Stage 4	-	-	14	15
Stage 5	-	-	9	12

6.3.3 Secondary Permeability Index

This Lugeon-test data is used to calculate the SPI by the method as proposed by Foyo et al. (2005), by Equation 3-9. Similarly to analysing Lugeon data via calculating the *Lu* value per step, the SPI classification also requires the identification of flow types in order to specifically identify any modifications to the joint characteristics induced from the Lugeon test. However, due to the limitation of single-pressure Lugeon-tests, the following was adopted, whereby; for laminar, turbulent, dilation, and void filling flow types, the SPI is averaged as all pressure intervals are the same, and; therefore, no modification occurs. More important to this study, was that if washout flow is identified, the SPI would be assigned to the highest value obtained. Additionally, Foyo et al. (2005) places emphasis on identifying hydraulic fracturing, however due to the low pressures used in the Lugeon-test, hydraulic fracturing was unlikely to be initiated.

The rock mass classification defined by the SPI, coupled with the degree of jointing from the drill core, permits the rock mass foundation to be zoned into different quality classes and each zone to be treated separately (Foyo et al., 2005). As there was no core available during the grouting operation at De Hoop Dam, to complete the ground treatment designation, the foundation mapping was used together with the SPI class (refer to section 3.4). In this regard, Class B zones (although there is no data with depth) would be classified as needing local treatment only if a significant geological feature such as a pegmatite vein, fracture zone, magnetite or anorthosite band, was identified and measured on the foundation mapping. The same assumption was used when designating the grout mix for Class C and D.

6.4 Analysis of Data

6.4.1 SPI Comparison with Grout Take

Lu values and SPI values are generally correlated because the SPI value is a direct function of the WPT as is the *Lu* value, besides the SPI being a more conservative indicator of grouting over the *Lu* value (Sadeghiyeh et al., 2013). In this regard, the *Lu* value from the primary grouting holes are not presented, and rather only the calculated SPI value and classes are compared against the grout take.

6.4.2 Comparison with Lu and RQD Values from Previous Detailed Investigation

The degree of jointing inferred from the production grout boreholes is then validated by 32 rotary cored boreholes drilled during the final detailed investigation, whose location coincided with the grout curtain axis as well as depth of foundation excavation (as the overburden had subsequently been removed). Unfortunately, investigation boreholes were only deep enough to meaningfully compare up to stage 2 depths in the grouting boreholes, whilst all investigation boreholes in the RSRF were too shallow to meaningfully compare. In this regard, the results and discussion focus on the left flank, whilst the RSRF is generally ignored. Additionally, *Lu* values stated on the investigation borehole logs were also used to compare calculated SPI-values from grout boreholes. Unfortunately, the raw data of these tests was not made available, and as such only the *Lu* values are stated, with no indication of the water take, nor pressures, nor flow types. The intention of this comparison was to correlate typical rock characterisation methods with depth, and in particular to compare the recorded RQD index (Deere, 1968). Furthermore, the borehole logs contain descriptions used to validate the presence and orientation of geological features (such as the pegmatite veins) within the rock mass.

6.4.3 Back Analysis of the Degree of Jointing from the Grouting Operation (Grout Mix and Success)

Due to the grouting boreholes being percussed, an investigation of the degree of jointing with depth was not directly possible. However, as the grout mix and success of the grouting is already known, a back-analysis can be conducted to infer the degree of jointing. The process involves assessing the SPI class, followed by a decision as to the success of the grout borehole, which is then compared to the grout mix. Based on the success of the grouting, a degree of jointing is assumed. This is then to be compared to the RQD obtained from the detailed exploratory investigation boreholes, and was used to verify whether the correct grout mix meant that the rock mass indeed showed the correct degree of jointing. Houlsby (1977) suggested the water take should show a marked reduction by the time a grout borehole spacing of 1.5 m is reached. In this regard for this research, it is assumed that a successful primary grouting borehole:

i. Did not require re-grouting, nor the localised used of tertiary and quaternary boreholes; and additionally,

ii. A *Lu* value below 1 is calculated in the WPT before tertiary, and quaternary holes were drilled (i.e., after secondary grouting).

If a thin grout mix is successfully used in a borehole, it is assumed that a high degree of jointing exists, whereas if a thick mix is applied successfully, it is assumed that a low degree of jointing exists. An unsuccessful thin grout mix assumes that a low degree of jointing exists; however, an unsuccessful thick mix assumes a high degree of jointing exists.

6.5 Geotechnical Character of the Foundation Rock Mass

6.5.1 Joint Sets and Their Properties

The foundation rock at De Hoop is characterised by large variations in the joint pattern over relatively small distances, which is typified by difficulty in foundation excavations to establish a relatively even foundation surface, resulting in considerable over-excavation in places. Furthermore, the presence of the Steelpoort fault, 500 m north of the dam wall, results in the structural complexity observed on the dam footprint. The dam is situated in a climatic zone where chemical disintegration is the dominant mode of weathering. The gabbro rock thus has an undulating weathering profile consisting of numerous sub-surface boulders and corestones. Generally, the joint spacing of the rock mass ranges from 20 mm, when it is highly fractured, to 600 mm when the joint spacing is wider, characterised by a blocky structure consisting of sub-vertical and sub-horizontal joints, with average block sizes varying between 50 mm to 700 mm. Generally, the joint spacing increases with depth at De Hoop Dam, but in some instances a highly jointed rock structure is still found 10 m to 15 m below NGL. Typically, three joint sets are observed in the foundation rock mass and are shown in Figure 6-2, with the properties of the dominant joint sets summarised in Table 6-3, for each section. The sub-horizontal joint system (J1) is highly undulating, with distinct convex-shaped joint surfaces, and has formed due to a combination of the stereotypical layering found within the RLS, as well as from lithostatic unloading to form stress-relief joints. Two steeply-dipping joint sets are also prevalent throughout the dam wall footprint, consisting of several, north-west striking (J2) pegmatite veins and fault zones, as well as north-east striking (J3) fault zones, which tend to become steeper towards the RSRF.

The fault zones are mostly only moderately weathered, with thicknesses varying between 10 mm and 200 mm with an average thickness of 20 mm. Minor fault zones encountered throughout the foundations strike roughly north-east (J3), as well as parallel or obliquely (J2) to the dam wall axis. These fault zones are characterised by linear structures with weathered contacts and some contain closely to very closely jointed rock, directly adjacent to the fault plane. Many of these fault zones also contain red sandy clay filling with thickness that can vary between 2 mm and 50 mm. This red clay infilling is not a result of rock weathering, but migrated into the open joints and fault zones, by means of normal soil migration processes.

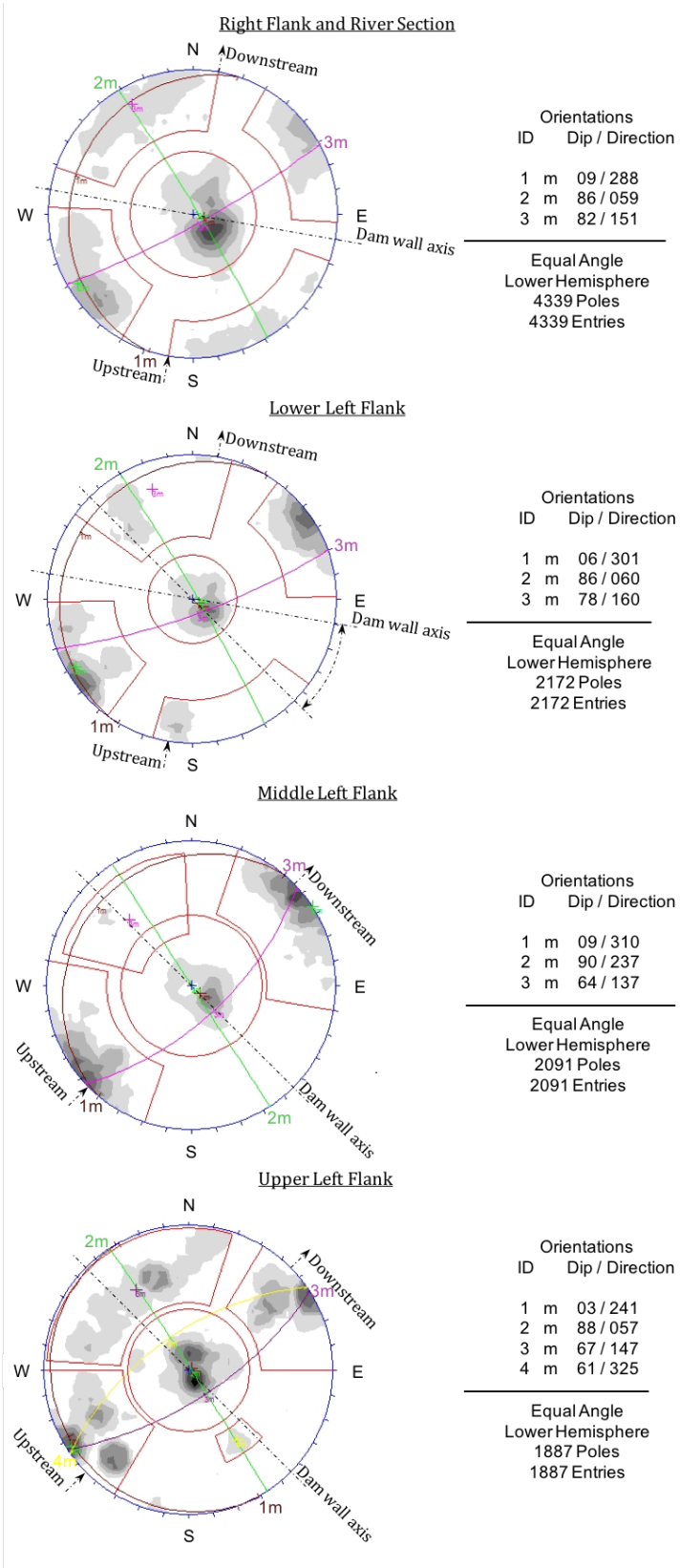

Figure 6-2. Stereographic projections of joint sets along the foundation of the dam wall.

Table 6-3. Properties of the dominant joint sets at the De Hoop dam site.

Joint Type	Persistence (m)	Roughness (JRC)	Spacing (mm)	Aperture (mm)	Water cond.	Infill
Stress-relief	>1	9 - 12 Rough, undulating	20-200	0.5	Dry	Stained; silt
Tension	1 - 2	8 - 10 Rough, planar	20-200	<0.5	Dry	Stained; sandy silt
Fault	3 - 10	10 - 13 Rough, undulating	20-200 (RSRF); 200-2000	2 - 50	Dry; slow seepage (RSRF)	Stained; weathered
Pegmatite Veins	1- 50	-	> 2000	10 - 200	Dry	Angular pegmatite/quartz gravel

At shallow depths, this clayey joint filling was also observed on the sub-vertical and sub-horizontal joints reaching thicknesses of up to 20 mm. It is common for dolerite to have also intruded these fault zones. Generally, these intrusions are localised and thin, with very closely spaced jointing adjacent to the intrusion. The pegmatite veins are generally steeply dipping features, and consist of angular pegmatite gravel and/or quartz gravel, which are loosely packed and could be excavated easily by a jack hammer or excavator. It is evident that the pegmatite veins are related to the fault zones on the dam footprint. The pegmatite veins intersect the dam wall axis perpendicularly in the ULF and MLF, and obliquely in the LLF and RSRF, and are continuous through the entire width of the dam wall footprint.

6.5.2 Geotechnical Properties

The geotechnical properties of the rock mass along the dam foundation is presented in Table 6-4. Typically, the best RMR values are encountered in the river section, whilst the poorest RMR values are obtained in the right flank.

Table 6-4. Geotechnical properties of the rock mass at the De Hoop dam site.

	Left flank			River section	Right flank
	Upper	Middle	Lower		
RMR	50 – 60	60-70	65-70	60-80	55-65 (35-45 jointed rock)

Poor rock mass quality is observed in the right flank (RMR of 55 to 65), characterised by blocky, highly jointed (vertically and sub-vertically) gabbro rock. The major constraints to the right flank can be ascribed to structural features and a very bouldery subsurface topography due to spheroidal weathering and sub-vertical stress-relief jointing. Poor features included: a near-vertical dyke dipping parallel with J3, consisting of highly weathered closely to very closely jointed dolerite; several thin (50 to 120 mm) fault zones, which strike almost parallel as well as sub-perpendicular to the Steelpoort River. Unfavourable conditions are, however, present due to weathered joints and intersecting fault zones. In some of the major fault zones, the presence of slickensided surfaces and talc indicate previous movement. The foundation rock in the river section consists of very good quality rock with RMR values varying from 60 to 80. The river section can be summarised as bluish grey, stained brown and orange, slightly weathered to unweathered, generally medium jointed, very hard rock gabbro. A major fault zone, the largest one encountered on the entire dam foundation, is observed in this section with two other minor but well defined fault zones, striking roughly northeast (J3). Most of these joints are stained green and consisted of talc infilling with thicknesses varying between 0.5 mm and 1.5 mm. The fault zones are characterised by moderately weathered rock with very closely to closely (20 – 200 mm) spaced joints. Numerous joints in the fault zones also show slickensided joint surfaces. Joints on the contacts of fault zones or weathered joints were damp in some cases. Slow water seepage is observed along larger fault zones and sub-horizontal dolerite dykes, with the water being clean and showing no sign of turbidity.

The left flank consists of rock of fair quality, which improves towards the lower left flank (LLF). In this regard only one of the poorer geological zones is located on the lower left flank, as most of the poorer zones occur on the middle (MLF) and upper left flank (ULF). Bluish grey, unweathered very hard rock gabbro occurred in the lower and middle left flank whereas this rock quality is less common in the upper left flank, possibly due to the influence of the nearby Steelpoort Fault. Poorer rock mass quality is a result of a combination of joint spacing, weathering and joint conditions. Furthermore, some geological features that cause poor foundation conditions on the left bank include; fault zones, pegmatite veins, a magnetite band and dolerite intrusions. Joint spacing is closer at the contacts of these and other structural features, which results in localised dental excavations. Some anorthosite bands are encountered in several areas on the left flank, usually in the vicinity of dolerite sills or larger fault zones. The anorthosite is moderately weathered and very closely to closely jointed along fault contacts whereas the rock quality becomes very good further away from theses structural features. A gradual transition zone usually occurs between the anorthosite bands and surrounding gabbro rather than distinct contacts. Numerous horizontal and vertical joints on the upper left flank contained sandy clay joint filling of between 0.5 mm and 20 mm in thickness. The thickness and quantity of the clayey infill decreases with depth, although at final foundation level, a few joints still contain a thin veneer of clayey soil.

6.6 Permeability of The Foundation Rock Mass

6.6.1 Lugeon Results

Lugeon values obtained from the Lugeon-tests are presented as frequencies in Figure 6-3 for each section along the dam wall axis, for each stage of the primary grouting boreholes. These values, therefore, represent pre-grouting rock mass permeability values. Comparing frequencies at Stage 1, it is clearly evident that the rock mass permeability becomes more watertight from the ULF through to the RSRF, with the percentage *Lu* values less than 3 being 31% in the ULF, 50% in the MLF, 65% in the LLF, and increasing to 82% in the RSRF. Additionally, this trend is observed for *Lu* values between 3 and 10, decreasing from 56%, to 50%, to 27%, to 14% from the ULF through to the RSRF, respectively. The ULF and MLF both record higher percentages of *Lu* values between 10 and 30, with 11% and 12%, respectively, compared to the LLF and RSRF, with percentages of 4% and 2% respectively. Lugeon values of between 30 and 60 are less frequent, whereby the MLF records the highest at 7%, with the ULF, LLF, and RSRF, recording 2%, 4%, and 2%, respectively. No *Lu* values greater than 60 are recorded along the entire length of the dam wall axis. Interestingly, this trend of an increasingly watertight rock mass from the ULF to the RSRF correlates with the same trend as observed in the RMR ratings given for the excavated foundation rock mass, whereby the ratings increase towards the Steelpoort River. The majority of the higher *Lu* values obtained in the RSRF are from the right flank, which also experienced poorer geotechnical zones, and lower RMR ratings.

This same trend does not exist for the deeper stages along the dam wall axis; however, it is evident that the rock mass becomes increasingly less permeable with depth. In Stage 2, all sections of the dam wall record significantly higher frequencies of *Lu* values less than 3. The 7% of *Lu* values between 3 and 10 recorded at Stage 2 depth in the ULF, are mainly due to the presence of several fault fractures, characterised by a very closely jointed rock mass adjacent to the fault. In Stage 3, all recorded *Lu* values were below 3, due to these fault fractures being less persistent and prevalent with depth. Below the MLF, a frequency of 9% is obtained for *Lu* values between 3 and 10 in Stage 2, and this drops to 2% in Stage 3 with a 2% recorded frequency of *Lu* values between 10 and 30. Again, some major fault zones are present below this zone of the dam wall, but are not a significantly permeable feature with depth, possibly due to tighter joint conditions with depth. However, the higher *Lu* values (3-10) recorded at this depth are attributed to the presence of several pegmatite veins, dolerite intrusions, and an anorthosite band in blocks 112 and 114. In the LLF in Stage 2, the lowest frequency of *Lu* values less than 3 is recorded (82%), together with the highest frequency of *Lu* values between 3 and 10 at 14%, as well as the only section of the dam wall to record *Lu* values of between 10 and 30 in this stage. Much like the MLF, these higher *Lu* values were obtained in zones that contain fault zones, an increased amount of pegmatite veins and dolerite intrusions.

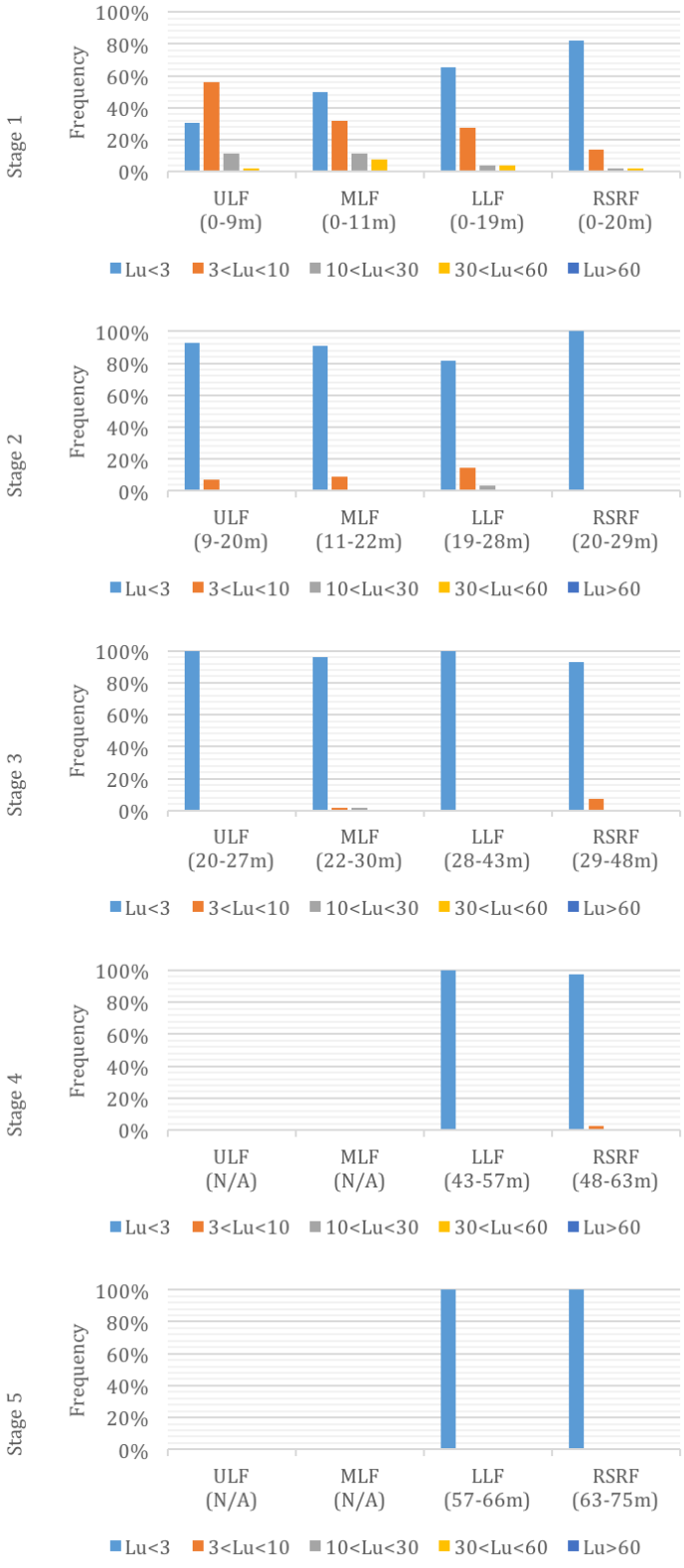

Figure 6-3. Lugeon results obtained along the dam wall per stage (m refers to metres below ground level).

Below Stage 3, the LLF becomes more watertight whereby for Stage 3, 4, and 5 all recorded frequencies of 100% for *Lu* values less than 3, for this section. From Stage 2 depth, the rock mass below the RSRF mostly records *Lu* values of below 3, with the exception of Stage 3 and 4, where some values between 3 and 10 are recorded. These higher *Lu* values were recorded mostly due to the presence of fault zones and dolerite intrusions in the right flank.

6.6.2 Hydromechanical Behaviour

As mentioned previously, simple single-pressure WPT's were undertaken primarily as a production test during grouting to monitor grout efficiency, whereby the test comprised of three different stages of 5 minutes each. In terms of assessing hydro mechanical behaviour, single-pressure WPT's only allow for washing out or void-filling flow behaviour to be identified. Washing-out flow behaviour was identified if Lu-values increased over the three stages, whilst void filling behaviour was identified as occurring when the Lu-value decreased over the three consecutive single-pressure stages. The hydromechancial flow behaviour types are shown in Figure 6-4, and show that although there is a general increase in the percentage of laminar/turbulent flow types observed with depth in the MLF, LLF, and RSRF of the dam, the presence of significant void filling and washout is evident. These flow types are typically identified when test sections intersect geological features, such as pegmatite veins, fault zones, and at contacts with dolerite intrusions.

Only in the ULF of the dam was there an obvious correlation where there is a decrease in void filling and washout flow types with depth (per stage), whereby other flow types increase from 39% in Stage 1 to 100% in Stages 2 and 3. This is most plausibly due to the presence of mostly fault fractures in the ULF, which tend to become less permeable with depth. This is in contrast to the MLF whereby several pegmatite veins and dolerite intrusions are present. The 2% of washing out flow type observed in Stage 1 in this section as well as the 6% in Stage 3 are likely due to the loose infilling that characterises the pegmatite veins and the closely jointed rock adjacent to dolerite intrusion contacts. Similarly, in the MLF although other flow types increase with depth per stage, a significant frequency percentage of washing out and void filling types are observed with depth. In the LLF a large percentage of void filling flow type is observed due to the presence of these pegmatite veins and a few dolerite intrusions. The frequency of other hydromechanical conditions does not seem to increase with depth, indicating the persistence of these major features with depth.

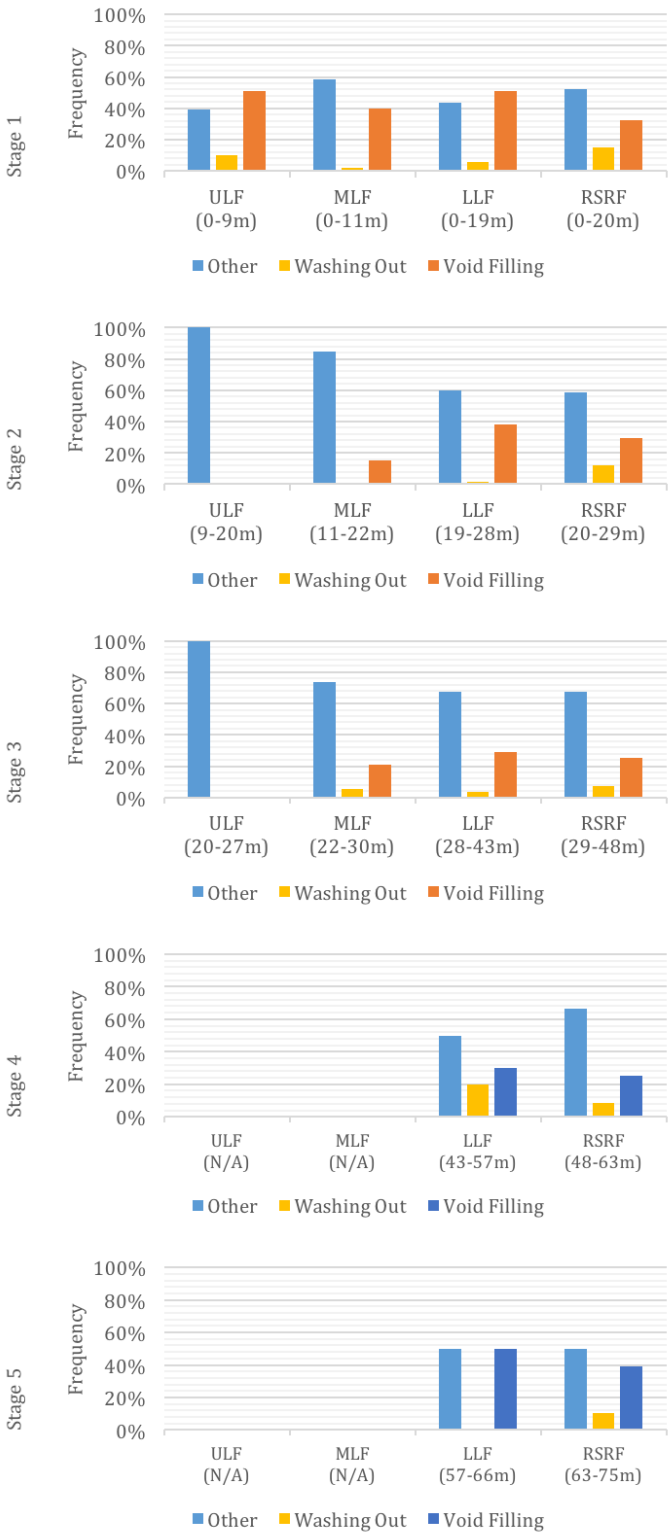

Figure 6-4. Flow types along the dam wall per stage (m refers to metres below ground level). Laminar, turbulent, and dilation flow types are classified as "Other" as they cannot be differentiated by single-pressure WPTs.

6.6.3 Secondary Permeability Index (SPI)

Table 6-5 shows an indication of the decrease in permeability towards the Steelpoort River. This is highlighted by the percentage of excellent quality rock (Class A SPI zones), and the increase in poor quality (Class C) from the RSRF through to the ULF. Each section of the dam wall is discussed in the following sections. However, caution must be maintained in comparing the percentages across sections of the dam wall, as they are not directly meaningful, because deeper boreholes were drilled in the LLF and RSRF compared to the ULF and MLF.

Table 6-5. Frequency percentages of SPI classes below the dam wall.

SPI	ULF	MLF	LLF	RSRF
Class A	5%	6%	28%	61%
Class B	36%	49%	32%	28%
Class C	58%	40%	37%	10%
Class D	1%	5%	3%	1%

Of the four classifications, the ULF has a large percentage of Class C present in the rock mass underlying it, followed by Class B (36%). This is largely due to several major fault zones that are present in the section. The presence of these faults and their associated closely spaced fractures also renders much of the area classified as fair quality rock (Class B). Inferred from the structural mapping of the foundation footprint, it was deemed that 27% of these in the Class B zone required local ground treatment, with two pegmatite veins, two dolerite intrusions, and a magnetite band intersecting this section. Only 1% of the ULF is classified as very poor quality (Class D) and deemed to require extensive ground treatment. This is due to a significant fault zone that dips away from the Steelpoort River from block 144 and underlies block's 144, 146, 148 and 150. Only 5% of the ULF is classified as Class A, requiring no ground treatment and 73% of Class B deemed not necessary for ground treatment. These zones are largely prevalent from blocks 124 to 136 of the ULF, and correspond with zones exclusive of large structural features and a wider joint spacing, inferred from the foundation mapping.

The MLF is underlain by a large percentage of fair quality rock (Class B), of which, based on the foundation mapping, only 15% was deemed necessary to treat the ground locally. With 40% of the rock mass zoned as Class C (poor quality), where ground treatment would be required, due to seven pegmatite veins that intersect this section. Several of these features also correlate with zones of extensive ground treatment as they categorise as very poor quality rock (Class D), the highest for Class D across the entire dam wall. Furthermore, two large dolerite intrusions are present as well as several large fault zones. The gabbroic rock mass in this section, which is not intruded by pegmatite veins nor dolerite and does not contain any

fault zones, typically classified as excellent quality rock (Class A), thus requiring no ground treatment.

Although the LLF contains six pegmatite veins, there is an obvious increase in the amount of excellent quality rock (Class A) beneath this zone at 28%. The influence of these pegmatite veins on permeability seemingly decreases with depth in this section, and in this regard the rock mass improves to Class A and Class B with depth. Again, based on observation of the foundation mapping, 30% of Class B is zoned as needing local ground treatment. Furthermore, the SPI of the rock mass also increases toward the Steelpoort River, from block 38 to block 12, and at shallow depths too. This trend agrees with the RMR obtained in the same blocks of the LLF toward the Steelpoort River.

For the SPI profile below the RSRF, it is apparent that a large portion of the rock is classed as excellent (Class A) at 61%, therefore needing no ground treatment. Furthermore 28% of this section is classed as Class B, of which only 16% is zoned as requiring local ground treatment. Towards the right flank, four large fault zones, and two large dolerite intrusions cause localised poorer zones of rock. In a single instance, one of the dolerite intrusions intersecting block 29 results in the zone could be classified as Class D.

6.7 Analyses and Discussion

6.7.1 Relationship Between SPI and Grout Take

The relationship between the SPI and grout take is presented in Figure 6-5, for each of the four sections of the dam wall, with the SPI plotted logarithmically. Generally, there is a better linear relationship from the ULF to the RSRF, whereby SPI values in the Class C and Class D range, result in larger grout takes. This relationship is not evident in the ULF, where very low (<12.5 kg/m) and low grout takes (12.5 – 25 kg/m) are recorded in SPI Classes C and D, with no higher grout takes recorded. This relation improves slightly in the MLF where poorer SPI values in Class C and Class D give rise to moderately low grout takes, and more so in the LLF where the same SPI classes result in moderate, moderately high and high grout takes. The same trend is evident in the RSRF where larger SPI values in Class C give rise to these moderately-high to high grout takes, resulting in a better linear relationship. Although there is a higher degree of scatter in Class C and D in the RSRF, the presence of higher grout takes at poorer SPI values suggest a better correlation with the ground treatment as designated by the SPI. At these larger SPI values, the rock is of poor quality in terms of watertightness, and predicting the accuracy of grout take is obviously difficult due to the inherent properties of the geologic media as well as that of the grout itself. Nevertheless, rock classified as poor (Class C) and very poor (Class D) should record these higher grout takes than the very low and low grout takes that occur in the ULF and MLF.

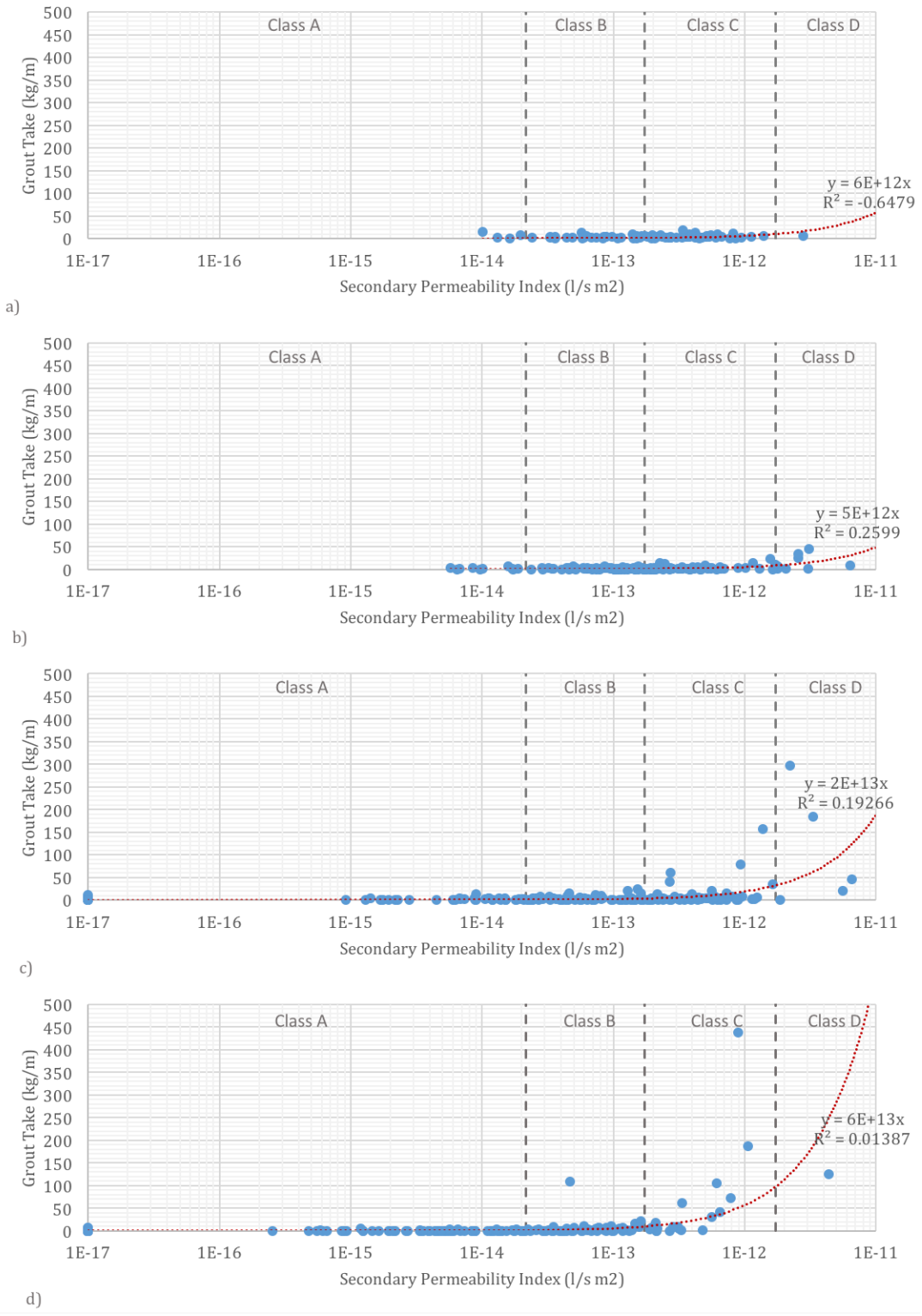

Figure 6-5. Relationship between SPI and grout take for the: a) ULF; b) MLF; c) LLF; and d) RSRF.

Poor correlation between water takes, from which the SPI is calculated, and grout takes is typical for most grouting operations. This is understandable because grout has different and variable properties (W:C ratio and additives). Furthermore, the calculation of grout takes (kg/m) does not take into account the factors of time and pressure as applied to water takes (litre/time/length/pressure). However, the better correlation of zones of higher permeability (larger SPI values) can be ascribed to early unsatisfactory results obtained with a thin mix (3:1 W:C) over a more successful thicker (0.8:1 W:C) mix. Instances of higher water takes, which occur in Class C and D rock followed by a low grout take (<5 kg/m) occur frequently when a 3:1 W:C (thin) mix is used, particularly in the ULF, rather than when a 0.8:1 (thick) mix is used. This is due to a generally less fractured rock with larger geological features which govern the permeability, and return void filling flow types (associated with pegmatite veins and fault zones). In cases where the initial thin mix was deemed unsatisfactory, a large number of primary boreholes have been regrouted successfully with the thicker mix. The general success of a thick mix, together with a large percentage of void filling flow types indicate that it is the presence of single highly permeable features in the rock mass that require treatment. These zones are associated with the pegmatite veins, fault zones and highly fractured rock at contacts of dolerite intrusions. Furthermore, this indicates the general impermeable and ungroutable nature of the gabbroic rock mass.

6.7.2 Comparison with Results from the Investigation Phase

Two distinct scenarios are observed when comparing SPI and grout take from grout boreholes, with *Lu* values and RQD values from exploratory boreholes. Representative charts from selected boreholes are shown in Figure 6-6. The first scenario exists whereby all parameters correlate, and is observed in 20 of the 32 grouting boreholes (63%) that are compared. In these instances (using Figure 6-6a as an example) an increasing SPI correlates with an increasing grout take, decreasing RQD, and increasing *Lu* value, with the converse also occurring. Interestingly, although much less prevalent, a second scenario occurs whereby a correlation between SPI and grout take from the grout boreholes, as well as RQD values from exploratory boreholes exists, but the *Lu* values obtained in the exploratory boreholes do not follow this trend. As exemplified in Figure 6-6b at stage 1, a high SPI (poor class) correlates with a high grout take, poor RQD, but a low (or zero) *Lu* value. It is also emphasised that the exploratory borehole was not drilled in the exact position of the grout borehole, but only within the same block along the dam wall axis. Therefore, any conclusion drawn to explain this must use caution. However, in these instances this may be explained by the presence of a single large permeable feature. In the example used in Figure 6-6b, a minor fault zone is present, and the WPT during the exploratory phase may not have intersected this feature. Furthermore, the lengthy test section during the WPT in the grout boreholes, together with the unloading of the rock mass during foundation excavation, might have represented the true permeability of the rock in this block more accurately.

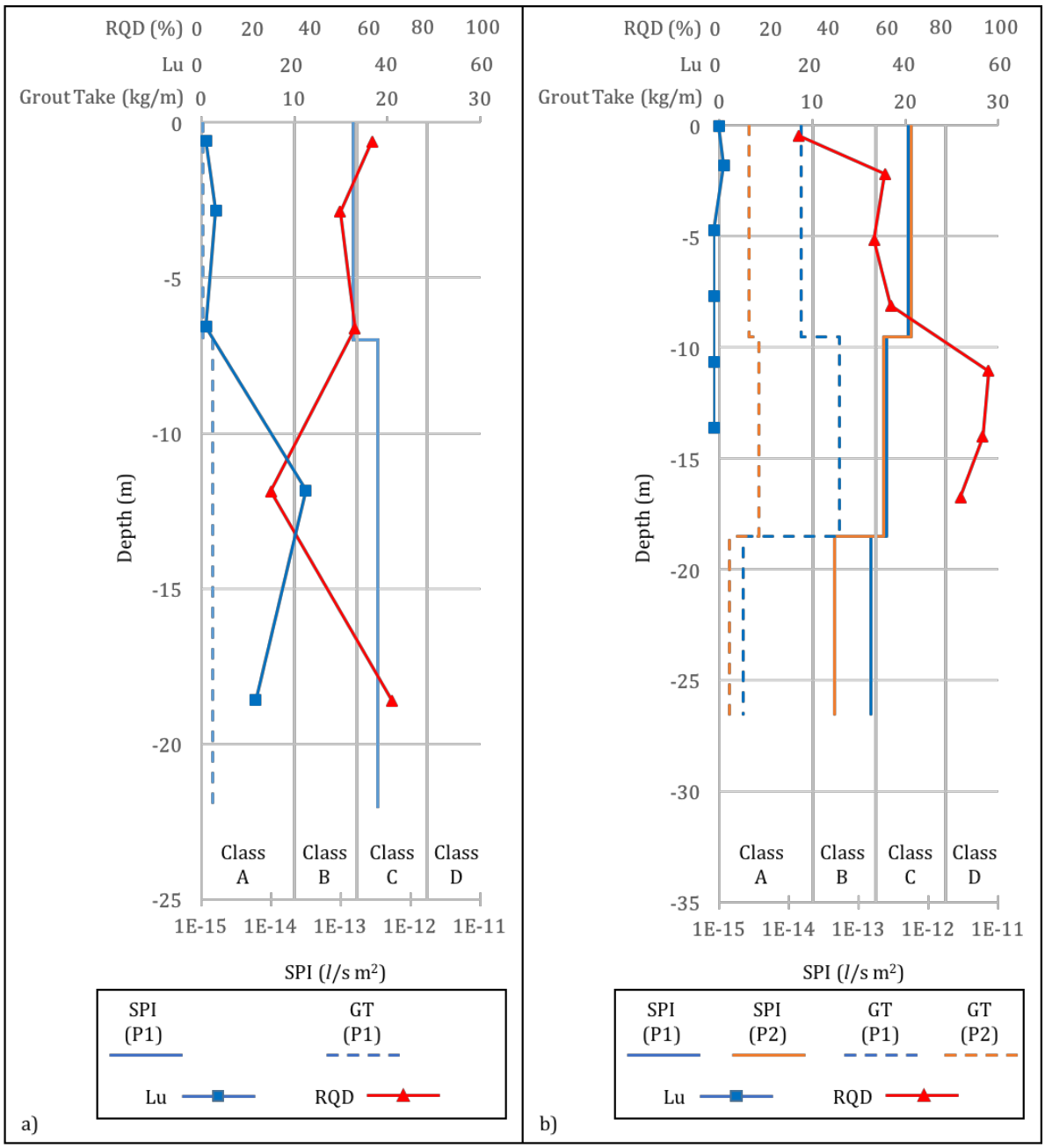

Figure 6-6. Comparison of SPI and grout take in the primary grouting boreholes, with Lugeon (Lu) values and Rock Quality Designation (RQD) values obtained in the exploratory boreholes. a) Representative example for scenario 1 from Block 134 in the ULF, whereby SPI increases, GT increases, Lu increases, and RQD increases. b) Representative example for scenario 2 from Block 80, whereby SPI class C correlates with a high GT and poor RQD, but a maximum *Lu* value of 2.

6.7.3 Validation of SPI Ground Treatment Based on Grouting

The validation is conducted for a number of boreholes, of which the results are presented in Table 6-6. Keeping with the example as shown in Figure 6-6a, Stage 1 in borehole P1 is classified as Class B, and the borehole is considered successfully grouted with a thin grout mix (3:1 W:C ratio), and; therefore, a high degree of jointing is inferred. The stated RQD values obtained in the exploratory borehole range from 51% to 62%, with no significant geological feature intersecting the test section. This suggests that the high degree of jointing is related to the rock mass and not a single feature of high conductivity, and; therefore, validates the required grout mix based on the ground treatment as proposed by the SPI. However, Class B rock quality of which a high degree of jointing exists should not require ground treatment. This may be validated further by the very low grout take (0.2 kg/m) recorded in this borehole at this stage. At stage 2, the borehole is considered successfully grouted with a medium mix of 1:1 W:C ratio. It is inferred that the section can be classified as having a low to medium degree of jointing. Upon validation with the RQD from the borehole, it is seen that the RQD is 27% at 12 m depth, and increases to 65% at 18 m depth. Upon consultation with the foundation mapping and exploratory borehole profiles it is evident that a fault zone intersects this section. According to the SPI ground treatment process, if there is a single feature of intense hydraulic conductivity, then indeed a medium or thick mix is required. In this case there is a low RQD value, localised to a portion of the test zone intersected by the fault, and the ground treatment is indeed validated by the degree of jointing.

Looking at borehole P1 and P2 at Stage 1 depth, in Figure 6-6b, the stage in each borehole is zoned as Class C, and considered to be successfully grouted with a thick mix (0.8:1 W:C). It is inferred that a low degree of jointing exists, whilst the RQD increases from 28% to 61%. Upon consultation with the foundation mapping, another fault zone intersects this stage, which results in the localised lower RQD value. Once again it is the presence of a single highly permeable feature that makes the choice of a thick grout mix successful. At Stage 2 in borehole P1, the SPI had decreased slightly, but still classifies as Class C. Again, a successful thick (0.8:1 W:C) grout mix infers a low degree of jointing. This also validates the SPI; however, the exploratory borehole does not extend the full depth of Stage 2. Nevertheless, at this stage it is inferred that the success of the thick mix is due to the presence of at least a single feature of high conductivity within a test section of low degree of jointing, as validated by the RQD. At Stage 2 in borehole P2, the SPI had also decreased slightly, but still remained classified as Class C. This stage was considered to be unsuccessfully grouted with a thick mix (0.8:1 W:C), which by back analysis infers a high degree of jointing. However, this contradicts the RQD values that increases with depth, and therefore invalidates the suggested ground treatment. This could plausibly be explained by the exploratory borehole not being an adequate representation of grout borehole P2. Furthermore, most exploration boreholes were drilled vertically and may not have intersected a distinct sub-vertical joint pattern, hence, not reflecting the true RQD value of the rock mass.

Table 6-6. Summary of primary grouting holes, and the inferred degree of jointing compared with RQD values obtained from the nearest exploratory investigation borehole.

ID[1]	SPI Class	Grout			Inferred degree of jointing[2]	RQD (%)[3]	Geological feature
		Mix (w:c)	Take (kg/m)	Success			
134/P1/1	B	3:1	0.2	Yes	H	51 - 62	None – closely jointed
134/P1/2	C	1:1	1.2	Yes	L-M	27 - 65	Fault (major)
124/P1/1	B	3:1	5.9	Yes	H	4-46	Dolerite-closely jointed at contact
122/P1/1	B	3:1	5.7	No	L	25-61	Dolerite-closely jointed at contact
122/P2/1	B	3:1	0.0	No	L	25-61	Dolerite-closely jointed at contact
118/P1/1	B	3:1	2.2	Yes	H	44-70	Fault (minor) with dolerite intrusion
118/P1/2	B	1:1	0.7	Yes	L-M	99	Dolerite
118/P2/1	C	3:1	4.1	Yes	H	44-70	Fault (minor) with dolerite intrusion
118/P2/2	B	1:1	7.2	Yes	L-M	99	Dolerite
110/P1/1	D	3:1	1.7	Yes	H	17-47	Fault (minor) with dolerite intrusion
110/P1/2	B	1:1	1.1	Yes	L-M	90-97	Dolerite
110/P2/1	C	3:1	0.0	Yes	H	17-47	Fault (minor) with dolerite intrusion
110/P2/2	C	1:1	1.9	Yes	L-M	90-97	Dolerite
98/P1/1	C	3:1	4.2	Yes	H	60-97	Fault (minor)
98/P12	B	1:1	0.5	Yes	L-M	33-97	Dolerite
98/P2/1	B	3:1	2.0	Yes	H	60-97	Fault (minor)
82/P1/1	C	0.8:1	1.8	No	H	26-51	None – closely jointed
82/P2/1	C	0.8:1	0.7	No	H	26-51	None – closely jointed
80/P1/1	C	0.8:1	8.8	Yes	L	28-61	Fault (minor)
80/P1/2	C	0.8:1	12.9	Yes	L	86-96	None
80/P2/1	C	0.8:1	3.2	No	H	28-61	None – closely jointed
80/P2/2	C	0.8:1	4.3	No	H	86-96	None – closely jointed
78/P1/1	C	0.8:1	0.1	No	H	39-92	Pegmatite vein
62/P1/1	C	0.8:1	1.6	No	H	50-100	Fault (major)
62/P2/1	C	0.8:1	1.7	No	H	50-100	Fault (major)
48/P1/1	C	0.8:1	3.3	Yes	L	58-100	None – closely jointed
48/P2/1	C	0.8:1	3.2	Yes	L	58-100	None – closely jointed

[1]Block/Borehole/Stage; [2]H-high, M-medium, L-low; [3]From investigation borehole

An example of an unsuccessful thin mix is evident in boreholes P1 and P2 in Block 122. In this case, Block 122 has a major fault zone intersecting it, indicating that a thick mix should have been chosen to locally treat this feature. The low RQD is localised to a section of the borehole at the contact with the dolerite intrusion. Borehole P1 and P2 in Block 82, are examples whereby a thick mix was unsuccessfully used as the rock mass is closely fractured. In this instance, the SPI ground treatment is validated, as a thin mix should have been used. A thick mix was used in Block 78 and was unsuccessful, inferring a high degree of jointing. However, a pegmatite vein intersects the test section, and although the test section may not be highly jointed, the pegmatite vein may need localised treatment via a thin mix, which would successfully penetrate the quartz gravel which characterise the infill of these pegmatite veins.

Overall, almost all of the compared boreholes showed a positive validation, with only a single borehole contradicting the SPI ground treatment. All successfully thin mixes coincide with minor fault zones with or without dolerite intrusions, as well as very closely jointed rock gabbro. The success of these thin mixes is attributed to the choice of the thin mixes, which adequately penetrates and seals the highly-jointed rock, that are characteristic of these features. Unsuccessful thin mixes are associated with the contacts of dolerite intrusions, which are generally highly weathered and fractured. Indeed, these zones are more successfully treated with a thick mix, and is validated by the success of thick mixes of borehole stages that intersect these intrusions. Unsuccessful thick mixes are mostly attributed to major fault zones, and in these cases although the grout mix may very well have been successful, the adequate sealing of these features will only occur with a closer spacing of curtain grout boreholes.

With regards to test sections zoned as Class B (ground treatment is needless if there is a high degree of jointing, and local treatment is required if a low degree of jointing exists), in addition to the example previously given in Block 134 (borehole P1, Stage 1), 3 more grout boreholes classified as Zone B and an inferred high degree of jointing were successfully grouted. The success of this grout may be attributed to the rock mass not needing any treatment, rather than the grouting process being successful. In all of these instances the grout takes are very low (<5 kg/m) which suggests that indeed the rock mass did not require treatment. Conversely, Class B sections with a low inferred degree of jointing were also mostly regarded as successful grouts, which needed to be treated locally, nonetheless. Considering the need to clarify ground treatment for Class B zones specifically, the test section could have been too long such that more than one condition exits, with regard to the inferred degree of jointing, therefore requiring separate ground treatments being necessary within one stage. Although it is suggested to conduct testing on a smaller section, this may be problematic when grouting as one cannot easily and cost-effectively change the grout mix design within a single stage.

6.7.4 Influence of Discontinuity Orientation on Validities

Based on the outcome of validation results for each of the Blocks as presented above, as well as the conclusion reached by Jones et al. (2016) who found that it is unlikely that only a single geometrical discontinuity property is responsible for Lugeon values at De Hoop dam, the

orientations of the joint sets were assessed by examining the stereographic projections of each specific Block. The stereographic projections for these blocks in the LLF, ULF, and MLF, are shown in Figure 6-7, Figure 6-8, and Figure 6-9, respectively.

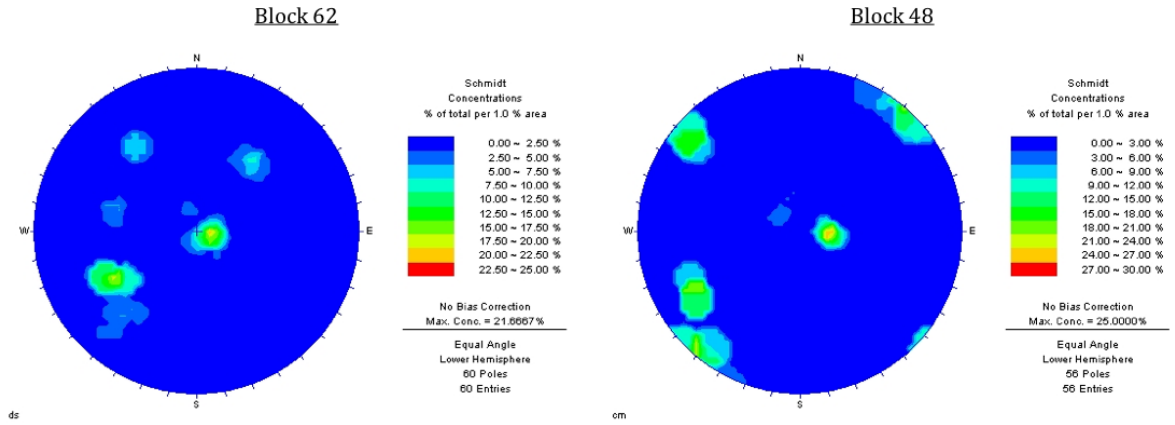

Figure 6-7. Stereographic projections of compared blocks in the LLF.

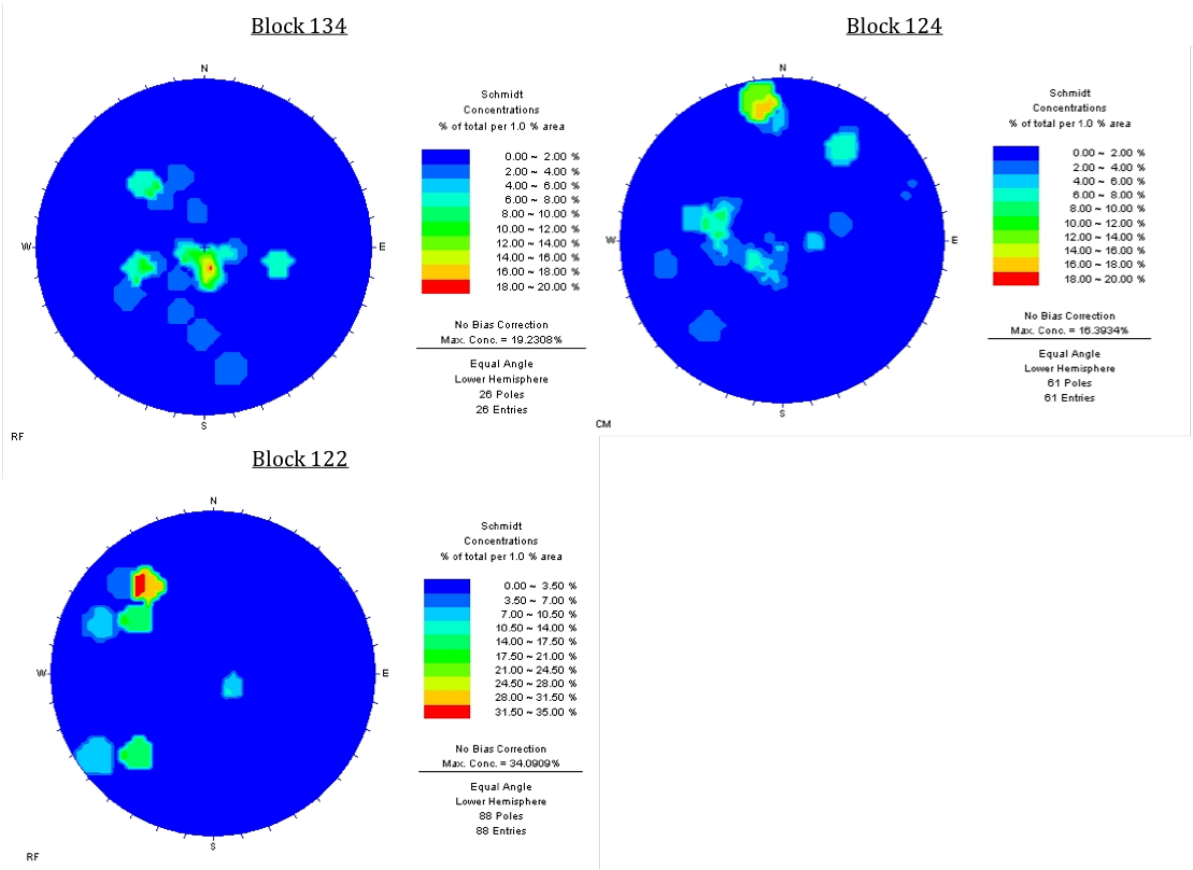

Figure 6-8. Stereographic projections of compared blocks in the ULF.

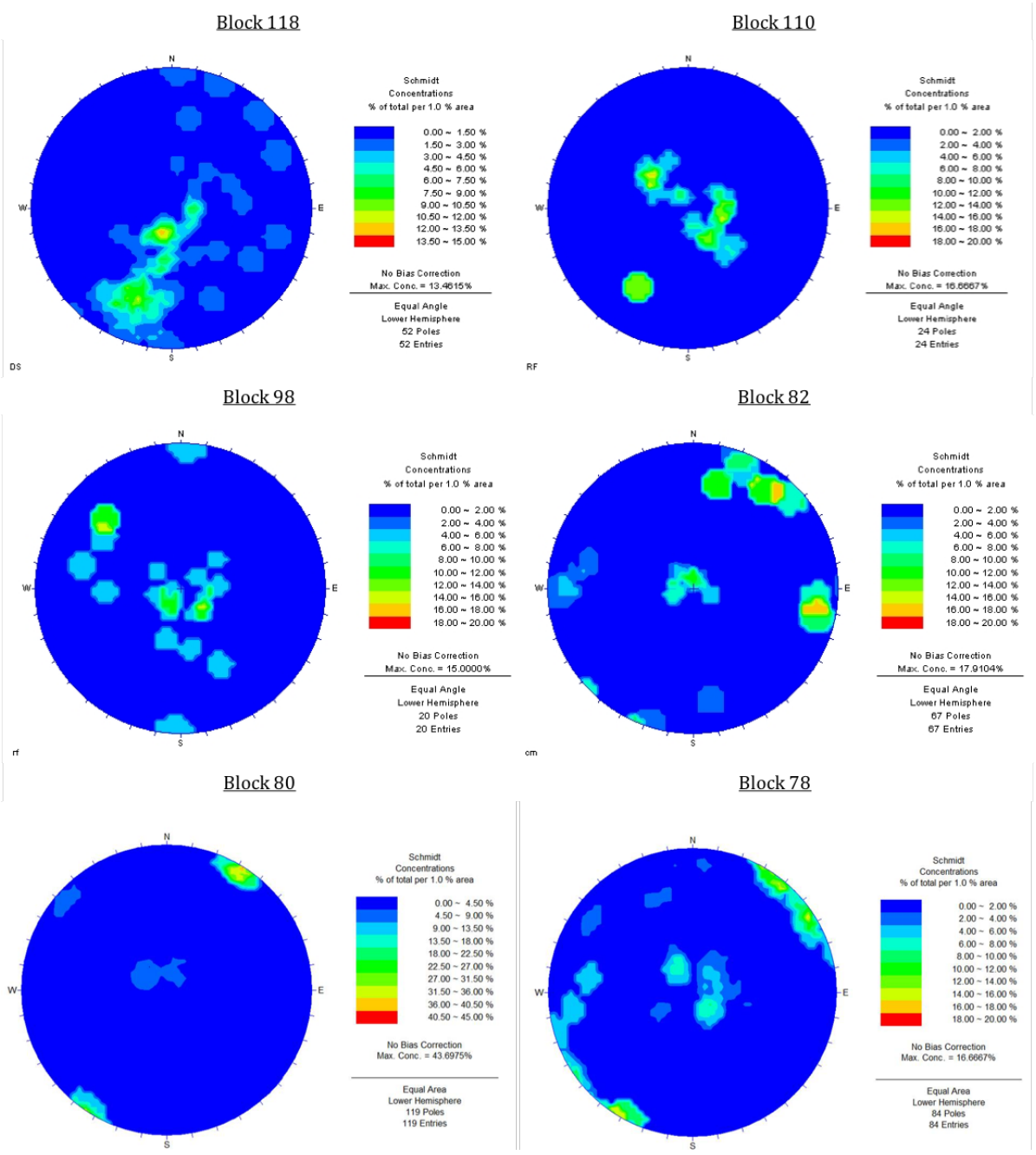

Figure 6-9. Stereographic projections of compared blocks in the MLF.

From the stereographic projections, it is observed that all blocks that showed an unsuccessful primary grout are characterised by prominent vertical and sub-vertical joint sets. These blocks include; 122, 82, 80, 78, and 62. In contrast, most successful grouts are found in blocks that have prominent horizontal and sub-horizontal joint sets, such as Blocks 134, 110 and 98. Only three blocks; 124, 118, and 48, that had successful grouts where characterised by prominent vertical joint sets. Notwithstanding, these blocks also have prominent sub-horizontal joint sets.

Although it is reasonable to argue that most significant geological features are non-horizontal, and are therefore more likely sub-vertically oriented features, stereographic projections of

blocks without the intersection of large geological features where isolated, comprising Block's 80, 82, and 134. Block 80 and Block 82 comprise mostly sub-vertical joints and both of these blocks showed no success of grouting, whilst Block 134 comprises mostly sub-horizontal joints and was successfully grouted. This observation alone could postulate that the orientation of discontinuities has an influence on unsaturated flow mechanisms of water pressure tests and the subsequent design of grouting programmes that are designed from conducting WPT's through various stages of the project life.

6.7.5 Influence of Degree of Saturation on Validities

The groundwater condition of the rock mass along the foundation was generally described as being dry except towards the lower left flank and within the river section. In the river section, the upstream and downstream excavation faces contained a few slow seeping joints. Examples of blocks within river section that exhibited these slow seeping joints is shown in Figure 6-10. Additionally, slow water seepage was also observed along larger fault zones and sub-horizontal dolerite dykes. Joints on the contacts of fault zones or weathered joints were damped in some cases.

Considering the generally poor correlation of grout takes with SPI in the ULF and MLF, as opposed to the better correlation in the LLF and RSRF. Notwithstanding, although this poor correlation can be ascribed to early unsatisfactory results obtained with a thin grout mix (3:1 W:C) over a more successful thicker (0.8:1 W:C) mix used in the LLF and RSRF, the implication of wetter joint conditions must be considered.

If these conditions become drier (and the groundwater table deeper) further away from the river section, it may be that Lugeon test interpretations are influenced when conducting the test in the unsaturated zone by misunderstanding unsaturated preferential flow paths and hydromechanical behaviour during the investigation phase. This is therefore likely a function of the complex interaction in a two-phase air-water system, rather than a single-phase water system in saturated conditions. Significant amounts of leakage that required remedial works occurred through the foundation rock mass in the left flank during reservoir impoundment and this may be a result of the change in hydraulic properties during the investigation phase (two-phase conditions in the intermediate fractured vadose zone) as opposed to the saturated phreatic conditions (single phase) after reservoir impoundment.

6.7.6 Limitations and Assumptions

The boreholes along the reference line of the dam axis were not being drilled deep enough during the investigation phase, as the actual founding levels were much deeper than expected in order to find satisfactory founding conditions. Therefore, boreholes were often too shallow to continue the comparison with grout boreholes at deeper stages. Unfortunately, the postulation of the unloading process during foundation investigation affects rock mass permeability, and therefore, lacks further validation. Furthermore, the exploratory boreholes

were not drilled at the exact localities of the grout boreholes, and considering the heterogeneous nature of the rock mass, large variations could exist over small distances.

Figure 6-10. Examples of blocks within the river section that exhibited slow water seepage: a) Block 5; b) Block 9; c) Block 10; and d) Block 11 (photographs courtesy of Knight Piésold).

6.8 Summary

A validation of the ground treatment as proposed by the SPI was conducted using the foundation rock at De Hoop Dam, South Africa. The following conclusions are presented:

- The overall permeability of the foundation rock mass before grouting is generally low (3.5 – 4.0 Lu), with the quality of rock in terms of the SPI increasing from the upper-left to the lower-left flank and towards the river section. Local poor-quality rock (Class C and D) occur in the upper 10 m, as the rock mass quality increases with depth, and as such most permeable characteristics are near-surface features. Zones of very poor and poor quality (Class C and D) were related to pegmatite veins, dolerite intrusions, anorthosite and magnetite bands, and major faults and associated fractured zones.
- Generally, a poor correlation of grout takes with SPI in the ULF and MLF can be ascribed to wetter joint conditions and early unsatisfactory results obtained with a thin

grout mix (3:1 W:C) over dryer and a more successful thicker (0.8:1 W:C) mix used in the LLF and RSRF, which show better correlation between low SPI values and higher grout takes.

- Calculated SPI values, and grout takes from the grout boreholes generally correspond to the RQD values and Lu values recorded during the final exploratory phase. However, in several instances the Lu values obtained in the exploratory boreholes do not follow this trend, most likely due to the WPT not having intersected this feature. Moreover, the lengthy test section during the WPT in the grout boreholes, together with the unloading of the rock mass during foundation excavation, might have represented the true permeability of the rock in this block more accurately. Although it is not advised to conduct WPT's over lengths greater than 5 m, it has been shown that even lengths twice as long have successfully zoned highly permeable geological features.
- Overall, the degree of jointing inferred from the success of the grout mix showed that almost all of the compared boreholes validated the ground treatment as suggested by the SPI. All successfully thin mixes coincide with minor fault zones with or without dolerite intrusions, as well as very closely jointed rock gabbro, whilst unsuccessful thin mixes are associated with the contacts of dolerite intrusions, which are generally highly weathered and fractured. This was highlighted by the success of thick mixes when applied to these intrusions. Unsuccessful thick mixes are mostly attributed to major fault zones, and in these cases, although the grout mix may very well have been successful, the adequate sealing of these features will only occur with a closer spacing of curtain grout boreholes.

The validations highlighted that the orientation of the joint set likely resulted in a positive or negative correlation between the parameters. Furthermore, results presented show an increasingly better correlation between Lugeon and grouting data for the foundation rock mass towards the river section. A possible contributor to this trend is the wetter nature of the fractures towards the river section, as opposed to the dry and unsaturated nature of fractures on the upper flanks, which may have influenced the flow regimes during the Lugeon tests. These two hypotheses govern the experimental studies that will be conducted in the subsequent chapters. Therefore, the experimental studies will focus on the different flow mechanisms in horizontal versus vertical fractures under conditions of variable saturation. Furthermore, the influence of conducting Lugeon-tests under conditions of variable saturation will also be investigated.

CHAPTER 7 EXPERIMENT 1: SMOOTH CLEAN OPEN VERTICAL AND HORIZONTAL FRACTURES

7.1 Introduction

The Cubic law is based on the parallel plate model theory, which enforces a number of assumptions to be valid. However, in natural conditions, more so in the intermediate fractured vadose zone, these assumptions are likely violated. Yet, there has been no proposed alternative. The following chapter presents the first qualitative experimental study that seeks to investigate the fundamental concept of the Cubic law under unsaturated conditions in an initially dry free-draining discrete fracture.

The experiment comprised of flow visualisation experiments conducted on transparent replicas of smooth parallel plates, with inlet conditions of constant pressure and differing flow rates over both vertical and horizontal inclination. It is understood that the Cubic law is not intrinsically applicable to unsaturated systems. However, part of the experiments aim of this study was to investigate the wetting of initially dry horizontal and vertical fractures and their intersections. Whether fractures in the experimental setup detailed in this chapter will truly saturate completely will determine whether the Cubic law applies at all.

Furthermore, this fundamental concept is tested using the geotechnical centrifuge. Due to the novelty of unsaturated fracture flow in the centrifuge, it is vital to first validate the fundamental conceptual models and assess whether similar flow mechanisms occur, as those presented in literature. The following chapter comprises verbatim excerpts from both Jones et al. (2018a), for the models tested at 1g, and Jones et al. (2017b) for the models tested at accelerated conditions.

7.2 Experiment Methodology

7.2.1 Set-up

7.2.1.1 Vertical Clean Smooth Parallel Plates (Model 1-1)

The vertical model test is performed on a fracture measuring 100 mm height x 110 mm width, with a constant aperture of 1 mm as shown in Figure 7-1a. Assuming saturated conditions, the fracture replica is therefore characterised by a hydraulic conductivity (K_f) of 9.18 x 10^{-1} m/s, and permeability (k_f) of 8.33 x 10^{-8} m^2.

Model preparation begins with the placement of a camera and metal support columns at the base of the model. Two acrylic sheets are bent into a L-section measuring 299.5 mm long and are placed in a strongbox with a total length of 600 mm. This allows for a constant

aperture of 1 mm to be maintained between the sheets, although some possible change in aperture due to slight bending is duly noted as a possible influence on the study.

A grid is placed on the outside of the opposite acrylic L-section, facing inwards, so that the geometry (width and lengths) of the flow mechanisms can be assessed. A back plate is then installed in the strongbox and three screw jacks confine the fracture against the window and back plate, where a water inlet container is constructed around the fracture. Foam sealant tape is placed around the interior and exterior perimeter of the water inlet container to maintain a watertight seal where potassium permanganate crystals are scattered to colour the water. It is assumed that the minimal amounts of potassium permanganate used did not influence the surface tension of water.

A scale is placed in the container in order to calculate a volumetric flux (Q_f) per unit width of the fracture. However, these initial intentions were not accomplished because constant head conditions were never achieved in the inlet container due the preferential flow mechanisms, as will be discussed in section '*Continuous influx'*. An overhead bracket with a water inlet pipe and a solenoid valve (electronic tap) is installed above the fracture, while an outlet is installed at the base of the model.

7.2.1.2 Horizontal Clean Smooth Parallel Plates (Model 1-2)

The horizontal model test is performed on a horizontal fracture measuring 270 mm length x 110 mm width, with a constant aperture of 1 mm, maintained by spacers. The hydraulic conductivity and the permeability of the fracture are the same as reported in the vertical experimental set-up.

The model is constructed using the same two L-section acrylic sheets, with one being inverted and slightly offset on top to allow for an inlet area as illustrated in Figure 7-1b. A grid is again placed on the outside of the opposite acrylic L-section, facing inwards, so that the geometry of the flow mechanisms can be assessed.

A water inlet container is constructed by jacking the back plate and sealing the interior and exterior perimeter with foam sealant to maintain a watertight seal, where potassium permanganate crystals are scattered to colour the water. An additional scale is placed in the inlet container to record the head to calculate the volumetric flux (Q_f) per unit width of the fracture.

A camera is placed on an overhead bracket above the horizontal fracture, while a second camera is placed on the right base of the model. A water inlet pipe and a solenoid valve are installed above the container while an outlet pipe is installed at the base of the model.

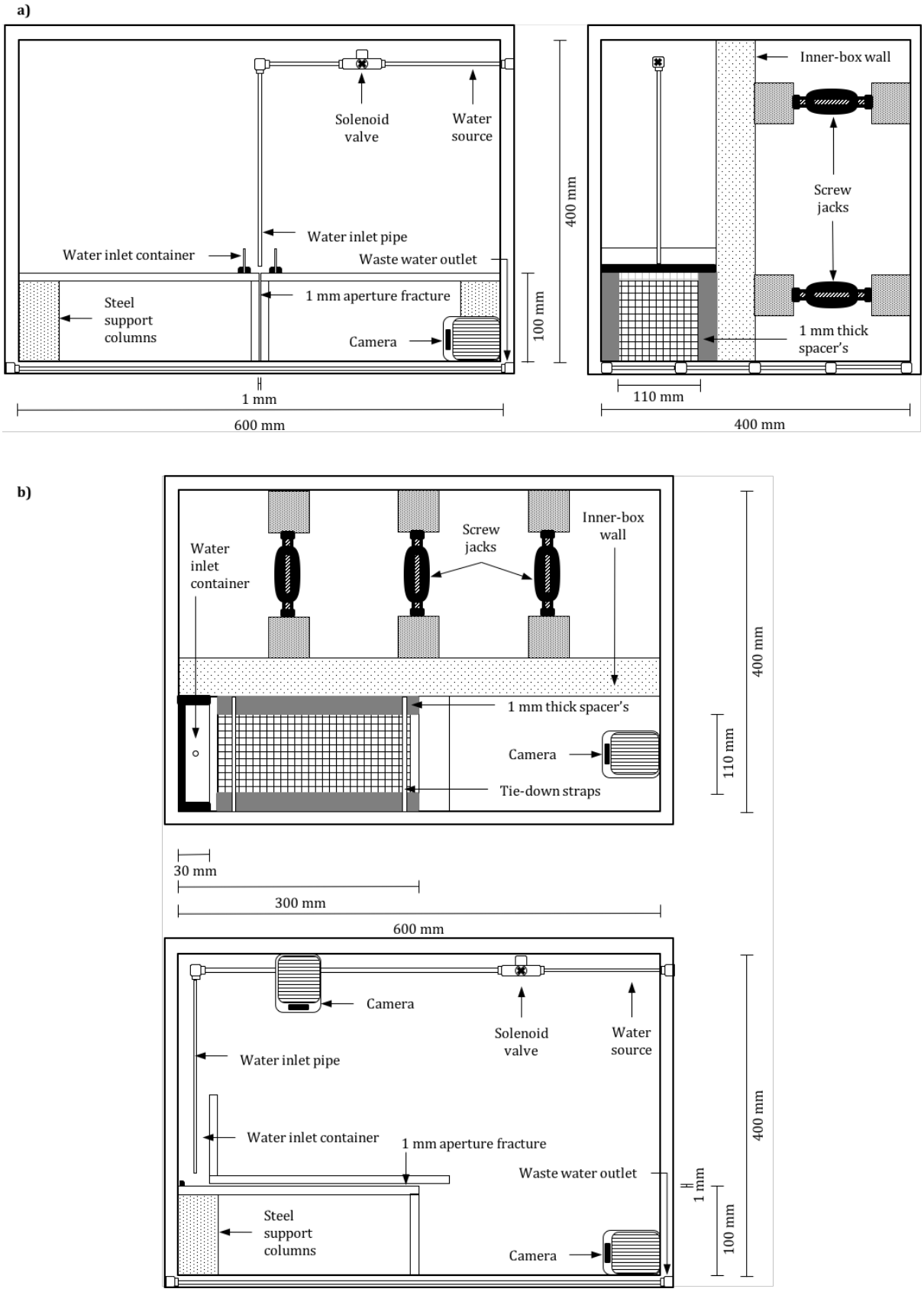

Figure 7-1 Model set up for the dry, smooth, parallel plate test for the a) vertical fracture (left: plan view; right: cross-sectional view), and b) the horizontal fracture.

7.2.2 Procedure

7.2.2.1 1g

The completed model is tested under intermittent and continuous influx conditions. For intermittent influx tests on the vertical fracture, the solenoid valve is opened and influx is introduced as individual droplets for 1 minute at approximately 0.5 l/hr, resulting in a droplet with a volume of approximately 0.13 ml every 3 seconds. For the intermittent influx test on the horizontal fracture, the solenoid valve is opened and influx is introduced as individual droplets for 10 minutes at a slightly higher influx rate of approximately 0.8 ml/hr.

The intermittent tests are then stopped, the model dismantled, dried, and reassembled for the continuous influx test. The continuous influx test consists of opening the solenoid valve and allowing an initial influx of 20 l/hr to enter into the model. This is followed by 3 minute interval stepped influx increases, where an additional 20 l/h is added to the current flux rate until a total constant flux of 100 l/h is obtained for 3 minutes. The water is then closed and the system is allowed to drain for an additional 3 minutes before repeating the same stepped flux procedure stated above, but following shortened time intervals of 1 minute between increases.

7.2.2.2 20g

The completed model is accelerated to 20g and tested under intermittent and continuous seepage conditions.

For intermittent seepage tests, the solenoid valve is opened and influx is introduced as individual droplets for 3 minutes (*20 hours, at prototype scale*) at approximately 0.6 l/hr, (*12 l/hr*). The centrifuge is then stopped, the model dismantled, dried, and then reassembled for the continuous seepage test.

The continuous seepage in the fracture consists of opening the solenoid valve and allowing an initial influx of 20 l/hr (*400 l/hr*) into the model. This is followed by 1-minute (*6.67 hours*) interval stepped influx increases, where an additional 20 l/h is added to the current flux until a total constant flux of 100 l/h (*2000 l/hr*) is obtained for 1 minute. The water is then closed and the system drains for an additional minute before repeating the same stepped flux procedure stated above, but following shortened time intervals of 30 seconds (*3.33 hours*) between increases. The flow rate is manually observed in the centrifuge control room by a flow meter. During high flow influx intervals (> 60 l/hr) cavitation occurs in the inlet pipes, whereby flow ceases temporarily causing a backpressure in the pipes and results in excess influxes being delivered to the model during re-stabilisation. Therefore, constant flow is not always achieved at these intervals, and although all the influxes results are presented, the discussion generally excludes the results of the intervals greater than 40 l/hr.

7.3 1g Results and Analyses

7.3.1 Vertical Fracture Flow Mechanism (Model 1-1)

7.3.1.1 Intermittent Influx

The flow mechanisms observed during the intermittent influx tests are shown as snapshots in Figure 7-2. The accompanying Figure 7-3 graphically depicts the input volume of each droplet as well as the approximate volumes of the sliding droplets and the static droplets in the fracture during the test.

An initial air-water meniscus in the form of a sliding droplet with an approximate volume of 0.120 ml initially invades into the fracture. This droplet advances through the vertical fracture with the thread snapping before it reaches the base of the fracture. This leaves a path of remnant static droplets on the vertical fracture with a total volume of approximately 0.092 ml.

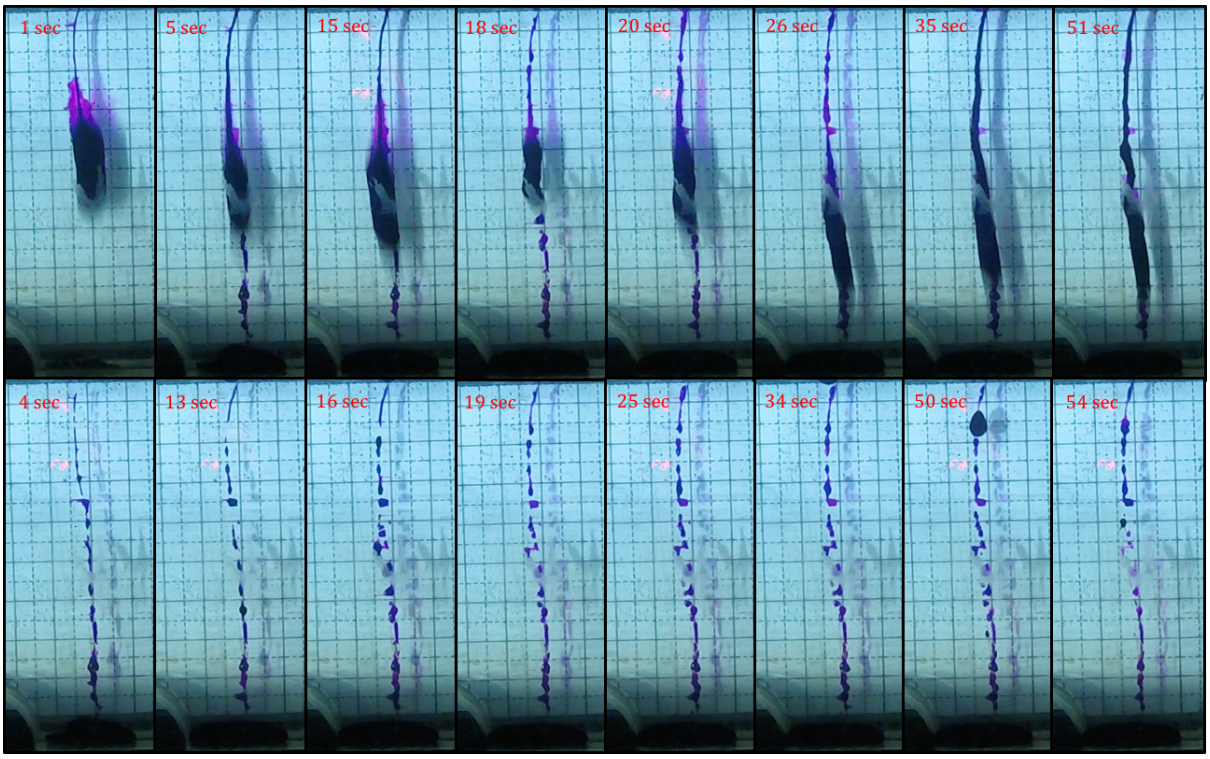

Figure 7-2 Screenshots of the intermittent influx experiment (5 mm x 5 mm grid). Each sliding droplet is shown in the top row, and the subsequent static droplets thereafter (before the following sliding droplet invades) are shown in the bottom row.

After 5 seconds, a second sliding droplet with an approximate volume of 0.125 ml follows the same flow path along the static droplets. Ten seconds thereafter, a third sliding droplet is observed in the fracture with a much larger volume of approximately 0.150 ml, and a fourth sliding droplet observed 3 seconds later with a much smaller volume of approximately 0.085 ml. At 26 seconds, a fifth sliding droplet with a volume of 0.115 ml enters the fracture and after a further 9 seconds, a seventh droplet with a volume of 0.194 ml invades into the fracture. Finally, at 51 seconds an eighth droplet with a volume of 0.200 ml enters the fracture.

As the test proceeds, the volume of remnant static droplets increases to a range of 0.120 ml to 0.132 ml. The remnant static droplets also result in the formation of elongated sliding droplets that almost span the entire height of the vertical fracture during each subsequent pulsation.

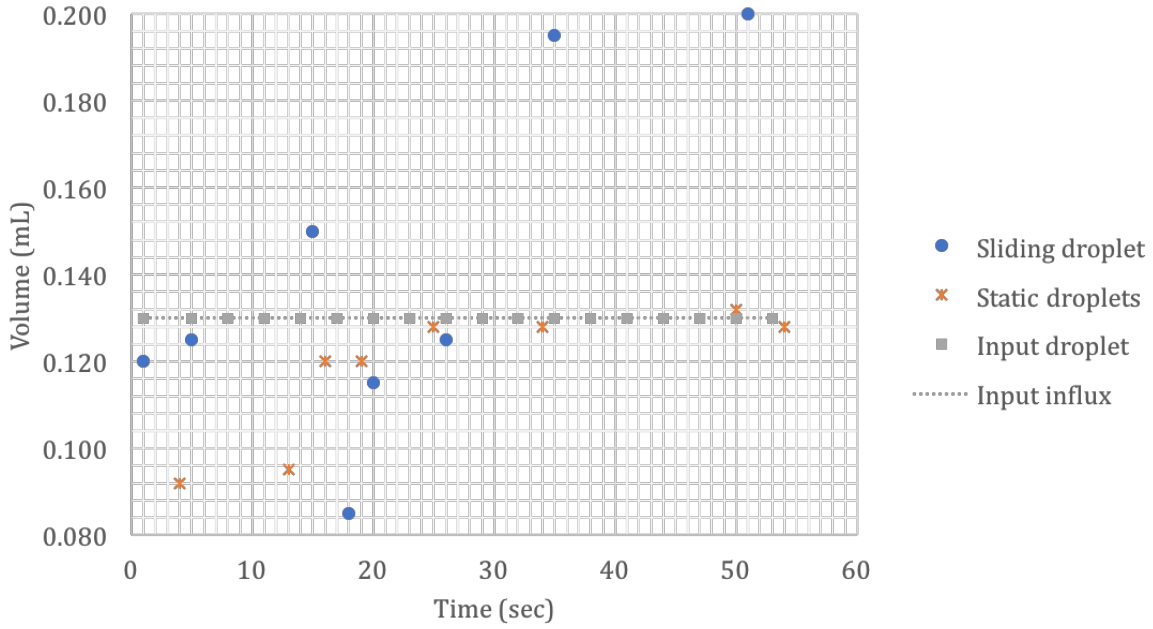

Figure 7-3 Graph depicting approximate volumes for each sliding droplet and static droplets during the intermittent influx test.

7.3.1.2 Continuous Influx

7.3.1.2.1 Wetting

Immediately after water is introduced at 20 l/hr, a breach occurs as a single droplet that invades into the vertical fracture. This air-water meniscus advances vertically through the fracture, without snapping (Figure 7-4). Assuming the droplet is constrained between both fracture walls, the droplet has a volume of approximately 0.1 ml. The thread immediately behind the droplet is 1 mm wide, and increasingly widens up to 4 mm width in order to accommodate a higher influx. Thereafter the thread begins to oscillate aggressively from approximately 5 mm width. With this increasing width of the initial continuous rivulet, water is seen spreading laterally along the top of the fracture.

A consequence of the oscillating rivulets is flow path switching, as annotated in Figure 7-5 panel I, with two separate flow paths initially evident. The oscillation of one of the flow paths, due to an increasingly larger influx of water being accepted, leads to an amalgamation of the two flow paths. During this amalgamation process, the excluded flow path increasingly loses its volume of water as supply is ceased. This leads to static droplets remaining on the excluded flow path.

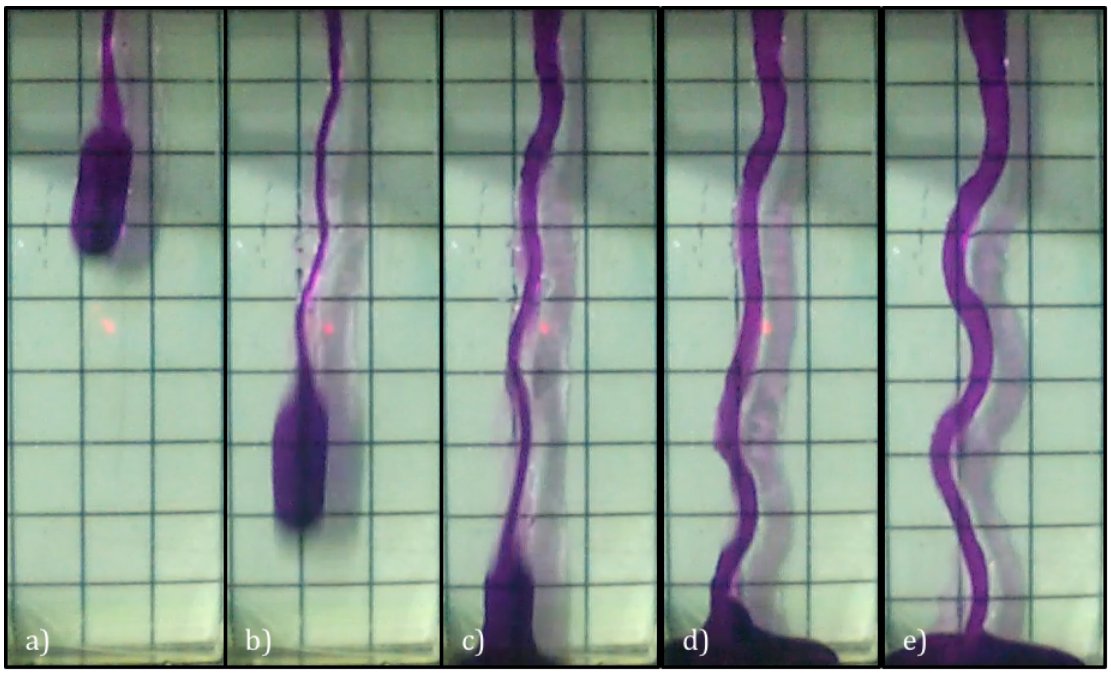

Figure 7-4 Initial invading droplet with continuous thread (10 mm x 10 mm grid).

During this flow path switching and amalgamation of rivulets, frequent large air (capillary) pockets (bubbles) are seen throughout the test at the base of the fracture. The formation of a snapping thread, as flow is ceased due to the oscillation, is exemplified in Figure 7-5 panel II, where it shows the cessation of input into a particular continuous rivulet due to the oscillation of the supplying-rivulet. Once water supply is ceased, the water volume held in the secondary-rivulet is drained until a point whereby the volume is at a low-threshold and the rivulet snaps, leading to static droplets scattered along the previous continuous flow path.

In addition to oscillating rivulets, intermittent rivulets with sliding droplets form from stable continuous rivulets that progress vertically down the fracture, as shown in Figure 7-5 panel III. Here, a supply of water is evident from the continuous rivulet, which then forms a droplet. Once the droplet accepts a sufficient volume, it forms a discrete sliding droplet that breaks off from the continuous rivulets along an intermittent rivulet or flow path. This occurs when the weight of the drop is greater than the surface tension and results in the vertical sliding of this droplet, which leaves behind scattered static droplets along this broken flow path. The subsequent sliding droplet, which forms at the end of the continuous rivulet, follows the same previously wetted path of static droplets.

Identical flow mechanisms are observed throughout the subsequent wetting intervals as shown by the snapshots for each interval in Figure 7-6. During the wetting interval at 40 l/hr, oscillating rivulets make contact with the spacers in the fracture and lead to preferential flow paths along these boundaries. Further increasing the influx rates into the vertical fracture resulted in a fixed set of rivulets occurring within the fracture. At the 20 l/h interval approximately 10% cross-sectional area contributes to flow, and even at the 100 l/h interval full saturation is not met, but rather only 45% cross-sectional area contributes to flow.

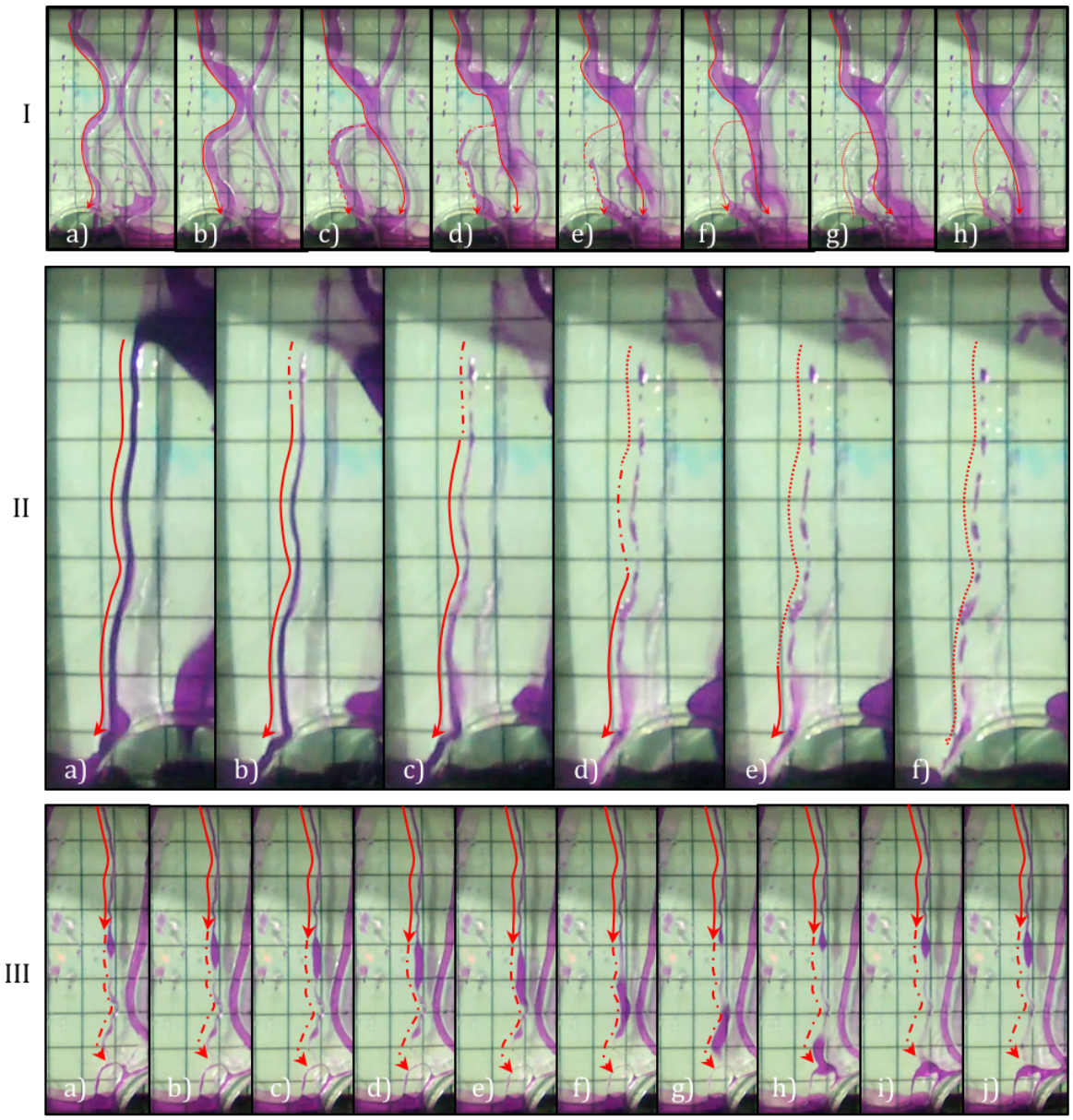

Figure 7-5 Observed flow instabilities and phenomenon. Panel I: Flow-path switching phenomenon due to oscillation of rivulets. Panel II: Snapping thread due to cessation of water supply, which forms static droplets along the previous flow-path. Panel III: Continuous thread to sliding droplet along an intermittent flow-path (10 mm x 10 mm grid).

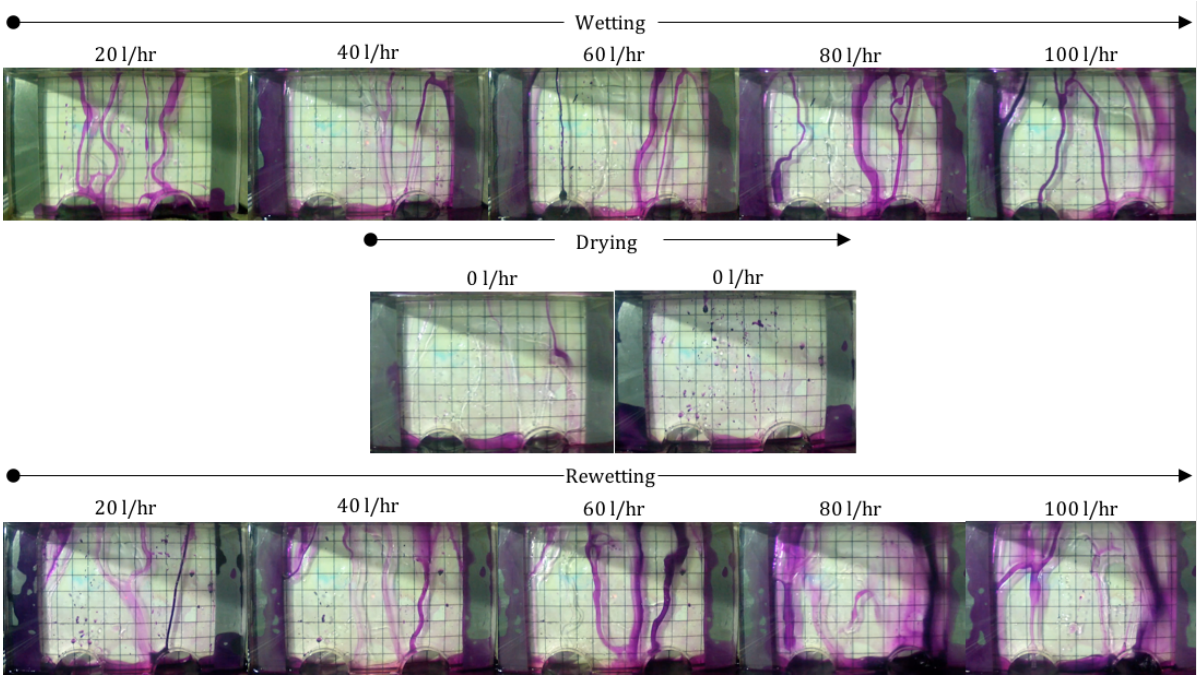

Figure 7-6 Snapshots of the vertical fracture at each interval for the continuous flow test, showing preferential flow paths in purple (10 mm x 10 mm grid).

7.3.1.2.2 Drying and Rewetting

When the water influx is ceased, the continuous rivulets snap as the volume of water in each rivulet drains at the base of the fracture. This leaves behind static droplets along the broken flow paths, with an occasional sliding droplet moving vertically down toward the base of the fracture.

Upon re-addition of water, the invading droplets with following continuous threads follow the flow paths along the static remnant droplets in the fracture. Each single droplet reconnects the static droplets and a new continuous rivulet forms. This process repeats itself, reconnecting all the remnant rivulets' pathways, while forming no new flow pathways within the fracture for all flow intervals in the rewetting cycle. The same flow mechanisms are again observed throughout all rewetting intervals, with rivulet oscillations and flow switching dominating the flow mechanism in the fracture.

7.3.2 Horizontal Fracture Flow Mechanism (Model 1-2)

7.3.2.1 Intermittent Influx

The wetting front is seen invading the horizontal fracture as a circular wetting front in Figure 7-7. Three minutes into the test, despite the wetting front being irregular, no air (capillary) pockets are left trapped within the horizontal fracture. The wetting front reaches the vertical outlet wall at 5 minutes 50 seconds into the test, but only breaches once the horizontal fracture is fully saturated 17 seconds thereafter.

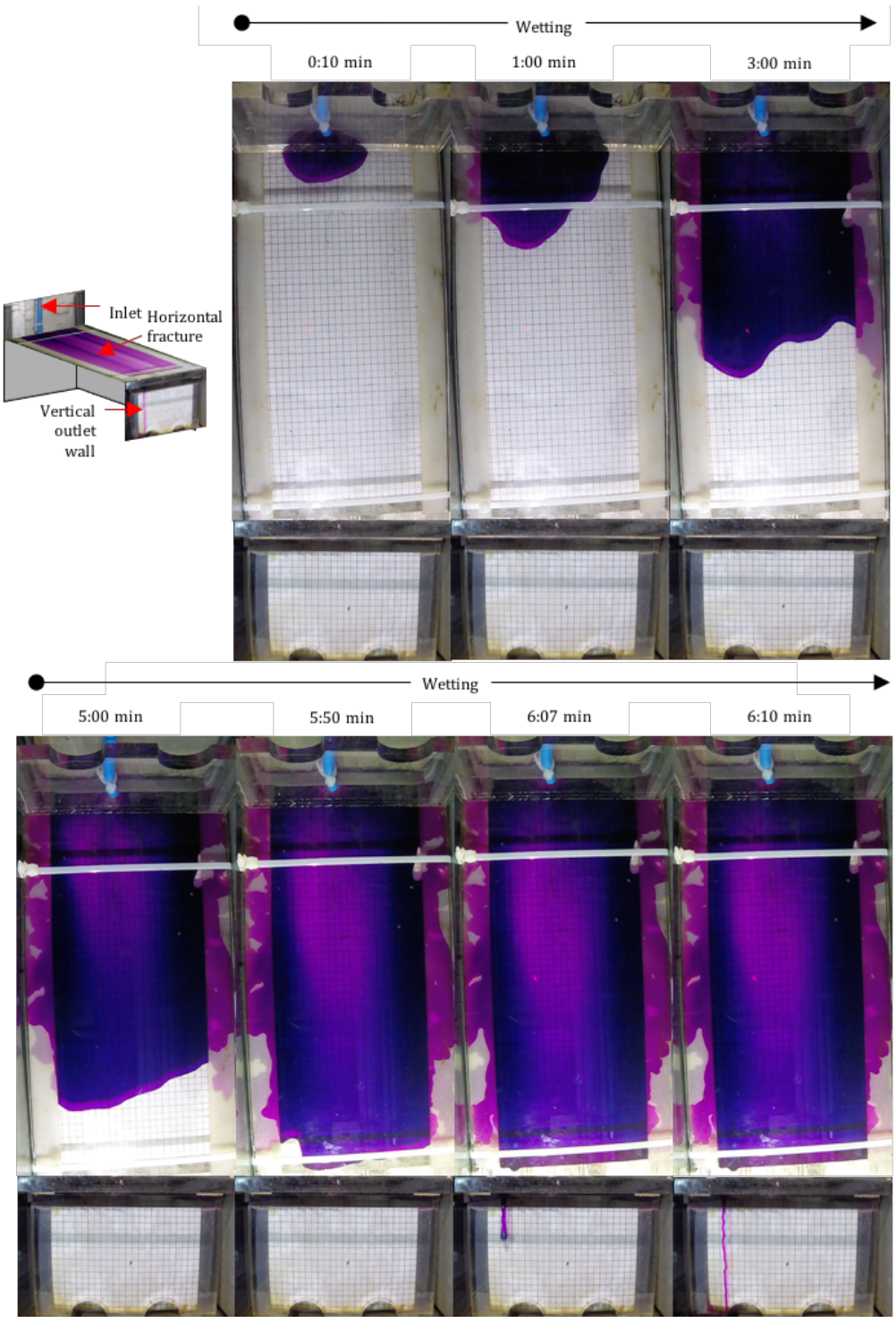

Figure 7-7 Invasion of the wetting front and subsequent outflow during the intermittent flow test in the horizontal fracture.

Throughout the test, the head in the inlet container is as large as the fracture aperture, at 1 mm. The outflow is located at a single discrete point at the vertical wall. The mechanism of the outflow is characterised by an initial advancing droplet that exits the horizontal fracture, with a thick thread (3 mm width) following it, as shown at 6:07 min in Figure 7-7. Once the

droplet reaches the base of the vertical wall a continuous rivulet is established whereby, for the duration of the test, it drains the horizontal fracture.

7.3.2.2 Continuous Influx

7.3.2.2.1 Wetting

The wetting front initially spreads elliptically (Figure 7-8), but changes to an irregular front at about 3 seconds. The wetting front reaches the vertical wall in 8.5 seconds as the horizontal fracture saturates, and forms rivulets down the vertical wall.

At 20 l/hr a constant head of 14 mm is maintained in the inlet container. This head thereafter increases to 17, 23, 31, and 33 mm for the 40, 60, 80, and 100 l/hr influx intervals, respectively.

Although the horizontal fracture remains saturated during all wetting intervals, flow down the vertical wall only occurs at 5 discrete points, as continuous rivulets. The width of the rivulets become increasingly larger at each successive wetting interval, whereby at the 80l/hr interval the 2 central rivulets join and become a large continuous rivulet. Throughout the testing, oscillating of the continuous rivulets occurs at the beginning of a new influx interval, but stabilise shortly thereafter.

7.3.2.2.2 Drying and Rewetting

When the water influx is ceased, the rivulets at the outlet vertical wall cease to flow almost immediately, with the 2 outer rivulets being the last to disappear and resulting in remnant static droplets on the vertical exit wall. In addition to the remnant static droplets, a large air pocket invades into the fracture from the inlet container side, whilst a smaller air pocket enters from the exit wall.

Upon rewetting at 20 l/hr, a circular wetting front invades the air pocket at the inlet. This wetting front splits the air pocket and forms smaller air pockets in the horizontal fracture. Some static pockets of air remain in the fracture and form capillary islands whilst others move parallel to the direction of flow. Some of the capillary islands are only mobilized as the influx rate is increased. One capillary island in particular remains static at both 40 l/hr and 60 l/hr interval, although, when the influx rate is increased to 80 l/hr, it is mobilised. A capillary island located adjacent to the spacer and near the fracture entrance remains stationary throughout all the rewetting intervals.

At the vertical wall, a single rivulet initially forms once the horizontal fracture is saturated in the 20 l/hr rewetting interval. This initial continuous rivulet mobilises at the same location of the thick central rivulet previously formed during the initial wetting cycle. A second rivulet forms during the 20 l/hr rewetting interval, corresponding to the same location as a rivulet at 40 l/hr in the wetting phase. A third and fourth rivulet, respectively form in the 60 l/hr interval.

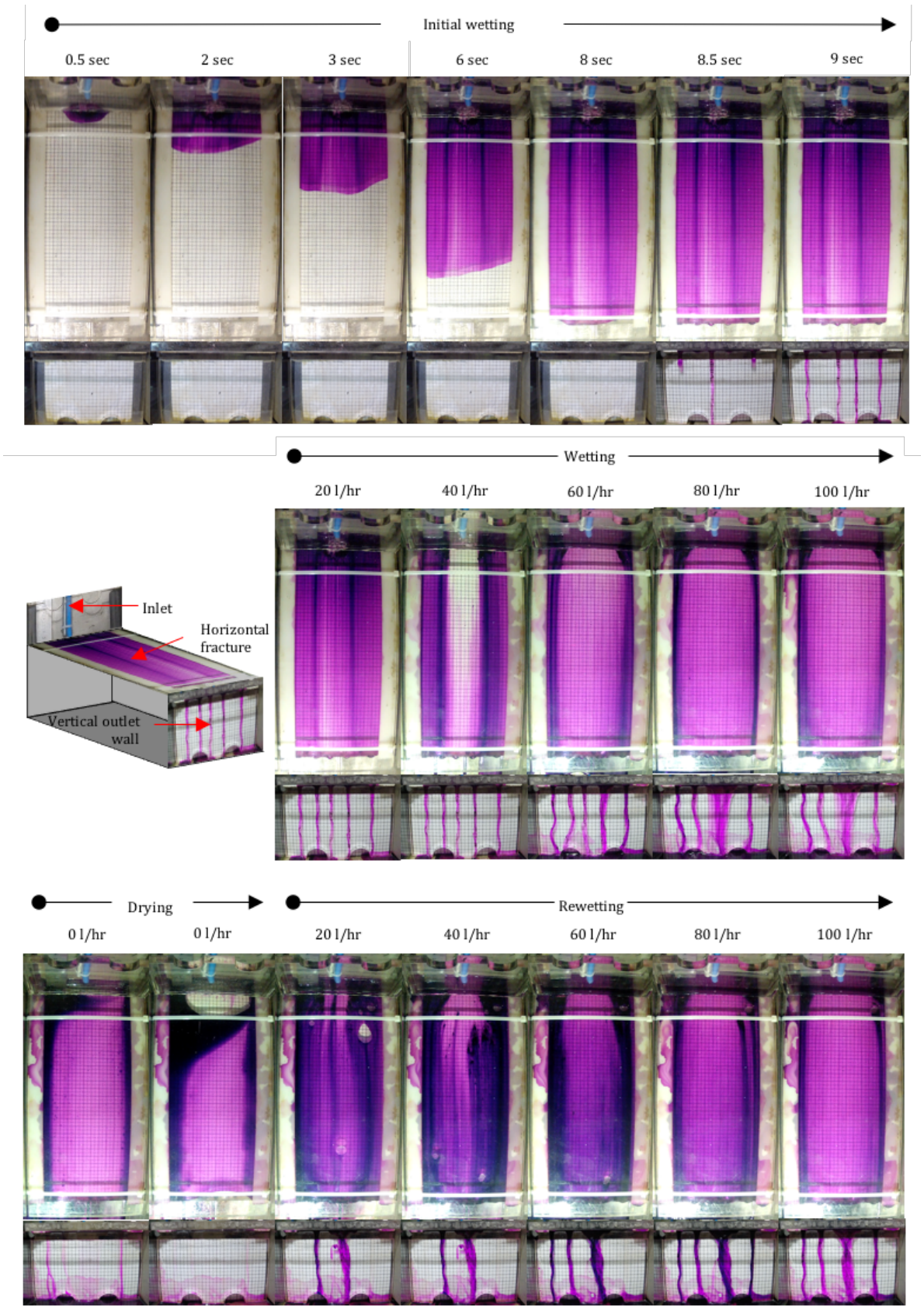

Figure 7-8 Invasion of the wetting front at 20 l/hr in the horizontal fracture, and screenshots of the horizontal fracture and vertical wall for the continuous flow experiment at each interval during the test.

The flow path geometries up to the 60 l/hr rewetting look dissimilar to the wetting phases for the same influx intervals. However, by the 100l/hr interval, the four rivulets that are present on the vertical face mirror the same as those observed in the corresponding interval during the wetting phase and also begin oscillating as the influx is increased at the start of each new interval, but settle soon thereafter as previously observed.

7.3.3 Analyses

7.3.3.1 Initial Fracture Wetting

For both influx scenarios of the vertical experiments, there appears to be an accumulation of water at the top entrance of the fracture. In the continuous influx experiment, the ponding of water could be due to the manner in which water enters the fracture, whereby the majority of continuous influx enters the fracture as the initial continuous rivulet, but a small proportion of the influx is rejected due to the aperture size. This results in lateral accumulation of rejected influx water such that new continuous rivulets occur adjacent to the initial continuous rivulet.

Likewise, in the droplet influx experiment, the ponding of water can also be attributed to water being rejected from entering into the fracture, as the capillary pressure is greater than the water pressure. This results in the accumulation of lateral water until a sufficient volume of water ponds that is capable of breaching the capillary forces. This can be illustrated in the example between the second and third sliding droplet, where 9 seconds pass indicating that three droplets were introduced from the inlet pipe, and on the fourth droplet a sufficient volume of water is present to create a breach at the entrance to the fracture. Subsequently, this breach releases a larger sliding droplet into the fracture in the form of the third observed sliding droplet, which is much larger in volume and consequently, the following sliding droplet has a much smaller volume. The volume of the sliding droplets normalises back to approximate influx volume whereby the ponding process is repeated.

The observed flow mechanisms for the vertical fracture with intermittent influx are similar to the phenomenon of the dripping faucet as stated by Su et al. (1999) and Glass and Nicholl (1996), whereby water breaks off from the liquid supply when the weight of the water is greater than the surface tension force. In contrast, Su et al. (1999) found that this flow mechanism is observed at flow rates of less than 8 ml/hour, which is far below that of the flow rate in this experiment. Furthermore, the difference between the static remnant droplets and sliding droplets will be dependent on the surface tension and wetting properties of the surface, as well as the volume of the droplets. However, when observing the flow mechanisms of the vertical fracture with continuous influx and the vertical exit wall in the horizontal experiment for both influx styles, the observed flow mechanisms are in agreement with a thread (rivulet) that does not snap as described by Su et al. (1999) at flow rates greater than 12 mL/hr.

In addition to the observed flow mechanisms within the vertical fracture experiments, a number of flow instabilities or phenomenon are also observed. This includes examples such as continuous rivulets that begin to oscillate at approximate widths of 4-5 mm, amalgamation of oscillating rivulets causing turbulent conditions that traps air pockets between flow paths, and continuous-to-intermittent rivulets where it is likely that the water supply to this flow path is

much less than the continuous rivulet observed in the fracture. Additionally, the preferential flow path observed along the boundaries created by the contact of oscillating rivulets could plausibly highlight the importance that fracture continuity and contact points have on governing flow paths (e.g. Berkowitz, 2002). The flow paths occupied by the different flow mechanisms are furthermore dependent on the wettability of the material, with previously wetted areas being the most likely to re-establish extinct flow paths.

The observations from the horizontal fracture support the Cubic law, whereby the entire horizontal fracture is saturated for both conditions of continuous influx and intermittent influx, before flow is observed exiting at the vertical wall. Although full saturation of the horizontal fracture is maintained, the vertical wall is variably saturated with water exiting the horizontal fracture at discrete points as rivulets. As the flow rate is increased per interval in the continuous flow test, these rivulets occupy an increasingly wider cross-sectional area of the vertical fracture as they carry an increasingly larger volume of water from the horizontal fracture. Despite this increasing cross-sectional area, full saturation is still not achieved, but rather only 20% to 45% at the highest inflow interval contributes to flow, and therefore opposes the Cubic law for fractures that are not horizontally inclined.

7.3.3.2 Linear Velocities and Volumetric Fluxes for Horizontal Experiments

Using the observed heads for each influx interval in the horizontal experiment for continuous influx experiment, the volumetric flux and linear velocity for the horizontal fracture can be calculated using the equations as outlined by Singhal and Gupta (2010). Then, by using the continuity principle, the linear velocity of the vertical exit fracture can be deduced. The calculated volumetric flow rate (Qf) and linear velocity for both the horizontal fracture (Vh) and the vertical fracture (Vv) are shown in Figure 7-9, where a linear relationship exists between Qf and Vh, but a less clear polynomial relationship exists between Qf and Vv.

However, the degree of saturation along the vertical fracture is dependent on the volumetric flux (Qf), thereby influencing the vertical linear velocity by controlling the cross-sectional drainage area, where higher degrees of saturation result in larger cross-sectional areas. Employing this reasoning, as well as the continuity principle with the horizontal linear velocity, results in the vertical linear velocity obtaining a wide range of values for all possible degrees of saturation as shown in Figure 7-10. From this graph, a clear relationship is evident whereby the vertical velocity (Vv) is proportional to the ratio of the horizontal velocity (Vh) and the vertical saturation (Sv), as shown in Equation 7-1.

$$V_{\mathrm{v}} \propto \frac{V_{\mathrm{h}}}{S_{\mathrm{v}}} \qquad \textbf{Equation 7-1}$$

This indicates that lower degrees of saturation result in a pressure reduction immediately and therefore an associated velocity increase and decrease in head elevation, which leads to large variation in vertical linear velocity. However, as the degree of saturation increases, the influence of different influx rates does not affect the calculated vertical linear velocities as they appear to approach a constant range.

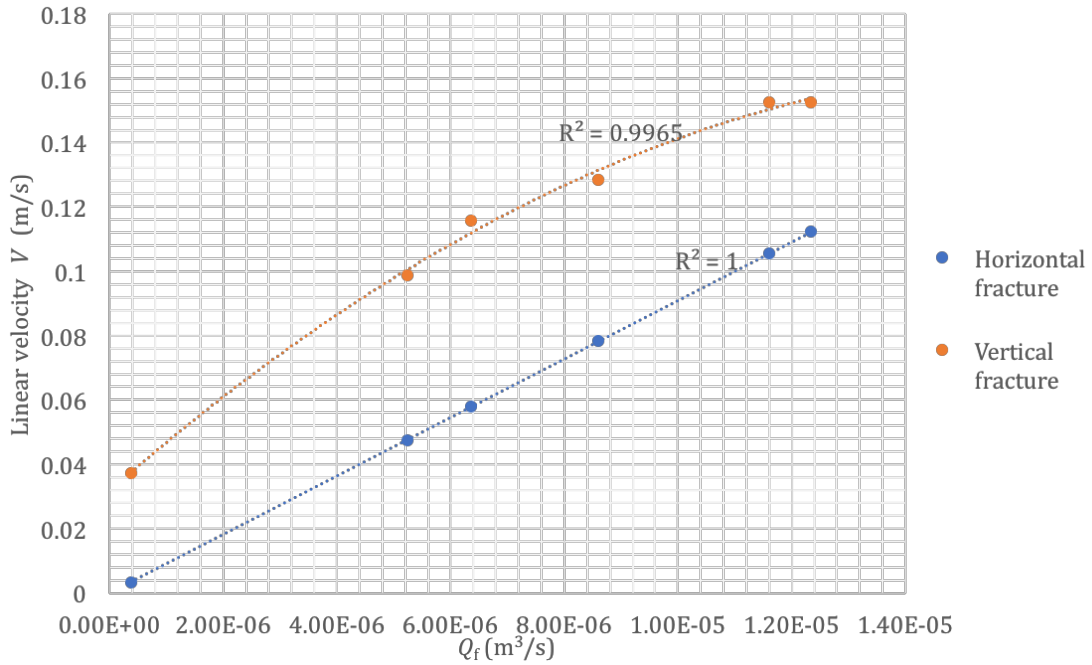

Figure 7-9 Graph depicting approximate volumes for each sliding droplet and static droplets during the intermittent influx test.

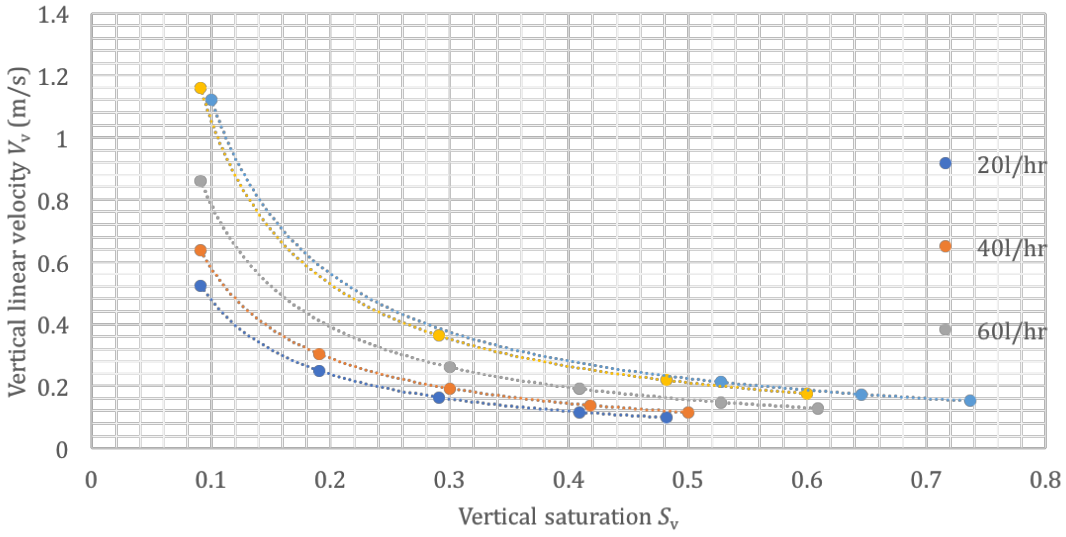

Figure 7-10 Graph depicting approximate volumes for each sliding droplet and static droplets during the intermittent influx test.

7.4 20g Results and Analyses

7.4.1 Vertical Fracture (Model 1-1)

The observed flow mechanisms in the vertical fracture for both the intermittent and continuous flow tests are summarised in Figure 7-11, and are described in the following sub-sections.

7.4.1.1 Intermittent Seepage

As shown in Figure 7-11, Panel A, an invasion of a 0.42 mm (*8 mm*) wide continuous rivulet, forming in approximately 0.1 seconds (*40 seconds*) through the length of the vertical fracture (Figure 7-11A-i to ii) over 90 mm (*1.8m*), occurs during the initial introduction of water in the intermittent flow test. A discontinuous path of discrete sliding droplets (Figure 7-11A-iii) forms adjacent to the initial rivulet, with an average width of 1 mm (*20 mm*) and travel at approximately 150 mm/s (*7.5 mm/s*).

A continuous rivulet, which does not extend the entire length of the vertical fracture, and at a length of approximately 20 mm, becomes discontinuous where sliding droplets develop and detach intermittently, as shown in Figure 7-11, Panel B. In this instance, there is not a sufficient volume of water to establish a continuous rivulet, and therefore discrete droplets break off from the rivulets when the weight of the drop is greater than the surface tension, resulting in static droplets occurring within the fracture once the rivulet snaps.

7.4.1.2 Continuous Flow

Flow switching of continuous rivulets occur due to meandering rivulets that oscillate, which leads to cessation of previous flow paths, and amalgamations with exiting flow paths, during the continuous flow tests, and is shown in Figure 7-11, Panel C. The rivulets are approximately 0.5 to 1 mm (*10-20 mm*) wide and meander the entire length of the fracture. Furthermore, the amalgamation during the flow switches are often dictated by the position of static droplets scattered throughout the fracture.

Two populations of oscillating rivulets appear to cross-cut one another without influencing the observed flow (Figure 7-11, Panel D). This highlights that rivulets do not form spanning liquid bridges constrained between both fracture walls, but rather indicates flow occurs on opposing walls as continuous rivulets within the fracture. This mechanism is further conceptualised in Figure 7-11D-iv; by a cross-sectional top-view sketch through the vertical fracture.

A summary of all continuous influx intervals is shown Figure 7-11, Panel E, and shows that throughout the test intervals, preferential flow paths, with oscillating rivulets, give way to a film flow at higher influxes (shaded portions in Figure 7-11E), but never fully saturates the width of the fracture. At 20 l/hr (*400 l/hr*), the preferential flow paths formed by the continuous rivulets saturate approximately 10% of the width of the fracture. This increases to 25% width area being saturated at 40 l/hr (*800 l/hr*); to 50% at 60 l/hr (*1200 l/hr*); and 70% at 80 l/hr (*1600 l/hr*), with full saturation not being achieved at 100 l/hr (*2000 l/hr*).

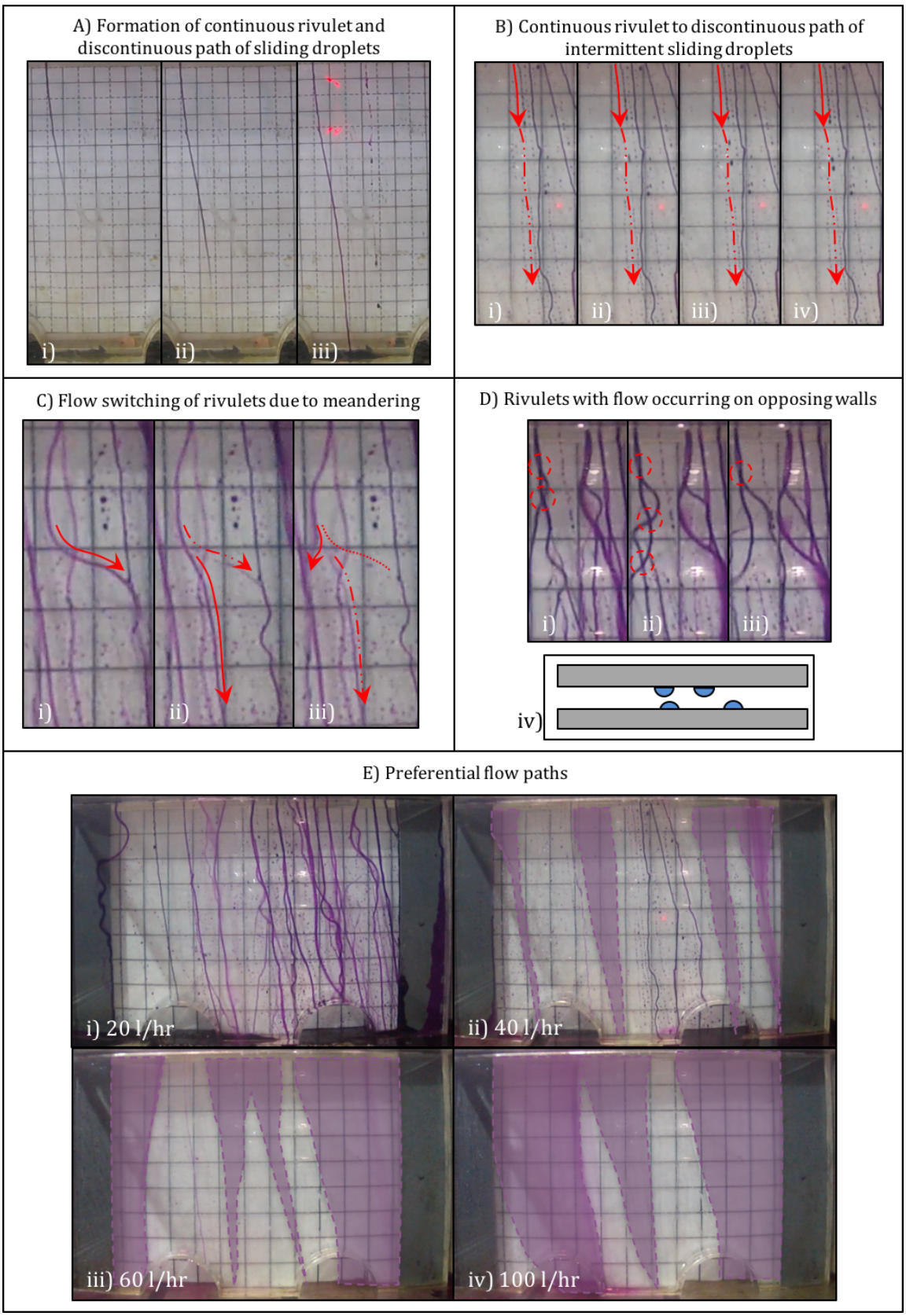

Figure 7-11. Flow mechanisms observed in the vertical fracture (A: 5 mm x 5 mm grid; B to E: 10 mm x 10 mm grid).

7.4.2 Horizontal Fracture (Model 1-2)

7.4.2.1 Intermittent Seepage

During the intermittent seepage test the wetting front is seen initially invading the horizontal fracture as a circular wetting front as shown in Figure 7-12, which eventually contacts the spacer. This boundary seems to act as a preferential flow path for the wetting front as it progresses through the fracture.

In the intermittent test, approximately 60% of the fracture saturates before the first discrete sliding droplet is noticed on the vertical wall at 112 seconds (*12.4 hours, at prototype scale*). Outflow along the vertical wall continues to occur at the localised point of the initial breach by subsequent sliding droplets.

7.4.2.2 Continuous Flow

Unlike the intermittent flow test, full saturation of the horizontal fracture occurs in the continuous flow test in 0.71 seconds (*4.7 minutes*), as shown in the initial wetting phase in Figure 7-13.

Upon saturation, a film of approximately 10 mm width (*200 mm*), is observed on the vertical wall with an additional narrow oscillating rivulet (similar to flow mechanism C in the vertical fracture). Increasing the influx to 40 l/hr widens the film to approximately 30 mm (*600 mm*), while maintaining oscillation in the rivulet. Upon increasing the influx to 60 l/hr, the film widens to 50 mm (*1000 mm*), and an additional 2 oscillating rivulets form. By 100 l/hr the width of the film is equivalent to the width of the horizontal fracture. Throughout all intervals, the film at the vertical exit wall sweeps to the right.

Upon rewetting, the capillary island that formed is mobilised, despite a small capillary island being trapped at the edge of the exit of the horizontal fracture. The water exiting along the vertical face follows the same flow mechanism as previously observed for all influx intervals.

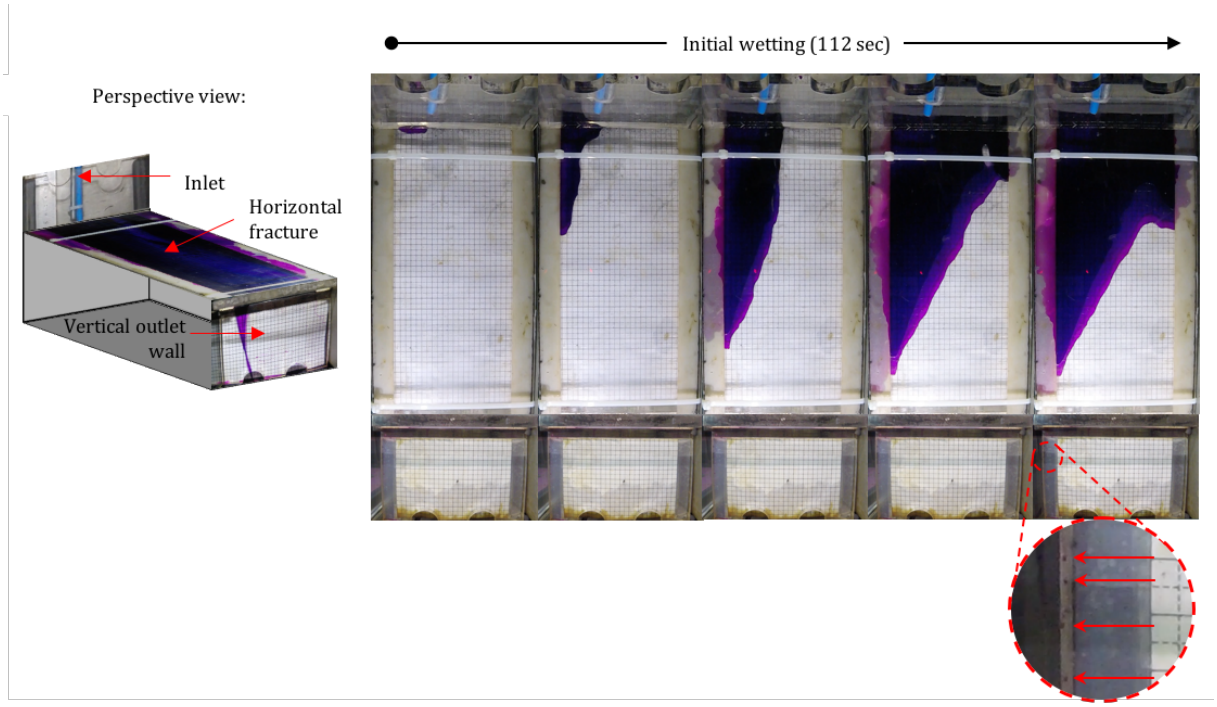

Figure 7-12 Snapshot of the wetting front of the horizontal fracture for the intermittent (droplet) flow experiment (5 mm x 5 mm grid). The insert shows perspective for the reader (horizontal fracture and unconfined vertical outlet wall), as well as the sliding droplets on the unconfined vertical outlet wall.

7.4.3 Analyses

The observed flow mechanism A (as shown in Figure 7-11 Panel A) of the initial invading rivulet, is dissimilar to the mechanism observed at high flow rates observed by Su et al. (1999), in that no prominent air-water meniscus (droplet) proceeds the rivulet. Nevertheless, once established the rivulet is maintained throughout the fracture indicating a similar observation to Su et al. (1999) for rivulets supplied by high flow rate. Furthermore, the discontinuous path of sliding droplets that forms adjacent is also similar to the flow mechanism observed at low flow rates by Su et al. (1999), and furthermore by results published by Ghezzehei and Or (2005). The presence of oscillating rivulets and flow switches (flow mechanism C, as shown in Figure 7-11 Panel C) indicate flow instabilities in unsaturated fractures, similar to the meandering rivulets presented by Ghezzehei (2004). These flow instabilities are plausibly an indication that the flow through an individual rivulet is approaching a maximum limit, for the specific contact angle and G level, specific to this test. The observation of non-interacting intersections between meandering rivulets (flow mechanism D, as shown in Figure 7-11 Panel D), as the two populations of rivulets are flowing on the opposite sides of the fracture walls, is an important observation indicating that the individual rivulets do not fill the fracture gap fully.

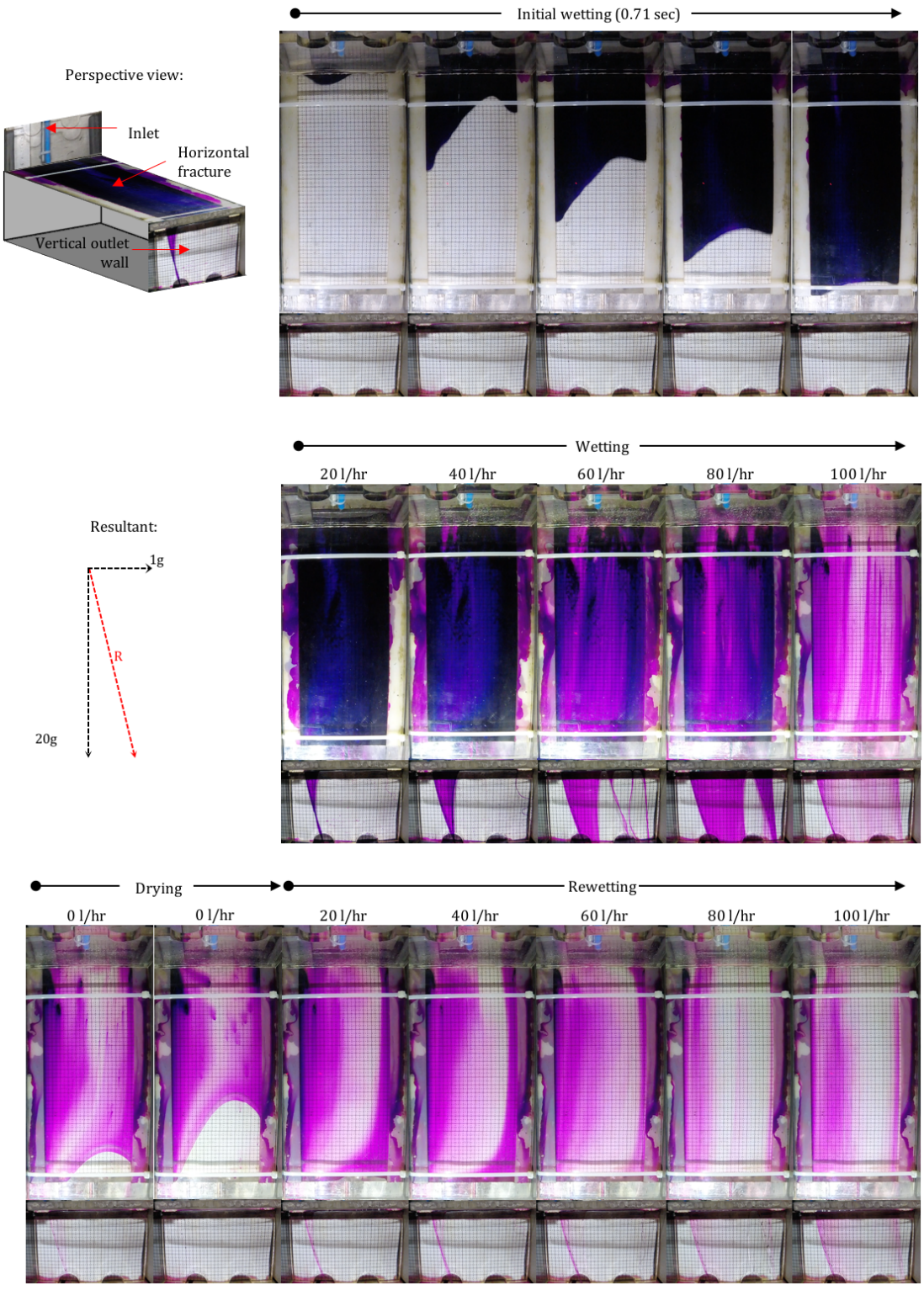

Figure 7-13 Screenshots of the horizontal fracture and vertical wall for the continuous flow experiment at each interval during the test, under 20g conditions (5mm x 5mm grid). The inserts show perspective for the reader (horizontal fracture and unconfined vertical outlet wall), as well as the resultant force acting on the film on the unconfined vertical outlet wall, causing it to sweep.

The observation of rivulets, and sliding droplet flow mechanisms, as well as film flow (only in the horizontal experiment) is important. If one considers the phase diagram of Ghezzehei (2004), contact angles of 70° for the acrylic Plexiglas used (e.g. Aouad et al., 2016; Della Volpe et al., 2002; Sumner et al., 2004) at the flow rates tested, rivulets and sliding droplets should dominate the observed flow mechanisms. The observation of co-existing droplet and rivulet flow mechanisms is likely a function of the test set-up, and not due to the same process as presented by Dragila et al. (2016). In these instances, directly beneath the inlet pipe, there is lateral accumulation of water above the fracture entrance. The continuous rivulet forms directly beneath the inlet pipe and is supplied by the majority of water being introduced. Conversely, the intermittent rivulet is being supplied by the rejected lateral accumulation of water above the fracture entrance, at a much lower flow rate. This discontinuous path of intermittent sliding droplets observed in flow mechanism A (as shown in Figure 7-11 Panel A), results from water ponding above the fracture growing to some critical size, and forming a thinning neck that eventually snaps, releasing a droplet from the top of the fracture. Similar reason can be used to explain flow mechanism B, whereby a continuous rivulet terminates to a discontinuous path of intermittent sliding droplets. Here a reduced influx for this particular feature, again from a lateral accumulation above the fracture entrance, results in an insufficient quantity of water to establish a fully-continuous rivulet, and instead an intermittent rivulet forms releasing sliding droplets when the weight of the droplet is greater than the surface tension.

The sweeping of the wide films at the vertical wall in the horizontal test is due to a resultant force, due to the interaction between the centripetal force acting perpendicular to the centrifuge platform and the gravity force acting towards the centre of the Earth. This influence is only noted for these films with large volumetric fluxes and are plausibly a function of the volume of water being transmitted. The path followed by the sliding droplets and rivulets within the fracture can be attributed to the wetting capability of the material as described by Doe (2001), whereby generally the same cross-sectional drainage area re-saturates during rewetting.

By treating the fracture width as a microscopic length (as discussed by Culligan and Barry, 1998), the scaled model results do not accurately represent natural conditions. In this instance, despite the similitude failure of the Capillary and Bond numbers, the Stokes number, which describes gravity driven flow instability, remains constant and suggests that the observed oscillating, meandering, flow switching and merging of rivulets within the model does occur in natural conditions. The observation of similar flow mechanisms in the fracture in the form of sliding droplets, and rivulets is consistent with those published in literature. This signifies that although the results from the geotechnical centrifuge model may not be scaled to prototype conditions, the observed flow mechanisms and flow instabilities are representative of natural conditions.

This good accordance between flow mechanisms observed in a geotechnical centrifuge and previous research indicates that the geotechnical centrifuge replicates variably saturated flow mechanisms acceptably. An important issue observed in replicating the parallel plate conceptual model, is that full saturation is never achieved in any of the vertical fractures (as a required assumption of the cubic law as stated by e.g. Silberhorn-Hemminger et al., 2005a;

Singhal and Gupta, 2010; Zimmerman and Bodvarsson, 1996), including that of the vertical wall of the horizontal test where the horizontal fracture is fully saturated. However, considering that the Cubic law is an expression for fracture permeability, the flow that you would get through a saturated fracture under the experimental conditions investigated is very likely to be much higher than the imposed flow rate, from the inlet pipe. Furthermore, full saturation is not even achieved in the horizontal fracture during the intermittent test.

As observed and analysed for the tests conducted at 1g, a plausible explanation could be in using the continuity principle, whereby water should theoretically be transported downward at significantly higher flow rates given the very low degree of water saturation in the vertical fractures compared to horizontal fractures. A reduced rate of input, results in a smaller cross-sectional drainage area and appearance of sliding droplets that form when the weight of the droplets, attached to the ponding of water in the horizontal fracture, are greater than the surface tension of the vertical wall and are released.

7.5 Summary

Experiment 1 consisted of flow visualisation experiments conducted on a transparent replica of the smooth parallel plate, with inlet conditions of constant pressure and differing flow rates over both vertical and horizontal inclination. Findings from this experiment showed that saturated laminar flow is not likely achieved, especially in non-horizontal fractures. In vertical fractures, preferential flow occupies the minority of cross-sectional area despite the water supply. Furthermore, geotechnical centrifuge modelling has been proven as a viable experimental tool for the replication of similar flow mechanisms for unsaturated fracture flow, as previously observed in literature.

CHAPTER 8 EXPERIMENT 2: NON-INCLINED ORTHOGONAL FRACTURE INTERSECTIONS

8.1 Introduction

In unsaturated fractured media, fracture intersections play a dominant role in controlling flow phenomenon such as flow focusing, fast preferential flow, intermittent flow episodes, flow switching and slender pathway flow (Evans et al., 2001; Pruess, 1999; Su et al., 1999; Wood et al., 2005). Behaviour at fracture intersections is controlled by the competition between capillary, gravitational, viscous, and inertial forces (Wood et al., 2005).

Several researchers (Glass et al., 2002a; Glass et al., 2003; Ji et al., 2004, 2006; Wood et al., 2004; Wood et al., 2002, 2005) have observed how the capillary barrier encountered at intersections initially stops seepage which allows for the focussing of flow through amalgamation of the fluid. Here, integrated flow occurs as sufficient fluid pressure must first be obtained before breaching the capillary barriers that exist at the fracture intersection.

Flow pathways can switch between fractures depending on the path of least resistance within each fracture intersection of the network. Slender pathways develop as fluid cascades through the fracture intersections, which results in a small area of the fractured media capable of rapidly transmitting large volumes of water.

The aim of this chapter is to investigate flow from the fundamental concept of the smooth parallel plates into a fracture intersection under conditions of variable saturation. A series of physical models incorporating individual discrete fractures and orthogonal intersections was created. This involved using smooth clean parallel plates in a horizontal and vertical orientation, under conditions of various continuous input fluxes from either the horizontal or vertical fracture, into the initially dry system. The following chapter comprises excerpts from Jones et al. (2017a).

8.2 Experiment-Specific Methodology

8.2.1 Set-Up

8.2.1.1 Flow from the Horizontal Fracture (Model 2-1)

Model 2-1 consists of a horizontal fracture measuring 270 mm length x 110 mm width, with flow occurring into a vertical fracture of 100 mm height and 110 mm width. Both fractures have a constant aperture of 1 mm maintained by spacers of 20 mm width on either side of the fracture resulting in a hydraulic conductivity (K_f) of 9.18×10^{-1} m/s, and permeability (k_f) of 8.33×10^{-8} m^2 (assuming saturated conditions).

The model is constructed using three L-section Plexiglas acrylic sheets, of which two sheets are placed opposing one another and the third being inverted and slightly offset on top to allow for an inlet area, as illustrated in Figure 8-1a. A grid, measuring 5 mm x 5 mm, is placed on the outside of the opposite Plexiglas L-section, facing inwards, for the geometry of the flow mechanisms to be assessed. A water inlet container is constructed by jacking a back plate and sealing the interior and exterior perimeter with foam sealant to maintain a watertight seal, where potassium permanganate crystals are scattered to colour the water.

An additional scale is placed in the inlet container to record the head in the inlet container to be used in calculating the volumetric flux (Q_f) per unit width of the fracture. A camera is placed on an overhead bracket above the horizontal fracture, while a second camera is placed on the right base of the model. A water inlet pipe and a solenoid valve (tap) are installed above the container while an outlet pipe is installed at the base of the model.

8.2.1.2 Flow from the Vertical Fracture (Model 2-2)

Model 2-2 comprises a vertical fracture measuring 201 mm length × 110 mm width, interested by an orthogonal horizontal fracture measuring 600 mm × 110 mm width. In the same manner as Model 2-1, both fractures have a constant aperture of 1 mm maintained by spacers of 20 mm width on either side of the fracture with the same characteristic hydraulic conductivity (K_f) and permeability (k_f).

To facilitate the construction of this model a fourth Plexiglas L-section is utilised. Two Plexiglas sheets placed opposing one another and the other two placed opposing each other and being inverted, as illustrated in Figure 8-1b. Cable tie-downs are used to secure the 4 sets of L-sections to each other during the test.

A 5 mm x 5 mm grid is used to assess the geometry of the flow mechanisms on the vertical fracture, above and below the intersection. Similarly, a 5 mm x 5 mm grid is placed facing upwards, on the horizontal fracture left of the orthogonal intersection. A second transparent grid of 10 mm x 10 mm is placed on the opposing right-hand side of the intersection of the horizontal fracture.

In a similar manner as in the previous experiment, the back plate is installed in the strongbox and three screw jacks confine the fracture against the window and back plate, where a water inlet container is constructed around the top of the vertical fracture. Foam sealant tape is placed, potassium permanganate crystals scattered, water inlet pipe, and a solenoid valve are installed with an outlet pipe installed at the base of the model.

In order to observe flow in the horizontal fracture, two cameras are placed on an overhead bracket on either side of the intersection. A third camera is placed on the right base of the model observing the vertical fracture below the intersection, and a fourth on the right of the horizontal fracture, observing the top vertical fracture perpendicularly.

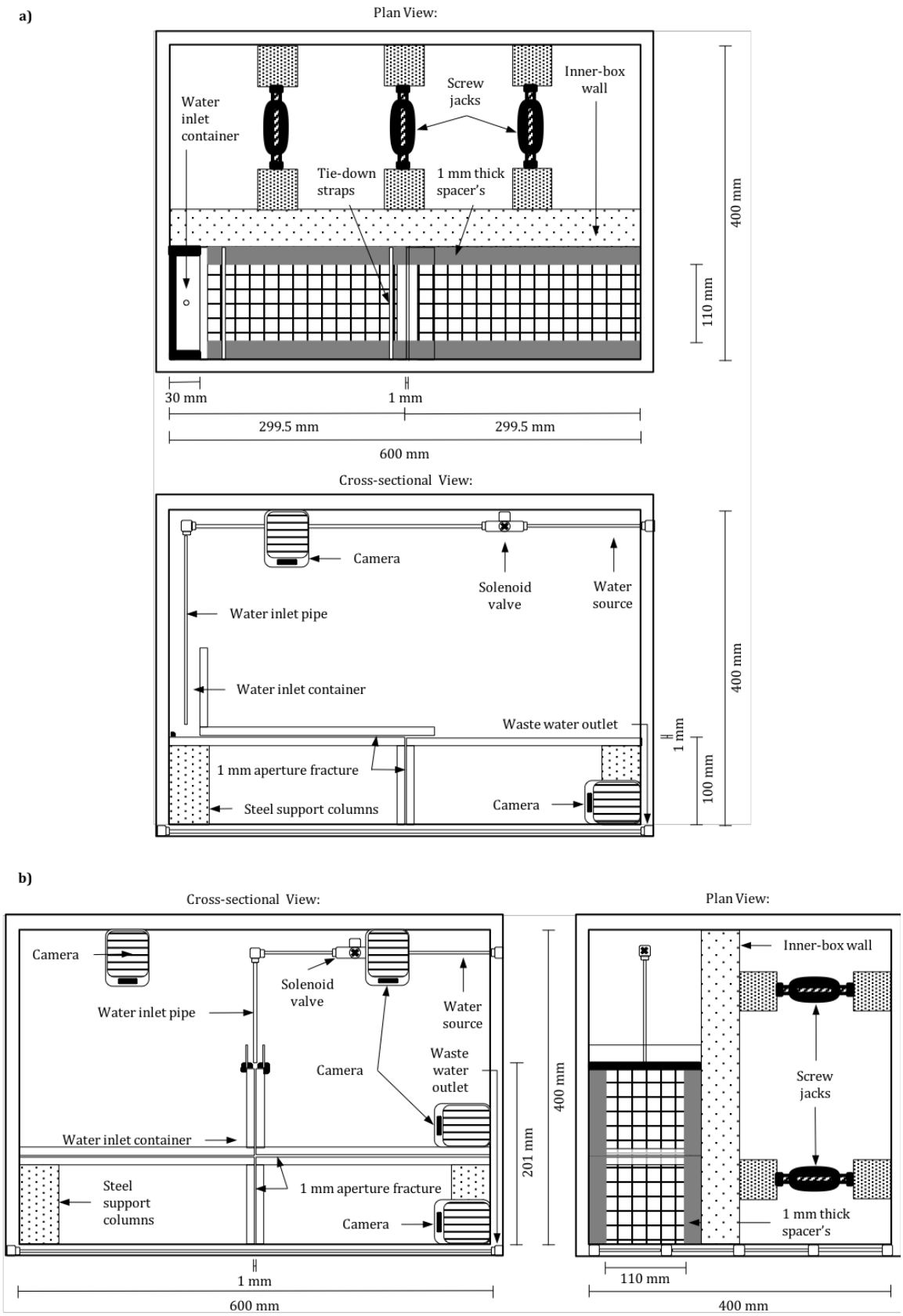

Figure 8-1. Test set-up for a) flow from a discrete horizontal fracture into an orthogonal intersection with a vertical fracture (Model 2-1); b) Flow from a discrete vertical fracture into an orthogonal intersection with a horizontal fracture (Model 2-2).

8.2.2 Procedure

8.2.2.1 Flow from the Horizontal Fracture (Model 2-1)

The following experiments were only tested under continuous flow conditions, in order to investigate if saturation of the vertical fracture would be achieved by the presence of an intersection and confinement (of the vertical fracture).

8.2.2.1.1 1g

The test begins when the solenoid valve is opened and an initial influx of 20 l/hr is allowed to enter the model. This is followed by 3-minute interval stepped influx increases, where an additional 20 l/h is added to the current flux rate until a total constant flux of 100 l/h is obtained for 3 minutes. The water is then closed and the system is allowed to drain for additional 3 minutes before repeating the same stepped flux procedure stated above, at shortened time intervals of 1 minute between increases.

8.2.2.1.2 20g

The completed model is accelerated to 20g and tested under continuous seepage conditions. The continuous seepage in dry fracture consists of opening the solenoid valve and allowing an initial influx of 20 l/hr (*400 l/hr*) into the model. This is followed by 1-minute (*6.67 hours*) interval stepped flux influx increases, where an additional 20 l/h is added to the current flux until a total constant flux of 100 l/h (*2000 l/hr*) is obtained for 1 minute. The water is then closed, and the system can drain for additional minute before repeating the same stepped continuous influx procedure stated above, at 30 seconds (*3.33 hours*) increase intervals.

The model is plagued by similar cavitation, which results in some capillary islands (air bubbles) in the horizontal fracture. Therefore, the visuals obtained from the camera and presented in the results are those during which there is a constant influx obtained for that specific influx interval.

8.2.2.2 Flow from the Vertical Fracture (Model 2-2)

8.2.2.2.1 1g

The completed model is tested under intermittent and continuous influx conditions. For intermittent influx tests on the vertical fracture, the solenoid valve is opened, and influx is introduced as individual droplets for 5 minutes at approximately 0.08 l/hr. Thereafter the intermittent rate is stepped up to approximately 0.5 l/hr, for 5 minutes. The intermittent tests are then stopped, the model dismantled, dried, and reassembled for the continuous influx test.

The continuous influx test consists of opening the solenoid valve and allowing an initial influx of 20 l/hr to enter the model. This is followed by 3-minute interval stepped flux influx increases, where an additional 20 l/h is added to the current flux rate until a total constant flux of 100 l/h

is obtained for 3 minutes. The water is then closed, and the system can drain for additional 3 minutes before repeating the same stepped flux procedure stated above, at shortened time intervals of 1 minute between increases.

8.2.2.2.2 20g

The completed model is accelerated to 20g and tested under intermittent and continuous seepage conditions. For intermittent seepage tests, the solenoid valve is opened, and influx is introduced as individual droplets for 3 minutes (*20 hours*) at approximately 0.6 l/hr, (*12 l/hr*). The intermittent test is not stopped, and instead the continuous influx tests are conducted immediately thereafter.

The continuous seepage into the initially dry fracture consists of opening the solenoid valve and allowing an initial influx of 20 l/hr (*400 l/hr*) into the model. This is followed by 1-minute (*6.67 hours*) interval stepped flux influx increases, where an additional 20 l/h (*400 l/hr*) is added to the current flux until a total constant flux of 100 l/h (*2000 l/hr*) is obtained for 1 minute. No rewetting phase is conducted. Similar cavitation in the inlet pipes occurs at higher flow influx intervals (>60 l/hr), and results are presented when a constant influx is achieved.

8.3 Results and Analyses

8.3.1 Flow from the Horizontal Fracture (Model 2-1)

8.3.1.1 1g

Wetting:

During wetting, the wetting front initially spreads irregularly from the point of inlet (Figure 8-2) and once confined between both spacers at 3 seconds, advances steadily toward the fracture intersection. The wetting front is preferentially lead by its contact with the left spacer, and upon reaching the intersection in 5.5 seconds, a single 7 mm wide rivulet cascades down the vertical fracture. The horizontal fracture does not fully saturate during the 20 l/h influx interval, with a large air pocket maintained above the intersection. The rivulet continues to be the only vertical flow feature during the 20 l/h influx interval. Despite the lack of full saturation of the horizontal fracture before the intersection, a constant head of 13 mm is maintained in the inlet container.

Upon increasing the influx to 40 l/h, the horizontal fracture fully saturates, and a second rivulet of 3 mm width forms along the opposing spacer within the vertical fracture. During the 40 l/h interval, a constant head of 16 mm is maintained in the inlet container. When the 60 l/h influx interval is initiated, a third rivulet of 8 mm width establishes in the centre of the vertical fracture. The rivulet oscillates and meanders for 8 seconds before it stabilises for the remainder of the influx interval. The oscillating of the rivulet occurs together with an invasion of a pool over the intersection into the opposing horizontal fracture, which also takes 8 seconds to establish. The constant head in the inlet container is at 23 mm for the 60 l/h interval, and thereafter increases to 24 and 25 mm for the 80 and 100 l/h influx intervals, respectively.

When the influx is increased to 80 l/h, the third middle rivulet widens to 11 mm, and again to 13 mm at the 100 l/h influx interval. Neither the first nor the second rivulet adjacent to the spacers widen during increasing influxes, and it is therefore evident that the central rivulet is carrying the increasing volume of fluid. By the 100 l/h influx interval, only 22% of the cross-sectional area of the vertical fracture is saturated, and transporting fluid. Although the horizontal fracture remains saturated from 40 l/h influx and all subsequent intervals thereafter, flow down the vertical fracture occurs only at three discrete points, as aperture-spanning continuous rivulets.

Drying and Rewetting:

When the water influx is stopped, the central rivulet is the first feature to cease flowing. This occurs almost immediately. The outer rivulets are the last to disappear, while slow hysteric drainage occurs for the water trapped within the spacer. In addition to the remnant static droplets, a large air pocket invades the fracture from the inlet container while a smaller air pocket enters from the intersection. Upon rewetting at 20 l/h, an irregular wetting front invades the air pocket from the inlet container. This wetting front splits the air into smaller air pockets in the horizontal fracture. Some static pockets of air remain in the fracture and form capillary islands while others move parallel to the direction of flow. Some of the capillary islands are mobilized only as the influx rate is increased. A single capillary island remains static throughout the rewetting intervals.

At the vertical fracture, the outer two-rivulet paths at the spacers remobilize, with a single pulsed flow occurring at the location of the central third rivulet at the beginning of the interval. The central rivulet is fully remobilized only at the beginning of the 40 l/h influx interval. During the 40 l/h interval two distinct contact angles are observed occurring on the opposing vertical fracture walls. Here, a wide film is evident against the back wall of the vertical fracture, while a narrower rivulet is observed against the front wall of the fracture. It is, however, likely that the flow of fluid is nevertheless aperture-spanning. Similar oscillating and meandering of the central rivulet is seen after the influx is increased for each subsequent interval.

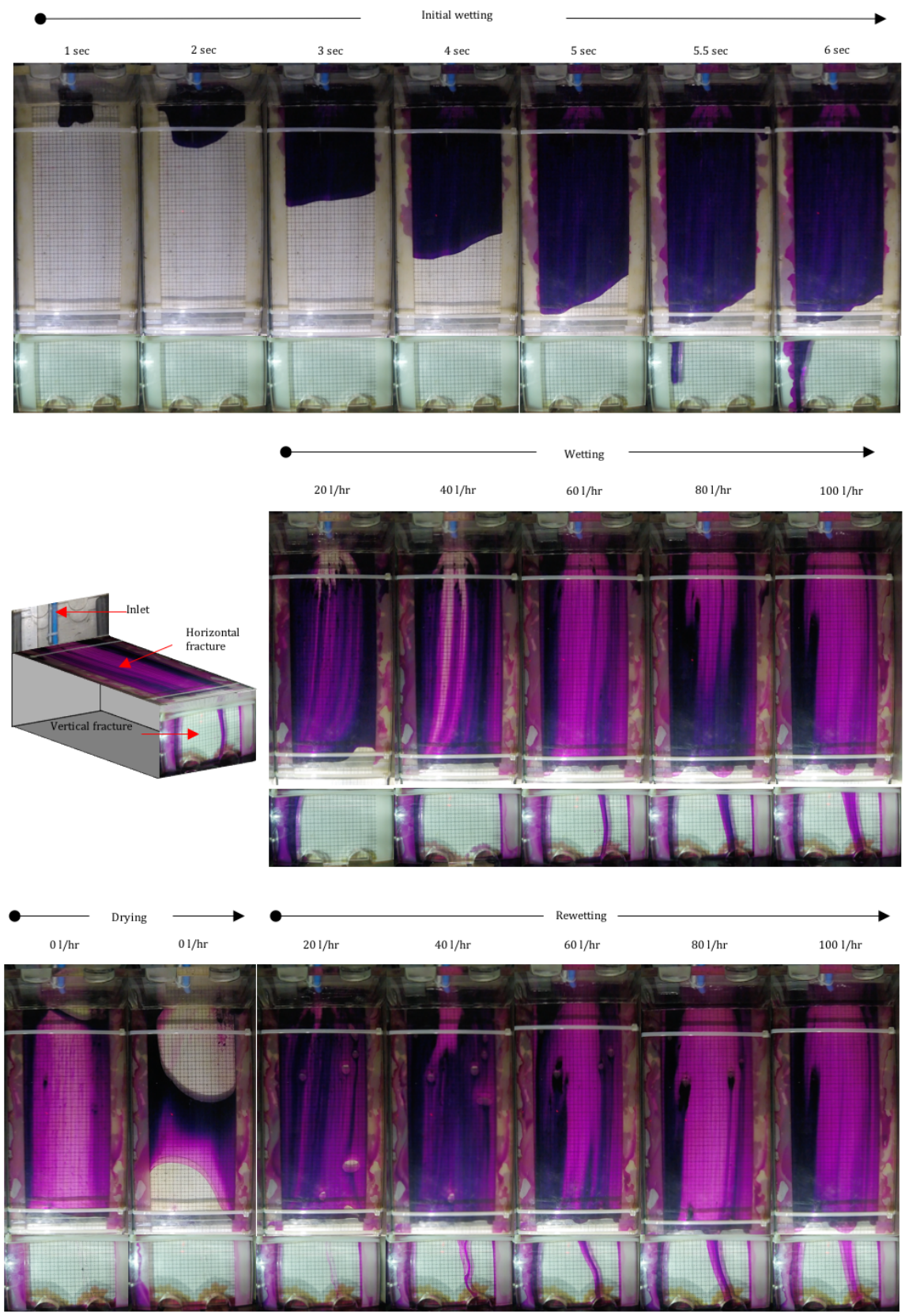

Figure 8-2. Invasion of the initial wetting front at 20 l/hr in horizontal fracture and screenshots of the horizontal fracture and vertical fracture for the continuous flow experiment at each interval during Model 1-1 at 1g.

8.3.1.1.1 Linear Velocities and Volumetric Fluxes

Using the observed heads for each influx interval in the Model 2-1 at 1g, the volumetric flux and linear velocity for the horizontal fracture can be calculated using the equations as outlined by Singhal and Gupta (2010). Then, by using the continuity principle, the linear velocity of the vertical exit fracture can be deduced. The calculated volumetric flow rate (Q_f) and linear velocity for both the horizontal fracture (V_h) and the vertical fracture (V_v) are shown in Figure 8-3, where a linear relationship exists between Q_f and Vh, but a less clear polynomial relationship exists between Q_f and V_h.

However, the degree of saturation along the vertical fracture is dependent on the volumetric flux (Q_f), thereby influencing the vertical linear velocity by controlling the cross-sectional drainage area, where higher degrees of saturation result in larger cross-sectional areas. Employing this reasoning and the continuity principle with the horizontal linear velocity, results in the vertical linear velocity obtaining a wide range of values for all possible degrees of saturation as shown in Figure 8-4.

Results indicate that lower degrees of saturation results in a pressure reduction immediately and therefore an associated velocity increase and decrease in head-elevation, which leads to large variation in vertical linear velocity. However, as the degree of saturation increases, the influence of different influx rates does not affect the calculated vertical linear velocity as they appear to approach a constant range, and this explains the relationship in Figure 8-4.

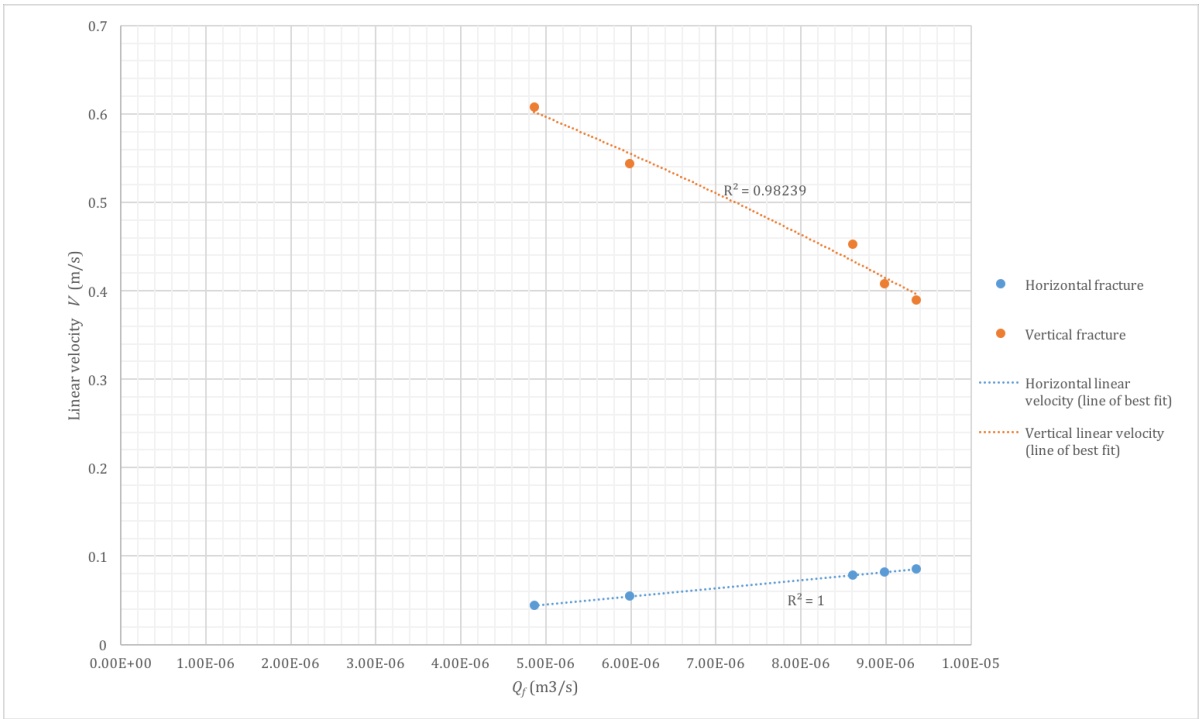

Figure 8-3 Relationship between the volumetric flux and the average linear velocity for the horizontal and vertical fractures, assuming the continuity principle.

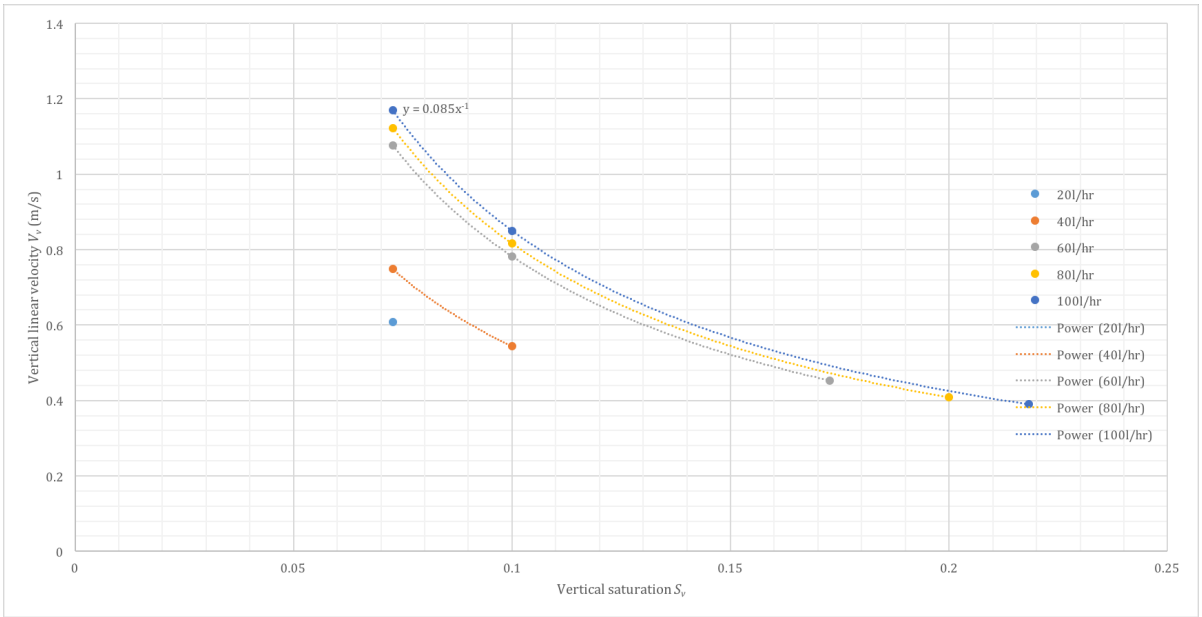

Figure 8-4. Possible vertical linear velocity calculations for all outflow scenarios (from a single rivulet to all observed rivulets).

8.3.1.2 20g

Wetting:

The wetting front initially spreads irregularly and saturates the entire fracture at 0.90 seconds (*6 minutes, at prototype scale*) as shown in Figure 8-5. During the 20 l/hr interval, an approximately 3 mm (*60 mm*) wide oscillating rivulet is present on the vertical fracture together with an additional narrow rivulet against the opposing side of the vertical fracture, against the spacer. Episodic influx during the 20 l/hr interval (due to cavitation occurring in the inlet pipe during the testing procedure) leads to occasional oscillating rivulets in the centre of the fracture.

During the 40 l/hr influx interval, two oscillating rivulets establish on the vertical fracture, whilst the left rivulet within the vertical fracture converts to an approximately 15 mm (*300 mm*) film. Fluid has accumulated onto the opposite side of the horizontal fracture, signifying that it moved across the intersection. This is due to the initial large influx of water wetting the fracture. This is exemplified during the 40 l/hr interval when it occurs again. There seems to be no significant flow into the opposite side of the intersection of the horizontal fracture thereafter.

The rivulet on the left widens to form a film of approximately 30 mm width at 60 l/hr. Additionally, three oscillating rivulets form in the middle portion of the vertical fracture, and the rivulet on the right side of the vertical fracture widens to 10 mm (200 *mm*). At 80 l/hr the films on either side of the fracture have again widened, whilst the central rivulets have amalgamated to form a third wide film of 10 mm (*200 mm*) width. Further increasing the influx results in the widening of the rivulets until 100 l/hr at which point the 2 wide films are present on the vertical fracture. Due to the resultant force, throughout all intervals, the film-flow at the vertical fracture sweeps to the right.

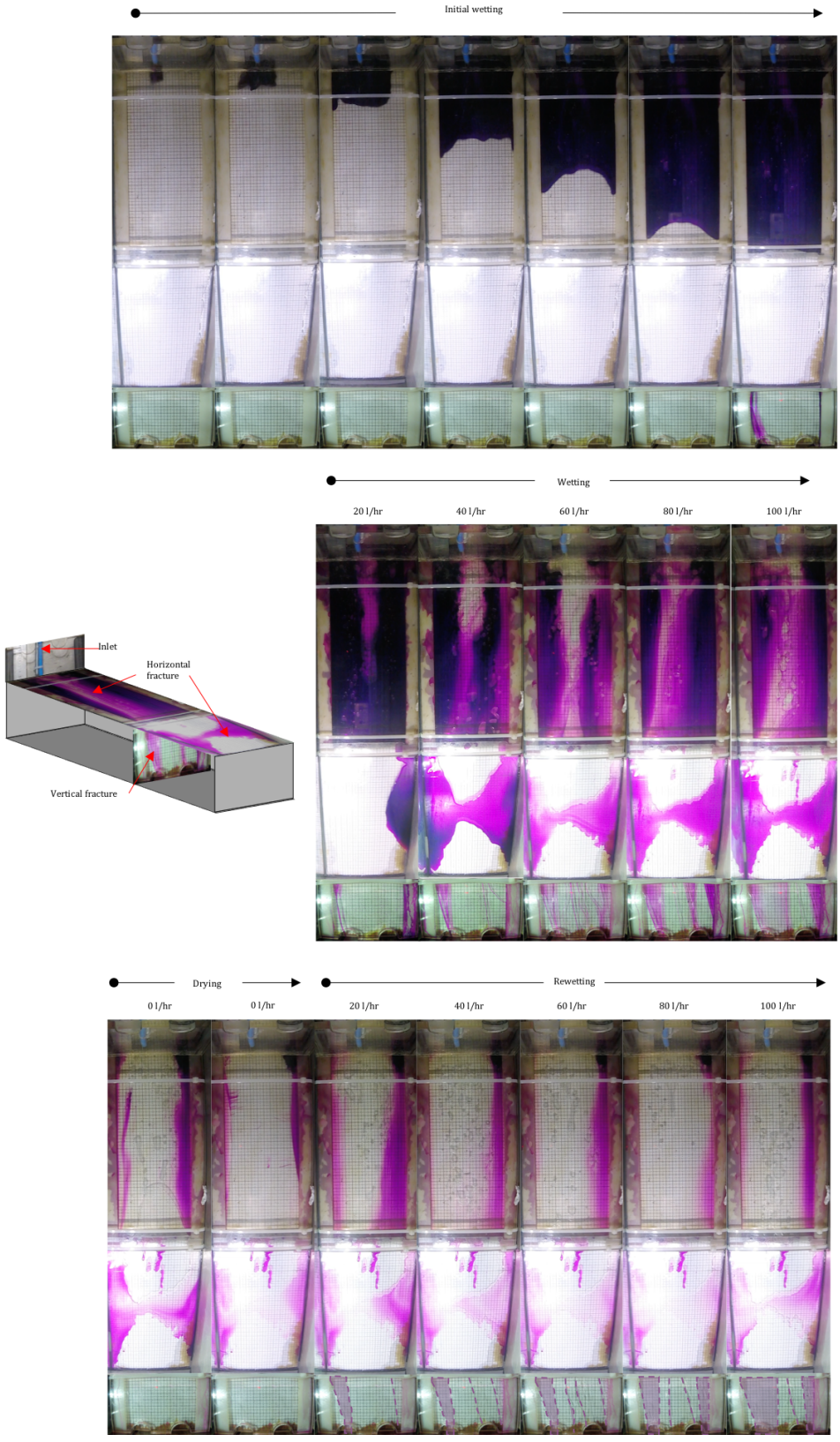

Figure 8-5. Invasion of the initial wetting front at 20 l/hr in horizontal fracture and screenshots of the horizontal fracture and vertical wall for the continuous flow experiment at each interval during the Model 2-1 at 20g.

Drying and Rewetting:

During the entire drying interval, the films and rivulets disappears, as an air pocket invades the horizontal fracture from the intersection. Some rivulets associated with the spacers hysterically drain a decreasing volume of water but never disappears. Upon rewetting, the air intrusion is mobilized. Despite when some of the trapped air pockets mobilise out of the horizontal fracture, the fluid exiting along the vertical fracture follows the same flow mechanism as previously observed for all influx intervals.

8.3.2 Flow from the Vertical Fracture (Model 2-2)

8.3.2.1 1g

8.3.2.1.1 Intermittent Influx

The flow mechanisms observed during the intermittent influx is shown as snapshots in Figure 8-6. An initial air-water meniscus in the form of a sliding droplet with an approximate volume of 0.09 ml initially invades into the vertical fracture, with a thread that does not snap above the intersection. As the sliding droplet passes the intersection and advances through the vertical fracture beneath, the thread snaps and leaves a path of remnant static droplets on the vertical fracture below the intersection. Throughout the intermittent testing interval, the thread above the intersection does not snap, whilst the vertical fracture below the intersection is characterized by a discontinuous path of snapping sliding droplets snap that behind leave static droplets on the fracture wall.

Invasion of the horizontal fracture occurs into the intersection as seen at 305 seconds into the test. At the same time, the character of the discontinuous path of sliding droplets on the vertical fracture below the intersection changes. Here, a new droplet invades a new discontinuous path of sliding droplets adjacent to the existing one. This occurs as the capillary barrier at the intersection, causes a lateral spreading along the intersection and encourages a subsequent invasion at a new entry point.

After 310 seconds, the flow rate is increased slightly, introducing a discrete droplet to the model more frequently. This increase corresponds to elongated threads (as seen at 326 seconds in Figure 8-6, instead of prominent air-water meniscus droplets advancing with a narrow thread behind. From 420 seconds, there is significant ponding within the horizontal fracture. The ponding is due to the increased wetting of the intersection. For the experiment, the maximum pool height (as calculated by the method of Ji et al., 2006) is 3.34 mm and a minimum height is 1.42 mm.

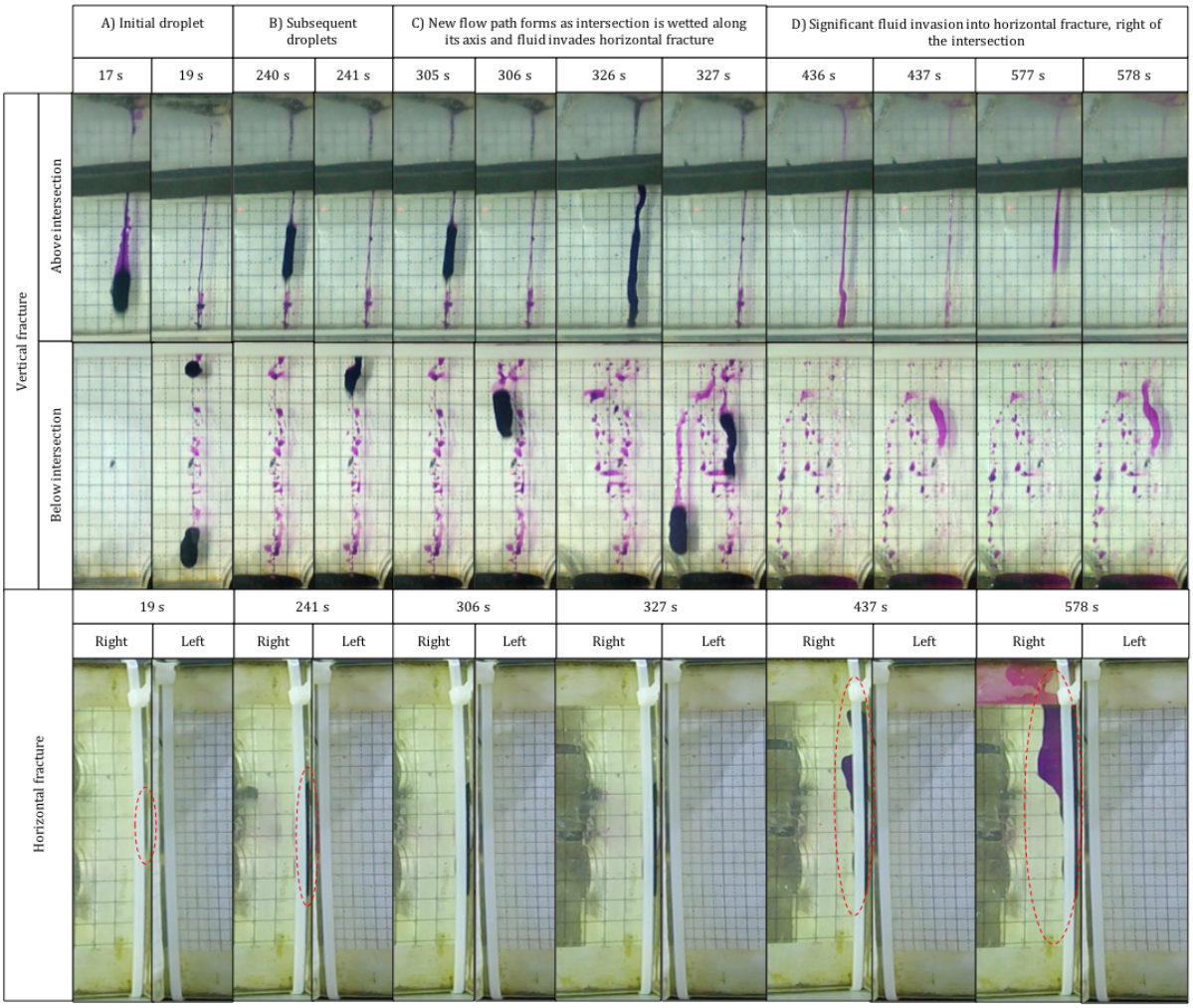

Figure 8-6. Flow mechanisms observed in the orthogonal intersection with flow from the vertical fracture above the intersection (Experiment 3-2) for the intermittent influx at 1g.

8.3.2.1.2 Continuous Influx

The flow mechanisms observed in the non-inclined orthogonal intersection with flow from the vertical fracture is shown in Figure 8-7.

Wetting:

During the continuous flow test at 20 l/hr, three rivulets oscillate throughout the vertical fracture. The oscillating and meandering of these rivulets leads to significant flow switching and amalgamations of flow paths. At the next influx interval of 40 l/hr, the central rivulet widens to 10 mm width. Occasionally oscillating rivulets and sliding droplets are also observed throughout these subsequent influx intervals. At 100 l/hr the rivulet has widened to form a film of 25 mm width.

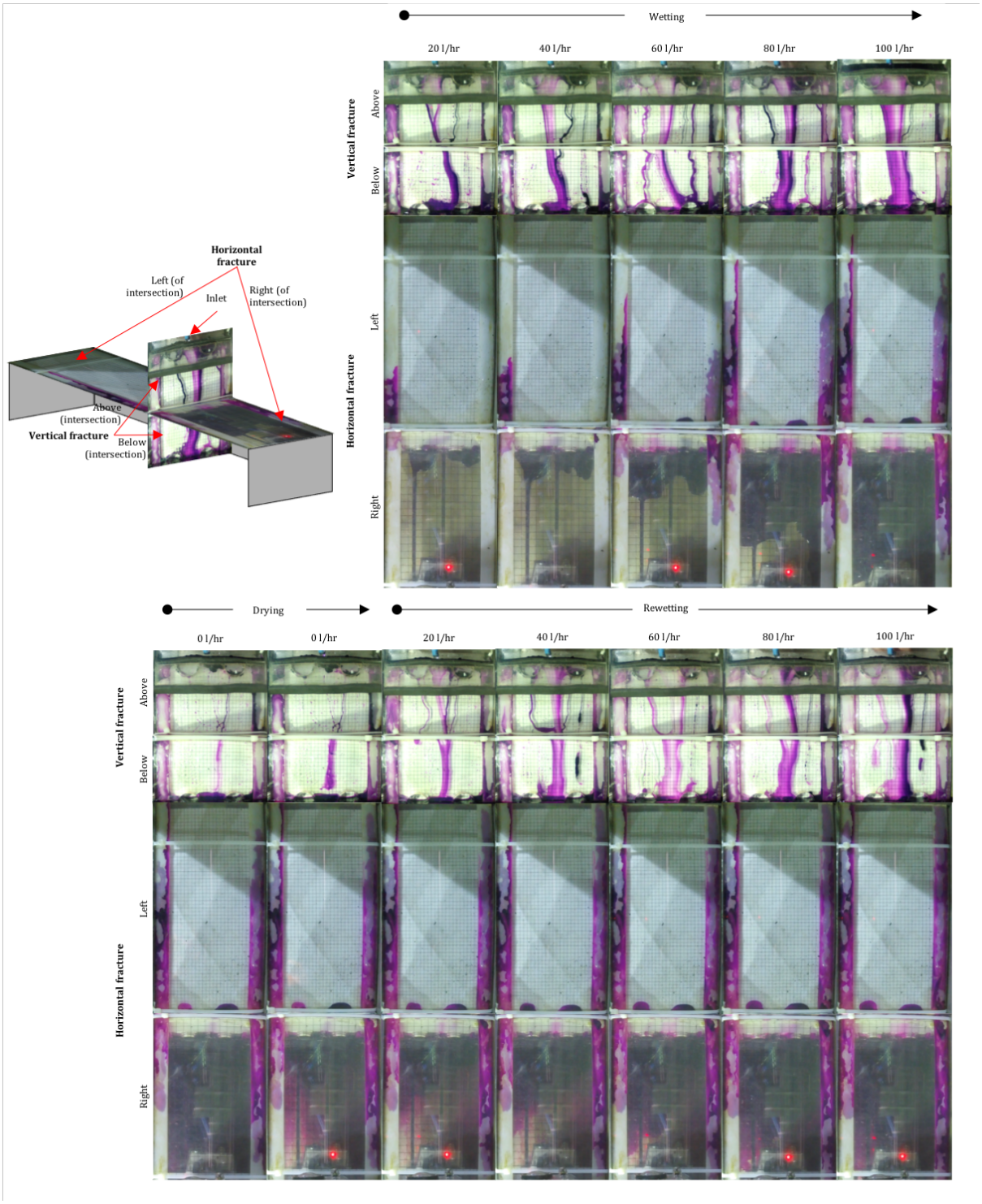

Figure 8-7. Flow mechanisms observed in the non-inclined orthogonal intersection with flow from the vertical fracture (Model 2-2) for the continuous influx at 1g.

Ponding into the horizontal fracture is seen occurring from 20 l/hr, and becomes prominent by 100 l/hr, where 1.55 ml has accumulated in the horizontal fracture. The fluid pool in the horizontal fracture does not occur where the main flow path is, but rather where a smaller rivulet carrying a smaller flux of water. Larger influxes do not lend themselves to invasion into large aperture open fractures. This is becomes more apparent when comparing how much

fluid invaded the horizontal fracture during the intermittent test. Moreover, significant invasion into horizontal spacers is observed, likely attributed to the smaller aperture between the spacers and the Plexiglas sheets which results in capillary-dominated flow.

Drying and Rewetting:

During the drying interval, the central rivulet as well as the central wide film never disappears. This is likely due to the pool of fluid above the inlet container as well as within the fracture supplying a low flow rate to these features. However, the ponds of water as seen in the horizontal fracture are not observed to shrink, and as such it is assumed that these ponds remain stagnant and non-conducting. During the rewetting interval at 20 l/hr there is no continuity of smaller left rivulet, as it is truncated on the pond in the horizontal fracture. Additionally, an air pocket is trapped on the vertical fracture below the intersection.

8.3.2.1.3 Relationship between Vertical Flow and Lateral Fluid Accumulation

Readings taken at regular intervals are used to calculate the volume of fluid in the horizontal fracture during the intermittent test of Model 2-1. This was compared against the cumulative volume that had passed through the vertical fracture. Any flow within the spacer is ignored as it is assumed that flow into the spacers is capillary controlled. Figure 8-8 shows this relationship between the cumulative volume of fluid passing through the vertical fracture before the intersection against the cumulative volume of fluid in the horizontal fracture for the intermittent influx test, and the continuous influx intervals test.

The data shows that high continuous influxes do not lend themselves to invasion into large aperture open fractures. This is because gravitational forces increase in the flow path, which result in fluid flowing in the direction of gravity. In contrast, at lower flow rates fluid flow is capillary-dominated, compared to gravitational forces, and as such fluid is encouraged to enter the horizontal fracture at the intersection.

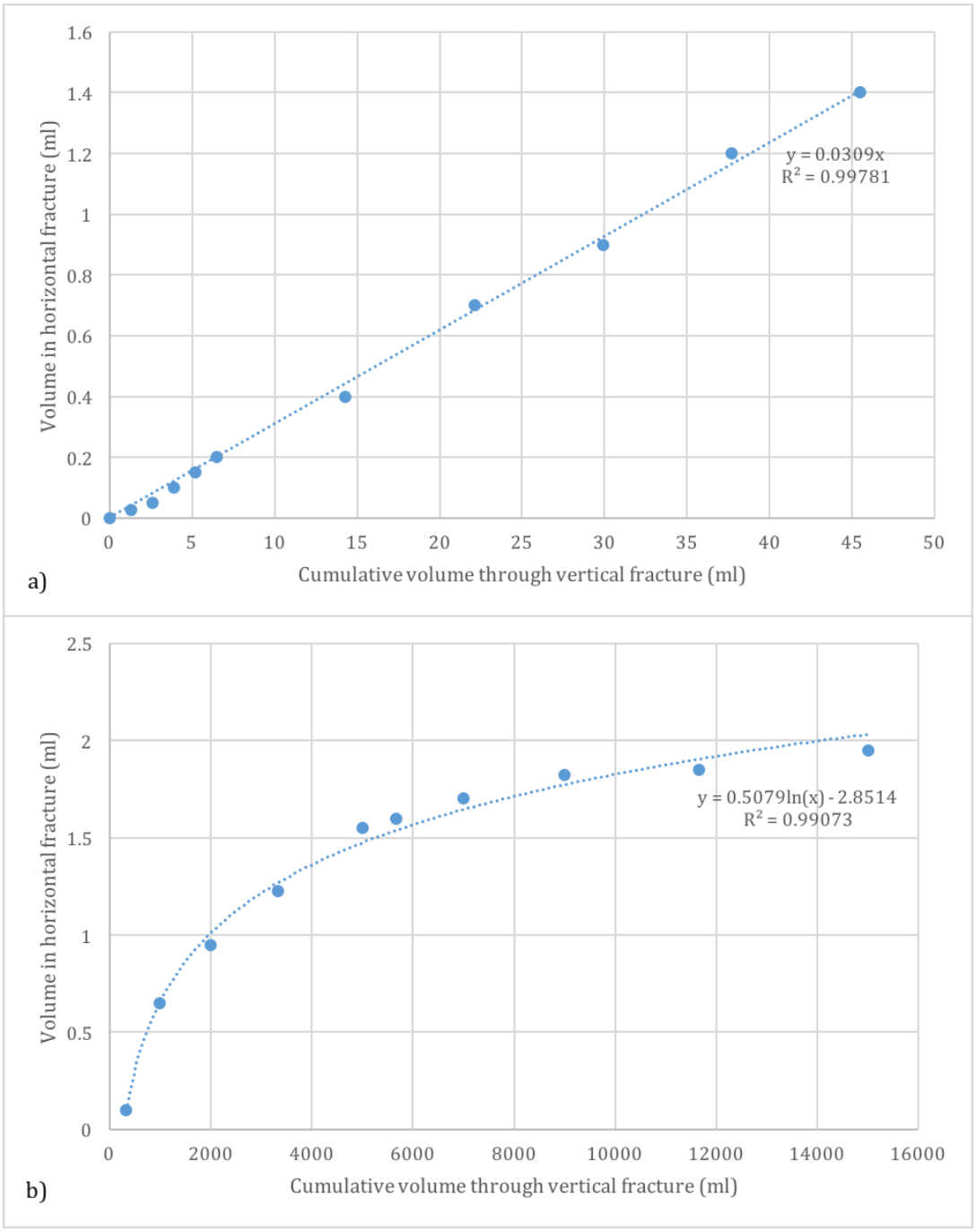

Figure 8-8. Relationship between cumulative volume passing through the vertical fracture, and the total volume in the horizontal fracture for flow from the vertical fracture into the intersection (Experiment 3-2) at 1g, for both the a) intermittent flow test, and b) the continuous flow test.

8.3.2.2 20g

8.3.2.2.1 Intermittent Influx

The observed flow behaviour of this and the influx once the test had begun, is shown in the Figure 8-9. During the process of accelerating the centrifuge to 20g, a small volume of water leaks from the inlet pipe, and is introduced onto the model before the intermittent test begins.

The invading droplet path is observed as a path comprising a continuous rivulet that ceases to become a discontinuous path of sliding droplets, that subsequently releases a droplet at the point of cessation of the continuous rivulet. This continuous-discontinuous point of the fluid path progressively lengthens down the vertical fracture until it reaches the intersection, at approximately 60 seconds into the intermittent test.

In several instances, the observed vertical flow paths that occur above the intersection are not always continued as a direct path below the intersection of the vertical fracture. Instead the flow path appears elsewhere (i.e. not directly beneath h the flow path above the intersection). This is due to the fluid wetting the intersection along its axis, in the form a lateral accumulation of fluid. The fluid flows vertically down its path above the vertical fracture, and once reaches this fluid pool at the intersection, the subsequent release of fluid from the pool occurs from another point within the fluid pond. The lateral accumulation of fluid into horizontal fracture from the intersection does not exceed 5 mm in length (*100 mm, at prototype scale*) for the premature flow path, whilst the discontinuous flow path during the intermittent test has a small pond of water less than 2 mm length (*40 mm*).

8.3.2.2.2 Continuous Influx

During the continuous influx test, only a small amount of fluid invades the right spacer on the right horizontal fracture, as seen in Figure 8-9, during the 20 l/hr influx interval. This is due to capillary-dominated flow supplied from a rivulet that oscillates across the spacer. During the 40 l/hr influx interval there is a much larger influx that invades the horizontal fracture, and likely initiated by the already wet spacer and its associated capillary forces, as smaller aperture fractures will wet first because the entry pressure required to break the capillary barrier is less. This invasion is a result of an oscillating rivulet, which crosses this portion of the intersection. During the subsequent wetting intervals, there is no further invasion into the horizontal fracture from the intersection, as the flow paths do not oscillate over this area of previous invasion.

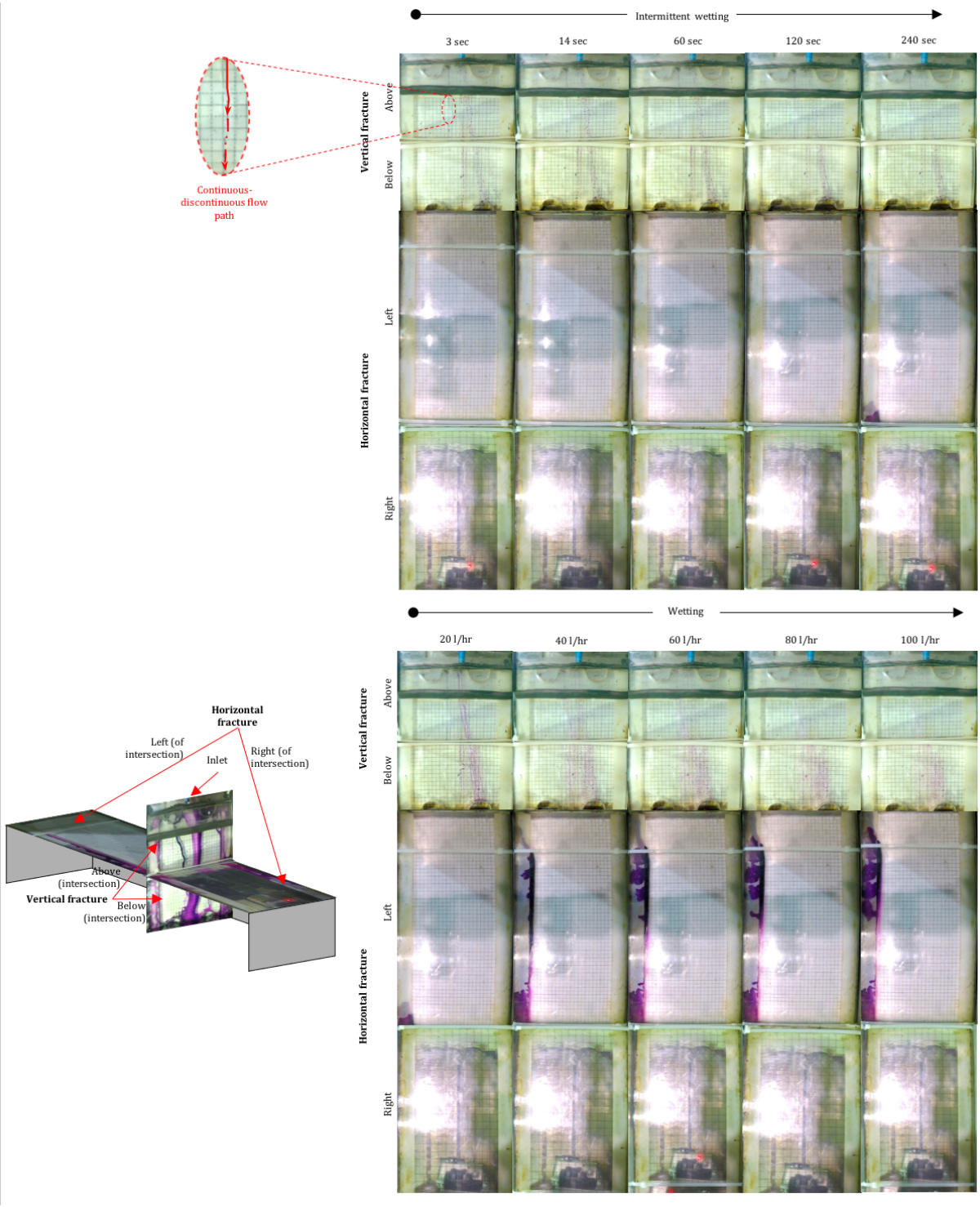

Figure 8-9. Flow mechanisms observed in the orthogonal intersection with flow from the vertical (Model 3-2) for the intermittent and continuous influx at 20g.

8.4 Summary

Experiments presented in previous chapters have focused on defining the most fundamental concepts of the vadose zone. The experiment outlined in this chapter built on these fundamental concepts, by investigating flow at non-inclined fracture intersections. The set of

experiments found that draining of a saturated horizontal fracture occurs by wider preferential capillary flow paths in the test with an intersecting vertical fracture, in comparison with test previously conducted with an unconfined vertical wall. Flow into a non-inclined open fracture intersection tends to accumulate parallel with axis of the intersection, instead of growing and receding pool heights as observed for smaller aperture models.

CHAPTER 9 EXPERIMENT 3: INCLINED ORTHOGONAL FRACTURE INTERSECTIONS

9.1 Introduction

The behaviour of variably saturated flow at fracture intersections will be controlled by competition between capillary, gravitational, viscous, and inertial forces (Wood et al., 2005). The balance between these forces will be highly dependent on intersection geometry with geometric variables that will influence unsaturated flow that includes the angle of intersection (see Wood et al., 2005). The aim of the experiments presented in this chapter is to investigate the role that the inclination of a fracture intersection has on variably saturated flow mechanisms. The aim is achieved by constructing a similar set of orthogonal intersections but inclined at an angle of 23° from the horizontal. Flow conditions are altered such that fluid is introduced from both above the intersection (from an inclined sub-vertical fracture) as well as up-dip of the intersection (from an inclined sub-horizontal fracture) over intermittent and continuous flow conditions.

9.2 Experiment-Specific Methodology

9.2.1 Set-up

9.2.1.1 Flow from the Inclined Sub-Horizontal (ISH) Fracture (Model 3-1)

Model 3-1 comprises an inclined sub-vertical (ISV) fracture measuring 201 mm length × 110 mm width, orthogonally interested by an inclined sub-horizontal fracture (ISH) measuring 600 mm × 110 mm width, inclined at 23° from the horizontal. Both fractures have a constant aperture of 1 mm maintained by spacers of 20 mm width on either side of the fracture, and assuming saturated conditions this results in a hydraulic conductivity (K_f) of 9.18×10^{-1} m/s, and permeability (k_f) of 8.33×10^{-8} m^2.

The model is constructed using four L-section Plexiglas acrylic sheets, of which two Plexiglas sheets placed opposing one another and the other two placed opposing each other and being inverted. Cable tie-down's are used to secure the 4 sets of L-sections to one another during the test. The model is then placed on the 23° concrete base. The compete set-up is illustrated in Figure 9-1a.

A 5 mm x 5 mm grid is used to assess the geometry of the flow mechanisms on the ISV fracture, above and below the intersection. Similarly, a 5 mm x 5 mm grid is placed facing upwards, on the bottom side of the ISH fracture up-dip and down-dip of the intersection. A back plate is installed in the strongbox and three screw jacks confine the fracture against the window and back plate, where a water inlet container is constructed around the entrance to the horizontal fracture in the left corner. Foam sealant tape is placed around the interior and

exterior perimeter of the water inlet container to maintain a watertight seal where potassium permanganate crystals are scattered to colour the water.

Two cameras are placed on an overhead bracket on either side of the intersection above the ISH fracture, while a third camera is placed on the right base of the model, and a fourth above the right horizontal fracture, observing the ISV fracture, above and below the intersection, respectively. A water inlet pipe and a solenoid valve are installed above the container while an outlet pipe is installed at the base of the model.

9.2.1.2 Flow from the Inclined Sub-Vertical (ISV) Fracture (Experiment 3-2)

Model 3-2 comprises a vertical fracture measuring 201 mm length × 110 mm width, interested by an orthogonal horizontal fracture measuring 600 mm × 110 mm width, inclined at 23° from the horizontal. In the same manner as Model 3-1, both fractures have a constant aperture of 1 mm maintained by spacers of 20 mm width on either side of the fracture with the same characteristic hydraulic conductivity (K_f) and permeability (k_f).

Two Plexiglas sheets placed opposing one another and the other two placed opposing each other and being inverted. Cable tie-downs are used to secure the 4 sets of L-sections to one another during the test. The model is then placed on the 23° concrete base. The compete set-up is illustrated in Figure 9-1b.

In a similar manner as in the previous experiment, 5 mm x 5 mm grids are placed to assess the flow path geometry, the back plate is installed, sealed water inlet container; potassium permanganate crystals scattered; water inlet pipe; and solenoid valve are installed.

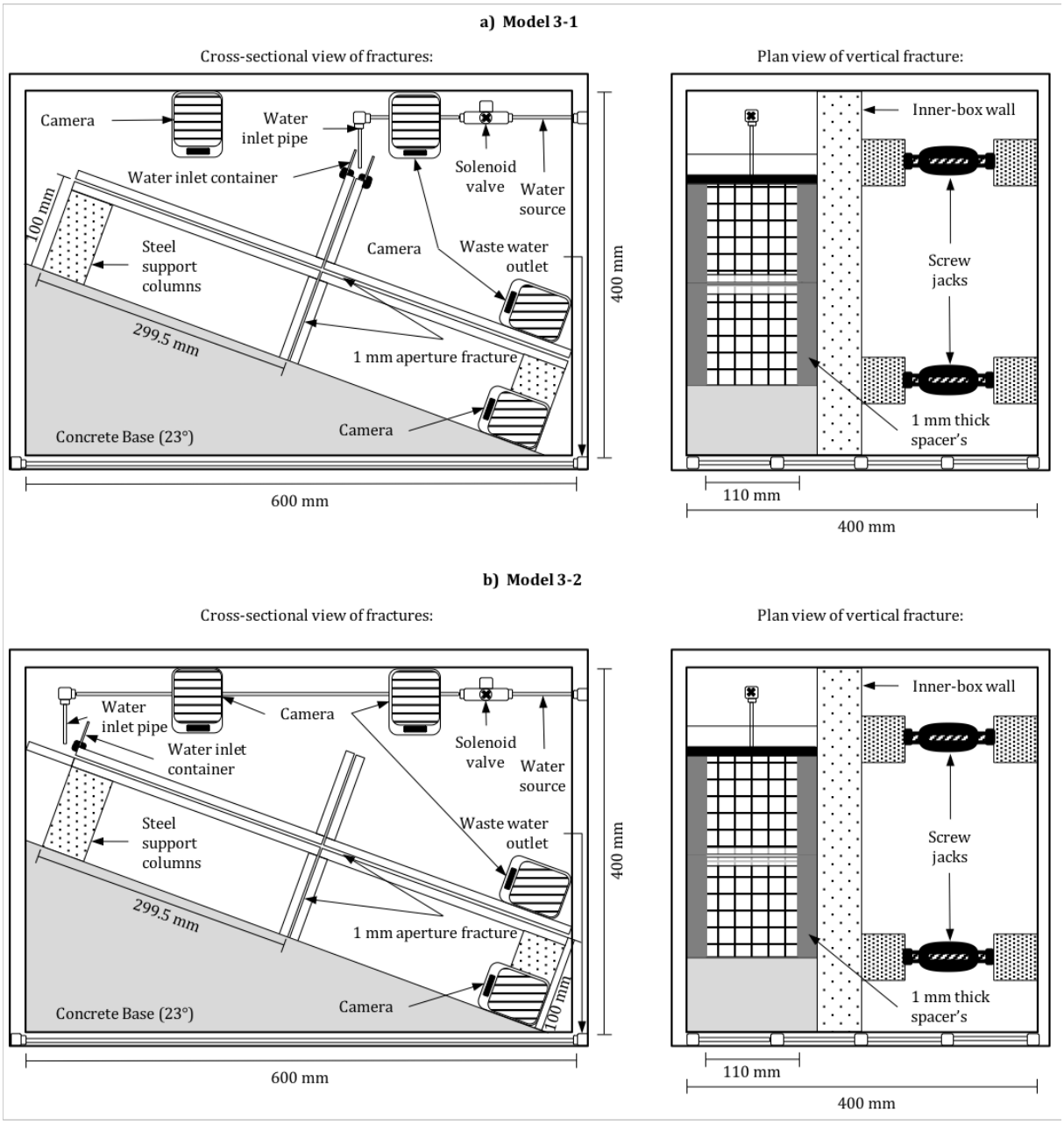

Figure 9-1. Test set-up for: a) flow from a discrete inclined sub-horizontal fracture into an intersection (Model 3-1); and b) flow from a discrete inclined sub-vertical fracture into an intersection (Model 3-2).

9.2.2 Procedure

9.2.2.1 Flow from the Inclined Sub-Horizontal (ISH) Fracture (Model 3-1)

9.2.2.1.1 1g

The completed model is tested under intermittent and continuous influx conditions. For the intermittent influx test, the solenoid valve is opened, and influx is introduced as individual droplets for 3 minutes at an influx of approximately 0.3 l/hr. Thereafter, the continuous influx is started by opening the solenoid valve and allowing an initial influx of 20 l/hr to enter the

model, for 1 minute. The water is then closed and the system can drain for 1 minute before repeating the same procedure by rewetting with an intermittent influx for 2 minutes, and then a continuous influx of 20 l/hr for 1-minute.

9.2.2.1.2 20g

The completed model is accelerated to 20g and tested under intermittent and continuous seepage conditions. For the intermittent influx test, the solenoid valve is opened and influx is introduced as individual droplets for 2 minutes (*13.3 hours, at prototype scale*) at an influx of approximately 0.6 l/hr (*12 l/hr*). Thereafter, the continuous influx is started by opening the solenoid valve and allowing an initial influx of 20 l/hr (*400 l/hr*) to enter the model for 1 minutes (*6.67 hr*). The water is then closed and the system is allowed to drain for 1 minute before repeating the same procedure by rewetting with an intermittent influx for 2 minutes, and then a continuous influx of 20 l/hr for 1-minute.

9.2.2.2 Flow from the Inclined Sub-Vertical (ISV) Fracture (Experiment 2-2)

9.2.2.2.1 1g

The completed model is tested under intermittent and continuous influx conditions. The intermittent influx begins by opening the solenoid valve and introduced fluid as individual droplets for 3 minutes at approximately 0.5 l/hr. This results in a droplet with a volume of approximately 0.13 ml every 3 seconds. Following the intermittent influx, the continuous influx is started by opening the solenoid valve and allowing an initial influx of 20 l/hr to enter the model, for 1-minute. This is followed by a 1 minute interval at 40 l/hr. The water is then closed and the system is allowed to drain for 1 minute before repeating the same stepped flux procedure stated above.

9.2.2.2.2 20g

The completed model is accelerated to 20g and tested under intermittent and continuous seepage conditions. The intermittent influx test starts by introducing fluid as individual droplets for 2 minutes (*13.3 hours, at prototype scale*) at an influx of approximately 0.8 ml/hr (*16 l/hr*). The continuous influx starts thereafter by opening the solenoid valve and allowing an initial influx of 20 l/hr (*400 l/hr*) to enter the model for 1 minutes (*6.67 hr*). This is followed by a 1minute (*6.67 hr*) interval at 40 l/hr (*800 l/hr*). The water is then closed and the system is allowed to drain for 1 minute before rewetting the model by repeating the same procedure as stated above.

9.3 Results

9.3.1 Flow from the Inclined Sub-Horizontal (ISH) Fracture (Model 3-1)

9.3.1.1 1g

The flow mechanisms observed during the experiment are shown in Figure 9-2.

9.3.1.1.1 Intermittent Influx Wetting

The first initial droplet makes contacts with the intersection, and spreads parallel with the axis of the intersection. Thereafter a breach occurs into the ISV fracture and a sliding droplet emerges in the vertical fracture below the intersection, 2 seconds thereafter. This is followed immediately by the formation of second flow path of discontinuous sliding droplets in the ISV fracture below the intersection. The pioneer droplet that travels along the flow path within the ISH fracture above the intersection path has a volume of 0.845 ml, whilst the volume of the sliding droplets below the intersection within the ISV is 0.450 ml and 0.250 ml respectively. This suggests that only 78% of the volume of the pioneer droplet above the intersection is accounted for below the intersection.

This percentage decreases to approximately 25% in the proceedings droplets. A third path of discontinues sliding droplets forms within the ISV fracture below the intersection 27 seconds after the first. This feature of a single flow path in the ISH fracture up-dip of the intersection, occurs with 3 flow paths in the ISV fracture below the intersection. This indicates lateral accumulation and spreading of the fluid along the intersection. Here, a pool of fluid spreads laterally as the droplet contacts the intersection, allowing a wider portion of fluid to form a locality for a droplet to breach into the ISV fracture. The second discontinuous flow path in the ISV fracture below the intersection (on the right) ceases to be used as a path for droplets after approximately 17 seconds with only 3 droplets passing along this flow path. Thereafter the first (middle) and third (left) paths are the only routes that transport fluid supplied from the intersection.

Approximately 140 seconds into the intermittent experiment a continuous rivulet establishes from the third flow path (left) on the ISV fracture, and is likely supplied by the pool of fluid before the intersection. The continuous rivulet snaps after approximately 12 seconds as the amount of water available to ensure its continuity is not capable of keeping the rivulet a continuous flow path. By 200 seconds into the intermittent influx interval, the lateral accumulation of the pool of fluid has spread across the entire length of the intersection entrance. At this point, the continuous rivulet re-establishes itself as the fluid pond can supply a constant volume of water to ensure the rivulet does not snap. Throughout the wetting intermittent influx interval, the droplets in the ISH fracture up-dip of the intersection follow a single flow path

9.3.1.1.2 Continuous Influx Wetting

At the start of the continuous influx interval at 20 l/hr, a pressure build-up releases a larger volume of water than the intended 20 l/hr. The ISH fracture is almost saturated, with several trapped air pockets (capillary islands) within it. This large volume of water initially introduced, causes a portion of fluid to cross the intersection and form 2 continuous oscillating rivulets on the lowers ISH fracture. This larger influx disappears after 5 seconds, where a stable 20 l/hr influx is obtained from the inlet pipe.

The rest of the 20 l/hr interval is characterised by oscillating rivulets in the upper ISH fracture, with fluid passing through the intersection and into the ISV fracture below the intersection.

Continuous rivulets and discontinuous paths of sliding droplets characterise the flow mechanisms in this fracture. Towards the end of the continuous influx interval (52 seconds) an oscillating rivulet contacts the left spacer and causes a volume of water to cross the intersection and move down the ISH down-dip of the intersection.

9.3.1.1.3 Drying and Rewetting

During the drying interval, it takes approximately 6 seconds for the rivulet in the ISV fracture to become extinct with remnant static droplets along the ISV fracture. This is a function of the diminishing volume of the fluid in the pond at the intersection. During the intermittent influx rewetting interval, fluid flows in the ISV fracture below the intersection along the spacer, and not within the aperture of the open fracture itself. The lateral ponding of fluid along the intersection at the base of ISH fracture up-dip of the intersection, remobilizes quicker due to the easier wettability of the material as static pools of water remain from the previous wetting phase. This is a function of the wettability combined with the small aperture of the spacer, which retains water longer than the larger 1 mm aperture, and subsequently drains longer, resulting in a hysteric behaviour.

When the droplets are reintroduced, they encounter the capillary barrier of the intersection, and flow laterally along the width of the intersection through the static fluid pond, before moving downwards along the spacer in the inclined sub-vertical fracture below the intersection. Once again during the continuous influx rewetting phase, towards the end of the interval, flow occurs on the ISH fracture down-dip of the intersection. Generally, similar flow mechanisms of rivulets and sliding droplets are observed within the model.

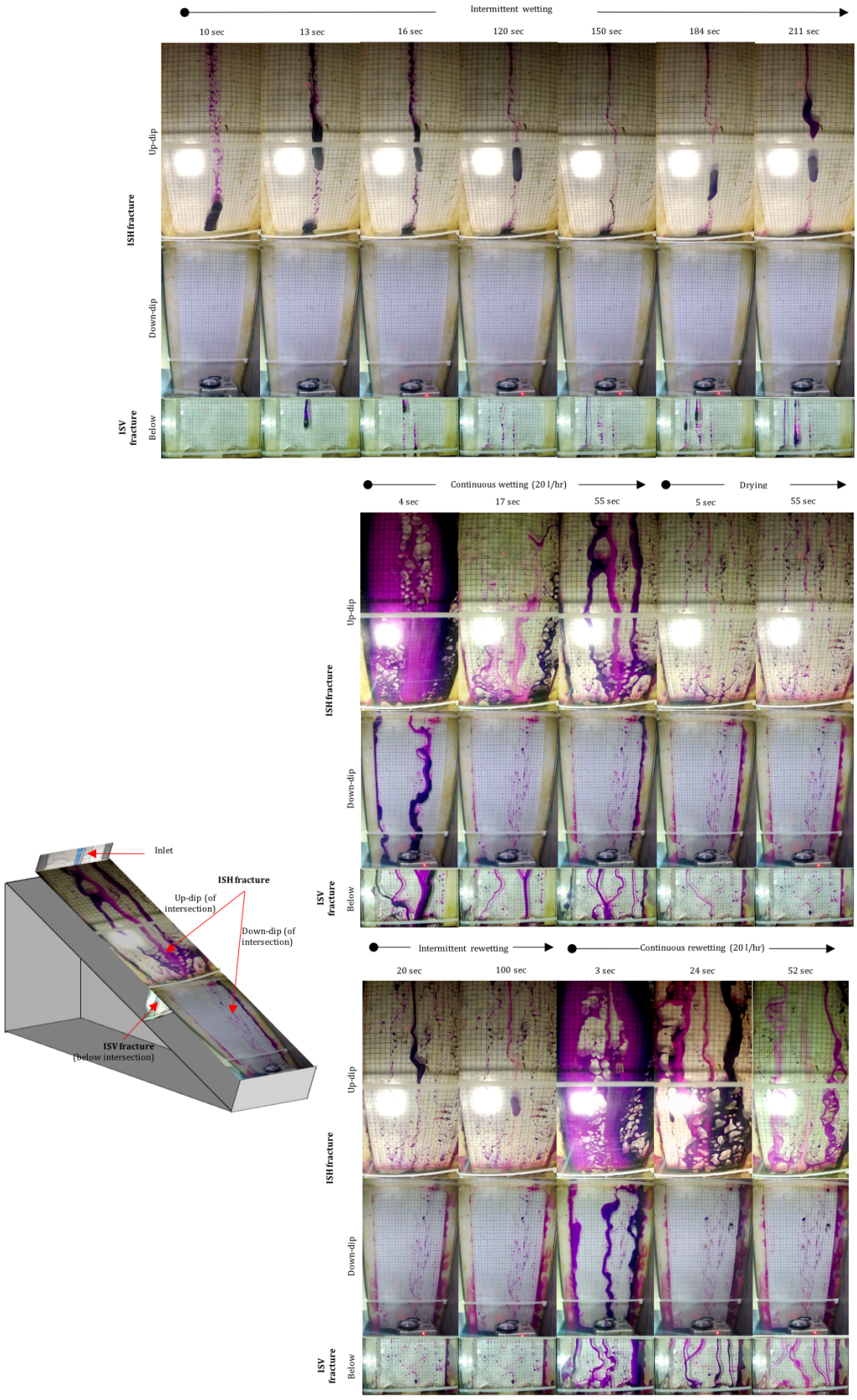

Figure 9-2. Flow mechanisms observed in the inclined orthogonal intersection with flow from the ISH fracture above the intersection (Model 3-1) for the intermittent and continuous influx at 1g.

9.3.1.2 20g

The flow mechanisms observed during the experiment are shown in Figure 9-3.

9.3.1.2.1 Intermittent Influx Wetting

At the initiation of the intermittent experiment, the invading fluid is a continuous flow path that contacts and travels against the spacer on the ISH fracture up-dip of the intersection. This preferential flow along the spacer, causes the continuous path to flow along the spacer below the intersection, in the ISV fracture. After initiating the intermittent flow interval for 10 seconds (*66 minutes*), two additional continuous rivulets and discontinuous paths of discrete sliding droplets are established in the ISH fracture up-dip of the intersection. At the same time, a second continuous rivulet forms within the ISV fracture below the intersection.

The spacers in both the ISH and ISV fractures are observed to have fluid flow within them. Approximately 30 seconds (*3.3 hours*) into the experiment this flow within the spacer appears to create a phreatic surface in the right spacer of the ISV fracture. This is due to the large influx flowing into it, as well as a pinching on the aperture (between the L-sections) towards the bottom, which therefore acts to choke flow out of the bottom of the spacer. At 60 seconds, discrete sliding droplets are seen flowing within the spacer itself.

Another discontinuous path of sliding droplets form on the opposite side of the ISH fracture, along the spacer, and causes a new discontinuous path of sliding droplets below the intersection on the ISV fracture. By 80 seconds (*8.8 hours*) into the interval, the phreatic surface has increased in height within the spacer due to the influx of water. Throughout the entire intermittent interval, the ISH fracture down-dip of the intersection does not have any water flowing within it.

9.3.1.2.2 Continuous Influx Wetting

At the initiation of the continuous influx at 20 l/hr, a film establishes in the ISH fracture, saturating approximately 60% of it. The larger influx causes fluid to cross the intersection onto the ISH fracture down-dip of the intersection, whereby flow occurs mostly as oscillating rivulets and some sliding droplets. During the continuous phase at 10 seconds (*66 minutes*) there is a slightly higher influx of water delivered to the model (due to cavitation and subsequent pressure build-up) and the film in the ISH fracture up-dip of the intersection and the ISV fracture below the intersection widen.

9.3.1.2.3 Drying and Rewetting

During the re-wetting intermittent influx, once again the droplets remobilise within the spacer. However, there are several discrete sliding droplets that slide down the ISV fracture, likely fed from the lateral accumulation of water on the fracture intersection. The movement of sliding droplets from the inlet container are difficult to see in still-picture but are observed where there is no more colouring on the right side of the ISH fracture (up-dip the intersection). Additionally, a few sliding droplets are observed on the ISH fracture below the intersection.

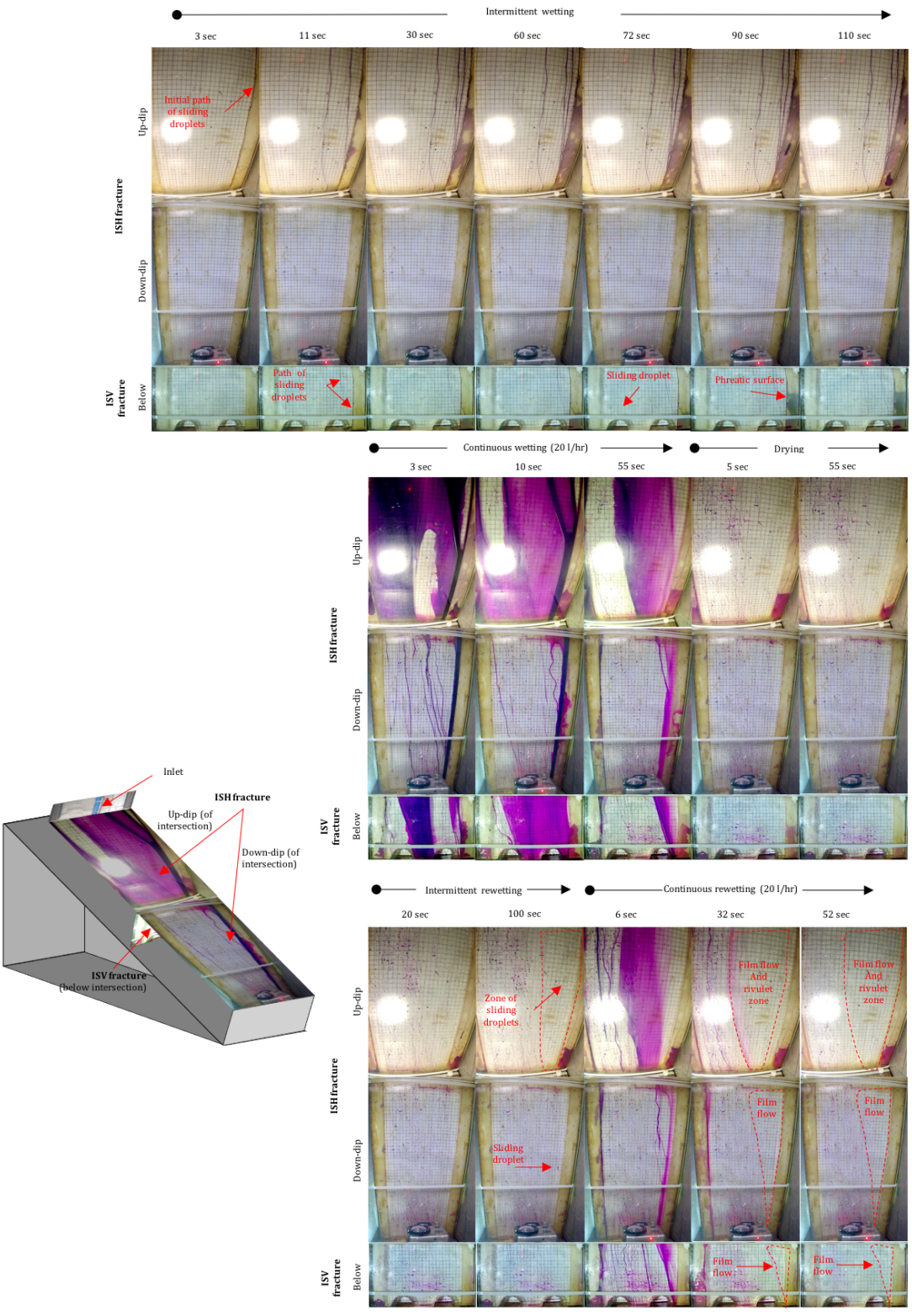

Figure 9-3. Flow mechanisms observed in the inclined orthogonal intersection with flow from the ISH fracture above the intersection (Model 3-1) for the intermittent and continuous influx at 20g.

9.3.2 Flow from the inclined sub-vertical fracture above the intersection (Experiment 2-2)

9.3.2.1 1g

The flow mechanisms observed during the experiment are shown in Figure 9-4.

9.3.2.1.1 Intermittent Influx Wetting

The initial 15 seconds of the intermittent influx is characterised by sliding droplets flowing along the ISV fracture above the intersection. These droplets are characterised by prominent air-water meniscus with a snapping thread, which leave static droplets along the flow path. The pioneer droplet that travels along this path is slightly larger in volume (0.245 ml), due to a threshold volume needed to breach into the fracture from the inlet container. Before the second droplet travels across the intersection, 2 episodic fluxes are observed in the ISV fracture below the intersection, with volumes of 0.075 and 0.025 ml respectively. This suggests that only 40% of the volume of the pioneer droplet above the intersection is accounted for below the intersection.

The proceeding droplets along this first flow path within the ISV fracture are approximately 0.11 ml in volume. All subsequent sliding droplets travelling through the ISV fracture below the intersection do not mirror the derivative droplets from above the fracture, and are all characterised by smaller volumes. This indicates that a portion of the volume of the fluid is ponding within the intersection, whilst the rest of that volume continues to move downward into the ISV fracture below the fracture.

A second path of discrete sliding droplets is formed 20 seconds into the intermittent influx, in the ISV above the intersection. Again, the pioneer droplet is larger in volume, at 0.28 ml, with 2 episodic fluxes observed below the intersection before the second droplet travels along this path. The volume of these episodic fluxes is 0.150 and 0.051 ml, respectively, accounting for 72% of the volume of the pioneer droplet volume above the intersection. At 30 seconds into the intermittent influx, the ponding at the intersection into the ISH fracture down-dip of the intersection has steadily grown, whereby at 70 seconds it is of sufficient volume to detach from the intersection, and travels down the ISH fracture down-dip of the intersection. This droplet forms a liquid bridge (aperture-spanning) between the fracture walls. The volume of this initial droplet is 0.240 ml, which is similar to the initial droplet released from the inlet container at the beginning of the interval.

A cumulative volume of 0.545 ml of fluid flows along this second flow path in the ISV above the intersection, before a sufficient quantity is transferred at the intersection to detach and move down the ISH fracture down-dip of the fracture. This is a significantly less than the first flow path, which at 130 seconds releases a droplet of 0.350 ml, after a cumulative volume of approximately 6.16 ml has passed through this flow path. The subsequent droplets along this second flow path are also 0.110 ml in volume, with approximately 60% of the volume of these droplets flowing below the intersection, while the remaining volume (±40%) remains in the

intersection, and ponds to form sliding droplets which moves down the ISH fracture below the intersection.

9.3.2.1.2 Continuous Influx Wetting

The 20 l/hr continuous influx interval consists mainly of a single oscillating rivulet on the ISV fracture above and below the intersection, throughout the 60 seconds of the interval. The frequency of sliding droplets along the ISH fracture increases, whereby a single droplet, on average 0.400 ml in volume (and sometimes up to 0.750 ml), is released from the intersection approximately every 15 seconds. Some of the rivulets on the ISV fracture above the intersection do not flow directly in line with the corresponding rivulets flowing on the vertical fracture below the intersection. Instead these rivulets feed the lateral pool at the intersection, where the sliding droplets are released into the ISH fracture down-dip of the intersection.

After approximately 10 seconds into the 40 l/hr interval, the discontinuous path on the right within the ISH fracture down-dip of the intersection forms a continuous rivulet. This is due to a wide capillary flow in the ISV fracture supplying this flow path. This flow feature carries the majority of the fluid such that the discontinuous flow path in the ISH fracture down-dip of the intersection is able to convert to a continuous flow path at approximately 20 seconds into the 40 l/hr influx. A secondary path of sliding droplets (of 0.125 ml) flows along the ISV fracture above the interaction, but does not transfer any water at the intersection into the ISH fracture and instead all the volume passes vertically through the intersection. This is likely to occur at the intersection when it is sufficiently wet, such that the small droplets continue beneath the intersection onto the vertical fracture below.

9.3.2.1.3 Drying and Rewetting

During the rewetting intermittent influx, the sliding droplets above the intersection (of the ISV fracture) are not directly in line with the paths that appear below the intersection, due to the ponding at the intersection and static fluid that remained throughout the drying interval. As observed during the intermittent wetting interval, a portion of the droplet volume continues to migrate sub-vertically, whilst the other portion spreads laterally at the intersection, and forms the ponding droplet at the down-dip side of the intersection on the ISH fracture.

A third discontinuous path of sliding droplets forms down-dip of the intersection of the ISH fracture approximately 40 seconds into the interval. Once this discontinuous flow path establishes, no sliding droplets are observed on the ISV fracture below the intersection, with some flow only occurring within the fracture. During the rewetting continuous influx intervals, the oscillating and meandering film on the vertical wall again widens when upping to 40 l/hr, and the discontinuous flow path on the ISV fracture down-dip of the intersection becomes a continuous rivulet.

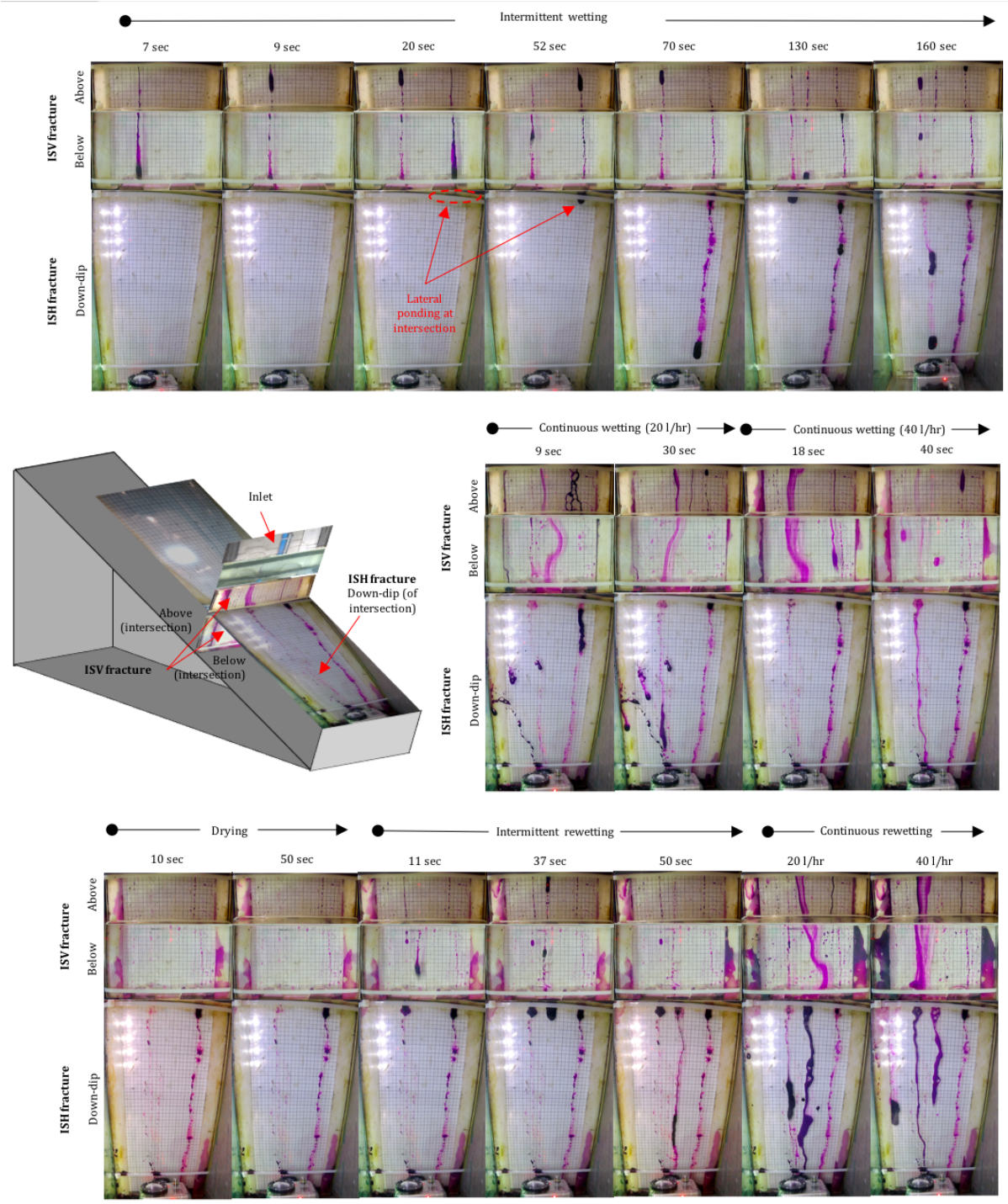

Figure 9-4 Flow mechanisms observed in the inclined orthogonal intersection with flow from the ISH fracture above the intersection (Model 3-2) for the intermittent and continuous influx at 1g.

9.3.2.2 20g

The flow mechanisms observed during the experiment are shown in Figure 9-5.

9.3.2.2.1 Intermittent Influx Wetting

The invasion of fluid during the intermittent influx is characterised by an invading continuous rivulet down the ISV fracture above the intersection. At the intersection, this invading pioneer rivulet changes direction and flows down the ISH fracture. At the same time, only a single discrete sliding droplet advances down the ISV fracture (below the intersection) and remains static at approximately 60 mm (*1.2 m*) down the fracture. The flow mechanism observed within the ISH fracture down-dip of the intersection is characterised by a continuous rivulet that ceases to become a discontinuous path releasing sliding droplets. This continuous-discontinuous flow path point steadily increases in length down the fracture as the flow path is supplied by fluid. Each droplet is released from the rivulet once a sufficient volume is accepted by the droplet, and it breaks off from the rivulet. While this point (continuous flow to discontinuous flow) moves down the ISH fracture, the discontinuous path at its end meanders and distributes sliding droplets down an extensive area of the ISH fracture.

At 10 seconds (*66 minutes*) into the intermittent influx, a similar path with the same flow mechanism forms against the spacer, and again a third at 15 seconds. On the ISV fracture above the intersection, there is only the 3 rivulets supplying the 3 continuous-discontinuous points present within ISH fracture. Shortly after the formation of the third flow path, the previous flow paths cease to release sliding droplets at the discontinuous point; however, the continuous rivulets are maintained along the length of the ISH fracture. Throughout the intermittent interval, no further flow is observed on the ISV fracture below the intersection, with only the single discrete droplet remaining static on the fracture wall. Although difficult to prove, it is assumed by the rounded shape of the droplet, that is flows as a film only on the lower fracture wall.

9.3.2.2.2 Continuous Influx Wetting

During the 20 l/hr continuous influx interval, the invading fluid forms films and oscillating rivulets within the ISV fracture above the intersection. This fluid then crosses the intersection vertically with the majority of the volume continuing into the ISV fracture below, and a portion of fluid moving at the intersection, into the ISH fracture. There are several examples where it is observed that these flow paths are flowing on opposite walls of the fracture (on the ISV fracture above the intersection), as the paths appears to cross each other but the population of fluids do not affect each other's flow (one such example is seen at 7 seconds in Figure 9-5).

Although there appears to be a similar observation on the ISH fracture, there is some leakage from the inlet container that spills onto the top of the model, with some rivulets flowing on the outside of the fracture. All flow paths within the ISH fracture down-dip of the intersection flow along the bottom fracture wall as films. When comparing fluid flow on a specific path from the ISV fracture above the intersection, to that below the intersection, and down-dip of the intersection (along the ISH fracture) 2 clear scenarios is evident. The first is that if a film is present above the intersection, that its width will narrow below the intersection, and an oscillating rivulet will be present on the ISH fracture. On the contrary, if a rivulet or a discontinuous path of sliding droplets travel along the ISV fracture above the intersection, that

this fluid will turn at the intersection and move downward along the ISH fracture. This second scenario is similar to that of the flow mechanism observed in the intermittent influx. Upon increasing the influx to 40 l/hr, the same scenarios can be identified, except that in scenario 1, the films in the ISV fracture widen above and below the intersection, with oscillating rivulets still present on the ISH fracture below the intersection.

9.3.2.2.3 Drying and Rewetting

Throughout the rewetting intervals, the same flow mechanisms are generally observed. Notwithstanding, this is difficult to observe as the potassium permanganate colouring ran out during this interval.

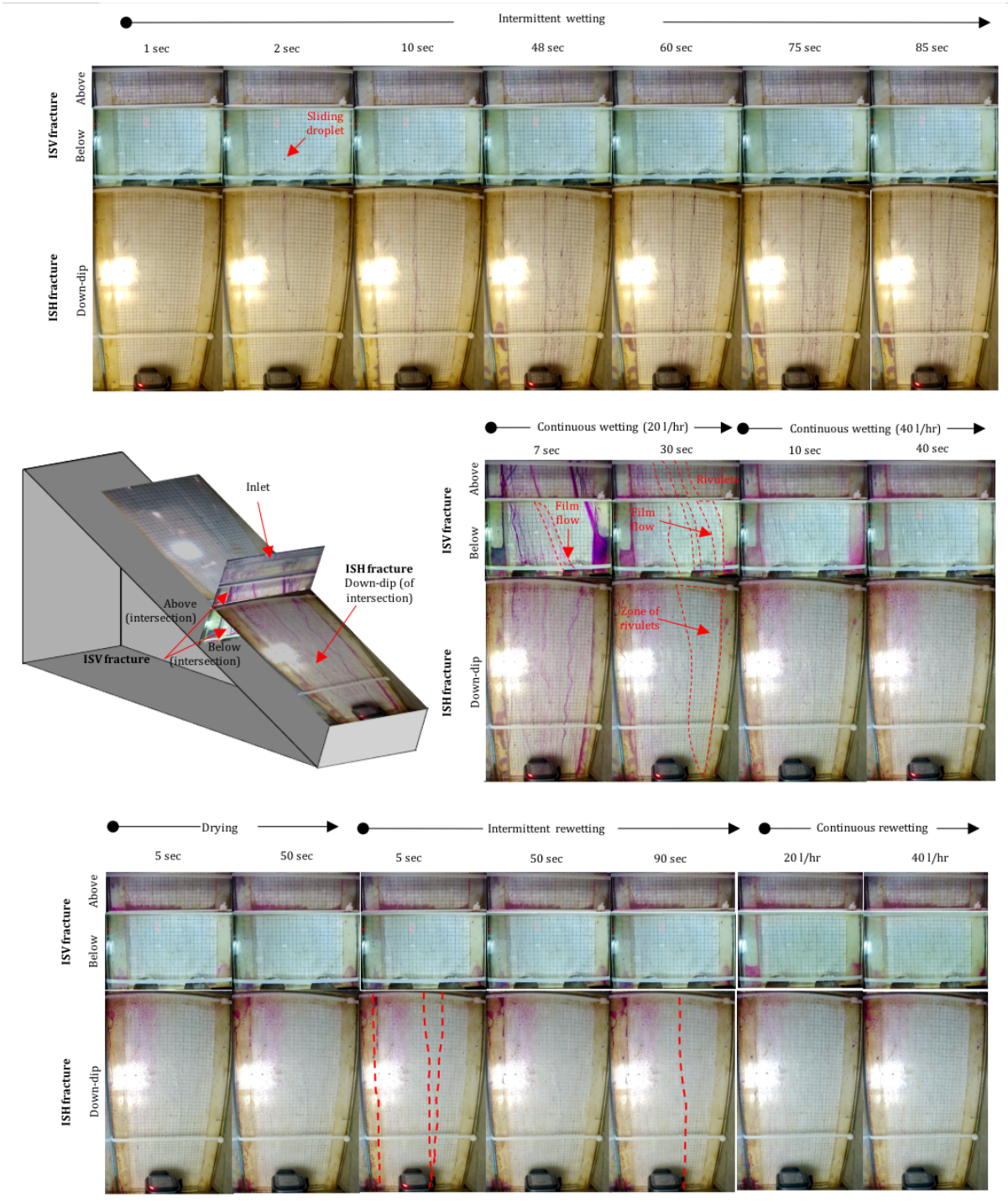

Figure 9-5. Flow mechanisms observed in the inclined orthogonal intersection with flow from the ISH fracture above the intersection (Model 3-2) for the intermittent and continuous influx at 20g.

9.4 Summary

The set of experiments as presented in this chapter found inclination of fracture intersections results in the inclined sub-horizontal fractures down-dip of the intersection becoming a conducting path for fluid flow. Notwithstanding, the majority of the volume of fluid is still transported vertically downwards and not laterally, and the amount of fluid that crosses the intersection is depend on the wettability of the material into which it flows.

Flow into this inclined sub-horizontal fracture is dependent on the direction of the flow of fluid entering the fracture (i.e. either from the ISV fracture above the intersection, or from the ISH fracture up-dip of the intersection). In the inclined orthogonal intersection with flow from the ISV fracture, as the fluid passes on the fracture, flow occurs toward the ISH fracture down-dip of the intersection. In contrast, this does not occur in the experiment where flow occurs from the ISH fracture up-dip of the intersection, as they are not connected. Instead here, the corner of intersection is encountered first which preferentially ensures the fluid flows vertically instead of laterally across the intersection.

CHAPTER 10 EXPERIMENT 4: LUGEON TESTS AT PARTIAL SATURATION

10.1 Introduction

Lugeon tests are the most common method used to assess the permeability of rock masses for engineering purposes. However, uncertainties arise through the often-unsaturated state of the rock mass, and the associated complexity of flow regimes and flow mechanisms in such unsaturated fractured geologic media. Both Ewert (1997a) and Widmann (1996) emphasised the uncertainties pertaining to Lugeon tests, and called early on for the better quantification and characterisation of flow path geometries, with limited studies that subsequently builds on the authors requests.

This chapter presents an experiment that assesses the flow behaviour when conducting Lugeon tests under conditions of variable saturation in an initially dry free-draining, smooth, clean, open, discrete fracture using geotechnical centrifuge modelling. The aim is achieved by qualitatively examining the geometry of the flow paths within the fractures, whilst measuring the flow rate under a series of ascending and descending pressure intervals. The Forchheimer relationship is used to predict the flow rate at the imposed hydraulic heads using the width of the flow path within the fracture. Empirical and experimental contributions eventually supply insight into improved interpretation and understanding of Lugeon tests at partial saturation. The following chapter comprises verbatim excerpts from Jones et al. (2018b).

10.2 Experiment-Specific Methodology

The physical models tested in this study are developed by conceptualising a Lugeon test, using a single-packer, conducted within an interval of impermeable rock intersected by a single, discrete fracture at the base of the test section. In addition, the rock mass is located within the fractured vadose zone, such that unsaturated conditions are prevalent, and furthermore that the geometry of the fracture is simplified to the fundamental concept of the smooth parallel plate model, from which the Cubic law is derived. Motivated by the results of Jones et al. (2018a), the first model consisted of a horizontal fracture, whilst a second model consisted of an fracture inclined at 23° from the horizontal. Furthermore, the inclined fracture is tested at both 1 mm and 0.50 mm apertures. The conceptualised field models alongside their appropriate centrifuge model is shown in Figure 10-1.

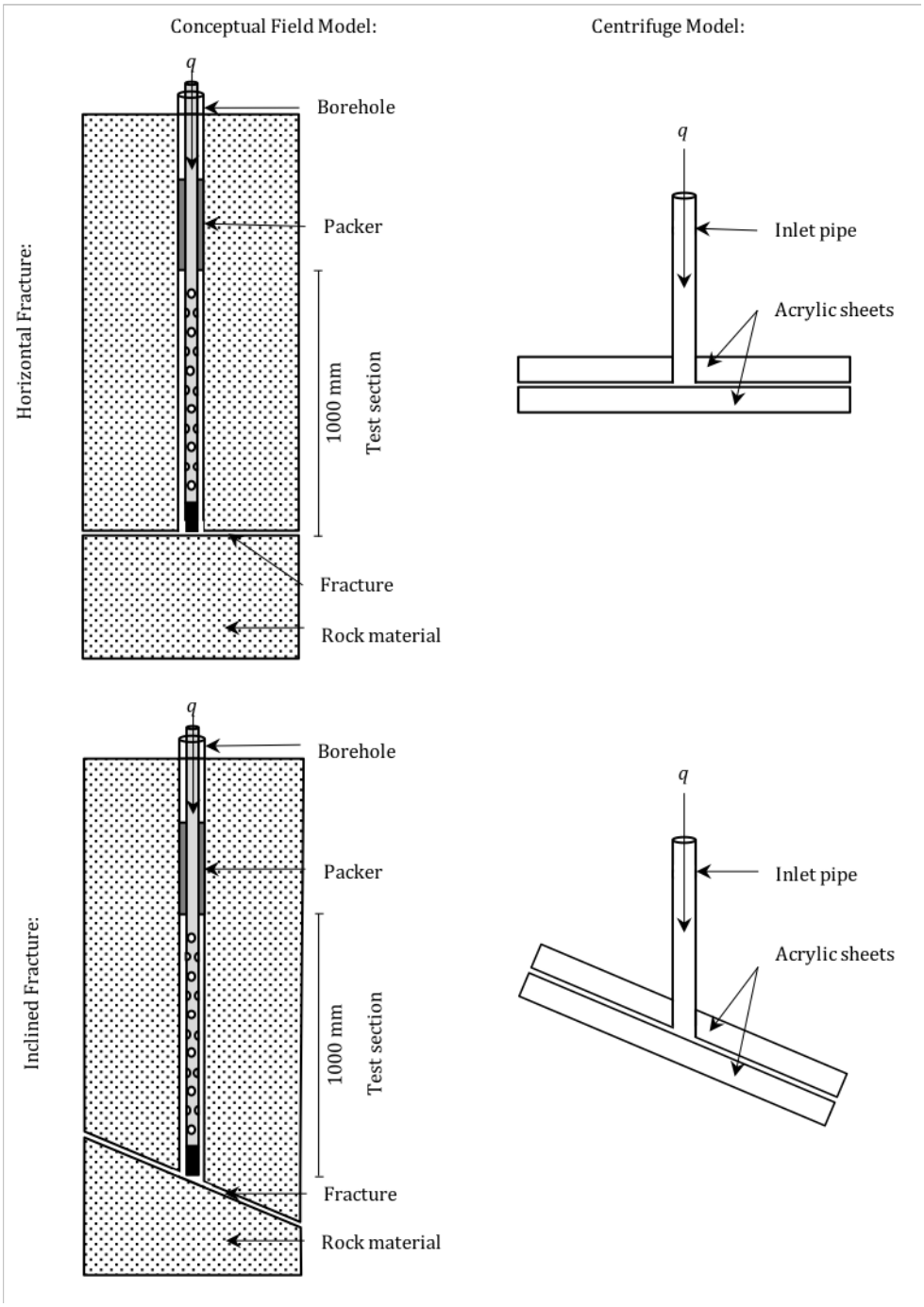

Figure 10-1 Conceptualised field model showing a single borehole packer test over a 1 m length test interval that intersects a single discrete fracture at the base of the test section, with the accompanying centrifuge model that was used to simulate it.

Within the centrifuge strongbox itself, where the model was constructed, the extent of the fracture is rectangular, with the long boundaries being discontinuous (i.e. terminating at this boundary), whilst being continuous along its short boundaries. As such, the fracture was open at the short boundaries such that flow could occur out of it, whilst fluid could not exit along the long boundaries. In order to simulate a radial borehole, the centrifuge model was constructed with an inlet pipe through the acrylic sheets, where the water was injected. The models are

tested under multiple pressure steps as would be conducted for Lugeon tests conducted in the field (as described by e.g. Royle, 2002; and Yihdego, 2017).

Lugeon tests are typically conducted at high hydraulic pressures. However, previous literature has shown that the onset of non-Darcian flow occurs at relatively low flow rates for saturated conditions (e.g. Konzuk and Kueper, 2004; Quinn et al., 2011; Ranjith and Darlington, 2007; Zimmerman et al., 2004). Therefore, the Lugeon test stages conducted in this experimental study were conducted at low hydraulic pressures, relative to those generally used for Lugeon tests in the field. The set-up for the models and the procedure followed for each test is discussed in the following sections. The three geotechnical centrifuge model tests were performed at a scale of 1:20 using the 150 G-ton geotechnical centrifuge housed in the Department of Civil Engineering at the University of Pretoria. Details of the centrifuge facility are described by Jacobsz et al. (2014) and studies by Jones et al. (2017b), Van Tonder and Jacobsz (2017) and Brouwers and Dippenaar (2018) detail the verification of the applicability of this specific geotechnical centrifuge for partially saturated flow modelling.

10.2.1 Set-up

10.2.1.1 Horizontal Fracture (Experiment 4-1)

The horizontal model test (Experiment 4-1) consisted of 2 acrylic Plexiglas sheets measuring 400 mm length x 290 mm width, separated by spacers along both the long boundaries as well as 4 rectangular (20 mm x 20 mm) spacers within the fracture, in order to maintain a constant aperture of 1 mm. Although the rectangular spacers are placed within the fracture to minimise bending of the acrylic sheets, possible change in aperture due to slight bending is duly noted as a possible influence on the study, particularly considering the accelerated conditions in the geotechnical centrifuge. An average contact angle for the acrylic sheets is reported as being approximately 70° by Della Volpe et al. (2002). Assuming saturated conditions, the fracture replica was therefore characterised by a hydraulic conductivity (K_f) of 9.18 x 10^{-1} m/s, and permeability (k_f) of 8.33 x 10^{-8} m^2. The model set-up is illustrated in Figure 10-2.

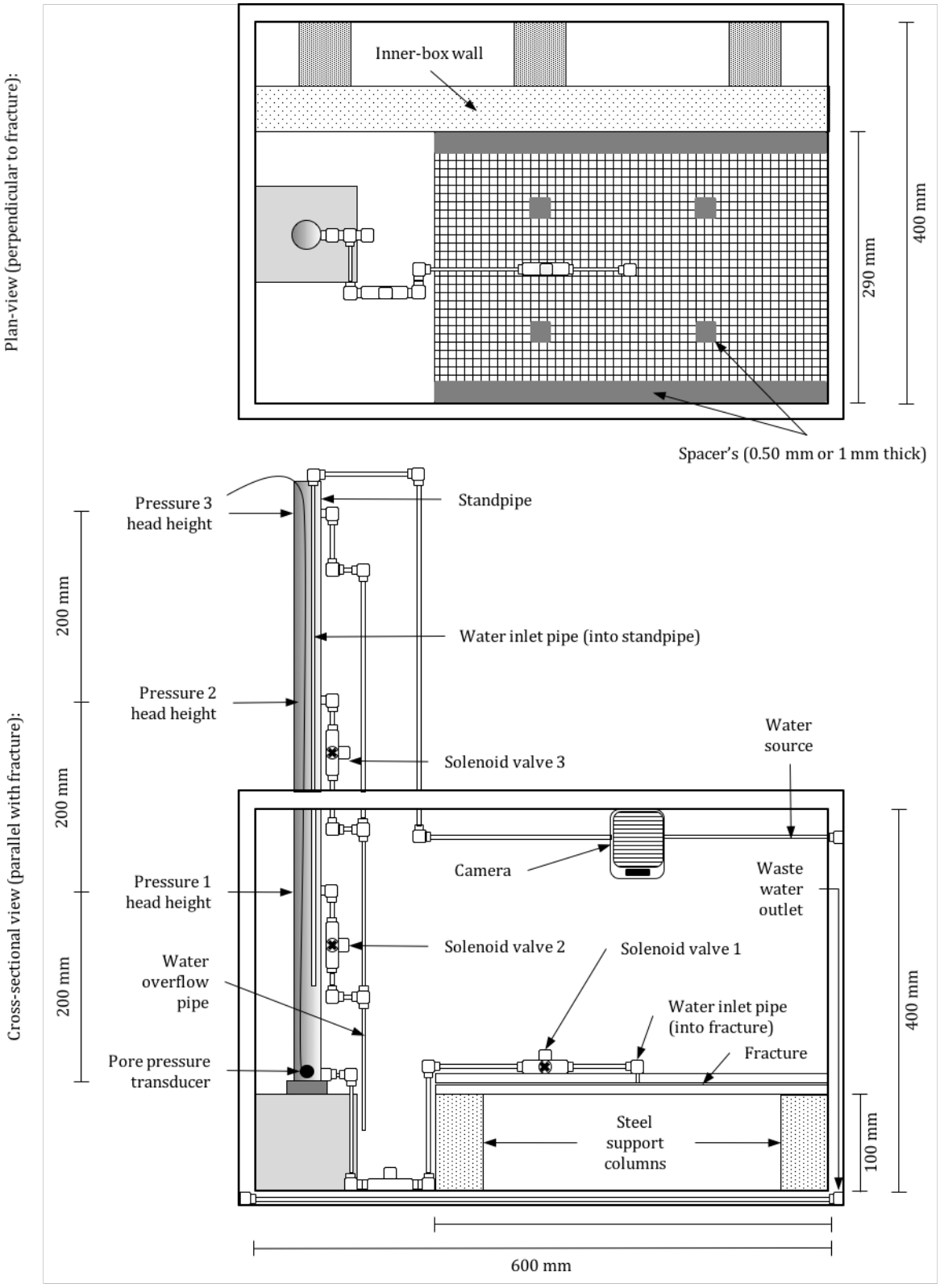

Figure 10-2 Test set-up for the Lugeon test on the horizontal fracture (Experiment 4-1).

The inlet pipe (simulating the borehole) was positioned in the centre of the fracture. A grid was placed on the outside of the bottom acrylic sheet, facing inwards, in order to assess the geometry of the flow path. A standpipe was constructed with 3 overflow levels each at different

heights, to test the model at 3 separate hydraulic pressures. These overflow levels were placed at heights of 200 mm, 400 mm, and 600 mm, respectively, above a pipe that connects to the fracture and was located at the bottom of the standpipe. This outlet pipe was placed at the same elevation as the inlet pipe into the fracture. A pore pressure transducer (PPT) was placed at the base of the standpipe to monitor the hydraulic pressure (hydraulic head) within the standpipe during each test. The water was introduced by a 4 mm inner diameter pipe that connected to the water source from the centrifuge platform, where the flow of water into the standpipe was controlled via a solenoid valve (electronic tap) located in the centrifuge control room. Potassium permanganate crystals were scattered at the base of the standpipe in order to colour the water that enters the standpipe. It was assumed that the addition of these minimal amounts of potassium permanganate did not influence the surface tension of the water.

The pipe connected to the base of the standpipe was connected to the inlet source of the fracture via a pipe with an inner diameter of 4 mm. The pipe was laid in the set-up such that it forms a u-bend to ensure it remained fully saturated during the test, and no air-locks develop within the system. Three solenoid valves (electronic taps) were placed in the model, with the first solenoid valve controlling the flow of fluid into the fracture. The second solenoid valve was placed directly below the lowermost overflow level (200 mm) such that it determines the hydraulic head when Pressure 1 as required, whilst the third solenoid valve controls the head height at the middle overflow level for Pressure 2. The valves are opened when a specific pressure interval is required, so that the water level could not rise higher than the required hydraulic pressure. Depending on when a specific hydraulic pressure was required, the corresponding solenoid valve was closed or opened such that the water level in the standpipe could rise or fall.

Each of the overflow levels were attached to an overflow pipe, which spilled the excess waste water into the centrifuge strongbox, and drained away thereafter. The inlet pipe to the fracture was connected to a drilled hole in the top of the acrylic sheet and fastened with epoxy and silicon to ensure that no leakage occured. The water flow was monitored visually in flight by using the flow metre located in the centrifuge control room. A camera was placed on an overhead bracket above the horizontal fracture.

10.2.1.2 Inclined Fractures (Experiment 4-2 and Experiment 4-3)

The inclined model test was performed on the same acrylic sheets (400 mm length x 290 mm width), set-up in a similar manner as the horizontal test, but placed on a concrete base inclined at 23°. The inlet pipe for the fluid source was positioned 300 mm above the bottom of the upper acrylic sheet. The model was tested at 2 apertures, namely; 1 mm (Experiment 4-2) and 0.5 mm (Experiment 4-3) respectively, both of which were maintained by spacer's that ran down the long-boundary of the fracture, with 6 rectangular spacers' (20 mm x 20 mm) placed within the fracture in order to mitigate bending of the acrylic sheet, although possible change in aperture due to bending is noted as an influence on the results of the model. As the same acrylic sheets are used, a similar contact angle is considered for the inclined experimental set up (ca. 70°). The model set-up is illustrated in Figure 10-3.

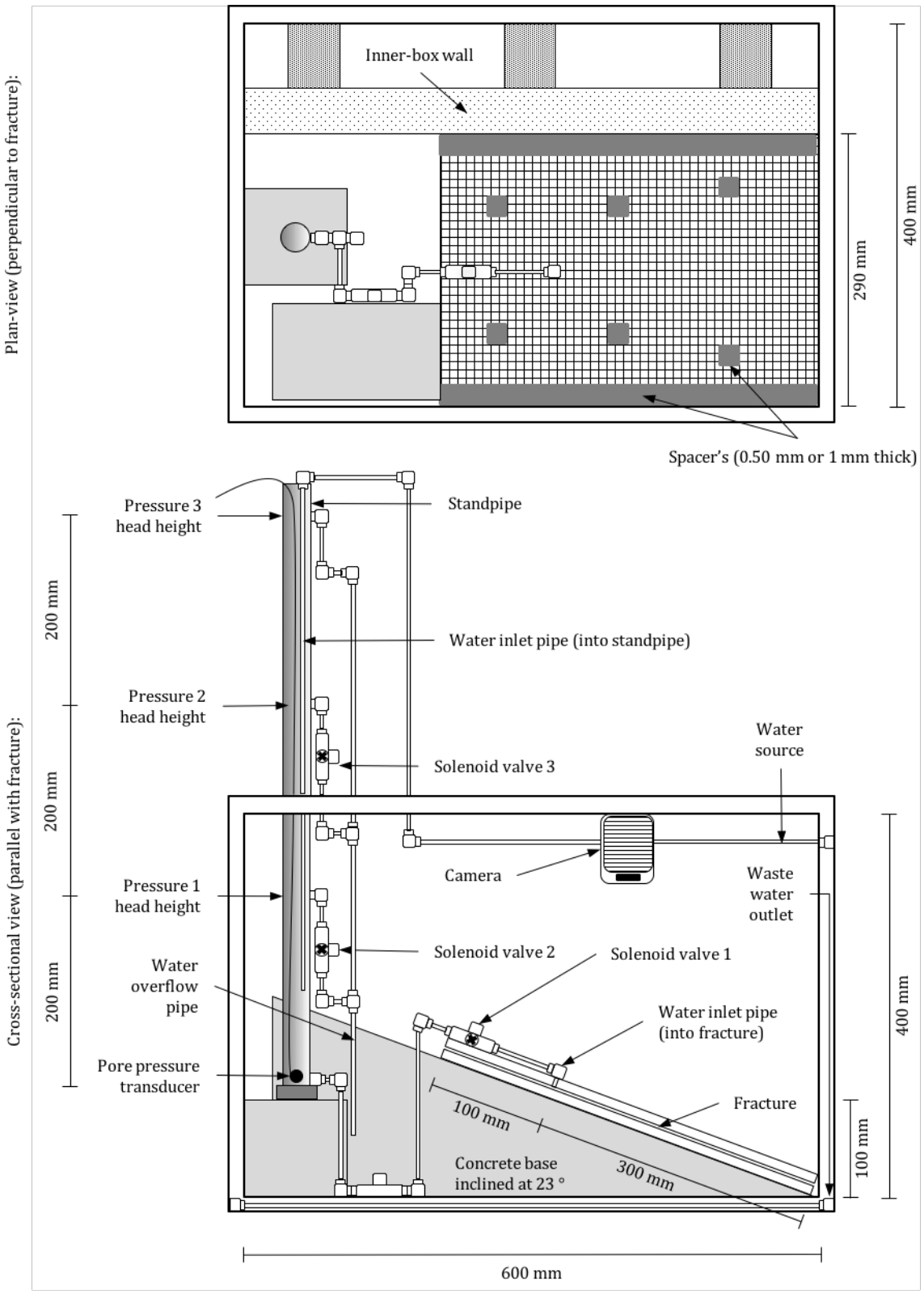

Figure 10-3 Test set-up for the Lugeon test on the inclined fracture's (Experiment 4-2 and Experiment 4-3).

Assuming saturated conditions, the fracture replica of the 1 mm model was therefore characterised by a hydraulic conductivity (K_f) of 9.18 x 10^{-1} m/s, and permeability (k_f) of 8.33

x 10^{-8} m^2, whilst the 0.50 mm model exhibited a hydraulic conductivity (K_f) of 2.30 x 10^{-1} m/s, and permeability (k_f) of 2.08 x 10^{-8} m^2. A grid was placed on the outside of the opposite Plexiglass sheet, facing inwards, so that the geometry of the flow paths could be assessed. The same standpipe with the three overflow levels was used, as was in the horizontal fracture model. The overflow levels were placed 200 mm, 400 mm, and 600 mm, respectively, above the base of the standpipe. The base of the standpipe was located at the same elevation as the inlet pipe into the fracture. A pore pressure transducer (PPT) was placed at the base of the standpipe monitor the hydraulic pressure (hydraulic head).

The lower outlet valve was also attached at the bottom of the standpipe which fed into a u-bend, ensuring that the pipe remained fully saturated during the test. Three solenoid valves were placed in the model, and were again opened or closed depending on what hydraulic head was required for each pressure interval. Water influx was also monitored in flight by a flow metre in the centrifuge control room. A camera was placed on an overhead bracket above the horizontal fracture.

10.2.2 Test Procedure

Three tests were conducted at 20g, namely, on i) the horizontal 1 mm aperture fracture model (Experiment 1), ii) the inclined 1 mm aperture fracture model (Experiment 2), and iii) the inclined 0.5 mm aperture fracture model (Experiment 3). Once the completed model was accelerated to the desired G-level, it was tested under multiple-pressures, consisting of 5 pressure steps in a series of ascending and descending intervals. The pressure recorded by the PPT at the base of the standpipe was used to monitor the required hydraulic pressure for each step. Each step was conducted until a constant head is achieved in the standpipe at the required pressure, whilst the constant flow rate being achieved during this constant head was recorded.

The hydraulic pressures at the base of the standpipe were 39.24 kPa, 78.48 kPa, and 117.72 kPa, for the respective 200 mm, 400 mm, and 600 mm overflow levels. However, as there was a 200 mm horizontal distance between the base of the standpipe and inlet pipe into the fracture, the corresponding hydraulic gradient resulted in the hydraulic pressures at the inlet into the fracture being less than those recorded in the standpipe. Therefore, these pressures were reduced in order to account for this loss of hydraulic pressure along the hydraulic gradient, which therefore resulted in the imposed pressure intervals for the tests being 18.9 kPa (Pressure 1), 33.5 kPa (Pressure 2), and 51.7 kPa (Pressure 3), for the respective 200 mm, 400 mm, and 600 mm overflow levels in the standpipe. Any frictional losses through the pipe that delivers the fluid from the standpipe to the model was assumed as negligible. An example of the data obtained from this pore pressure is shown in Figure 10-4 for the inclined 1 mm fracture model (Experiment 2).

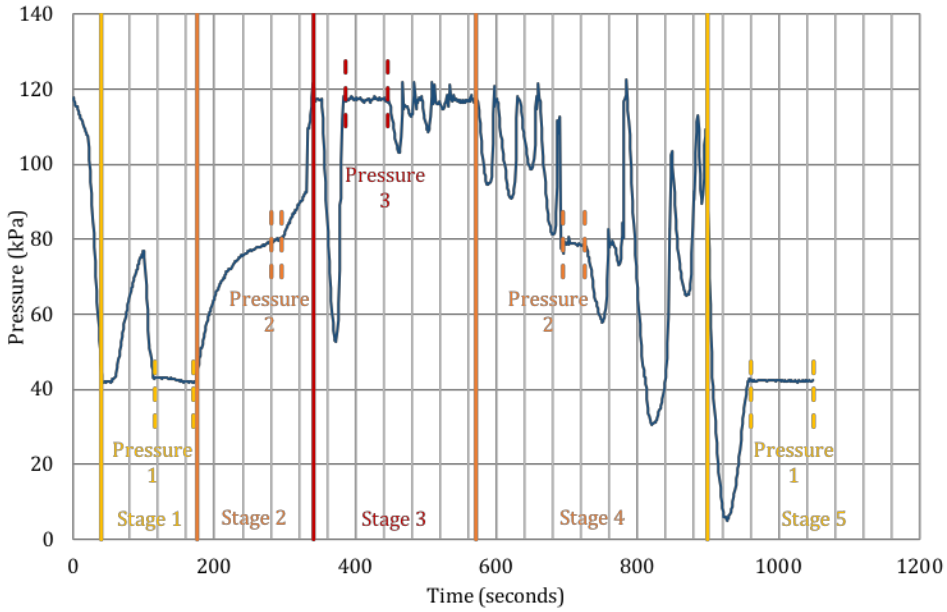

Figure 10-4 Representative example of the data obtained from the pore pressure transducer (PPT) at the base of the standpipe, for the inclined 1 mm aperture fracture model (Experiment 4-2); flow rates were measured when constant head conditions were achieved at each stage (i.e. between the dotted lines).

Before initiation of the test, solenoid valve 1 was closed, whilst solenoid valve 2 and 3 remained open, and fluid was added to the standpipe via the water source pipe by opening the tap in the centrifuge control room. Upon initiating the test, solenoid valve 1 was opened which allowed the fluid to enter the fracture. In the centrifuge control room, the flow rate delivered to the model was monitored by a flow meter attached to the water source tap, whilst the hydraulic pressure in the standpipe was monitored in-flight by a data acquisition system attached to the PPT. This resulted in water being added to the standpipe, with the water level rising to the first overflow height at 200 mm (Pressure 1), where any waste-water was discarded through the overflow pipe.

The flow rate into the standpipe was adjusted until equilibrium was achieved between the flow being delivered and the required constant hydraulic head for the first pressure step. Once equilibrium was achieved, during Stage 1 at Pressure 1 (18.9 kPa), the flow rate was recorded and solenoid valve 2 was closed such that the hydraulic head increases to Pressure 2 (33.5 kPa) for Stage 2 of the test. Once again, the water influx was managed at the control room until a constant flow was obtained and recorded. When constant head conditions were achieved and the flow rate recorded at Pressure 2 during Stage 2, solenoid 3 was closed and the water level rises to the constant head required Pressure 3 (51.6 kPa), such that Stage 3 of the test commences. Similarly, the flow rate was recorded once equilibrium (constant flow rate at a constant head) was achieved. For the subsequent stages, solenoid valve 3 was reopened, initiating the series of decreasing pressure steps, whereby the water level dropped back to Pressure 2 (33.5 kPa) for Stage 4, and the flow rate was recorded at a constant head conditions in order to ensure similarity to the rate achieved in the corresponding ascending

step. Once recorded, solenoid 2 is reopened so that the water level dropped back to Pressure 1 (18.9 kPa) for Stage 5, with the flow rate being recorded again at constant head conditions. Once the flow rates were recorded for all stages (ascending and descending pressure intervals), the test is stopped.

10.3 Results

10.3.1 Experiment 4-1: Horizontal 1 mm aperture fracture

At the initiation of Stage 1 into the test, the hydraulic head rapidly decreased in the standpipe as fluid entered the fracture, causing a deficit water balance in the standpipe. The invasion of fluid from the inlet occurred as an advancing finger of fluid within the first second of the interval, and thereafter this finger established as a horizontal rivulet. Within the first 2 seconds, 3 additional rivulets had extended towards the long boundaries of the fracture where the fluid ponded against the spacers, and moved laterally towards the short boundaries of the fracture, where it exited. Some of the major flow paths meandered and oscillated, which is indicative that the flux rate within these rivulets was high (from the resulting boundary between inertial, viscous, capillarity and gravitational forces). The observed flow behaviour for each stage is shown in Figure 10-5. As surplus water was added to the standpipe, the hydraulic head reached the required level at 160 seconds (17.8 hours) for the flow rate at Pressure 1 (18.9 kPa) to be recorded. Once reached, Pressure 1 was maintained for 85 seconds (9.44 hours) where a constant flow rate of 0.67 l/min (13.4 l/min) was recorded. Italicised values in parentheses refer to the full prototype scale values (e.g. time, volumetric flow rate, linear dimensions, etc.).

Stage 2 was initiated at 305 seconds (*33.9 hours*) into the test. However, cavitation that occurred in the water source pipe that fed water into the standpipe resulted in difficulty in obtaining the constant head required for this pressure interval. Nevertheless, Pressure 2 (33.5 kPa) was obtained for 20 seconds (*2.2 hours*) where a constant flow rate of 1.15 l/min (*23 l/min*) was recorded flowing into the fracture. Stage 3 is started 765 seconds (*85 hours*) into the test, with a flow rate of 1.50 l/min (*30.0 l/min*) being recorded when the required constant head (51.6 kPa) was achieved for 80 seconds (*8.89 hours*) at 885 seconds (*98.3 hours*) into the test. During the subsequent descending stages, similar flow rates confirmed those recorded during the ascending stages at the same pressures. When there was a deficit of flow into the standpipe and the water level decreased, cavitation occurred and the rivulets within the fracture diminished, resulting in some flow paths disappearing with static droplets remaining along the extinct flow paths. When the water level in the standpipe recovered, and fluid reinvaded the fracture, flow re-established along these extinct paths, which was likely a function of their favourable wettability.

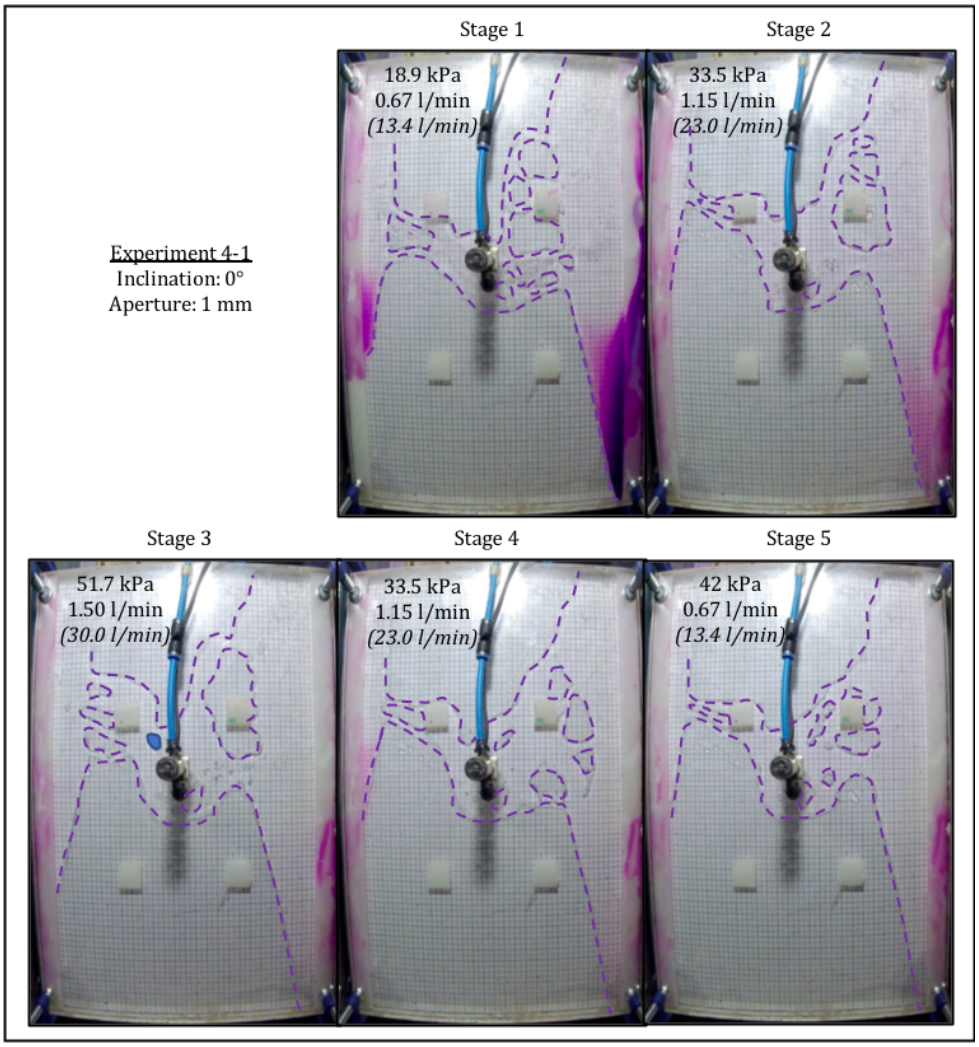

Figure 10-5 Flow behaviour during each stage of Experiment 4-1 (dotted lines indicate flow path (rivulets) boundaries; italicised values in parentheses refer to prototype scale).

The tendency for the flow paths to meander circularly outwards from the inlet and towards the spacers along the length of the fracture, was due to a combination of the position of the maximum centrifugal force acting perpendicular at the centre of the fracture (i.e. centrifugal force becomes decreasingly less than 20g further from this axis), coupled with the large capillary barrier that was present at the short unconfined boundaries of the fracture. Furthermore, the rectangular spacers within the fracture also acted to dictate the positions of these flow paths due to their inherent capillarity (and the ensuing hysteric behaviour). It is assumed that all rivulets were aperture-spanning, based on the sharp meniscus that formed; and was identified by the reflection of light off the edges of the rivulets.

Despite the rivulets forming liquid bridges across the aperture of the fracture (1 mm), the fracture area (perpendicular to the fracture) did not saturate during the experiment, and flow occurs preferentially. In this regard, the percentage area of the fracture (290 x 400 mm – *5.8 m x 8 m*) that saturated (area perpendicular to the fracture) during Pressure 1 is approximately 28%, increasing to 31% at Pressure 2, and then to 40% during Pressure 3. There was clearly

a gradual increase in the saturation adjacent to the inlet upon each increasing pressure interval, however; increases in the saturation was more noticeable in the fluid fingers farther from the inlet. This gradual increase in saturation at higher pressures was not constant across all fluid fingers, where instead some flow paths were narrower from one interval to the next; others were often wider.

10.3.2 Experiment 4-2: Inclined 1 mm aperture fracture

As Stage 1 was initiated, the hydraulic head rapidly increased as an excess amount of water was delivered to the standpipe. Fluid entered the fracture as a single wide rivulet that flows down the inclination of the fracture, establishing along its length within 1 second (*6.67 mins*). During Stage 1, the maximum width of the flow path was approximately 40 mm (*800 mm*) wide. Between 75 (*8.3 hours*) and 130 seconds (*14.4 hours*) into the test, a constant flow rate of 0.67 l/min (*13.4 l/min*) was recorded at the constant head achieved at Pressure 1 (18.9 kPa). The observed flow behaviour for each stage is shown in Figure 10-6. Stage 2 commences at 135 seconds (*15.0 hours*) into the test, and the hydraulic head gradually rised to the constant head required at Pressure 2 (33.5 kPa). A constant flow rate of 1.15 l/min (*23.0 l/min*) was achieved for 15 seconds (*1.6 hours*) during Stage 2 at the constant head for Pressure 2. The flow path increased to a width of 50 mm (*1.0 m*) during this Stage 2. A constant flow rate of 1.46 l/min (*29.2 l/min*) was recorded at 345 seconds (*38.3 hours*) during Stage 3 when a constant head was achieved at Pressure 3 (51.73 kPa). The width of the flow path increased slightly to 55 mm (*1.1 m*) during Stage 3. The wide rivulet that established within the fracture exhibits a wavy surface. During the subsequent descending stages, similar flow rates confirmed those recorded during the ascending stages at the same pressures.

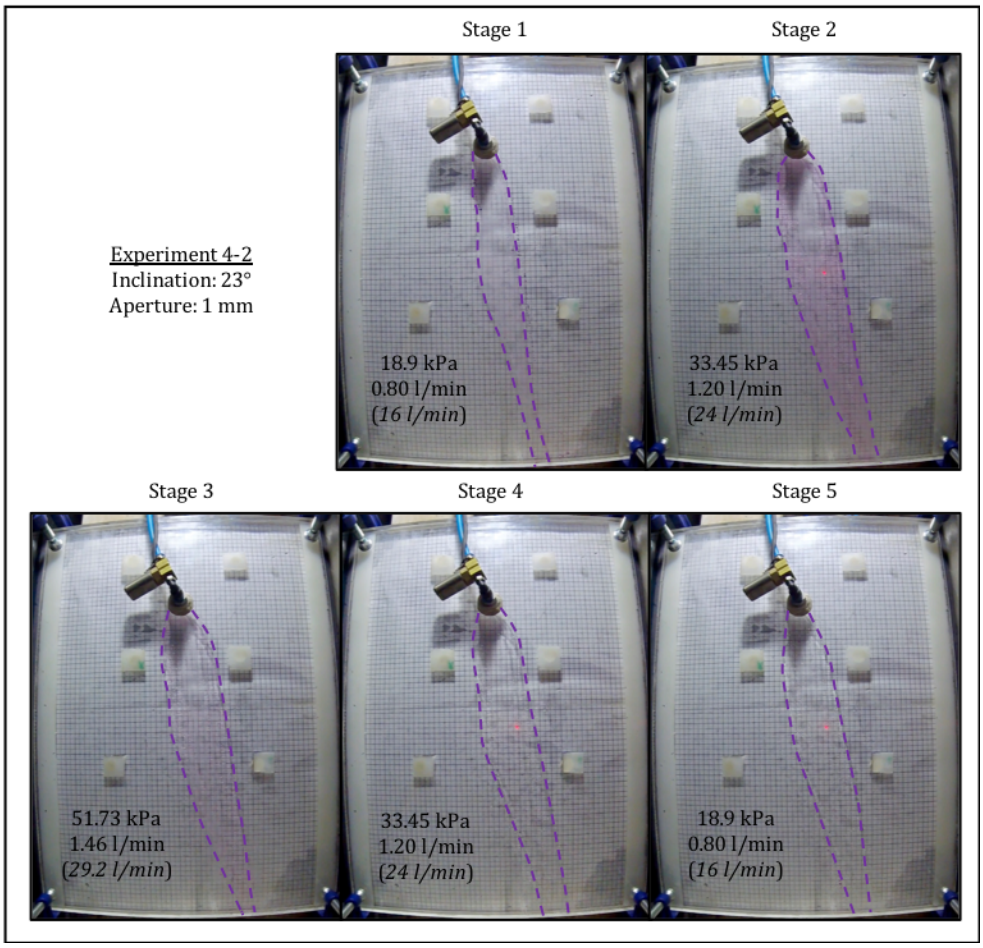

Figure 10-6 Flow behaviour during each stage of Experiment 4-2 (dotted lines indicate flow path (rivulet) boundaries; italicised values in parentheses refer to prototype scale).

The dimensions of the flow path was characterised by no noticeable increase in the saturation adjacent to the inlet during the increasing and decreasing pressure intervals. This cross-sectional width within the fracture (area parallel with fracture) directly adjacent to the inlet (borehole) remained the same at approximately 17 mm (*340 mm*). It was likely that upon increasing the pressure, the width of saturation increased, but this was likely not seen at the qualitative resolution of the camera and grid that was used. However; farther from the inlet, it is clear that the width of the flow path increases markedly upon the increasing pressure intervals. Here, the flow path attained its maximum width at 60 mm (*1.2 m*) down-dip of the inlet along the flow path, and increased from 35 mm at Stage 1 to 55 mm at Stage 3. Further along the flow path, the width pinched and became increasingly narrower towards the fracture exit, at its lower short boundary. Based on the flow of fluid from the inlet, fluid likely flowed up-dip of the inlet, but was mostly concealed by the opaque sealant surrounding it. This saturation that occurs up-dip of the inlet was therefore assumed to be a maximum of 10 mm (*200 mm*). Overall, the percentage area (area perpendicular to fracture) of the fracture that saturates during Pressure 1 is approximately 11%, increasing slightly to 13% at Pressure 2, and at the highest imposed hydraulic head (Pressure 3) the degree of saturation had only increased to approximately only 14%.

10.3.3 Experiment 4-3: Inclined 0.5 mm aperture fracture

The hydraulic head decreased as fluid entered the fracture during the initiation of Stage 1, causing a deficit water balance in the standpipe. Fluid entered the fracture as a single wide rivulet that flowed down the inclination of the fracture, establishing along its length within 1 second (*6.67 mins*). During Stage 1, the maximum width of the flow path was approximately 50 mm (*1.0 m*) wide. The observed flow behaviour for each stage is shown in Figure 10-7. During Stage 1, between 20 (*2.2 hours*) and 110 seconds (*12.2 hours*) into the test a constant flow rate of 0.63 l/min (*12.6 l/min*) was recorded at the constant head achieved at Pressure 1 (18.9 kPa).

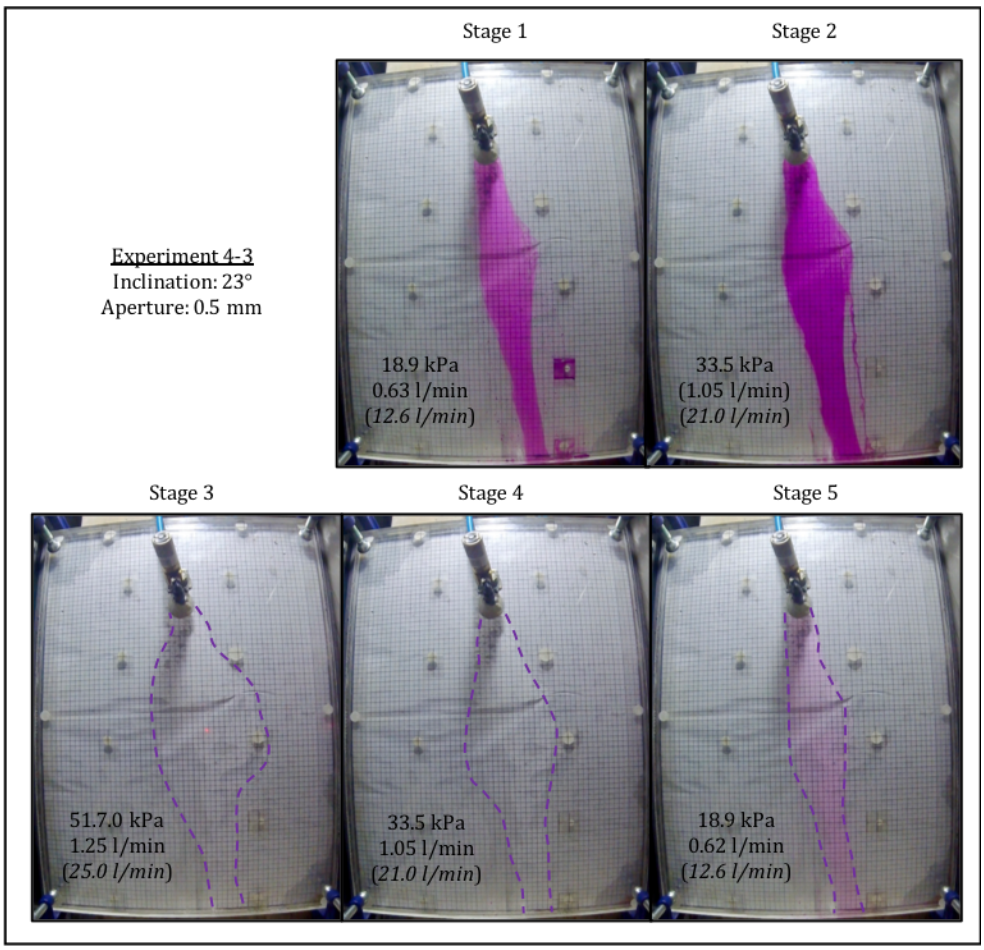

Figure 10-7 Flow behaviour during each stage of Experiment 4-3 (dotted lines indicate flow path (rivulets) boundaries; italicised values in parentheses refer to prototype scale).

Stage 2 commenced at 115 seconds (*12.8 hours*) into the test, however; due to cavitation in the water source pipe from the centrifuge platform it was difficult to achieve constant flow under the required constant head. Nevertheless, a constant flow rate of 1.05 l/min (*21.0 l/min*) was achieved for 7 seconds (*46 minutes*) towards the end of Stage 2 at the constant head for Pressure 2 (33.5 kPa). The flow path increased to a width of 65 mm (*1.3 m*) during Stage 2. A constant flow rate was achieved at 520 seconds (*57.8 hours*) during Stage 3 when a

constant head was achieved at Pressure 3 (51.73 kPa). The maximum width of the flow path increased to approximately 110 mm (*2.2 m*) during Stage 3. During the subsequent descending stages, similar flow rates confirmed those recorded during the ascending stages at the same pressures.

Throughout the increasing and decreasing pressure intervals, the dimensions of the flow path were characterised by no noticeable increase in the saturation adjacent to the inlet, and remained the same at approximately 70 mm (*1.40 m*). Once again, although possible widening did occur, this was not observable at the test resolution, which was dictated by qualitative nature of the camera and grid. The saturation up-dip was also assumed to be no more than 10 mm (*200 mm*) as it was mostly obscured by the sealant around the inlet. The flow path farther from the inlet markedly increased in width at higher pressures. Here, the flow path attains a maximum width 130 mm (*2.6 m*) down-dip of the inlet along the flow path, and increased from 50 mm at Stage 1 to 110 mm wide by Stage 3. Further along the flow path, this width again pinched and became increasingly narrower towards the fracture exit, at its lower short boundary. The overall percentage area of saturation (area perpendicular to the fracture) during Pressure 1 was approximately 11%, increasing slightly to 13% at Pressure 2, and at the highest imposed hydraulic head (Pressure 3) the percentage saturation had only increased to approximately 20%.

10.4 Analyses and Discussion

10.4.1 Lugeon (Lu) values

Assuming the length of the test interval, *L*, was assumed to be 1 m at prototype scale (50 mm in model dimensions) for the tests (i.e. 1 fracture intersects the 1 m test interval), the recorded flow rates (at prototype scale) are used to calculate the *Lu*-number for each step by Equation 3-2, with the calculated *Lu*-number per pressure interval for each test is shown in Figure 10-8. When inspecting the calculated *Lu*-number for each pressure step, the value calculated for the peak pressure at Stage 3 (51.7 kPa) is less than those for the two medium-pressures (Stage 2 and 4) at 33.5 kPa, as well as those for the low-pressure Stages (1 and 5) at 18.9 kPa. This suggests that all experiments display turbulent flow behaviour patterns. In this regard, the appropriate *Lu*-value is taken at the highest pressure (51.7 kPa) at Stage 3. Therefore, the reported *Lu*-value for Experiment 4-1 (horizontal 1 mm aperture fracture) is 591, whilst for Experiment 4-2 (inclined 1 mm aperture fracture) the *Lu*-value is 576, with Experiment 4-3 (inclined 0.50 mm aperture fracture) recording the lowest *Lu*–value of 493. These might appear unrealistically high, but considering the nature of the idealised smooth, parallel, clean, open fracture that was tested; the resulting high hydraulic conductivity should be represented by excessively high Lugeon-value's, respective to typical values obtained during field investigations.

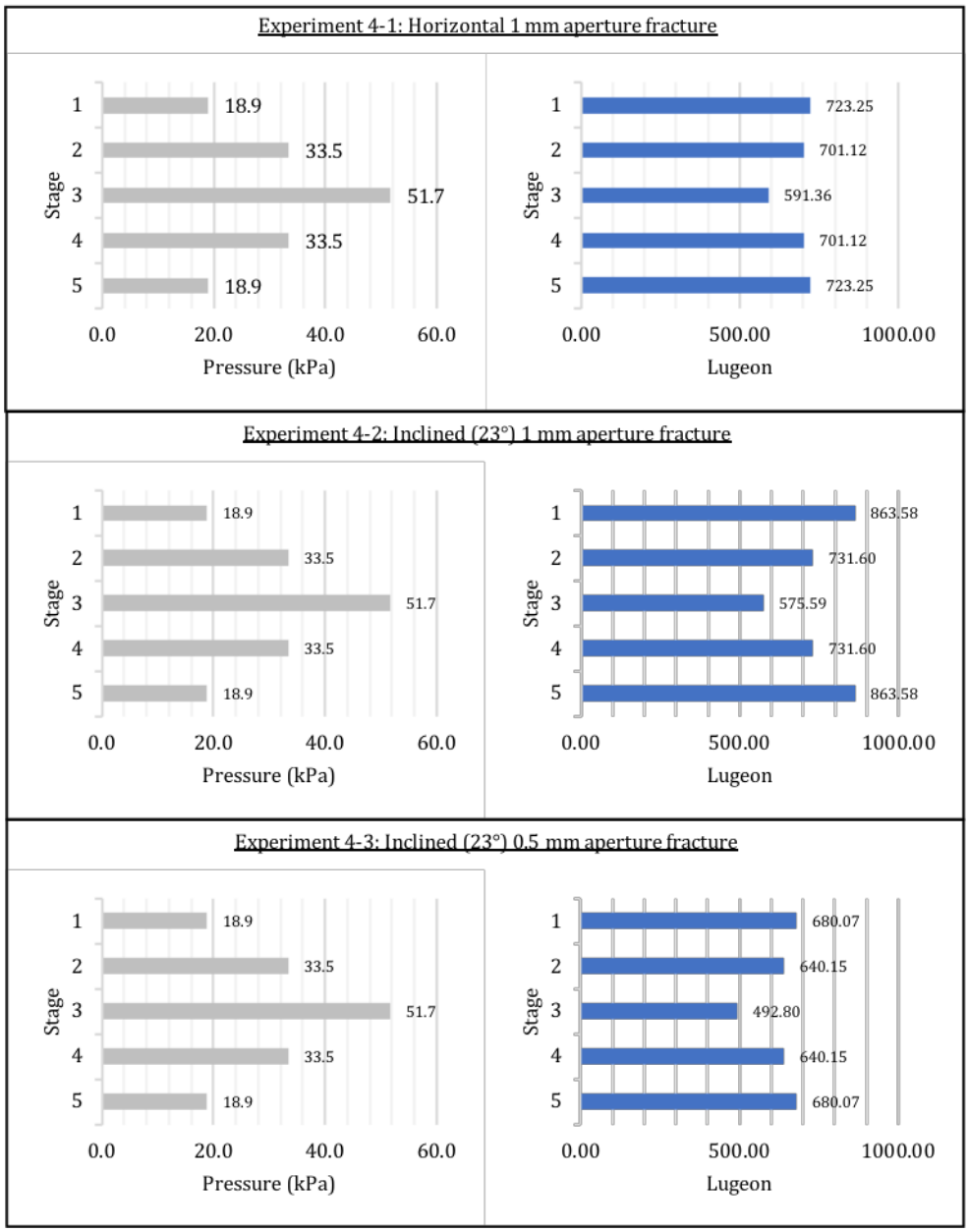

Figure 10-8 Pressures and corresponding Lugeon numbers for each stage during each experiment.

Although each experiment showed turbulent flow patterns, the most prominent turbulent pattern is seen in Experiment 4-2 (inclined 1 mm aperture). In this model, there is a noticeable decrease in the *Lu*–number as the pressure increases. In comparison, the tests conducted on Experiment 4-1 (horizontal 1 mm aperture fracture), and Experiment 4-3 (inclined 0.5 mm aperture fracture) are less prominent. In both of these tests, the decrease in the *Lu*–number between the lowest (18.9 kPa during Stage 1 and 5) pressure and the middle pressure (33.5 kPa during Stage 2 and 4) is not as significant as that recorded during Experiment 4-2 (inclined 1 mm aperture). This likely indicates differing onsets of non-linear flow (laminar to turbulent), whereby this point occurs at the highest-pressure interval (Stage 3) for Experiment 4-1 and Experiment 4-3. This observation is likely due to the stabilisation of fluid flow due to the increased saturation in the horizontal Experiment 4-1 (and associated tendency to simpler

single-phase flow conditions), and the smaller aperture of the inclined Experiment 4-3, respectively. Furthermore, results show that calculated *Lu*-values for the 1 mm aperture fractures (Experiment 4-1 and Experiment 4-2) are similar. In comparison, the *Lu*-value for Experiment 4-3 is lower and this phenomenon is associated with the smaller aperture that results in a lower hydraulic conductivity.

10.4.2 Pressure-Flux (PQ) relationships

The recorded pressures (expressed in mH_20) at prototype scale, versus the recorded fluxes (expressed in m^3/sec) at prototype scale are constructed for all experiments and are presented in Figure 10-9.

The diagrams largely reiterate the observations of the *Lu*-numbers, and show a gradual non-linear relationship during each of the experiments. Comparison of Experiment 4-1 and 4-2 (1 mm aperture fractures) show that similar fluxes (*Q*) are observed for the second (3.35 mH_20) and third (5.17 mH_20) hydraulic heads. The fluxes at these respective hydraulic heads are 3.38×10^{-4} m^3/sec and 5.0×10^{-4} m^3/sec for Experiment 1 and 4.0×10^{-4} m^3/sec and 4.9×10^{-4} m^3/sec for Experiment 4-2. Conversely, different fluxes are recorded at the lowest hydraulic head of 1.89 mH_20, whereby; during the lowest imposed hydraulic head (1.89 mH_20), a flux of 2.21×10^{-4} m^3/sec is recorded in Experiment 4-1, whilst in Experiment 4-2 a flux of 2.65×10^{-4} m^3/sec is recorded. This results in different points on the graph where linear flow ceases, and non-linear flow behaviour begins. In Experiment 4-1, this point occurs closer to the second hydraulic head (3.35 mH_20), whilst the non-linear behaviour gradually begins occurring after the first hydraulic head interval (1.89 mH_20) in Experiment 4-2. The observation of a linear relationship occurring at higher hydraulic heads in Experiment 4-1 is likely due to the higher degree of saturation in the fracture, between the first and subsequent hydraulic heads. The observation of this difference, between horizontal and inclined experiments, is indicative of the importance that the fracture orientation has on non-linear behaviour.

The influence of the decrease in aperture is highlighted during Experiment 4-3 (0.50 mm aperture), where all recorded fluxes are lower at the same hydraulic heads. The yield point at which linear behaviour ceases in Experiment 4-3 also occurs at the second hydraulic head. This can be explained by the effect that the decrease in aperture has on the hydraulic conductivity and resulting flux that can be accommodated through the fracture, which also acts to stabilises flow, and thus the onset of non-linear flow occurs gradually at increasing hydraulic heads.

Transmissivity was estimated using the Thiem equation, and the results presented in Table 10-1. Values for the radius of influence cited in literature have been used in field studies where one could not directly observe the radius directly. However, due to the transparency of the acrylic sheets used in this study, the radius of influence is equivalent to the cross-sectional area of the saturated flow path within the fracture aperture (i.e. parallel to fracture), directly adjacent to the inlet pipe. All values used to calculate the transmissivities by Equation 3-7 are prototype scale values.

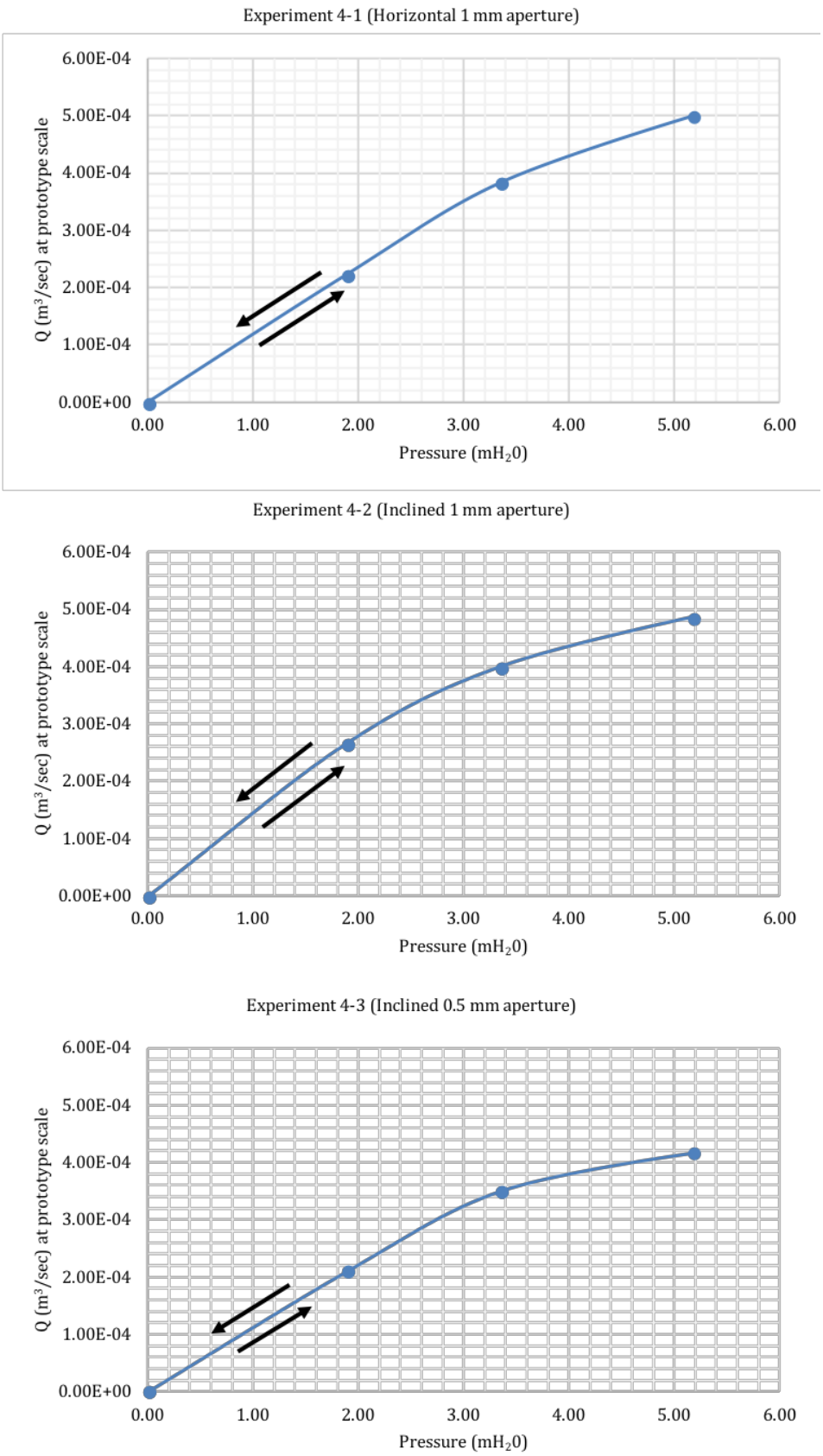

Figure 10-9 Pressure versus flux (*PQ*) diagrams per experiment.

Table 10-1 Calculated *T* values, as well as *Re* and F_o numbers (at prototype scale) for the first pressure step in the experiments.

Model	r_o (mm)*	T (m^2s^{-1})	*Re*	F_o
Experiment 4-1	22 (*0.44 m*)	3.85E-05	698	1.86
Experiment 4-2	17 (*0.34 m*)	3.19E-05	881	1.18
Experiment 4-3	70 (*1.40 m*)	4.97E-05	169	0.50

*ro = w

10.4.3 Reynold's Number (Re) and Forchheimer Number (F_o)

For fluid flow in fractures flow conditions are represented by the Reynold's Number (*Re*) and Forcheimer Number (F_o). Due to *Re* not being uniquely defined over the radial flow area as the hydraulic gradient decreases away from the borehole wall along the fracture, following the approach used by both Iwai (1976) and Quinn et al. (2011), all *Re* and *Fo* numbers are calculated for flow at the borehole wall where velocities are highest using Equation 2-16 and Equation 2-19 respectively. The calculated *Re* and F_o the first pressure interval for each model is presented in Table 10-1.

The volume of fluid flowing through the fracture renders the calculated *Re* high for both Experiment 4-1 and Experiment 4-2 (1 mm apertures). The *Re* is however lower in the horizontal test (Experiment 1) due to the lower flow rates, which is also likely a function of an increase in saturation around the borehole, which might act to stabilise flow due to the tendency to simpler single-phase flow conditions. The *Re* drops in Experiment 4-3 (0.5 mm aperture) due to the decrease in aperture, which results in a low hydraulic conductivity, resulting in a smaller flux through the fracture and a stabilisation of the flow path.

Considering previous results of laboratory experiments using single fractures (see for e.g. Konzuk and Kueper, 2004; Nicholl et al., 1999; Zimmerman et al., 2004) who observed the onset of non-linear flow to occur between a *Re* of between 1 and 5, the results presented here show that at the first pressure interval, flow has already entered the non-linear zone. The prevalence of this non-linear flow is in accordance with Widmann (1996), who states that flow is usually turbulent adjacent to a borehole during Lugeon tests due to the high flow velocities and associated pressure losses. Furthermore, the Forchheimer number (F_o) at the lowest hydraulic head in each test is also far greater than published values, such as Zeng and Grigg (2006) who suggest a critical F_o of 0.11, and Macini et al. (2011) who suggest a critical F_o of 0.40. Based on the calculated *Re* and F_o number's, the deviation is attributed to inertial effects that contribute to increasing non-linearity, as the fluid bends at the entrance to the fracture from the inlet, which is a phenomenon observed by Iwai (1976) for radial flow from a borehole.

10.4.4 Flow Mechanisms

In the models tested, flow occurs as rivulets that constitute the minority of the fracture, and gradually increase in cross-sectional width upon at increasing hydraulic pressures. These

preferential flow paths are highly anisotropic are characterised by instability, turbulence, non-uniformity, and irregularity. The flow paths in the inclined experiments are mostly characterised by a narrow width adjacent to the inlet (borehole), which widens further away to a maximum width, and then narrows again towards the fracture exit. Although lacking quantitative evidence, this could plausibly be the point identified by Widmann (1996), at which turbulent flow ceases and laminar flow establishes along the path. Notwithstanding, the widening outwards from the borehole to the position of the maximum width, is likely a function of the continuity principle; whereby a decrease in velocity results in an increase in saturation. The subsequent narrowing of the flow path width might thereafter be a function of the capillary barrier that is present at the short boundary of the fracture exit, which would result in a decrease in saturation and increase in velocity in order to breach the capillary barrier.

The observation of this increase and subsequent narrowing of the flow path dimensions farther from the borehole, highlights the importance of the statement by Widmann (1996) who called for a better understanding of the change in flow path geometry. Importantly, this change in dimension away from the borehole is not a function of any geometrical fracture property, but rather a function of the phase conditions (i.e. two-phase flow due to unsaturated conditions) within the fracture itself. This is particularly critical considering the homogenous nature of the model fracture (i.e. smooth parallel plates).

The flow observations are a function of the prevalence of cohesion, which results in gravity-driven flow in the open non-horizontal (Experiment 4-2 and 4-3) fractures at the higher degrees of saturations when modelling the Lugeon test. The observation of wide rivulets for these inclined fractures (Experiment 4-2 and 4-3) are in accordance with Su et al. (1999) for rivulets supplied by high flow rates, as well as the flow regime boundary diagram presented by Ghezzehei (2004). The prevalence of these observed wide rivulets occur due to the higher contact angle (and therefore reduced wettability) of the acrylic sheets as the material is moderately hydrophobic.

Under increasing influxes conditions these flow paths become unstable and these wide rivulets exhibited a wavy surface. In order to identify the flow regime boundaries for these waves, the classification provided by Patnaik and Perez-Blanco (1996, as cited in Ghezzehei 2004) is utilised, where the Re is multiplied by 4 to obtain the Re_s. The Re_s value for all Experiment's is greater than 200, suggesting that the main cause of the perturbation is an inertial force, whereby for Experiment 4-3 the resulting waves are laminar ($200 < Re_s < 1000$), and for Experiment 4-1 and Experiment 4-2 they are turbulent ($1000 < Re_s < 4000$). The implication is that the observed waves roll over the substrate film at a much higher velocity than the substrate. The implication for this is that stable flow regimes (rivulets and film) do not apply in this range, but the flow is not yet fully turbulent (i.e. Re_s is not greater than 4000).

The horizontal fracture (Experiment 4-1) mostly comprises fluid fingers which meander away from the inlet source (i.e. borehole). In contrast to the results presented by Jones et al. (2018a) the fracture does not fully saturate, because there is an insufficient volume of water provided from the inlet source to fully saturate the cross-sectional width of the fracture aperture (i.e. the Cubic law flux), whilst the hydraulic head in this research is almost 2 orders of magnitude

higher than the hydraulic heads recorded by Jones et al. (2018a). Unlike the experiments conducted by Jones et al. (2018a) who had a line source as their inlet, the inlet in these experiments is a much smaller point source, and is not be able to deliver the amount of fluid required to saturate the horizontal fracture.

10.4.5 Prediction of Non-Linear Results

In order to assess the non-linear results obtained in the experiments, the Forchheimer relationship as proposed by Schrauf and Evans (1986), in Equation 2-15, was used to predict the flow rate of the models at the imposed hydraulic heads. This allowed for the measured experimental results to be compared against the predicted values (both at prototype scale). Considering the smooth parallel Plexiglas sheets used in this study, a value of 12 is used for the coefficient a_D. and a friction factor f_D of 0.064 was used, resulting in the coefficient b_D equalling 0.032

In order to calculate the Forchheimer relationship using Equation 2-15, w is assumed as the width of the flow path (cross-sectional area of fracture at prototype scale) adjacent to the inlet pipe, rather than the full width of the fracture. However, the inherent problem with this approach is that the flow path width changes upon increasing the imposed hydraulic head. Nevertheless, due to the increase in width not being observed at the resolution of the experiments, a single representative width is used. The was deemed as appropriate due to the qualitative nature of the experimental data. The predicted flow (m^3/sec) for the models at each tested hydraulic head (mH_20) is shown in Figure 10-10. The Forchheimer equation is compared with respect to its ability to predict the observed Q on the basis of the imposed hydraulic head (mH_20), with the results shown in Table 10-2.

For this comparison, the Forchheimer model predicted the Q from the measured hydraulic pressure (dH), and these results are compared to the measured Q. In general, the Forchheimer model performs well in predicting the measured Q within the data collected for the experiments. The differences for all experiments show that the variance between the measured flow rate and the flow rate predicted by the Forchheimer model do not vary by more than 5% for any pressure interval in any of the centrifuge models tested. Experiment 4-2 (inclined 1 mm aperture) shows the best fit between the measured data from the centrifuge model and the flow rate predicted by the Forchheimer relationship.

By back-analysis, using the width of the flow path (w) used in the Forchheimer relationship, and assuming a Re of 5 (as cited in literature as being the critical value where linear flow cease), the Q value at which flow deviates from linearity can be calculated. The calculated flow rates are summarised in Table 10-3 and shows that flow deviates from linearity at very small injections (Q) for all centrifuge models tested.

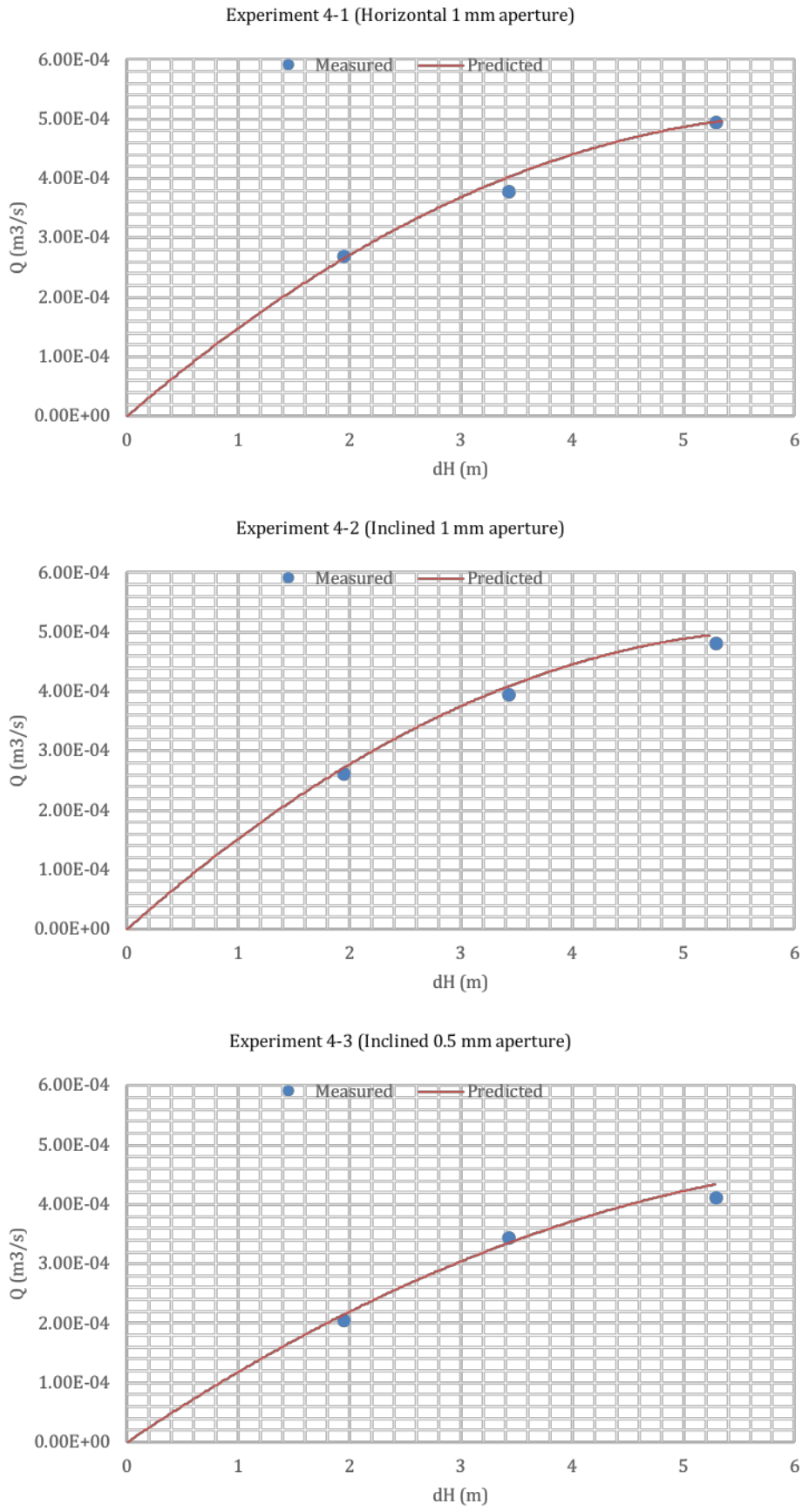

Figure 10-10 Forchheimer model prediction with measured values for each experiment.

Table 10-2 Comparison of predicted Forchheimer Equation with the measured data for each model (values are at prototype scale).

Measured *dH* (m)	Measured *Q* (m^3/sec)	Forchheimer *Q* (m^3/sec)	*w* at prototype scale (m)	Forchheimer % difference from measured *dH*
		Experiment 4-1 (Horizontal 1 mm)		
1.9266	2.73E-04	2.63E-04		-3.7%
3.4112	3.83E-04	4.00E-04	0.44	+4.4%
5.2751	5.00E-04	4.95E-04		-1.0%
		Experiment 4-2 (Inclined 1 mm)		
1.9266	2.67E-04	2.68E-04		+0.4%
3.4112	4.00E-04	4.05E-04	0.34	+1.3%
5.2751	4.87E-04	4.93E-04		+1.2%
		Experiment 4-3 (Inclined 0.50 mm)		
1.9266	2.10E-04	2.13E-04		+1.4%
3.4112	3.50E-04	3.34E-04	1.40	-4.8%
5.2751	4.17E-04	4.36E-04		+4.6%

Table 10-3 Measured flow rate (prototype scale) at which flow deviates from linearity assuming a *Re* of 5 for all centrifuge models.

	Experiment 4-1	Experiment 4-2	Experiment 4-3
Q (m^3/sec)	1.96E-6	1.51E-6	6.23E-6

10.5 Empirical Comparisons

The hydraulic conductivities (*K*) are calculated empirically using the measured Lugeon-values by the relationship proposed by Barton (2004) and Weaver and Bruce (2007) in Equation 3-4, and converted to transmissivities (*T*) using Equation 2-9 (Singhal and Gupta, 2010). These empirically derived *T* values are compared to the measured *T* values for the linear portion of the pressure-flux relationship and are presented in Table 10-4. Additionally, the saturated hydraulic conductivity (K_{sat}) and transmissivity (T_{sat}), as calculated using Equation 2-6 and Equation 2-9 (Singhal and Gupta, 2010) is presented. The results show the measured *T* values are 3 orders of magnitude less than those calculated empirically from the measured *Lu*-value. Such large discrepancies highlight the underestimation of hydraulic parameters derived using empirical relationships between hydraulic conductivity and *Lu*-values. Notwithstanding, the T_{sat} values calculated using the Cubic law differs by approximately 1.5 orders of magnitude compared to the T_{meas} values. This trend (of the T_{emp} values derived from the *Lu*-values being different to the measured T_{meas} and Cubic law derived T_{sat} values), is due to the empirical calculation from the *Lu*-value being a reflection of rock mass permeability (where several fractures will intersect the Lugeon test section). The published empirical

relationship is derived from field tests. In contrast, the measured and Cubic law derived transmissivities are representative of the hydraulic parameters of the individual discrete fracture (i.e. aperture). Notwithstanding, neither calculation accounts for the flow path behaviour (and degree of saturation) during Lugeon-testing and will also result in large uncertainties when defining the permeability of the fracture.

Table 10-4 Comparison of measured transmissivity values compared to values empirically derived from the measured Lugon-value.

Experiment	K_{sat} ($m.s^{-1}$)[a]	T_{sat} ($m^2.s^{-1}$)[a]	Measured		Empirical	
			T_{meas} ($m^2.s^{-1}$)	*Lu*-value	K_{emp} ($m.s^{-1}$)[b]	T_{emp} ($m^2.s^{-1}$)[a]
4-1	9.18E-01	9.18E-04	3.85E-05	591.36	7.69E-05	7.69E-08
4-2	9.18E-01	9.18E-04	3.19E-05	575.59	7.48E-05	7.48E-08
4-3	2.30E-01	2.30E-04	4.97E-05	492.80	6.41E-05	3.21E-08

[a]Singhal and Gupta (2010); [b]Barton (2004) and Weaver and Bruce (2007)

10.6 Summary

An experimental study using geotechnical centrifuge modelling to investigate the flow behaviour during Lugeon tests through a smooth, clean, open fractures under conditions of variable saturation is undertaken. The major findings of the research presented in this paper is summarised as follows:

- Flow from the inlet source (representing a borehole) occurs as preferential paths of turbulent, non-uniform, irregular rivulets that occupy the minority of the fracture area. The observation of such anisotropy is critical considering the homogeneity (i.e. smooth, parallel, and open) of the model fractures.
- Flow rates are not proportional to the cube of the aperture in unsaturated fractures, and under these conditions, as gravitational forces increase, a linear flow relationship ceases and flow is instead characterised by a non-linear relationship.
- Assuming a critical Reynolds Number of 5, back-analysis indicates that flow deviates from non-linearity at small fluxes which is consistent with previously published literature. Furthermore, this deviation from linearity at small fluxes is likely as a result of inertial effects due to fluid bending at the inlet source into the fracture.
- Deviation from linear flow occurs at higher hydraulic heads for flow in the inclined 0.50 mm aperture fracture (Experiment 4-3), as well as the horizontal fracture (Experiment 4-1). This can be attributed to the smaller aperture in Experiment 4-3, and the increased saturation in the fracture for Experiment 4-1, respectively. Conversely, deviation is observed at lower hydraulic heads in the inclined 1 mm aperture fracture (Experiment 4-2).
- Predicted results using the Forchheimer law compare well with the measured experimental results, when using the width of the flow path adjacent to the inlet source. The Forchheimer relationship has been used to describe non-linear flow in saturated

fractures due to the effects of fracture geometry (e.g. roughness, aperture etc.) and it is shown here that it may also be useful to better quantify flow through discrete fractures in the fractured vadose zone.

CHAPTER 11 DISCUSSION

11.1 Introduction

This final discussion is intended to coalesce the main findings of the flow mechanisms and quantitative data obtained during the tests, in order to elaborate on the critical contributions to the science of unsaturated flow in fractured rock masses. These critical findings are discussed such that they begin to extrapolate the experimental observations towards the implications on field techniques, by first linking them to the postulations from the De Hoop Dam case study. This preliminary extrapolation to field scale is the first step in understanding the application of the findings to applied rock engineering and hydrogeological practices. Additionally, the limitations of this research and the way forward for future research is discussed.

11.2 Assessing Geotechnical Centrifuge Modelling in Addressing Variably Saturated Fracture Flow

The observation of rivulets, and sliding droplet flow mechanisms, as well as film flow during the experiments is important. If one considers the phase diagram of Ghezzehei (2004), contact angles of 70° for the acrylic plexiglass used (e.g. Aouad et al., 2016; Della Volpe et al., 2002; Sumner et al., 2004) at the flow rates tested, rivulets and sliding droplets should dominate the observed flow mechanisms.

The sweeping of the wide films on vertical fracture walls, is due to a resultant force acting at an angle, due to the interaction between the centripetal force acting perpendicular to the centrifuge platform and gravity force acting towards the centre of the Earth. This influence is only noted for these films with large volumetric fluxes and are plausibly a function of the volume of water being transmitted. The path followed by the sliding droplets and rivulets within the fracture can be attributed to the wetting capability of the material as described by Doe (2001); whereby, generally the same cross-sectional drainage area re-saturates during rewetting.

When conducing physical models using the geotechnical centrifuge, it is important to evaluate the similitude between the tested model and the relevant prototype conditions. For immiscible fluid flow, similitude of the Capillary and Bond numbers, which describe the interaction of gravitational, capillary and viscous forces, only occurs when the characteristic length being investigated is macroscopic (Culligan and Barry, 1998), and for immiscible fluid flow in fractures it is important that inertial forces are negligible (Levy et al., 2002).

In the models constructed this is not the case as the 1 mm aperture is treated as a microscopic length and therefore means that scaled model results do not accurately represent natural conditions. Furthermore, calculation of the dimensionless α according to Levy et al. (2002) will result in the α always being greater than 2, and is described by the third regime as proposed by Levy et al. (2003), where inertial forces dominate flow. Notwithstanding, the

dimensionless α value is formulated for immiscible fluid flow between DNAPL and water and during derivation, which imposes an assumption that the density difference between the two fluids is small. This however, is not the case for these experiments and is therefore not applicable.

Despite the similitude failure of the Capillary and Bond numbers due to the fracture aperture being treated as microscopic, the Stokes number, which describes gravity driven flow instability, remains constant and suggests that the observed oscillating, meandering, flow switching, merging of rivulets, and wavy films within the model do occur in natural conditions. This reasoning is further supported through similar observations of flow mechanisms in the fracture in the form of sliding droplets with continuous threads, and the establishment of rivulets for both the 1g experiments and 20g accelerated experiments.

This signifies that although the results from the geotechnical centrifuge model may not be scaled to prototype conditions, the observed flow mechanisms and flow instabilities are representative of natural conditions. This good accordance between flow mechanisms observed in a geotechnical centrifuge and previous research indicates that the geotechnical centrifuge replicates variably saturated flow regimes acceptably.

11.3 Partially to Fully Saturated Flow through Smooth, Clean, Open Fractures

Smooth parallel plate models are constructed to evaluate how flow occurs through single horizontal and vertical fractures, aiming to assess the mechanisms and the applicability of the Cubic law in unsaturated conditions. Although full saturation is observed in the horizontal, smooth, clean, parallel plates test, this saturation is lost as the fluid exits at the vertical wall or fracture intersection. Here the flow regime is observed as exiting at discrete points of the fracture as non-uniform separate rivulets or droplets. Whereas horizontally orientated models appear to achieve full saturation under variable water supplies, the vertically orientated models never achieved near-saturated conditions. The validity of the Cubic law can be questioned from the results on a vertical, smooth, clean, parallel fracture, seeing that:

- Full saturation is not ever truly achieved, regardless of water supply;
- Flow remains as oscillating rivulets and, occasionally, as localised films (sheets) with substantial air pockets;
- Flow achieved is neither uniform and laminar; and
- The same flow regimes are observed even when water supply is from a saturated horizontal fracture with the same aperture.

If a fairly basic test such as this, aiming to directly mimic the smooth parallel plates model, violates the basic assumptions of the Cubic law, its use in numerical models should also be queried, for conditions of variable saturation. In aiming to understand discrete fracture flow at partial saturation, it becomes increasingly evident that a more fundamental knowledge gap exists in the understanding of not how *much* water flows through fractures, but rather how water flows through fractures *per se*. Using black box model or volume-effective approaches (i.e. bulk flow methods) can generally be estimated with a fair amount of confidence; however,

the problem faced relates to how water is transferred through individual fractures. In this regard, this research has proved, for instance, that:

- Saturated or annular flow is not likely achieved, especially in non-horizontal fractures, resulting in failure of the Cubic law.
- Preferential flow still occupies the vast minority of cross-sectional area in a vertical fracture, even if the water supply implies that it should achieve near-saturation.
- Movement of water through the fractured vadose zone becomes a matter of the continuity principle, whereby water is transported downward at significantly higher flow rates given the very low degree of water saturation in the vertical fractures compared to horizontal fractures.

The flow mechanisms observed in the experiments described above have been conceptualised in a flow chart, as presented in Figure 11-1. The flow chart, which adopts a similar type as presented in Indraratna et al. (2002), separates the observed flow types within the vertical fracture and from the horizontal fracture for different degrees of saturation from the different input influxes. The flow relationship observed in the vertical experiments as described in this paper can be summarised as follows:

a) Initial dry scenario of the vertical fracture representing a single-phase air flow system, where the air pressure is far greater than the water pressure.
b) Upon wetting, in both the intermittent influx and initial invading rivulet of the continuous influx tests, the fracture becomes that of a two-phase flow, represented by droplet flow (intermittent influx) and film flow (continuous test). In this scenario, the air pressure is still higher than the water pressure.
c) At higher influxes, in the continuous flow intervals, large air pockets are seen in the fracture. This flow represents a tendency to a more complex flow system, whereby flow is turbulent, non-uniform, and not saturated. It is inferred here, that if the vertical flow changes in orientation (vertical to inclined), the flow will revert to a two-phase flow system as shown in the horizontal scenario, b).
d) During the drying interval, static droplets are left as remnants on the fracture walls. These static droplets do not move as the surface tension is far greater than the weight of each droplet. Upon rewetting of the fracture, a two-phase flow system is again mobilised and the cycle loops towards b). If the cycle is not repeated, it is inferred that continued drying would occur until the system reverts back to a) whereby a single-phase air flow system is prevalent.
e) As full saturation is never achieved (or otherwise only achieved at unrealistically large influxes), the flow chart cannot progress towards a single-phase water flow system.

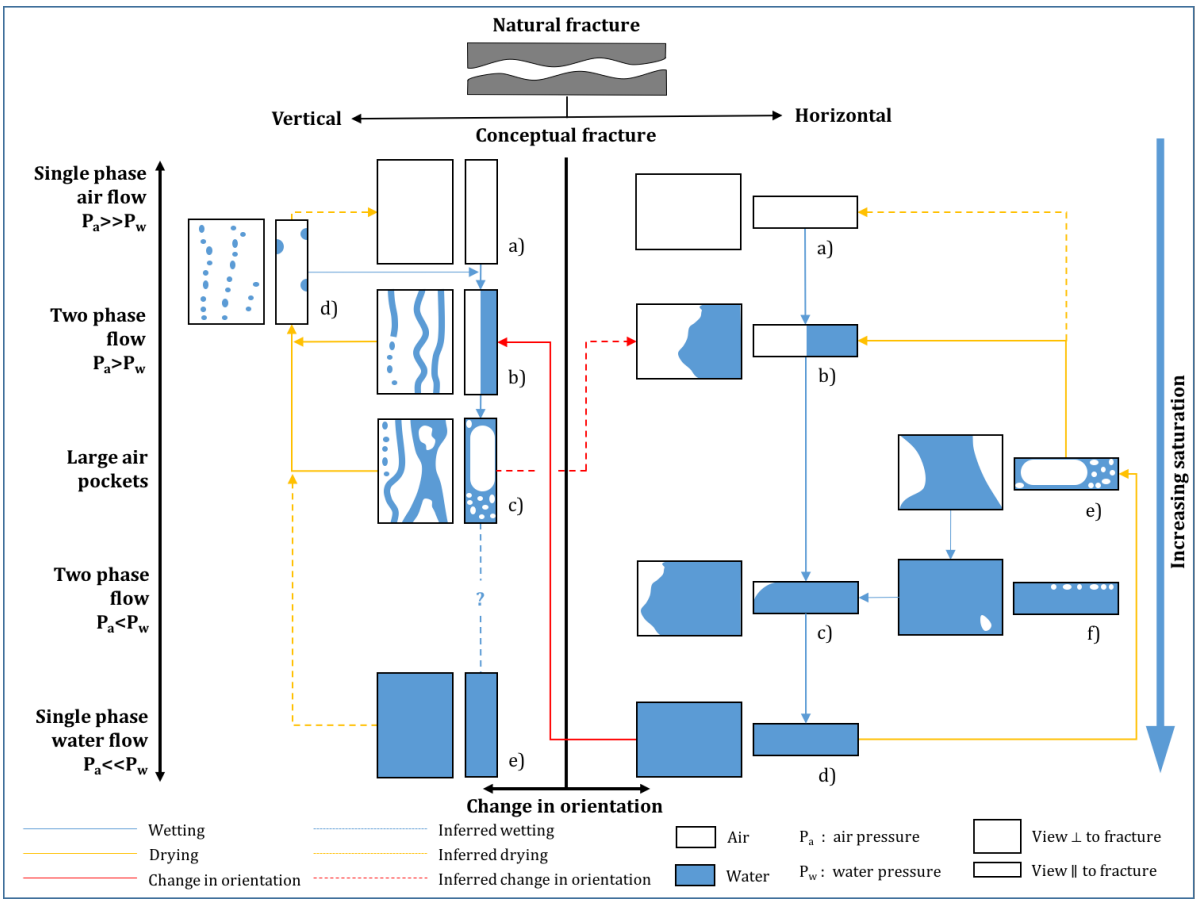

Figure 11-1. Flow relationships observed during the smooth parallel fracture experiments.

Subsequently, the flow relationship observed in the horizontal experiments as described in this thesis can be summarised as follows:

a) The initial dry scenario of the horizontal fracture also represents a single-phase air flow system.
b) Upon initial saturation, the fracture becomes that of a two-phase flow as the wetting front advances through the fracture. In this two-phase flow, the air pressure is still greater than the water pressure.
c) With increasing saturation of the horizontal fracture by the wetting front advancing through, the two-phase flow is characterised by a water pressure which is greater than the air pressure.
d) As saturation of the horizontal fracture occurs, the system becomes that of a single-phase water flow, whereby the air pressure is far less than the water pressure. At this point the water moves out of the saturated horizontal fracture onto the vertical face, whereby there is an immediate pressure reduction, with an associated velocity increase and a decrease in hydraulic head due to the change in elevation. Here the system reverts to b) on the vertical scenario, whereby a two-phase flow system occurs. Subsequently, this flow is then adsorbed into the process as discussed for the vertical scenarios, otherwise drying of the horizontal fracture will lead to a drying of the vertical

exit wall, and as such vertical scenario b) will move to scenario d). Notwithstanding, although full saturation is observed briefly in the 20g tests, the influx that this was observed at is deemed unrealistic for natural systems, and therefore can be disregarded for the purpose of the flowchart.

e) Subsequently, in the horizontal fracture upon drying, large air pockets invade and the system moves back to being that of a two phase flow at b). If drying continues, then the inferred progression will be back to that of a single-phase air flow system as represented by a).
f) If rewetting occurs, smaller air pockets are trapped in the fracture and represent a two-phase flow system, until the fracture is fully saturated and the cycle repeats.

11.4 Variably Saturated Flow at Fracture Intersections

The logical progression from the smooth parallel plate fundamental concept is the investigate how variably saturated flow occurs at fracture intersection. This progression allows for the systematic understanding of flow relationships in the context of the fracture network, and to assist in beginning to understand the observed field relationships.

11.4.1 Flow from a Horizontal Fracture to the Vertical With and Without an Intersection

When the vertical face (unconfined) in Experiment 1-2 is replaced with an intersecting vertical discontinuity (confined) in the form of a T-intersection as conducted in Experiment 2-1, there are some notable differences in the vertical flow mechanism. In the experiment without an intersection (Experiment 1-2), as the flow rate is increased per interval, the rivulets occupy an increasingly wider cross-sectional area of the vertical wall as they carry an increasingly larger volume of water from the horizontal fracture. Despite this increasing cross-sectional area, full saturation is still not achieved along the vertical face but rather only 20%, at the lowest influx interval, to 45% at the highest inflow interval, contributes to flow. When the unconfined vertical wall is replaced with an intersecting vertical discontinuity (Experiment 2-1), in the form of a T-intersection, only 22% of the vertical fracture contributes to flow.

Furthermore, there are 3 notable differences in the vertical flow mechanism observed between the confined intersection (Experiment 2-1) compared to unconfined experiment (Experiment 1-2) conducted without an intersection, namely:

1. The geometry of the vertical outflow occurs as fewer but wider rivulets, as opposed to the thinner and more frequent rivulets. The influx intervals in both tests are the same, and therefore the same volume of fluid is being transported along the vertical, but with different cross-sectional area saturation. This can be explained by the presence of the vertical fracture, where cohesive (water-water attraction) forces must overcome adhesive forces (water-Plexiglas attraction), which results in the formation of less rivulets, and more single wider flow paths.
2. The heads recorded in T-intersection experiment are lower than those reported during Experiment 2-1. This is also likely a function of the degree of saturation on the

intersecting vertical fracture compared to that of the vertical wall, as less rivulets occupy less cross-sectional area.

3. Although oscillation of rivulets occurs at the start of each new influx, and then stabilise, in the T-intersection experiment a fluid pool accumulates and spans across the fracture intersection, with the establishment of this fluid pool coinciding with the oscillation of the rivulets on the vertical fracture.

The proportional relationship between vertical velocity (V_v) and horizontal velocity (V_h), in both experiments (1-2 and 2-1) indicates that lower degrees of saturation results in a pressure reduction immediately and therefore an associated velocity increase and decrease in head-elevation, which leads to large variation in vertical linear velocity. As the degree of saturation increases, the influence of different influx rates does not affect the calculated vertical linear velocity as they appear to approach a constant range.

The observations from the horizontal fracture in both experiments follows the Cubic law, whereby the horizontal fracture is almost completely saturated (besides minor air pockets at lower influx intervals in the T-intersection experiment), before flow is observed exiting at the vertical wall or intersection. Although full saturation of the horizontal fracture is maintained, vertical flow is characterised by variably saturated flow with water exiting the horizontal fracture at discrete points as rivulets. Although previous experimental studies on fracture intersection has focused on flow occurring from the vertical fracture above an intersection, these findings of preferential flow paths emphasise the need to better understand the formation of slender pathways to develop from saturated horizontal fractures.

11.4.2 Flow into Non-Inclined Fracture Intersections

The findings of variably saturated flow from the vertical into non-inclined intersections echoes those of Ji et al. (2004); whereby, increasing the supply rate leads to the formation of continuous fluid rivulets that cross the intersection without interruption. This occurs despite some lateral ponding accumulating in the horizontal fracture at lower wetting continuous flow rates. Furthermore, the observations support the conceptual model of Glass et al. (2003); whereby, horizontal fractures on either side of the intersection are non-conducting in the role of unsaturated flow and fracture intersections.

When analysing the draining and rewetting intervals of their experiments, Glass et al. (2003) found that during reinvasion, intersections in the drained, stagnant initial state do not behave as capillary barriers. The fracture network is rapidly spanned, with fingers growing sequentially below each intersection, and suggests that open fracture intersections and investigated here also have a large hysteretic response. In this regard, when these intersections are initially dry, they wet under near zero pressure. Conversely, when the intersection is pre-wet, they are either initially filled with water or their invasion is facilitated to fill at pressures comparable to those of the fractures.

Glass et al. (2003) emphasise that this hysteretic behaviour shows the importance of the initial phase structure to guide the invasion process and thus emphasizes the critical importance of

history. Additionally, the scenario of only one side of the horizontal fracture filling, resonates with the findings of Wood et al. (2002), whereby discharge of the pool above the intersection involves at least partial filling of a horizontal fracture, as opposed to the more idealized concept of a perfect geometry leading to symmetric behaviour, and filling of both sides of the horizontal fracture.

Again, the observations in the experiment conducted show that unsaturated flow both focuses and converges flow (e.g. Experiment 2-2 at high continuous flow rates) as well as split flow (e.g. Experiment 2-2 at 1g and Experiment 3-1 at 1g) much like the dual behaviour reported by Glass et al. (2002a); LaViolette et al. (2003); and Nicholl and Glass (2002). Notwithstanding, a larger portion of flow splitting is observed, as opposed to the fewer flow converging scenarios, which also echo the findings of LaViolette and Glass (2004)

The findings of the intermittent influx at Experiment 2-2 at 1g also resonate the observations of the largest aperture fracture (0.671 mm) of Ji et al. (2006). Here, one of the horizontal fractures remains dry, whilst the other fills with fluid, and a stable tendril (rivulet) below the intersection is not developed. The maximum pool height (as calculated by the method of Ji et al., 2006) is 3.34 mm and a minimum height is 1.42 mm. This shows good agreement with the observations in the model for the initial invading droplet during the intermittent influx.

As the test progresses, however, the pool spreads laterally and parallel with the axis of the intersection. Within these larger aperture fractures, this pulsation whereby the pool grows and falls as the hysteric gate opens, might be offset, and rather it is the lateral spreading of fluid parallel with the intersection axis that is more important in this specific (wide, open) geometry. Inertial forces at the higher continuous flow rates used, will act to keep the capillary barrier open, and thus causing the rivulet to span across the intersection un-disrupted, as argued by Glass et al. (2003).

The lack of pool height as outlined in other previous literature, are therefore not a requirement for, where instead the pool of fluid spans either side of the intersection, as suggested by Wood et al. (2005). It is therefore alternatively proposed that for large aperture open fractures (as tested) that lateral pooling is less significant into the non-conducting horizontal fracture, where instead it is the lateral pooling parallel with the axis of the intersection that is the most relevant mechanisms at intersections characterised by such geometry.

11.4.3 Influence of the Orientation of Fractures on Flow at Intersections

In the 1g experiments, flow occurs as droplets occurring as liquid bridges (aperture-spanning flow) between the fracture walls, whilst in the 20g tests the flow paths occur as sliding droplets, rivulets and films only on the bottom fracture. The 20g therefore agrees with literature such as Doe (2001); Dragila and Wheatcraft (2001); Hsieh et al. (2001); Brouwers (2017); and Brouwers and Dippenaar (2018), where free film flow occurs on the lower fracture wall surface of the inclined intersection. In both the 1g and 20g experiments, the biggest influence that inclination has on flow at intersection is that the inclined sub-horizontal fracture becomes conducting. Flow in the inclined sub-horizontal fracture will depend on the wettability of the

material into which is flows, and can vary even in the same material (as observed in experiment 3-2 where one of the flow paths releases sliding droplets into the inclined sub-horizontal fracture after passing much less volume through it than the adjacent flow path).

Comparing Experiment 3-1 and 3-2 (specifically at 1g), it is obvious that the direction of flow of fluid entering the fracture is important, as suggested by Wood et al. (2005). In the inclined orthogonal intersection experiments with flow from the inclined sub-vertical fracture; as the fluid passes down the fracture, at the intersection it turns toward the inclined sub-horizontal fracture down-dip of the intersection. This does not occur in the experiment where flow occurs from the inclined sub-horizontal fracture up-dip the intersection, as they are not connected. Instead in this experiment, the corner of intersection is encountered first which results in the fluid preferentially flowing sub-vertically instead of sub-laterally across the intersection.

At extremely high flow rates (observed in the continuous influx intervals) the orientation of the fracture also had no influence on diverting flow into an inclined sub-horizontal fracture, where continuous rivulets crossed the intersection and continued in the inclined sub-vertical fracture below it, much like that observed in the non-inclined experiments. Only small volumes of water diverted into the inclined sub-horizontal fracture and released a sliding droplet which travelled along the down-dip intersection. When flow does occur in the inclined sub-horizontal fracture down-dip of the intersection, snapping rivulets form, as observed in Experiment 3-1 at 1g. This occurs as the amount of water available to ensure its continuity is not capable of keeping the rivulet a continuous flow path. This process might be enhanced in natural fractures where apertures vary, and contact angles are lower. In this regard, supply rates and apertures may allow a rivulet or film to be maintained for much longer.

11.5 Implications of Non-Linear (Non-Darcian) Flow in Variably Saturated Fractures

Although Experiment 4 aimed at quantifying the non-linear flow behaviour, it is duly noted that the calculation of the Forchheimer relationship is based on a fixed width at each interval. This is likely unrealistic, as in natural fractures where apertures are smaller, the cross-sectional area of saturation is likely to widen upon increasing hydraulic pressures. Therefore, using this approach will be difficult to adopt and estimate in practice. This possible widening in the cross-sectional area of saturation was difficult to quantify, as small increases in the width were not possible to observe as the scale was not at a resolution great enough to assess the increase in flow path width.

Although it is cautioned against the extrapolation of the results of this idealised model set-up to an *in-situ* rock mass, the potential relevance of these fundamental findings to broader field applications cannot be ignored due to the repeated call for a systematic understanding of the preferential flow paths that govern rock mass permeability. The potential for the misunderstanding of non-linear behaviour during Lugeon tests at partial saturation is essential when considering that turbulent behaviour is the result of fluid flow conditions, instead of the geometric properties of a fracture(s). This can result is a misinterpretation of the hydrological nature of fractures within the rock mass; whereby, non-linear behaviour is attributed to the presence of a rough fracture set (resulting in a pressure drop formed by eddies within the

roughness of the fracture) instead of the flow behaviour being a function of the unsaturated conditions.

Furthermore, Lugeon tests conducted in an initially unsaturated rock mass might misrepresent the hydrogeological regime, which would behave differently under saturated conditions. One can hypothetically exemplify this by considering Lugeon tests conducted within the intermediate vadose zone (unsaturated rock mass) during investigation of a dam site, and could lead to a mischaracterisation of the rock mass permeability. This misunderstanding would only become apparent once saturated phreatic conditions are achieved after reservoir impoundment. This postulated implication is illustrated in Figure 11-2, and described hereafter.

Consider a discrete discontinuity, within this rock mass, which intersects a Lugeon-test section being undertaken during the exploration phase of a reservoir site along the dam wall centreline footprint. The rock mass is located within the intermediate fractured vadose zone, such that the discontinuity is in turn characterised by variably saturated conditions. Based on the experimental results (Experiment 4), this fracture may result in the Lugeon-tests exhibiting a turbulent flow behaviour. In such an instance, the Lugeon-value is taken from the highest imposed hydraulic pressure. However, theoretically if the discontinuity is saturated, then flow should be laminar, and the Lugeon-numbers over all pressure stages are averaged to give the Lugeon-value. This will result in a lower Lugeon-value for the unsaturated discontinuity (during the exploration phase in the intermediate vadose zone) compared to the Lugeon-value of the saturated discontinuity (after reservoir impoundment and the subsequent formation of phreatic conditions), which will be higher.

The corresponding *PQ* diagram for the unsaturated discontinuity is non-linear. Therefore, the flow recorded at the highest imposed hydraulic pressure (typically equivalent to the anticipated hydraulic head once reservoir impoundment has occurred) during the Lugeon-test would result in the incorrect estimation of the flux that is to occur through the fracture. During dam construction and subsequent reservoir impoundment, the rock mass becomes increasingly saturated (due to the formation of phreatic conditions). This saturation (single phase flow through a smooth parallel open fracture) theoretically should result in a linear flow relationship through this fracture. Therefore, under the imposed hydraulic head of the reservoir, the flux that occurs through the same discontinuity will be much higher than that estimated during the Lugeon-test during the exploration phase. Therefore, this leads to an underestimation of the hydraulic conductivity of the fracture, and shows how variably saturated fracture conditions can have different implications for a project over its life cycle (from investigation, to construction and monitoring). The same application can be hypothetically exemplified for an unlined water tunnel, which will introduce water (which will increase saturation due to the formation of phreatic conditions) into the rock mass during the project life cycle. Flow through an unsaturated fracture would therefore also be underestimated and incorrectly designed for in the grout operation during tunnelling, and potentially leading to significant water losses. Notwithstanding, it is noted that these hypothetical examples do not take into account the complex effects of grouting operations.

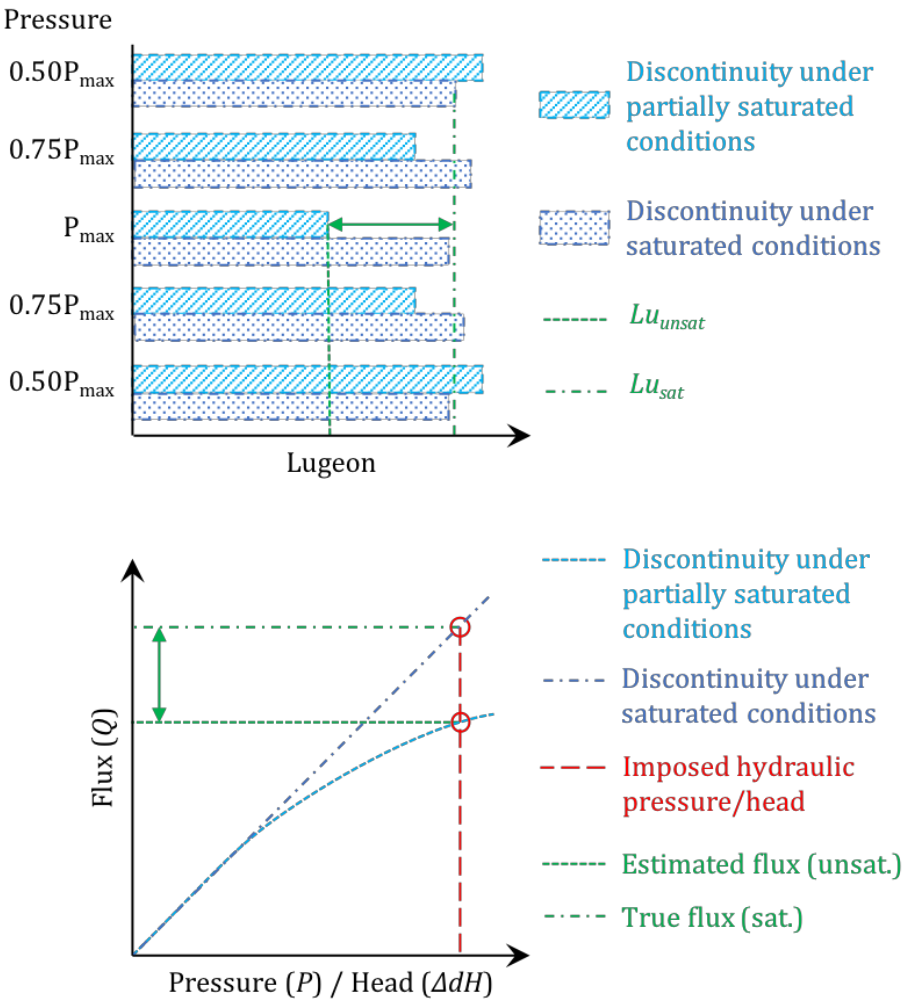

Figure 11-2 Schematic showing how the flux occurring through a fracture can be underestimated during the investigating phase, when Lugeon-tests are conducted under variably saturated conditions.

Although the findings are preliminary in their fundamental concept, they have significant relevance in the investigation and design for dam sites, where rock mass permeability derived from Lugeon tests are underestimated. This lack of understanding fracture flow mechanisms in unsaturated conditions in the field, is supported by the field relationships analysed at De Hoop Dam, where better correlations between Lugeon test and the grouting operations occurred towards the river section where wetter conditions were encountered (as opposed to the drier unsaturated conditions at the left flank). Significant amounts of leakage that required remedial works occurred through the foundation rock mass in the left flank during reservoir impoundment and based on the experimental results is a result of the underestimation of the hydraulic properties during the Lugeon-tests conducted during the investigation phase as well as Lugeon-tests conducted in primary grout boreholes during construction.

This misinterpretation could also be exemplified by an opposing example; whereby, a transport tunnel, which is initially (during investigation phases) under conditions of higher saturation. When the tunnel is constructed, it acts as a drainage feature and de-saturates the rock mass.

This would result in a lower *Lu*-value (and subsequent hydraulic conductivity value) during construction than that quantified during the Lugeon test (and subsequent hydraulic conductivity) during the investigation phase, intersected by a fracture. Consequently, the grouting strategy would have been overdesigned for the fracture, as the it would accurately be characterised by a lower hydraulic conductivity later on in the project life cycle.

11.6 Characterisation of Variably Saturated Rock Masses

Critical fracture parameters such as orientation, aperture, roughness, infill, connectivity (continuity) and spacing are included in the standard joint line survey data collection process during geotechnical site investigations. The data are applied in rock engineering to model the rock mass with regards to its classification, subsequent support (i.e. for tunnelling), dam foundation stability, rock slope stability analysis, etcetera. The potential for investigating the possible link between discontinuity descriptors and rock mass permeability cannot be overemphasised. Such a link would benefit fieldwork greatly, in developing better hydrogeological models for input into rock engineering and geotechnical applications. Such implication will assist in the better interpretation of Lugeon test results. Subsequent applications will likely assist in planning grouting programs with better accuracy. Notwithstanding, this would involve correlating this complicated topic of two-phase preferential (variably saturated) flow with the rheology of grout.

In order to better classify unsaturated rock masses according to its permeability, it might be necessary to assign a single number to describe a set of observed variables. However, any correlation needs to understand and interpret the role of each variable on the rock mass permeability. Traditional rock mass classification systems take observations of several engineering geological characteristics and assign numbers to them, which are then summed in some way to give a single value, and is often assumed to represent total knowledge of the rock mass. Based on recent statements by Eggers (2016), there will be significant danger in using this approach to describe and represent rock mass permeability, because a classification rating provides no information on the collection of physical attributes that make up a rock mass and therefore a rating is unable to promote an understanding of the fracture properties on unsaturated flow behaviour and process.

Although this study has not necessarily provided an answer, or provided a new replacement to describe unsaturated fracture flow through discrete fractures, it does explain the flow deviations for commonly applied saturated approaches. In this regard, previous saturated conditions assumed or used in calculations are incorrect, as this research has identified how fractures and their orientations can influence flow mechanisms. This has implications in pore pressures, where saturations of 20% to 30% (as observed) suggest a reduced pore pressure on the individual fracture surfaces. Larger flow rates and degrees of saturation are anticipated from horizontal compared to vertical or inclined discontinuities. This implies that the recording of fracture orientations is as important (or arguably more important) than recording fracture geometrical properties such as roughness and aperture, when considering rock mass permeability. Furthermore, it is clear that the fracture width needs to be adjusted for the flow path width in correctly calculating the hydraulic properties of variably saturated fractures.

11.7 Limitations and Lessons Learnt

The research as discussed in this thesis is limited to the smooth parallel acrylic fractures with open (0.5 mm to 1 mm), clean apertures, modelled at accelerated conditions in a geotechnical centrifuge. With this is mind, the hydraulic conductivity of fractures is dependent on the fracture aperture, roughness, infill, stress conditions and geometrical properties, and these properties will have needed to be represented accurately in subsequent studies. However, with little advancements with regards to the implications of partially saturated flow on permeability assessments, starting at fundamental concepts is essential. Notwithstanding, future experiments need to address the utilisation of better analogue rock material, as well as consideration of the fracture network (e.g. intersections of discrete fractures). Specifically, the materials used to address unsaturated flow in fractures will need to better mimic the surface characteristics (i.e. contact angle) such as promoting stable film flow on natural fracture surfaces.

As it has been duly noted previously, the calculation of the Forchheimer relationship is based on a fixed width at each interval and in natural fractures where apertures are smaller, the cross-sectional area of saturation is likely to widen upon increasing hydraulic pressures. Therefore, using this approach will be difficult to adopt and estimate in practice. Nevertheless, the Forchheimer relationship performs significantly well, but additional quantitative studies (both laboratory and field) are required to aid in developing better numerical models. At this stage, any further quantification of parameters using existing empirical approaches will obscure the findings, as most such approaches have very specific limitations, none of which this research aimed to duplicate.

11.8 Recommendations for Future Research

The findings as presented in this thesis need to be validated against similar tests conducted in both the laboratory as well as in at a larger scale in the field. This can be done both in the mesoscale laboratory experiments on fractures and fracture networks to observe flow regimes on natural rock surface. Such experimental work will need to be linked to a larger controlled field experiment, which would subsequently allow linking large-scale data between the smaller-scale individual processes.

The following outlines the fracture properties that need to be incorporated into experimental modes, before progressing to larger field-scale models and data:

i. Roughness.

Both small-scale (asperities) and large-scale (waviness) roughness will need to be considered. This will ultimately result in between modelling contact angles closer to reality and would allow a comparison to identify the likelihood of adhesion to discontinuity surface. Such influence may result in significant lateral flow as water moves into near-horizontal discontinuities due to adhesive forces exceeding cohesive forces. Furthermore, the role that contact obstacles have on variably saturated flow processes will need to be investigated over varying inclinations (i.e. vertical versus horizontal)

ii. Aperture.

Subsequent studies will need to address analogous apertures. In the experiments presented in this thesis, the large apertures provide less contact area between fluid and fracture surface and thus favour gravity forces. Conversely, narrower apertures will provide more contact between fluid and the fracture surface, and therefore likely to favour capillary forces. Aperture studies will need to supplement the findings already made by Segole (2018), by modelling tighter aperture fractures consistent with *in situ* fractures.

iii. Orientation

Although addressed in the experimental setups in this thesis, additional models will need to incorporate other discontinuity parameters into the investigation of the influence of orientation on variably saturated flow processes. Furthermore, orientations other than vertical, horizontal and 23° inclined fractures will need to be addressed.

iv. Infill

The influence of infill material obviously affects the aperture available for the transmission of fluid. In this regard, the infill aperture refers to the aperture with infill material of given hydraulic conductivity, which is different from that of the rock itself, will need to be modelled over the hydraulic aperture, which refers to the open aperture that can be related to a localised smooth parallel plate model.

v. Material type (i.e. contact angle and its relationship to wettability, imbibition etc.)

The rock material type will also need to be modelled more accurately. The type of rock material will influence the flow due to differing contact angles, and the rock forming minerals' role on wettability. The incorporation of rock material will likely result in imbibition, and will need to be quantified using a dual-porosity model.

vi. Intersections

Future models will need to consider all the above variables and begin modelling them to the understanding of the fracture network. The logical process is to model the above variables at fracture intersections and increase the scale thereafter.

vii. Field testing

Further validation will also be quantified *in situ* via field testing techniques, such as comparing results from Lugeon tests to that of optical and acoustic televiewers down boreholes. More complex field quantification, such as 3D permeability testing (or hydrotomography - see Quadros and Correa Filho, 1993, for example), should also be incorporated into this field quantification.

11.9 Summary of Research and Main Findings

Variably saturated flow through discrete open fractures is investigated. The initial phase comprises the analyses of results from field data from the investigation phase and grouting operations at De Hoop Dam. This was conducted in order to guide an experimental phase by identifying the field parameters that influence variably saturated flow process *in situ*. Subsequently, a series of experimental studies using geotechnical centrifuge modelling to investigate the flow behaviour through discrete smooth, clean, open fractures under conditions of variable saturation is undertaken. The major findings of the research presented in this thesis is summarised as follows:

- The validations on the field data from De Hoop Dam highlight that the orientation of the joint set likely results in a positive or negative correlation between the compared parameters. Furthermore, an increasingly better correlation between Lugeon and grouting data for the foundation rock mass towards the river section is noticeable, where wetter (increasingly saturated) conditions are encountered.
- Flow visualisation experiments are conducted on a transparent replica of the smooth parallel plate model, with inlet conditions of constant pressure and differing flow rates over both vertical and horizontal inclination. Findings from this initial experiment show that saturated laminar flow is not likely achieved, especially in non-horizontal fractures, where instead preferential flow occupies the minority of cross-sectional area despite the water supply. Furthermore, geotechnical centrifuge modelling is shown to replicate similar flow mechanisms for unsaturated fracture flow, as previously observed in literature.
- Investigation of variably saturated flow through non-inclined fracture intersections find that draining of a saturated horizontal discontinuity occurs by wider preferential capillary flow paths with an intersecting vertical discontinuity, in comparison with an unconfined vertical wall. Flow into a non-inclined open fracture intersection tends to accumulate parallel with axis of the intersection, instead of growing and receding pool heights as observed for previous smaller aperture models as presented in literature.
- Observation of flow through inclined fracture intersections shows that the inclination of fracture intersections results in an inclined sub-horizontal fractures down-dip of the intersection becoming a conducting path for fluid flow. Furthermore, flow into an inclined sub-horizontal fracture is dependent on the direction of the flow of fluid entering the fracture intersection (i.e. either from an inclined sub-horizontal fracture up-dip of the intersection or an inclined sub-vertical fracture below the intersection).
- Non-linear flow during Lugeon tests shows that predicted results using the Forchheimer law compare well with the measured experimental results, when using the width of the flow path adjacent to the inlet source. The Forchheimer relationship has been used to describe non-linear flow in saturated fractures due to the effects of fracture geometry (e.g. roughness, aperture etc.). However, results presented here show that it is a useful relationship to better quantify flow through discrete fractures in the fractured vadose zone.

- A contributor to the observed field relationships at De Hoop Dam, based on the experimental results, is the degree of saturation of the rock mass, which influences the flow regimes during the Lugeon tests. This highlights the implication that variably saturated conditions in fractured rock masses can have at different stages of a project life cycle.

CHAPTER 12 CONCLUSIONS

In conclusion:

i. Geotechnical centrifuge modelling is a proven and viable experimental tool for the replication of similar flow mechanisms for variably saturated fracture flow, as previously observed in literature;
ii. Findings from this research proved that saturated laminar flow is not likely achieved, especially in non-horizontal fractures. In vertical fractures, preferential flow occupies the minority of cross-sectional area despite the water supply;
iii. Movement of water through the fractured vadose zone is a matter of the continuity principle, whereby water is transported downward at significantly higher flow rates given the very low degree of water saturation. Based on the analyses and results, it is hypothetically improbable to achieve saturation in vertical fractures under free-draining wetting conditions. It does become possible under extremely excessive water inflows or when not free-draining. However, the converse is not true, as a wet vertical fracture can be drained;
iv. Furthermore, measured flow behaviours of the preferential pathways in variably saturated fracture indicate non-linear (non-Darcian) flow that can be successfully described and evaluated using the Forchheimer law. The Forchheimer relationship can therefore in the future be used to describe variably saturated flow in discrete, open fractures; and
v. This study does not provide an answer or a new replacement to describe variably saturated fracture flow through discrete open fractures; however, it ultimately begins to provide preliminary answers to explain the flow deviations for commonly applied saturated Darcian-based approaches. In this regard, previous saturated conditions assumed or used in calculations are incorrect, as this research emphasises how fractures, their variably saturated conditions and their orientations influence flow mechanisms.

The research underlines primary issues, that have not previously been published, on variably saturated flow. The relevance of how flow occurs through fractures at partial saturation in the rock engineering context is understated, especially given the quest to achieve better quantification of permeability calculations from Lugeon tests during site investigation stages. The results prove that using broad empirical correlations to define hydraulic conductivities of Lugeon test intervals from Lugeon-values is cautioned. Classical and commonly used volume-effective (bulk) approaches do not contribute to fundamental research questions and require a deeper understanding of the small-scale processes in the porous fractured systems that characterize the intermediate fractured vadose zone. Ultimately, finding a suitable representation of an analogous fractured rock mass is difficult, and at process scale's the best one can do is to isolate individual processes.

Although fundamental studies are gradually improving our understanding, many more studies are required to obtain a unified view of unsaturated (preferential) flow through fractures. More importantly, additional studies will allow to link observed processes in between scales. Ultimately, continued research into each isolated process, will formulate a clear understanding of *how* flow occurs through discrete unsaturated fractures, before the necessary and more precise quantification of *how-much* flow occurs through these fractures.

The implications of better understanding of partially saturated flow through rock mass fracture networks are numerous. Worldwide surface infrastructure is presently extending skywards as well as to deeper depths below surface. The increased need for natural resources also implies deeper mines, larger dewatering cones around mines, dewatering of rock aquifers, increased size and toxicity of waste disposal sites, deep nuclear waste repositories, both on land surface and in subsurface excavations. Prospects of deep hydraulic fracturing (fracking) for shale gas or coal-bed methane raise questions about upward migration of hydrocarbon liquids and gases, potentially rendering groundwater aquifers susceptible to contamination. These anthropogenic activities impact on the hydrosphere and lithosphere and need to be quantified to determine negative impacts and remedial measures.

The quantification of water movement through rock masses also has enormous economic implications. Water inflow into deep mines, building basements, civil engineering tunnels (water and transport), subsurface waste disposal sites (nuclear and other) and large rock caverns (hydro-electric and storage facilities), and through dam wall foundations, needs to be quantified to create safe operational conditions whilst optimising the design.

Linking available data from atmospheric water, surface water and groundwater is an issue, as the vadose zone is often seen as a bulk (black box) systems not demanding sufficient investigation and understanding. Furthermore, geotechnical applications frequently base investigations on conservative saturated estimates, and do not incorporate the very significant influence of changing saturation. This research shows that: i) saturated estimates from testing cannot be expanded into the project life cycle; ii) empirical approaches can be more wrong than right; and iii) designs cannot be optimised without a very good understanding of the extremely complex flow conditions in natural and engineered rock masses.

ACKNOWLEDGEMENTS

Undoubtedly, the most pleasant part of completing such work is the opportunity to thank those who were involved; however, the list of expressions of gratefulness is always inadequate and incomplete. This page of acknowledgements cannot begin to satisfy the overwhelming gratitude that I have for those that were involved.

To my supervisors, Louis Van Rooy, and Matthys Dippenaar, your support and mentorship, over many coffees and beers is enormously appreciated. Thank you for allowing me the opportunity to conduct this work under your guidance and knowledge; but mostly, thank you for your friendship and memories that we have shared over the past years. The Kalahari seems to be a mecca for producing theses, papers, and poignant research questions, and I look forward to many more trips with you (albeit without the incorporation of any theses). Gratitude is further extended to the examiners, for the time taken to examine and contribute to this thesis.

A huge amount of appreciation is extended to the Water Research Commission (WRC) for their financial assistance by project K5/2326, as well as to the project reference group: Dr Shafick Adams; Professor Danie Vermeulen; Dr Jaco Nel; Mr Martiens Prinsloo; Mr Dawid Mouton; and Mr Frikkie Koen. Your supervision, comment and input provided valuable direction to this research. I would also like to thank the Department of Water and Sanitation (DWS) of South Africa as well as Knight Piésold for making the De Hoop Dam data available. To my research colleagues; Luke Brouwers, Katlego Segole, Kobus Roux, and André Joubert thank you for your input and beverages shared. The financial assistance of the National Research Foundation (NRF) is also hereby acknowledged.

Lastly, the role that my family had on this work is enormous, and the amount of gratitude I owe them immense. To my beautiful wife, Taryn, thank you for your unwavering support and love throughout this endeavour. This would not have been possible without you. Evenings and weekends will be delightfully different from now on. To my beautiful daughter, Isla, thank you for ensuring the speedy finalisation of this thesis. To my parents; Aethel, Basil, Colin, and Margaret, thank you for the sacrifices you have made for me, and for providing me with the opportunity, as well as teaching me the dedication that is required, to be able to achieve such a monumental task.

“Pro Aris, Et Focis”

REFERENCES

ACTIDYN-SYSTEMES, S. (2011). *Civil Engineering Centrifuge - Model C67-4; Technical Description, Report Number: TD C67-40-0000 Rev. b.* Report TD C67-40-0000 Rev. b.,

ANON. (1977). The description of rock masses for engineering purposes: Report by the Geological Society Engineering Group Working Party. *Quarterly Journal of Engineering Geology and Hydrogeology*, 10(4), 355-388, doi: 10.1144/gsl.Qjeg.1977.010.04.01.

AOUAD, W., LANDEL, J.R., DALZIEL, S.B., DAVIDSON, J.F. & WILSON, D.I. (2016). Particle image velocimetry and modelling of horizontal coherent liquid jets impinging on and draining down a vertical wall. *Experimental Thermal and Fluid Science*, 74429-443, doi: http://dx.doi.org/10.1016/j.expthermflusci.2015.12.010.

AYDIN, A. (2001). Fracture void structure: implications for flow, transport and deformation. *Environmental Geology : International Journal of Geosciences*, 40(6), 672-677.

BARNARD, H.C. (2000). *An Explanation of the 1:500 000 General Hydrogeological Map: Johannesburg 2526*. Department of Water Affairs and Forestry, Pretoria, South Africa.

BARTON, N. (1982). *Modelling rock joint behavior from in situ block tests: implications for nuclear waste repository design.* Terra Tek, Inc. Report No. ONWI-308, Salt Lake City, UT (USA).

BARTON, N. (2004). The why's and how's of high pressure grouting-Part. *Tunnels & Tunnelling International*28.

BARTON, N. (2008). Training course on rock engineering (p. 502), Organised by ISRMTT and CSRS, course coordinator: Rajbal Singh, 10-12 December. New Delhi, India, 501.

BARTON, N., BANDIS, S. & BAKHTAR, K. (1985). Strength, deformation and conductivity coupling of rock joints. *International Journal of Rock Mechanics and Mining Sciences & Geomechanics Abstracts*. Elsevier, 121-140.

BARTON, N., BUEN, B. & ROALD, S. (2001). Strengthening the case for grouting. *T & T international*, 33(12), 34-36.

BARTON, N., BUEN, B. & ROALD, S. (2002). Strenghthening the case for grouting. *T & T international*, 34(1), 37-39.

BARTON, N. & CHOUBEY, V. (1977). The shear strength of rock joints in theory and practice. *Rock mechanics*, 10(1-2), 1-54.

BARTON, N. & DE QUADROS, E.F. (1997). Joint aperture and roughness in the prediction of flow and groutability of rock masses. *International Journal of Rock Mechanics and Mining Sciences*, 34(3-4), paper no. 252, doi: http://dx.doi.org/10.1016/S1365-1609(97)00081-6.

BARTON, N., LIEN, R. & LUNDE, J. (1974). Engineering classification of rock masses for the design of tunnel support. *Rock mechanics*, 6(4), 189-236.

BEAR, J. (1972). Dynamics of fluids in porous media. *American Elsevier, New York*.

BERKOWITZ, B. (2002). Characterizing flow and transport in fractured geological media: A review. *Advances in Water Resources*, 25(8–12), 861-884, doi: http://dx.doi.org/10.1016/S0309-1708(02)00042-8.

BIENIAWSKI, Z.T. (1989). *Engineering rock mass classifications: a complete manual for engineers and geologists in mining, civil, and petroleum engineering*. John Wiley & Sons.

BODVARSSON, G., BANDURRAGA, T. & WU, Y. (1997). The site-scale unsaturated zone model of Yucca Mountain, Nevada, for the viability assessment. *Yucca Mountain Characterization Project Report LBNL-40376, UC-814, Earth Sciences Division, Lawrence Berkeley National Laboratory, Berkeley, Calif*.

BROUWERS, L.B. (2017). *Geotechnical Centrifuge Modelling of Variably Saturated Flow at the Soil-Rock Interface.* Unpublished MSc Dissertation, University of Pretoria.

BROUWERS, L.B. & DIPPENAAR, M.A. (2018). Partially saturated flow from sand into a discrete smooth open vertical fracture at the soil-rock interface: experimental studies. *Bulletin of Engineering Geology and the Environment*, doi: https://www.doi.org/10.1007/s10064-018-1258-x.

BROWN, E.T. (1981). Rock characterization, testing & monitoring: ISRM suggested methods.

BROWN, S.R. (1987). Fluid flow through rock joints: the effect of surface roughness. *Journal of Geophysical Research: Solid Earth*, 92(B2), 1337-1347.

BRUSH, D.J. & THOMSON, N.R. (2003). Fluid flow in synthetic rough-walled fractures: Navier-Stokes, Stokes, and local cubic law simulations. *Water Resources Research*, 39(4).

BUTTERFIELD, R. (2000). Scale-Modelling of Fluid Flow in Geotechnical Centrifuges. *Journal of the Japanese Geotechnical Society: Soils and Foundation*, 40(6), 39-45.

CAWTHORN, R.G., EALES, H.V., WALRAVEN, F., UKEN, R. & WATKEYS, M.K. (2006). The Bushveld Complex. *In*: JOHNSON, M.R., ANHAEUSSER, C.R. & THOMAS, R.J. (eds.) *The geology of South Africa*. Geological Society of South Africa, Johannesburg / Council for Geoscience, Pretoria, 261-268.

CAWTHORN, R.G. & WEBB, S.J. (2001). Connectivity between the western and eastern limbs of the Bushveld Complex. *TECTONOPHYSICS -AMSTERDAM-*, 330(3-4), 195-209.

CECCONI, M., CROCE, P. & VIGGIANI, G. (2006). Physical modelling of block toppling. *Physical Modelling in Geotechnics, Two Volume Set: Proceedings of the Sixth International Conference on Physical Modelling in Geotechnics, 6th ICPMG'06, Hong Kong, 4-6 August 2006*. CRC Press, 325.

CHEN, Y.-F., ZHOU, J.-Q., HU, S.-H., HU, R. & ZHOU, C.-B. (2015). Evaluation of Forchheimer equation coefficients for non-Darcy flow in deformable rough-walled fractures. *Journal of Hydrology*, 529, Part 3993-1006, doi: http://dx.doi.org/10.1016/j.jhydrol.2015.09.021.

CHEN, Z.Y., ZHANG, J.H., WANG, W.X. & XING, Y.C. (2006). Centrifuge modelling of rock slopes. *In*: NG, C.W., WANG, Y.-H. & ZHANG, L. (eds.) *Physical Modelling in Geotechnics, Two Volume Set: Proceedings of the Sixth International Conference on Physical Modelling in Geotechnics, 6th ICPMG'06, Hong Kong, 4-6 August 2006*. CRC Press, 19-28.

CHERUBINI, C., GIASI, C.I. & PASTORE, N. (2012). Bench scale laboratory tests to analyze non-linear flow in fractured media. *Hydrol. Earth Syst. Sci.*, 16(8), 2511-2522, doi: 10.5194/hess-16-2511-2012.

CHIKATAMARLA, R., LAUE, J. & SPRINGMAN, S. (2006). Modelling of rockfall on protection galleries. *6th International Conference on Physical Modelling in Geotechnics*, 331-336.

CLARKE, B., UKEN, R. & REINHARDT, J. (2009). Structural and compositional constraints on the emplacement of the Bushveld Complex, South Africa. *Lithos*, 111(1), 21-36.

COOK, N. (1992). Natural joints in rock: Mechanical, hydraulic and seismic behaviour and properties under normal stress. *International Journal of Rock Mechanics and Mining Sciences & Geomechanics Abstracts*, 29(3), 198-223.

CULLIGAN, P. & BARRY, D. (1998). Similitude requirements for modelling NAPL movement with a geotechnical centrifuge. *Proc. Instn Civ Engrs Geotech. Engng*180-186.

CULLIGAN-HENSLEY, P.J. & SAVVIDOU, C. (1995). Environmental geomechanics and transport processes *In*: TAYLOR, R. (ed.) *Geotechnical centrifuge technology*. CRC Press, 201-271.

DEERE, D. (1968). Geological Considerations. Rock Mechanics in Engineering Practice. Stagg, RG and Zienkiewicz, DC (eds.), 1-20. New York, New York: John Wiley Publishing.

DELLA VOLPE, C., MANIGLIO, D., MORRA, M. & SIBONI, S. (2002). The determination of a 'stable-equilibrium'contact angle on heterogeneous and rough surfaces. *Colloids and Surfaces A: Physicochemical and Engineering Aspects*, 206(1), 47-67.

DIPPENAAR, M.A. & VAN ROOY, J.L. (2016). On the cubic law and variably saturated flow through discrete open rough-walled discontinuities. *International Journal of Rock Mechanics and Mining Sciences*, 89:200-211, doi: http://dx.doi.org/10.1016/j.ijrmms.2016.09.011.

DIPPENAAR, M.A., VAN ROOY, J.L., BREEDT, N., HUISAMEN, A., MURAVHA, S.E., MAHLANGU, S. & MULDERS, J.A. (2014). *Vadose zone hydrology: Concepts and techniques.* Water Research Commision (WRC) Report TT584/13, Pretoria.

DOE, T.W. (2001). What do drops do? Surface wetting and network geometry effects on vadose-zone fracture flow. *Conceptual models of flow and transport in the fractured vadose zone*243-270.

DRAGILA, M.I., HAY, K.M. & WHEATCRAFT, S.W. (2016). 9. Initial pipe development within epikarst microfractures. *Geological Society of America Special Papers*, 516129-136.

DRAGILA, M.I. & WEISBROD, N. (2003). Parameters affecting maximum fluid transport in large aperture fractures. *Advances in Water Resources*, 26(12), 1219-1228.

DRAGILA, M.I. & WEISBROD, N. (2004). Flow Across an Unsaturated Fracture Intersection. *DYNAMICS OF FLUIDS IN FRACTURED ROCK*27.

DRAGILA, M.I. & WHEATCRAFT, S.W. (2001). Free-surface films. *Conceptual models of flow and transport in the fractured vadose zone*217-241.

DU PLESSIS, C.P. & WALRAVEN, F. (1990). The tectonic setting of the Bushveld Complex in Southern Africa, Part 1. Structural deformation and distribution. *Tectonophysics*, 179(3), 305-319, doi: 10.1016/0040-1951(90)90296-K.

DU-TOIT, W.H., MULLIN, H. & JONCK, F. (1998). *1 : 500 000 Hydrogeological Map Series of the Republic of South Africa, Pietersburg 2326.* 1:500 000 Hydrogeological map series of the Republic of South Africa.

EALES, H.V. & CAWTHORN, R.G. (1996). The Bushveld Complex. *In*: CAWTHORN, R.G. (ed.) *Layered Intrusions.* Elsevier, Amsterdam, 181–230.

EBEL, B.A. & NIMMO, J.R. (2009). *Estimation of unsaturated zone traveltimes for Rainier Mesa and Shoshone Mountain, Nevada Test Site, Nevada, using a source-responsive preferential-flow model.* US Geological Survey-Henderson, Nevada,

EGGERS, M.J. (2016). Diversity in the science and practice of engineering geology. *Geological Society, London, Engineering Geology Special Publications*, 27(1), 1-18.

EID, H.T. (2007). A technique for estimating permeability of a randomly fractured rock mass. *Acta Geotechnica*, 2(2), 97-102.

EINSTEIN, H.H., LI, V., WHITMAN, R.V., VENEZIANO, D., REYES, O., IGLESIA, G. & LEE, J.-S. (1990). *Stochastic and Centrifuge Modelling of Jointed Rock.* DTIC Document,

EVANS, D.D., RASMUSSEN, T.C. & NICHOLSON, T.J. (2001). Flow and transport through unsaturated fractured rock: An overview. *Flow and transport through unsaturated fractured rock*1-18.

EWERT, F. (2003). Discussion of Rock Type Related Criteria for Curtain Grouting. *Proceedings of the Third International Conference on Grouting and Ground Improvement, ASCE Special Publication*.

EWERT, F.-K. (1985). *Rock grouting with emphasis on dam sites*. Springer-Verlag, Berlin ;.

EWERT, F.-K. (1992). Evaluation and interpretation of water pressure tests. *In*: BELL, A.L. (ed.) *Grouting in the ground.* . Thomas Telford, 141-162.

EWERT, F.-K. (1997a). Permeability, groutability and grouting of rocks related to dam sites. Part 1: Grouting examples and ground water flow in rock. *Dam Engineering*, 831-76.

EWERT, F.-K. (1997b). Permeability, groutability and grouting of rocks related to dam sites. Part 2: Permeability testing by means of water pressure tests. *Dam Engineering*, 8123-176.

EWERT, F.-K. & HUNGSBERG, U. (2018). *Rock Grouting at Dam Sites*. Springer, Cham, Switzerland.

FABRYKA-MARTIN, J., DIXON, P., LEVY, S., LIU, B., BRENNER, D., WOLFSBERG, L., TURIN, H. & SHARMA, P. (1996). Implications of environmental isotopes for flow and

transport in the unsaturated zone at Yucca Mountain, Nevada. *Geol. Soc. Am. Abstr. Programs*, A-414.

FORCHHEIMER, P. (1901). Wasserbewegung durch boden. *Zeitz. Ver. Duetch Ing.*, 451782-1788.

FOYO, A., SÁNCHEZ, M.A. & TOMILLO, C. (2005). A proposal for a Secondary Permeability Index obtained from water pressure tests in dam foundations. *Engineering Geology*, 77(1–2), 69-82, doi: http://dx.doi.org/10.1016/j.enggeo.2004.08.007.

GARNIER, J., GAUDIN, C., SPRINGMAN, S., CULLIGAN, P., GOODINGS, D., KONIG, D., KUTTER, B., PHILLIPS, R., RANDOLPH, M. & THOREL, L. (2007). Catalogue of scaling laws and similitude questions in geotechnical centrifuge modelling. *International Journal of Physical Modelling in Geotechnics*, 7(3), 1.

GAUDIN, C., WHITE, D., BOYLAN, N., BREEN, J., BROWN, T. & DE CATANIA, S. (2010). A miniature high speed wireless data acquisition system for geotechnical centrifuges. *Proceedings of 7th International Conference on Physical Modelling in Geotechnics, Zurich, Switzerland*, 229-234.

GHEZZEHEI, T.A. (2004). Constraints for flow regimes on smooth fracture surfaces. *Water Resources Research*, 40(11), n/a-n/a, doi: 10.1029/2004WR003164.

GHEZZEHEI, T.A. & OR, D. (2005). Liquid fragmentation and intermittent flow regimes in unsaturated fractured media. *Water Resources Research*, 41(12).

GLASS, R.J. & NICHOLL, M.J. (1996). Physics of gravity fingering of immiscible fluids within porous media: An overview of current understanding and selected complicating factors. *GEODERMA*, 70(2/4), 133-164.

GLASS, R.J., NICHOLL, M.J., PRINGLE, S. & WOOD, T. (2002a). Unsaturated flow through a fracture–matrix network: Dynamic preferential pathways in mesoscale laboratory experiments. *Water Resources Research*, 38(12).

GLASS, R.J., NICHOLL, M.J., RAJARAM, H. & WOOD, T.R. (2003). Unsaturated flow through fracture networks: Evolution of liquid phase structure, dynamics, and the critical importance of fracture intersections. *Water Resources Research*, 39(12).

GLASS, R.J., NICHOLL, M.J., RAMIREZ, A.L. & DAILY, W.D. (2002b). Liquid phase structure within an unsaturated fracture network beneath a surface infiltration event: Field experiment. *Water Resources Research*, 38(10).

GONZÁLEZ DE VALLEJO, L.I. & FERRER, M. (2011). *Geological engineering*. CRC Press/Balkema, Leiden, The Netherlands :.

GUDMUNDSSON, A., GJESDAL, O., BRENNER, S.L. & FJELDSKAAR, I. (2003). Effects of linking up of discontinuities on fracture growth and groundwater transport. *Hydrogeology Journal*, 11(1), 84-99.

GÜNZEL, F. & DAVIES, M. (2006). Influence of warming permafrost on the stability of ice filled rock joints. *Proceedings, 6th International Conference on Physical Modelling in Geotechnics*, 343-348.

GUROCAK, Z. & ALEMDAG, S. (2012). Assessment of permeability and injection depth at the Atasu dam site (Turkey) based on experimental and numerical analyses. *Bulletin of*

Engineering Geology and the Environment, 71(2), 221-229, doi: 10.1007/s10064-011-0400-9.

GUSTAFSON, G. & FRANSSON, Å. (2006). The use of the Pareto distribution for fracture transmissivity assessment. *Hydrogeology Journal*, 14(1-2), 15-20.

HAIMSON, B.C. & DOE, T.W. (1983). State of stress, permeability, and fractures in the Precambrian granite of northern Illinois. *Journal of Geophysical Research: Solid Earth*, 88(B9), 7355-7371.

HAKAMI, E. & LARSSON, E. (1996). Aperture measurements and flow experiments on a single natural fracture. *International Journal of Rock Mechanics and Mining Sciences & Geomechanics Abstracts*. Elsevier, 395-404.

HAMM, S.-Y., KIM, M., CHEONG, J.-Y., KIM, J.-Y., SON, M. & KIM, T.-W. (2007). Relationship between hydraulic conductivity and fracture properties estimated from packer tests and borehole data in a fractured granite. *Engineering Geology*, 92(1–2), 73-87, doi: http://dx.doi.org/10.1016/j.enggeo.2007.03.010.

HOEK, E. & BRAY, J. (1981). *Rock slope engineering*. Rev. 3rd ed. ed. Institution of Mining and Metallurgy, London :.

HOLLAND, M. (2012). Evaluation of factors influencing transmissivity in fractured hard-rock aquifers of the Limpopo Province. *Water SA*, 38(3), 379-380.

HOSSEINIAN, A., RASOULI, V. & UTIKAR, R. (2010). Fluid flow response of JRC exemplar profiles. *In*: ZHAO, J., LABIOUSE, V., DUDT, J.-P. & MATHIER, J.-F. (eds.) *Rock Mechanics in Civil and Environmental Engineering*. CRC Press, 239.

HOULSBY, A. (1976). Routine interpretation of the Lugeon water-test. *Quarterly Journal of Engineering Geology and Hydrogeology*, 9(4), 303-313.

HOULSBY, A.C. (1977). Engineering of grout curtains to standards. *International Journal of Rock Mechanics and Mining Sciences & Geomechanics Abstracts*, 15(1), A20, doi: http://dx.doi.org/10.1016/0148-9062(78)90919-1.

HOULSBY, A.C. (1990). *Construction and design of cement grouting: a guide to grouting in rock foundations*. John Wiley & Sons.

HSIEH, P.A., BAHR, J.M., DOE, T.W., FLINT, A.L., GEE, G., GELHAR, L.W., SOLOMON, D.K., VAN GENUCHTEN, M. & WHEATCRSAFT, S.W. (2001). Panel Report. *Conceptual models of flow and transport in the fractured vadose zone*. National Academies Press, Washington, DC, 9-44.

HUDSON, J.A. (1989). *Rock mechanics principles in engineering practice*.

INDRARATNA, B., PRICE, J., RANJITH, P. & GALE, W. (2002). Some aspects of unsaturated flow in jointed rock. *International Journal of Rock Mechanics and Mining Sciences*, 39(5), 555-568, doi: http://dx.doi.org/10.1016/S1365-1609(02)00057-6.

INDRARATNA, B. & RANJITH, P. (2001). *Hydromechanical aspects and unsaturated flow in jointed rock*. A.A. Balkema Publishers, Lisse [Netherlands] ;.

ITOH, K., TOYOSAWA, Y., KUSAKABE, O., NG, C., ZHANG, L. & WANG, Y. (2006). Centrifugal modelling of rockfalls. *Proceedings of the 6th International Conference on*

Physical Modelling in Geotechnics–ICPMG, Hong Kong (Ng CWW, Zhang LM and Wang YH (eds)). Taylor & Francis, London, UK, 349-354.

IWAI, K. (1976). *Fundamental studies of fluid flow through a single fracture*, Ph. D. Thesis, Univ., California, Barkeley.

JACOBSZ, S. (2011). A geotechnical centrifuge for TUKS. *Civil Engineering Magazine*, 19(3)(3), 46-48.

JACOBSZ, S. (2013a). Centrifuge modelling of a soil nail retaining wall. *Journal of the South African Institution of Civil Engineering*, 55(1), 85-93.

JACOBSZ, S. (2013b). Geotech@ TUKS. *Civil Engineering Magazine*, 21(3)(3), 61-66.

JACOBSZ, S., KEARSLEY, E. & KOCK, J. (2014). The geotechnical centrifuge facility at the University of Pretoria. *ICPMG2014–Physical Modelling in Geotechnics: Proceedings of the 8th International Conference on Physical Modelling in Geotechnics 2014 (ICPMG2014), Perth, Australia, 14-17 January 2014*. CRC Press, 169.

JAVADI, M., SHARIFZADEH, M., SHAHRIAR, K. & MITANI, Y. (2014). Critical Reynolds number for nonlinear flow through rough-walled fractures: The role of shear processes. *Water Resources Research*, 50(2), 1789-1804.

JI, S.H., NICHOLL, M.J., GLASS, R.J. & LEE, K.K. (2004). Influence of a simple fracture intersection on density-driven immiscible flow: Wetting vs. nonwetting flows. *Geophysical research letters*, 31(14).

JI, S.H., NICHOLL, M.J., GLASS, R.J. & LEE, K.K. (2006). Influence of simple fracture intersections with differing aperture on density-driven immiscible flow: Wetting versus nonwetting flows. *Water Resources Research*, 42(10).

JONES, B.R. (2014). *Geotechnical centrifuge modelling of the behaviour of a compressible clay horizon underlying a reinforced sand foundation.* M.Sc. Dissertation (unpublished), University of Pretoria.

JONES, B.R., BROUWERS, L.B. & DIPPENAAR, M.A. (2018a). Partially to fully saturated flow through smooth, clean, open fractures: qualitative experimental studies. *Hydrogeology Journal*, 26(3), 945-961, doi: 10.1007/s10040-017-1680-3.

JONES, B.R., BROUWERS, L.B., DIPPENAAR, M.A. & VAN ROOY, J.L. (2017a). Experimental studies of variably saturated flow from a horizontal discontinuity to the vertical with and without an intersection *In*: JOUGHIN, W. (ed.) *AfriRock 2017 ISRM International Symposium 'Rock Mechanics for Africa'*. SAIMM, Cape Town, South Africa, 605-618.

JONES, B.R., BROUWERS, L.B., VAN TONDER, W.D. & DIPPENAAR, M.A. (2017b). Assessing geotechnical centrifuge modelling in addressing variably saturated flow in soil and fractured rock. *Environmental Science and Pollution Research*, 24(15), 13203-13223, doi: https://doi.org/10.1007/s11356-016-8333-2.

JONES, B.R., VAN ROOY, J.L. & DIPPENAAR, M.A. (2018b). Lugeon tests at partial saturation: experimental and empirical contributions. *Rock mechanics and rock engineering*, doi: https://doi.org/10.1007/s00603-018-1592-0.

JONES, B.R., VAN ROOY, J.L. & DIPPENAAR, M.A. (2018c). On the Differing Role of Contact Obstacles on Variably Saturated Flow in Vertical and Horizontal Fractures. *In*: CATO, K. & SHAKOOR, A. (eds.) *IAEG/AEG Annual Meeting Proceedings, San Francisco, California, 2018 - Volume 4*. Springer International Publishing, Cham, 83-88.

JONES, B.R., VAN ROOY, J.L., DIPPENAAR, M.A., BROUWERS, L.B., ROUX, J.I., JOUBERT, A. & SEGOLE, K.P. (2016). *Advances in the Understanding of Variably Saturated Fracture Flow (Project K5/2326).* Water Research Commision (WRC), Pretoria, South Africa.

JONES, B.R., VAN ROOY, J.L. & MOUTON, D.J. (2018d). Verifying the Ground Treatment as Proposed by the Secondary Permeability Index during Dam Foundation Grouting. *Bulletin of Engineering Geology and the Environment*, doi: https://doi.org/10.1007/s10064-017-1219-9.

JOSEPH, P. & EINSTEIN, H. (1988). *Rock modeling using the centrifuge.* DTIC Document,

KISHIDA, K., SAWADA, A., YASUHARA, H. & HOSODA, T. (2013). Estimation of fracture flow considering the inhomogeneous structure of single rock fractures. *Soils and Foundations*, 53(1), 105-116, doi: http://dx.doi.org/10.1016/j.sandf.2012.12.007.

KONZUK, J.S. & KUEPER, B.H. (2004). Evaluation of cubic law based models describing single-phase flow through a rough-walled fracture. *Water Resources Research*, 40(2), n/a-n/a, doi: 10.1029/2003WR002356.

KUMAR, P. (2007). Scaling laws and experimental modelling of contaminant transport mechanism through soils in a geotechnical centrifuge. *Geotechnical and Geological Engineering*, 25(5), 581-590.

KUMAR, S., ZIMMERMAN, R.W. & BODVARSSON, G.S. (1991). Permeability of a fracture with cylindrical asperities. *Fluid Dynamics Research*, 7(3), 131-137, doi: http://dx.doi.org/10.1016/0169-5983(91)90053-L.

LAUT, P. (1975). Application of centrifugal model tests in connexion with studies of flow patterns of contaminated water in soil structures. *Geotechnique*, 25(2), 401-406.

LAVIOLETTE, R.A., GLASS, R., WOOD, T.R., MCJUNKIN, T.R., NOAH, K., PODGORNEY, R.K., STARR, R.C. & STONER, D.L. (2003). Convergent flow observed in a laboratory-scale unsaturated fracture system. *Geophysical research letters*, 30(2).

LAVIOLETTE, R.A. & GLASS, R.J. (2004). Self organized spatio-temporal structure within the fractured Vadose Zone: The influence of dynamic overloading at fracture intersections. *Geophysical research letters*, 31(18).

LEE, C.-H. & FARMER, I.W. (1993). *Fluid flow in discontinuous rocks*. 1st ed. ed. Chapman & Hall, London ;.

LEVY, L.C., CULLIGAN, P.J. & GERMAINE, J.T. (2002). Use of the geotechnical centrifuge as a tool to model dense nonaqueous phase liquid migration in fractures. *Water Resources Research*, 38(8).

LEVY, L.C., CULLIGAN, P.J. & GERMAINE, J.T. (2003). Modelling of DNAPL behavior in vertical fractures. *International Journal of Physical Modelling in Geotechnics*, 3(1), 01-18.

LI, B., JIANG, Y., KOYAMA, T., JING, L. & TANABASHI, Y. (2008). Experimental study of the hydro-mechanical behavior of rock joints using a parallel-plate model containing contact areas and artificial fractures. *International Journal of Rock Mechanics and Mining Sciences*, 45(3), 362-375, doi: http://dx.doi.org/10.1016/j.ijrmms.2007.06.004.

LI, X., WARTMAN, J., TANG, H., YAN, J., LUO, H. & HU, W. (2014). Dynamic Centrifuge Modelling Tests for Sliding Rock Slopes. *Landslide Science for a Safer Geoenvironment*. Springer, 75-79.

LIU, E. (2005). Effects of fracture aperture and roughness on hydraulic and mechanical properties of rocks: implication of seismic characterization of fractured reservoirs. *Journal of Geophysics and Engineering*, 2(1), 38.

LIU, H.-H., WEI, M.-Y. & RUTQVIST, J. (2013). Normal-stress dependence of fracture hydraulic properties including two-phase flow properties. *Hydrogeology Journal : Official Journal of the International Association of Hydrogeologists*, 21(2), 371-382.

LIU, Q.-Q. & FAN, H.-G. (2012). The characteristics and estimation of flow through a single rough-walled fracture. *Journal of Hydrodynamics, Ser. B*, 24(3), 315-322, doi: http://dx.doi.org/10.1016/S1001-6058(11)60250-3.

LOOK, B.G. (2014). *Handbook of geotechnical investigation and design tables*. CRC Press.

LOUIS, C. (1969). Étude des écolements d'éau dans les roches fissurées et de leur influence sur la stabilité des massifs rocheurs. *BRGM. Bulletin de la Direction des Études et Récherches. Serie A.(3)*5-132.

LUGEON, M. (1933). *Barrages et Géologie - Méthodes de recherches, terrassement et imperméabilisation*. libr. de l'Université.

MACINI, P., MESINI, E. & VIOLA, R. (2011). Laboratory measurements of non-Darcy flow coefficients in natural and artificial unconsolidated porous media. *Journal of Petroleum Science and Engineering*, 77(3), 365-374.

MAINI, Y.N. (1972). *In situ hydraulic parameters in jointed rock: their measurement and interpretation*, University of London.

MÉHEUST, Y. & SCHMITTBUHL, J. (2001). Geometrical heterogeneities and permeability anisotropy of rough fractures. *Journal of Geophysical Research: Solid Earth*, 106(B2), 2089-2102.

NEUMAN, S.P. (2005). Trends, prospects and challenges in quantifying flow and transport through fractured rocks. *Hydrogeology Journal*, 13(1), 124-147.

NICHOLL, M. & GLASS, R. (2007). Wetting phase permeability in a partially saturated horizontal fracture. *Proc. 5 th Ann. Int. Conf. On High Level Rad. Waste Mgmt*, 22-26.

NICHOLL, M., GLASS, R. & NGUYEN, H. (1993). Wetting front instability in an initially wet unsaturated fracture. *Proceedings of the Fourth High Level Radioactive Waste Management International Conference*.

NICHOLL, M., GLASS, R. & WHEATCRAFT, S. (1994). Gravity-driven infiltration instability in initially dry nonhorizontal fractures. *Water Resources Research*, 30(9), 2533-2546.

NICHOLL, M. & GLASS, R.J. (2002). *Field investigation of flow processes associated with infiltration into an initially dry fracture network at Fran Ridge, Yucca Mountain, Nevada: A photo essay and data summary.* Sandia National Labs.,

NICHOLL, M., RAJARAM, H., GLASS, R. & DETWILER, R. (1999). Saturated flow in a single fracture: Evaluation of the Reynolds equation in measured aperture fields. *Water Resources Research*, 35(11), 3361-3373.

NONVEILLER, E. (2013). *Grouting theory and practice*. Elsevier.

ÖGE, İ.F. & ÇIRAK, M. (2017). Relating rock mass properties with Lugeon value using multiple regression and nonlinear tools in an underground mine site. *Bulletin of Engineering Geology and the Environment*, doi: 10.1007/s10064-017-1179-0.

OR, D. & GHEZZEHEI, T.A. (2007). Traveling liquid bridges in unsaturated fractured porous media. *Transport in Porous Media*, 68(1), 129-151.

OR, D. & TULLER, M. (2000). Flow in unsaturated fractured porous media: Hydraulic conductivity of rough surfaces. *Water Resources Research*, 36(5), 1165-1177.

ORON, A.P. & BERKOWITZ, B. (1998). Flow in rock fractures: The local cubic law assumption reexamined. *Water Resources Research*, 34(11), 2811-2825.

PALMSTROM, A., BLINDHEIM, O. & BROCH, E. (2002). The Q-system-possibilities and limitations. *Norwegian annual tunnelling conference on Fjellsprengningsteknikk/Bergmekanikk/Geoteknikk, Oslo*, 41.41-41.38.

PALMSTROM, A. & BROCH, E. (2006). Use and misuse of rock mass classification systems with particular reference to the Q-system. *Tunnelling and Underground Space Technology*, 21(6), 575-593, doi: http://dx.doi.org/10.1016/j.tust.2005.10.005.

PALMSTROM, A. & STILLE, H. (2010). *Rock engineering*. Thomas Telford, London, United Kingdom.

PATNAIK, V. & PEREZ-BLANCO, H. (1996). Roll waves in falling films: an approximate treatment of the velocity field. *International journal of heat and fluid flow*, 17(1), 63-70.

PERRITT, S. & ROBERTS, M. (2007). Flexural-slip structures in the Bushveld Complex, South Africa? *Journal of Structural Geology*, 29(9), 1422-1429, doi: http://dx.doi.org/10.1016/j.jsg.2007.06.008.

PHILLIPS, R. (1995). Centrifuge modelling: practical considerations. *Geotechnical centrifuge technology*34-60.

PRUESS, K. (1999). A mechanistic model for water seepage through thick unsaturated zones in fractured rocks of low matrix permeability. *Water Resources Research*, 35(4), 1039-1051.

PYRAK, L.R., MYER, L.R. & COOK, N.G.W. (1985). Determination of fracture void geometry and contact area at different effective stress. *Eos Trans. AGU*, 66(46).

PYRAK-NOLTE, L.J., COOK, N.G.W. & NOLTE, D.D. (1988). Fluid percolation through single fractures. *Geophysical research letters*, 15(11), 1247-1250, doi: 10.1029/GL015i011p01247.

QIAN, J., ZHAN, H., ZHAO, W. & SUN, F. (2005). Experimental study of turbulent unconfined groundwater flow in a single fracture. *Journal of Hydrology*, 311(1–4), 134-142, doi: http://dx.doi.org/10.1016/j.jhydrol.2005.01.013.

QUADROS, E. & CORREA FILHO, D. (1993). Scale effects on the hydraulic properties determined by in situ 3-D tests. *ISRM International Symposium on Rock Mechanics, EUROCK*, 313-321.

QUINN, P.M., CHERRY, J.A. & PARKER, B.L. (2011). Quantification of non-Darcian flow observed during packer testing in fractured sedimentary rock. *Water Resources Research*, 47(9).

QUIÑONES-ROZO, C. (2010). Lugeon test interpretation, revisited. *Collaborative Management of Integrated Watersheds, 30rd Annual USSD (United States Society on Dams) Conference. US Society on Dams, Denver*, 405-414.

RANJITH, P. & DARLINGTON, W. (2007). Nonlinear single-phase flow in real rock joints. *Water Resources Research*, 43(9).

RAVEN, K.G. & GALE, J.E. (1985). Water flow in a natural rock fracture as a function of stress and sample size. *International Journal of Rock Mechanics and Mining Sciences*, 22(4), 251-261.

ROYLE, M.R. (2002). Standard operating procedures for borehole packer testing, p 22.

RUTH, D. & MA, H. (1992). On the derivation of the Forchheimer equation by means of the averaging theorem. *Transport in Porous Media*, 7(3), 255-264.

SADEGHIYEH, S., HASHEMI, M. & AJALLOEIAN, R. (2013). Comparison of permeability and groutability of Ostur dam site rock mass for grout curtain design. *Rock mechanics and rock engineering*, 46(2), 341-357, doi: 10.1007/s00603-012-0282-6.

SCHOFIELD, A.N. (1988). An introduction to centrifuge modelling. *In*: CRAIG, W.H., JAMES, R.G. & SCHOFIELD, A.N. (eds.) *Centrifuges in soil mechanics*. Balkema, Rotterdam, 1-9.

SCHRAUF, T. & EVANS, D. (1986). Laboratory studies of gas flow through a single natural fracture. *Water Resources Research*, 22(7), 1038-1050.

SCOATES, J. & FRIEDMAN, R. (2007). Determining the Age and Cooling History of the World's Largest Layered Intrusion: U-Pb Zircon-Rutile Geochronology of the Merensky Reef, Bushveld Complex, South Africa. *AGU Fall Meeting Abstracts*, 1102.

SEGOLE, K.P. (2018). *Modelling joint parameters to understand the influence of a pegmatite vein on excessive seepage at the De-Hoop dam, South Africa.* Unpublished MSc Dissertation, University of Pretoria.

SHARP, J.C. (1970). Fluid flow through fissured media. *Ph. D. thesis, Univ. of London, Imp. Coll. of Sci. and Technol.*, 181.

SILBERHORN-HEMMINGER, A., SÜS, M. & HELMIG, R. (2005a). Natural fractured porous systems. *In*: DIETRICH, P., HELMIG, R., SAUTER, M., HÖTZL, H., KÖNGETER, J., AND TEUTSCH, G. (ed.) *Flow and transport in fractured porous media.* . Springer, Berlin, 16-24.

SILBERHORN-HEMMINGER, A., SÜB, M. & HELMIG, R. (2005b). The discrete model concept. *In*: DIETRICH, P., HELMIG, R., SAUTER, M., HÖTZL, H., KÖNGETER, J., AND TEUTSCH, G. (ed.) *Flow and transport in fractured porous media*. Springer, Berlin, 32-44.

SINGH, B. & GOEL, R. (2011). *Engineering rock mass classification: tunnelling, foundations and landslides*. Elsevier.

SINGHAL, B.B.S. & GUPTA, R.P. (2010). *Applied hydrogeology of fractured rocks*. 2nd ed. ed. Springer, Dordrecht ;.

SISAVATH, S., AL-YAARUBY, A., PAIN, C.C. & ZIMMERMAN, R.W. (2003). A Simple Model for Deviations from the Cubic Law for a Fracture Undergoing Dilation or Closure. *Pure and Applied Geophysics*, 160(5), 1009-1022.

SOUTH AFRICAN COMMITTEE FOR STRATIGRAPHY, S.A.C.S. (1980). *Stratigraphy of South Africa. Part 1*. 8 ed. Republic of South Africa, Dept. of Mineral and Energy Affairs, Geological Survey, [Pretoria] :.

STILLE, H., GUSTAFSON, G. & HASSLER, L. (2012). Application of New Theories and Technology for Grouting of Dams and Foundations on Rock. *Geotechnical and Geological Engineering*, 30(3), 603-624, doi: 10.1007/s10706-012-9512-7.

STONE, K.J.L., MAQUIN, M., RICHARDS, D.J. & MONTOUCHET, M. (2013). Physical and numerical modeling of problems in homogeneous and fractured soft rock masses. *ICPMG2014 Physical Modelling in Geotechnics*. CRC Press, 413-417.

SU, G.W., GELLER, J.T., PRUESS, K. & WEN, F. (1999). Experimental studies of water seepage and intermittent flow in unsaturated, rough-walled fractures. *Water Resources Research*, 35(4), 1019-1037.

SUMNER, A.L., MENKE, E.J., DUBOWSKI, Y., NEWBERG, J.T., PENNER, R.M., HEMMINGER, J.C., WINGEN, L.M., BRAUERS, T. & FINLAYSON-PITTS, B.J. (2004). The nature of water on surfaces of laboratory systems and implications for heterogeneous chemistry in the troposphere. *Physical Chemistry Chemical Physics*, 6(3), 604-613, doi: 10.1039/B308125G.

TAYLOR, R. (1995). Centrifuges in modelling: Principles and scale effects. *In*: TAYLOR, R. (ed.) *Geotechnical centrifuge technology*. CRC Press, 20-34.

THUSYANTHAN, N. & MADABHUSHI, S. (2003). Scaling of seepage flow velocity in centrifuge models. *CUED/D-SOILS/TR326*1-13.

TOKUNAGA, T.K. & WAN, J. (1997). Water film flow along fracture surfaces of porous rock. *Water Resources Research*, 33(6), 1287-1295.

TOKUNAGA, T.K. & WAN, J. (2001). Approximate boundaries between different flow regimes in fractured rocks. *Water Resources Research*, 37(8), 2103-2111.

TOKUNAGA, T.K., WAN, J. & SUTTON, S.R. (2000). Transient film flow on rough fracture surfaces. *Water Resources Research*, 36(7), 1737-1746.

VAN TONDER, W.D. & JACOBSZ, S.W. (2017). Seepage column hydraulic conductivity tests in the geotechnical centrifuge. *Journal of the South African Institution of Civil Engineering*, 59(3), 16-24.

VEGTER, J. & SEYMOUR, A. (1995). *1 : 7 500 000 Depth to Groundwater Level Map, Groundwater Resources of the Republic of South Africa - Sheet 2.* Groundwater Resources of the Republic of South Africa - Sheet 2.

WALSH, J.B. (1981). Effect of pore pressure and confining pressure on fracture permeability. *International Journal of Rock Mechanics and Mining Sciences & Geomechanics Abstracts*, 18(5), 429-435, doi: http://dx.doi.org/10.1016/0148-9062(81)90006-1.

WEAVER, K.D. & BRUCE, D.A. (2007). *Dam Foundation Grouting*. ASCE Press.

WEISS, M., RUBIN, Y., ADAR, E. & NATIV, R. (2006). Fracture and bedding plane control on groundwater flow in a chalk aquitard. *Hydrogeology Journal*, 14(7), 1081-1093.

WENZEL, L.K. (1936). *The Thiem method for determining permeability of water-bearing materials and its application to the determination of specific yield; results of investigations in the Platte River valley, Nebraska.* US Department of the Interior, Geological Survey,

WIDMANN, R. (1996). International society for rock mechanics commission on rock grouting. *International Journal of Rock Mechanics and Mining Sciences & Geomechanics Abstracts*. Elsevier, 803-847.

WITHERSPOON, P.A. (1986). Flow of groundwater in fractured rocks. *Bulletin of the International Association of Engineering Geology*, 34(1), 103-115.

WITHERSPOON, P.A., WANG, J.S.Y., IWAI, K. & GALE, J.E. (1980). Validity of Cubic Law for fluid flow in a deformable rock fracture. *Water Resources Research*, 16(6), 1016-1024.

WITTKE, W. (1990). Rock Mechanics: Theory and Applications with Case Histories,‖ Springer. Berlin.

WOOD, T., GLASS, R., MCJUNKIN, T., PODGORNEY, R., LAVIOLETTE, R., NOAH, K., STONER, D., STARR, R. & BAKER, K. (2004). Unsaturated Flow through a Small Fracture–Matrix Network. *Vadose Zone Journal*, 3(1), 90-100.

WOOD, T.R. (2005). *The Role of Fracture Intersections in Fluid Flow in Unsaturated Fractured Rock Networks*, University of Idaho.

WOOD, T.R., NICHOLL, M.J. & GLASS, R.J. (2002). Fracture intersections as integrators for unsaturated flow. *Geophysical research letters*, 29(24).

WOOD, T.R., NICHOLL, M.J. & GLASS, R.J. (2005). Influence of fracture intersections under unsaturated, low-flow conditions. *Water Resources Research*, 41(4).

YEO, W. (2001). Effect of contact obstacles on fluid flow in rock fractures. *Geosciences Journal*, 5(2), 139-143.

YIHDEGO, Y. (2017). Hydraulic In situ Testing for Mining and Engineering Design: Packer Test Procedure, Preparation, Analysis and Interpretation. *Geotechnical and Geological Engineering*, 35(1), 29-44, doi: 10.1007/s10706-016-0112-9.

ZEIGLER, T.W. (1976). *Determination of Rock Mass Permeability.* Army Engineer Waterways Experiment Station, Vicksburg.

ZENG, Z. & GRIGG, R. (2006). A criterion for non-Darcy flow in porous media. *Transport in Porous Media*, 63(1), 57-69.

ZHANG, Z., NEMCIK, J. & MA, S. (2013). Micro- and macro-behaviour of fluid flow through rock fractures: an experimental study. *Hydrogeology Journal*, 21(8), 1717-1729.

ZHOU, J.-Q., HU, S.-H., FANG, S., CHEN, Y.-F. & ZHOU, C.-B. (2015). Nonlinear flow behavior at low Reynolds numbers through rough-walled fractures subjected to normal compressive loading. *International Journal of Rock Mechanics and Mining Sciences*, 80202-218, doi: http://dx.doi.org/10.1016/j.ijrmms.2015.09.027.

ZIMMERMAN, R.W., AL-YAARUBI, A., PAIN, C.C. & GRATTONI, C.A. (2004). Non-linear regimes of fluid flow in rock fractures. *International Journal of Rock Mechanics and Mining Sciences*, 41, Supplement 1163-169, doi: http://dx.doi.org/10.1016/j.ijrmms.2004.03.036.

ZIMMERMAN, R.W. & BODVARSSON, G.S. (1996). Hydraulic conductivity of rock fractures. *Transport in Porous Media*, 23(1), 1-30.

ZIMMERMAN, R.W., CHEN, D.-W. & COOK, N.G.W. (1992). The effect of contact area on the permeability of fractures. *Journal of Hydrology*, 139(1), 79-96, doi: http://dx.doi.org/10.1016/0022-1694(92)90196-3.

ZIMMERMAN, R.W., KUMAR, S. & BODVARSSON, G.S. (1991). Lubrication theory analysis of the permeability of rough-walled fractures. *International Journal of Rock Mechanics and Mining Sciences & Geomechanics Abstracts*, 28(4), 325-331, doi: http://dx.doi.org/10.1016/0148-9062(91)90597-F.

ZIMMERMAN, R.W. & YEO, I.W. (2000). Fluid Flow in Rock Fractures: From the Navier-Stokes Equations to the Cubic Law. *DYNAMICS OF FLUIDS IN FRACTURED ROCK*213-224.